REPORT DOCUMENTATION PAGE

1. REPORT DATE (DD-MM-YYYY)	2. REPORT TYPE	3. DATES COVERED (From - To)
30-06-2008	Final Report	27-09-2002 to 31-03-2008

4. TITLE AND SUBTITLE
Studies of the Origin and Evolution of Ionospheric Irregularities and Their Effects on AF Systems

5a. CONTRACT NUMBER
F19628-02-C-0087

5b. GRANT NUMBER

5c. PROGRAM ELEMENT NUMBER
61102F

6. AUTHOR(S)
C.E. Valladares, R. Sheehan, and E. MacKenzie

5d. PROJECT NUMBER
2301

5e. TASK NUMBER
SD

5f. WORK UNIT NUMBER
A4

7. PERFORMING ORGANIZATION NAME(S) AND ADDRESS(ES)
Boston College
Institute for Scientific Research
140 Commonwealth Avenue
Chestnut Hill, MA 02467-3862

8. PERFORMING ORGANIZATION REPORT NUMBER

9. SPONSORING / MONITORING AGENCY NAME(S) AND ADDRESS(ES)
Air Force Research Laboratory
29 Randolph Road
Hanscom AFB, MA 01731-3010

10. SPONSOR/MONITOR'S ACRONYM(S)
AFRL/RVBXI

11. SPONSOR/MONITOR'S REPORT NUMBER(S)
AFRL-RV-HA-TR-2008-1054

12. DISTRIBUTION / AVAILABILITY STATEMENT
Approved for Public Release; Distribution Unlimited.

13. SUPPLEMENTARY NOTES

14. ABSTRACT
We conducted a comprehensive investigation of the Earth's ionosphere under quiet and disturbed magnetic conditions. During magnetic storms, we determined that two plasma processes can produce mid-latitude irregularities. One was related to the auroral oval dynamics and produced short-scale structures. The other was SED-related and generated large-scale irregularities. We also studied the characteristics of the TIDs that were generated near the northern and southern ovals during a magnetic storm, and found a pronounced inter-hemispheric asymmetry. We discovered that airglow intensity of polar cap patches can vary due to the passage of gravity waves. A numerical simulation reproduced the variability of the airglow emissions within the patches. Other studies involved analyzing in detail the preconditioning of the low-latitude ionosphere before the onset of plasma bubbles, comparing the statistics of zonal drifts as observed by different UHF scintillation systems, and understanding the electro-dynamics of the low and middle latitude ionosphere during super storms. We directed two campaigns with the Sondrestrom radar in coordination with the Qaanaaq and Ny Alesund imagers. We operated an all-sky imager at Vize Island during two winters observing a type of auroral arcs that extend equatorward from the cusp. We also supported the AFRL-SCINDA program with technical, logistic and management efforts.

15. SUBJECT TERMS
Plasma structures, Geomagnetic storms, Total electronic content

16. SECURITY CLASSIFICATION OF:			17. LIMITATION OF ABSTRACT	18. NUMBER OF PAGES	19a. NAME OF RESPONSIBLE PERSON
a. REPORT	**b. ABSTRACT**	**c. THIS PAGE**	SAR	117	Todd Pedersen
UNCLASSIFIED	UNCLASSIFIED	UNCLASSIFIED			**19b. TELEPHONE NUMBER** (Include area code) 781-377-2845

AFRL-RV-HA-TR-2008-1054

Studies of the Origin and Evolution of Ionospheric Irregularities and Their Effects on AF Systems

C. E. Valladares
R. Sheehan
E. MacKenzie

Boston College
Institute for Scientific Research
140 Commonwealth Ave.
Chestnut Hill, MA 02467-3862

Final Report

30 June 2008

2008 1204208

DTIC COPY

NOTICE AND SIGNATURE PAGE

AFRL-RV-HA-TR-2008-1054 HAS BEEN REVIEWED AND IS APPROVED FOR PUBLICATION IN ACCORDANCE WITH ASSIGNED DISTRIBUTION STATEMENT.

//Signature//

//Signature//

TODD PEDERSEN
Contract Manager

JOEL MOZER, Chief
Space Weather Center of Excellence

Table of Contents

Figures

1. INTRODUCTION

Much research during this contract has focused on the ionospheric effects of intense magnetic storms, particularly in the equatorial and mid-latitude regions, on the characterization of traveling ionospheric disturbances (TIDs) during these events, on the formation and evolution of polar cap patches during geomagnetic storms, and on the background conditions of the low latitude ionosphere during the existence of plasma irregularities. These ionospheric effects have a serious impact on communication and navigation systems. Over the five-year span of this contract, the Air Force Research Laboratory (AFRL) has supported a SCINDA program to specify and forecast low-latitude scintillations. SCINDA is a real-time, data-driven communication outage forecast and alert system developed to assist users of space-based communication and navigation systems. SCINDA was also designed to support research on the formation of low-latitude ionospheric structures. Several efforts have been conducted under this contract in support of this task.

2. IONSPHERIC EFFECTS DURING MAGNETIC STORMS

2.1. Mid-Latitude Plasma Structuring Observed During Large Magnetic Storms

Multi-technique observations conducted during the October 29-31, 2003, magnetic storm were utilized to investigate the processes that produce mid-latitude ionospheric irregularities during large magnetic storms. The observations included VHF scintillation (S_4) from Hanscom AFB, 2-D maps of Total Electron Content (TEC) and TEC fluctuations, views of daytime aurora, and TIMED GUVI images. These observations indicated that two distinct classes of plasma processes produced mid-latitude ionospheric irregularities. One was associated with auroral plasma processes; the other, with storm-induced density (SED) gradients, a part of which occurred in close proximity to sub-auroral polarizations streams (SAPS) electric fields. The auroral oval, observed as far south as Hanscom AFB on this day, is linked with the small-scale structuring responsible for amplitude scintillation. The larger scale-length irregularities associated with intense TEC fluctuations, observed equatorward of the auroral oval, were linked with SED gradients. This work is summarized in the paper, "Two components of ionospheric plasma structures at mid-latitudes observed during the large magnetic storm of October 30, 2003," by Sunanda Basu, S. Basu, J. J. Makela, R. E. Sheehan, E. MacKenzie, P. Doherty, J. W. Wright, M. J. Keskinen, D. Pallamraju, L. J. Paxton, and F. T. Berkey, *Geophys. Res. Lett.*, 32, L12S06, doi:10.1029/2004GL021669, 2005.

2.2. Simultaneous Observations of Plasma Structuring at Equatorial and Mid-Latitudes

To investigate the near simultaneous formation of ionospheric plasma density structures at middle and equatorial latitudes during the intense magnetic storms of October 29-31, 2003, July 15, 2000, and March 30-31, 2001, scintillation observations from 3 stations: Ancon, Ascension Island, and Hanscom AFB were systematically analyzed. The evolution of plasma structures was explored by using amplitude scintillation of satellite signals at 250 MHz and by considering the detection of plasma bubbles with DMSP satellites. The sharp onset of amplitude scintillation at Hanscom AFB was attributed to the auroral oval moving unusually south and reaching typical sub-auroral locations. These mid-latitude scintillation events occurred at the time of rate of

change in Dst index > 50 nT, caused by rapid ring current injections. During the magnetic storm of October 29-31, 2003, amplitude scintillation was not observed at Ancon, but was seen at Ascension Island at approximately 20 UT on both October 29 and October 30. There were also times amplitude scintillation events were observed at Hanscom AFB, preceding the Ascension Island onset by approximately 25 minutes. The magnetic storm of July 15-16, 2000 exhibited a similar pattern. During the magnetic storm of March 31 - April 1, 2001, equatorial scintillation observations were not available for comparison with amplitude scintillations observed at Hanscom AFB. It was found that DMSP detected deep plasma density depletion in the longitudinal region corresponding to local sunset during the onset of the magnetic storm. Comparisons of amplitude scintillation (S_4) observed at the equatorial stations of Ancon, Peru and Ascension Island with that observed at the mid-latitude Hanscom AFB station have corroborated that intense scintillation is seen in the longitude sectors for which the time of large rate of change of Dst index corresponds to local sunset. This work concluded that the onset of equatorial scintillations is delayed from that at mid-latitudes by about 20 minutes, which can be accounted for by considering instantaneous electric field penetration and plasma instability growth time of the equatorial irregularities. This effort is described in the paper, "Near-simultaneous plasma structuring in the mid-latitude and equatorial ionosphere during magnetic superstorms," by S. Basu, Sunanda Basu, K..M. Groves, E. MacKenzie, M.J. Keskinen, and F.J. Rich, *Geophys. Res. Lett.*, 32, L12S05, doi:10.1029/2004GL021678, 2005.

2.3. Equatorial Ionosphere Response to Penetration Electric Fields

The response of the equatorial ionosphere at dusk to penetration electric fields during intense magnetic storms of the October 29-31, 2003, and November 20, 2003, was studied using space- and ground-based diagnostics that provided the vertical and latitudinal structures of the ionosphere. During the October 2003 storm, DMSP measured equatorial plasma bubbles and deep plasma bite-outs in the time frame of both the rapid decrease in sym-H and sym-H minimum. One of the DMSP passes was close to the Ascension Island sub-ionospheric intersection point, linking the plasma bubbles with intense amplitude scintillation that was observed at Ascension Island during this storm. Another DMSP pass observed a deep plasma bite-out in conjunction with a large height increase suggesting a plasma uplift of the low-latitude ionosphere. A similar multi-technique approach was used to study the November 20, 2003, magnetic storm. TEC values measured by the TOPEX satellite, close to the DMSP track, showed low TEC near the magnetic equator with very high TEC at the crest of the equatorial anomaly, indicating plasma uplifted near the magnetic equator and then transported along magnetic field lines. Based on these observations, it was concluded that for both storms, the dusk sector corresponding to the UT interval between the fast decrease of the SYM-H index and minimum SYM-H value dictates the longitude interval populated by equatorial plasma bubbles and depletions. It was also found that in the dusk sector, the eastward penetration electric field, associated with rapid SYM-H decrease, adds to the postsunset eastward electric field. It was concluded that the enhanced E field at dusk causes the rapid uplift of the ionosphere and sets off plasma instabilities to form bubbles and bite-outs. This investigation is described in the paper entitled, "Response of the equatorial ionosphere to prompt penetration electric fields during intense magnetic storms," by S. Basu, Sunanda Basu, F.J. Rich, K.M. Groves, E. MacKenzie, C. Coker, Y. Sahai, P.R. Fagundes, and F. Becker-Guedes, *J. of Geophys. Res.*, 112, A08308, doi:10.1029/2006JA012192, 2007.

2.4. The Ionospheric Response in the Brazilian Sector

A close comparison of the ionospheric conditions during a magnetically disturbed day with the previous undisturbed day was conducted to understand the variability that a storm produces at low latitudes. It was found that after 4 hours from the storm's sudden commencement, the ionosonde data on November 20, 2003, indicated the presence of TID-type perturbations associated with gravity waves, a feature not seen in ionosonde observations of November 19 (quiet day). An ionospheric sounder located near the magnetic equator observed an unusual lifting of the F region at about 16 UT. The TEC at locations away from the equator showed unusually high TEC values, indicating the development of a strong fountain effect during the storm's main phase. During the quiet day, TEC observations did not exhibit this level of enhancement. This study is described in the paper, "The ionospheric response in the Brazilian sector during the super geomagnetic storm on 20 November 2003," by F. Becker-Guedes, Y. Sahai, P. R. Fagundes, E. S. Espinoza, V. G. Pillat, W. L. C. Lima, Sunanda Basu, S.. Basu, Y. Otsuka, K. Shiokawa, E. M. MacKenzie, X. Pi, and J. A. Bittencourt, *Ann. Geophys.* 25, 863-873, 2007.

2.5. Neutral Composition Enhancements Due to Magnetic Storms

It was found that during the storm of 6 November 2001, the daytime red line emissions at Carmen Alto, Chile, were 2-3 times larger in the morning (0530-0830 LT) on the disturbed day compared to the quiet days. We interpreted that these emission enhancements were due to an increase in the neutral density brought in from high latitudes as a direct effect of the magnetic storm. This work is described in the paper entitled, "Magnetic storm-induced enhancement in neutral composition at low latitudes as inferred by $O(^1D)$ dayglow measurements from Chile," by D. Pallamraju, C. Chakrabarti, and C. E. Valladares, *Ann. Geophys.*, 22, 3241-3250, 2004.

2.6. Simultaneous Observation of TIDs in Both Hemispheres During a Geomagnetic Storm

Using TEC values collected by 263 GPS receivers, it was demonstrated that TIDs can propagate simultaneously in the Northern and Southern hemispheres and at high, mid, and low latitudes. The TID observations pertained to the magnetically disturbed period of October 29-30, 2003. It was found that in the northern hemisphere, the preferred scale size varied between 1500 and 1800 km; the propagation velocity was near 700 m/s and the perturbation amplitude about 1-TEC unit (TECu). In the southern hemisphere, the scale size of the TECP was as large as 2700 km, the velocity was about 550 m/s, and the TECP amplitude was 3 TECu. It was suggested that the differences in the local conductivity between northern and southern auroral ovals possibly created a different Joule heating energy term, changing the characteristics of the source regions in the opposite auroral ovals. This investigation is described in the paper, "Simultaneous Observation of traveling ionospheric disturbances in the northern and southern hemispheres," by C. E. Valladares, J. Villalobos, M.A. Hei, R. Sheehan, Su. Basu, E. MacKenzie, P.H. Doherty, and V. H. Rios, submitted to *Annales Geophysicae*, 2007. A copy of this paper is attached to this report (Appendix A).

2.7. Theoretical Modeling of the Low-Latitude Ionosphere Response to a Large Geomagnetic Storm

We studied the ionospheric response in the Peruvian sector to large upward drifts (> 50 m/s) by theoretically calculating plasma densities as a function of altitude, latitude, and local time using the time-dependent LLIONS model. We chose three large storms in 2003 (29 and 30 October and 20 November). Our results indicated that the large upward plasma drift on October 29 produced equatorial anomaly crests at ±20° dip latitude rather than the usual ±16° dip latitude. Comparison of the theoretically calculated ionospheric parameters with ground-based GPS observations of TEC values and DMSP in-situ density values demonstrated that when realistic values of the vertical drift were incorporated, the comparisons were in reasonable agreement. This investigation is described in the paper entitled, "Theoretically modeling the low-latitude, ionospheric response to large geomagnetic storms," by D. Anderson, A. Anghel, E. Araujo, V. Eccles, C. E. Valladares, and C. Lin, *Radio Sci.*, *41*, RS5S04, doi:10.1029/2005RS003376, 2006.

2.8. Polar Cap Patches During a Geomagnetic Storm

We investigated the characteristics of polar cap patches during the recovery phase of the major magnetic storm of November 20, 2003. During this event, the Qaanaaq imager observed elongated, rounded, and small-scale break-off patches. The Qaanaaq imager also observed sudden intensifications in the patch airglow brightness when the F-region altitude descended.

The Sondrestrom incoherent scatter (IS) radar measured additional patches placed close to, but poleward of, the oval-polar cap line. The DMSP-F13 satellite, passing near Qaanaaq and Sondrestrom, intersected topside density enhancements which coincided with the imager, digisonde, and IS patches.

We also developed a trajectory analysis technique able to step backward in time the location of the patches to investigate the origin and formation mechanism of the polar cap patches. Based on this analysis, it was concluded that most of the patches seen between 2000 and 2400 UT were part of the tongue-of-ionization (TOI), previously reported by *Foster et al.* [2005]. However, the patches observed by the Sondrestrom radar near the polar cap boundary were probably circulating along a reduced afternoon cell, producing elongated and stretched density enhancements.

We inspected the SuperDARN velocities at the time patches were entering the polar cap (1941 UT). We concluded that there was spatial and temporal agreement between a narrow channel of enhanced SuperDARN velocities (green velocities) and a sector of reduced densities. It was suggested that the polar cap patches were formed by a large plasma jet that was confined to a narrow longitudinal band.

We investigated the variability of the patch brightness using the Global Theoretical Ionospheric Model (GTIM) code to conduct numerical simulations of the polar cap ionosphere. Inputs to the model were the SuperDARN convection patterns and a variable upward/downward component of the neutral wind, as was observed within the polar cap during the transit of large-scale gravity waves (GW). The numerical results indicate that variations in the airglow intensity of about 450 Rayleighs can be produced by a constant 75-m/s downward vertical wind. We concluded that airglow images collected deep inside the polar cap, together with a robust trajectory analysis and Super DARN measurements can be used to discern different formation

4

mechanisms of polar cap patches. This work effort is described in the paper entitled, "Polar cap patches observed during the magnetic storm of November 2003: observations and modeling," by C. E. Valladares, T. Pedersen, and R. Sheehan, submitted to *J. Geophys. Res.* A copy of this paper is included in this report (Appendix A).

Figure 1. 630.0-nm airglow emissions from Qaanaaq, Greenland observed at 2009 UT on November 20, 2003, projected to 250-km altitude. The trajectory of the DMSP-F13 pass is plotted in red. The red dots indicate the minute at which the satellite passed near Qaanaaq. The density measured by the DMSP-F13 satellite is shown in the right panel. Enhanced densities corresponding to polar cap patches and measured by the Sondrestrom radar during two consecutive composite scans are indicated in green.

We inspected the SuperDARN velocities as the time patches were entering the polar cap (1941 UT). We concluded that there was spatial and temporal agreement between a narrow channel of enhanced SuperDARN velocities (green velocities) and a sector of reduced densities. It was suggested that the polar cap patches were formed by a large plasma jet that was confined to a narrow longitudinal band.

We investigated the variability of the patch brightness using the Global Theoretical Ionospheric Model (GTIM) code to conduct numerical simulations of the polar cap ionosphere. Inputs to the model were the SuperDARN convection patterns and a variable upward/downward component of the neutral wind, as was observed within the polar cap during the transit of large-scale gravity waves (GW). The numerical results indicate that variations in the airglow intensity of about 450 Rayleighs can be produced by a constant 75-m/s downward vertical wind. We concluded that airglow images collected deep inside the polar cap, together with a robust trajectory analysis and SuperDARN measurements, can be used to discern different formation mechanisms of polar cap patches. This work effort is described in the paper entitled, "Polar cap patches observed during the magnetic storm of November 2003: observations and modeling," by

C. E. Valladares, T. Pedersen, and R. Sheehan, submitted to *J. Geophys. Res.* A copy of this paper is included in this report (Appendix A).

2.9. Numerical Simulation of Low-Latitude TEC During the Storm of November 9, 2004

We conducted a careful analysis and simulations of the TEC data collected near the western coast of South America during the days of the magnetic storm of November 2004. On November 9, 2004, the Jicamarca IS radar observed the largest ExB vertical drifts that have ever been observed (120 m/s). These drifts were followed by large downward drifts, which persisted between 21 (16) and 02 UT (21 LT). TEC latitudinal profiles (see Figure 2a), observed on November 09, show a strong anomaly formed in response to the upward drifts and a sudden decay that starts near 21 UT (16 LT). However, it is only the northern crest that decays rapidly as the southern crest remains near 90 TEC units. We conducted simulations of the equatorial ionosphere using the LLIONS model and found that a constant northward 50-m/s meridional wind can explain the slow decay of the southern crest. The northward meridional wind was able to lift the southern hemisphere densities, in this way counter-acting the downward ExB motion of the ionosphere. Figure 2b shows the results of the modeling work.
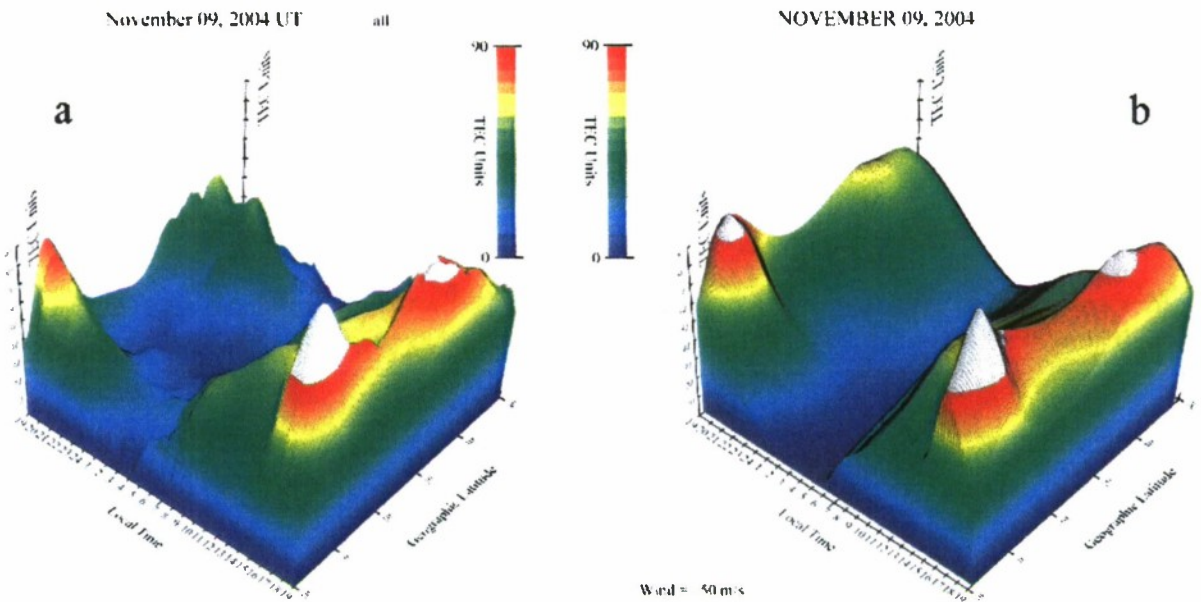
Figure 2. (a) Three-dimensional map of TEC measured by the chain of GPS receivers near the west coast of South America. (b) TEV value calculated by the LLIONS model using Jicamarca drift values and a northward wind equal to 50 m/s.

3. DEVELOPMENT OF AN EMPIRICAL THERMOSPHERIC DENSITY MODEL

We developed a simple algorithm that contained the local time, latitude, altitude, and solar flux dependence of the dTc parameter (differential Tc). The temperature Tc is defined as the global nighttime minimum of the exospheric temperature for quiet magnetic conditions. Values of dTc were input to the Jacchia71 model to achieve a better agreement with the true densities. The satellite drag measurements that were used corresponded to 38 satellites and for the years

between 1979 and 2003. The new altitude, longitude, latitude, solar cycle, dependencies of the thermospheric density reduced the standard deviation to 10% for the new model compared to 16% for the Jacchia model. New exospheric temperature and semiannual density equations were employed to represent the thermospheric density variations. The temperature corrections were also developed for diurnal effects. This effort is described in the paper, "The JB2006 empirical thermospheric density model," by B. R. Bowman, W. K. Tobiska, F. A. Marcos, and C. E. Valladares, *J. Atm. and Solar-Terr. Phys.*, 70, 5, 774-793, 2008.

4. STUDIES OF EQUATORIAL PLASMA STRUCTURES

4.1. Multipoint Observations of Equatorial Plasma Bubbles

Comparison between observations with the JULIA radar, the Ancon scintillation monitor, and the plasma density sensor on-board the DMSP satellites were carried out for years 1998 and 1999. It was observed that DMSP detected bubbles on only 9 of the 29 nights when JULIA observed plumes. It also compared the number of nights with $S_4 > 0.8$ at Ancon with the DMSP observations for data accumulated between May 1994 and the first quarter of 2001. It was concluded that for solar minimum conditions, DMSP encountered very few plasma bubbles. However, for years near solar maximum, the scintillation and DMSP data sets were well-correlated. There were more nights with S_4 values larger than 0.8 at Ancon than plasma bubbles encountered by DMSP satellites. It was found that the correlation coefficient between bubble observations and scintillation activity was equal to 0.88. This pointed out that bubble detection at 840 km is a good indicator that scintillation activity is occurring near the spacecraft's longitude. This study is fully described in the paper entitled, "Multipoint observations of equatorial plasma bubbles," by W. J. Burke, C.Y. Huang, C.E. Valladares, J.S. Machuzak, L.C. Gentile, and P.J. Sultan, *J. Geophys. Res., 108*(A5), 1221, doi:10.1029/2002JA009382, 2003.

4.2. Characteristics of the TEC Latitudinal Profiles During Low-Latitude Scintillation Events

We used a network of GPS receivers with sufficient latitudinal span to measure the TEC at both crests of the equatorial anomaly. The network also provided the latitudinal extension of GPS scintillations and TEC depletions. Additionally, density profiles collected with the Jicamarca digisonde and JULIA power maps were used to investigate the background conditions of the nighttime ionosphere that prevailed during the formation and the persistence of plasma depletions. It was demonstrated that multiple sights of TEC depletions from different stations can be used to estimate the drift of the background plasma, the tilt of the plasma plumes and, in some cases, even the approximate time and location of the depletion onset. It was demonstrated that scintillations/depletions can occur when the TEC latitude profiles are symmetric, asymmetric or highly asymmetric; this is during the absence of one crest. Comparison of the location of the northern crest of the equatorial anomaly and the maximum latitude of scintillations revealed that for 90% of the days, scintillations were confined within the boundaries of the 50% decay limit of the anomaly crests. Our results were in agreement with early results endorsing the view that GPS scintillations/TEC depletions mainly occur when the altitude of the magnetic equator F region was above 500 km. Nevertheless, in many instances, GPS scintillations and TEC depletions were observed to exist when the F layer is well below

500 km or to persist when the F layer undergoes its typical nighttime descent. Close inspection of the TEC profiles during these events indicated that the ratio of the crest-to-equator TEC was above 2 and the crests were displaced 10° or more from the magnetic equator. These findings provided experimental verification that the Rayleigh-Taylor instability mechanism, when applied to low latitudes, needs to include flux-tube integrated quantities. This work is further explained in the paper entitled, "Latitudinal extension of low-latitude scintillations measured with a network of GPS receivers," by C. E. Valladares, J. Villalobos, R. Sheehan, and M.P. Hagan, *Annales of Geophys.*, 22, 3155 - 3175, 2004. A copy of this paper is attached to this report (Appendix A).

4.3. Effect of the Reverse Fountain on Scintillation Inhibition

We advance the idea that the seeming control that the reverse fountain effect exerts on inhibiting or suppressing GPS scintillations may be related to the redistribution of the density and plasma transport from the crests of the anomaly toward the equatorial region and, then, to much lower altitudes, and the simultaneous decrease of the F-region altitude. These two effects originate a decrease of the crest/trough ratio and a reduction of the crests separation, making the whole flux tube more stable to the RTI. The correspondence between crest separation, altitude of the equatorial F region, the onset of depletions, and the altitude (latitude) extension of plumes (GPS scintillations) can be used to track the fate of the density structures. This investigation is further explained in the paper entitled, "Latitudinal extension of low-latitude scintillations measured with a network of GPS receivers," by C. E. Valladares, J. Villalobos, R. Sheehan, and M.P. Hagan, *Annales of Geophys.*, 22, 3155 - 3175, 2004.

4.4. Model of the Equatorial Zonal Drift

We constructed an empirical model of average drift over a wide range of Kp, solar flux conditions, day of the year and local time. The drift measurements were obtained using UHF scintillation receivers equipped with antennas spaced in the east-west direction that operated at Ancon since 1994. A complete description of the equations and coefficients to be used to derive the values of the zonal drift were also presented in the Appendix of the publication. This study also found that vertical drifts could contribute to the variability of drift measurements, especially for low elevation observations. We found that our zonal drift model agrees well with other models that have been derived based on radar or satellite observations. For a complete list of the coefficients, see the publication entitled, "Equatorial ionospheric zonal drift model and vertical drift statistics from UHF scintillation measurements in South America," by R. Sheehan and C. E. Valladares, *Annales of Geophys.*, 22, 3177 – 3193, 2004. A copy of this paper is attached to this report (Appendix A).

4.5. Longitudinal Variability of Low-Latitude Scintillations

We used TEC values and scintillation indices collected by 10 GPS receivers located near the western coast of South America to find the maximum latitude to which the irregularities extend and to infer the maximum altitude of the plasma bubbles. We consistently observed a greater number of GPS scintillation events at the eastern longitudes over the Amazon rainforest. It was suggested that this finding could be explained by a larger population of gravity waves at the

longitudes east of the Andes. This work is described in the paper entitled, "A Latitudinal network of GPS receivers dedicated to studies of equatorial spread-F," by C. E. Valladares, R. Sheehan, and J. Villalobos, *Radio Sci.*, 39, RS1S23, doi: 10.1029/2002RS002853, 2004. A copy of this paper is attached here (Appendix A).

4.6. Longitudinal Variability of Equatorial Plasma Bubbles

We compared observations of equatorial plasma bubbles by the DMSP and ROCSAT satellites and found that the longitudinal distributions were qualitatively similar, with both showing significantly fewer occurrences than expected near the west coast of South America. A chain of GPS receivers extending from Colombia to Chile measured a west-to-east gradient in S_4 values confirming the satellite results. We suggested that precipitation of energetic particles from the inner radiation belt causes the dearth of plasma bubbles. Enhancements in the postsunset ionospheric conductance near the South Atlantic Anomaly cause a decrease in growth rate for the generalized Rayleigh-Taylor instability. A description of this work is contained in the paper "Longitudinal variability of equatorial plasma bubbles observed by DMSP and ROCSAT-1" by W. J. Burke, L. C. Gentile, C. Y. Huang, C. E. Valladares, and S. Y. Su, *J. Geophys. Res.*, 109, A12301, doi: 10.1029/2004JA010583, 2004.

4.7. Longitudinal Variability of Plasma Structuring Between the American and Asian Sectors

We used ground-based measurements from the SCINDA network, the GUVI imager, TOPEX, and a chain of GPS receivers in combination with the USU GAIM assimilation model to closely study the relationship between the large-scale ionization distribution and small-scale irregularities at low latitudes in both scintillating and non-scintillating longitude sectors. Under quiet magnetic conditions, we observed intense scintillation activity in the South American-Atlantic sector, whereas, an absence of scintillations was seen in the far east Asian sector. It was found that the USU-GAIM assimilation model reproduced quite well the TEC observed by GUVI and TOPEX in the Asian sector. However, the model did not specify the background ionosphere in the American sector. This work is described in the paper entitled, "Extreme longitudinal variability of plasma structuring in the equatorial ionosphere on a magnetically quiet equinoctial day," by S. E. McDonald, Sunanda Basu, S. Basu, K. M. Groves, C. E. Valladares, L. Scherliess, D. C. Thompson, R. W. Schunk, J. J. Sojka, L. Zhu, *Radio Sci.*, *41*, RS6S24, doi:10/1029/2005RS003366, 2006.

4.8. Relationship between Pre-Reversal Maximum Velocity and Peak-to-Valley Ratio of Anomaly TEC

We used the low-latitude density model developed at AFRL to demonstrate that a linear relationship with statistically significant correlation coefficients existed between the maximum value of the postsunset plasma drift velocity (pre-reversal enhancement) and the peak-to-valley ratio of the anomaly TEC. This relationship was successfully validated using Jicamarca drift velocity to drive the density model and TEC values measured by a latitudinal network of GPS receivers in South America. It was found that the maximum value of the postsunset vertical plasma drift velocity is important for determining both the intensity and the latitudinal

distribution of equatorial scintillation. However, it was also found that a crucially important parameter was the meridional neutral wind velocity. This study is described in the paper entitled, "Theoretical relationships between maximum value of the post-sunset drift velocity and peak-to-valley ratio of anomaly TEC," by B. Basu, J. M. Retterer, O. de la Beaujardiere, C. E. Valladares, and E. Kudeki, *Geophys. Res. Lett.*, 31, L03807, doi: 10.1029/2003GL018725, 2004.

4.9. Short-Term Relationship Between Solar Soft X-Ray Irradiances and Equatorial TEC

The main finding of this study consisted of TEC showing a more significant correlation with soft X-ray irradiances than with F10.7. It was found that X-rays lead the TEC by approximately 0.8-1.3 days. The magnitude of these short-term (27 days or less) changes is approximately 0.18 of the total TEC. It was also demonstrated that geomagnetic activity, as represented by Ap, could account for half as much variation in TEC (0.1 of total TEC) as the solar irradiance. This work is described in "On the short-term relationship between solar soft X-ray irradiances and equatorial total electron content (TEC)" by X. Wang, R. Eastes, S. Weichecki Vergara, S. Bailey, C. E. Valladares, and T. Woods, *J. Geophys. Res.*, 111, A10S15, doi:10.1029/2005JA011488.

4.10. Short Term Relationship Between Solar Soft X-Ray Irradiances and Equatorial Plasma Density

This study used equatorial peak electron density measured by the Jicamarca digisonde and solar soft X-ray measurements from both the SNOE and TIMED satellites, as well as EUV measurements from the TIMED satellite. Similar to the previous study, we found higher correlations between soft X-rays with foF2 at short time scales (27 days or less) than EUV does. We also found that for the short term variations, both SNOE and TIMED observations, had a higher correlation in the morning (~0.46) than in the afternoon (~0.1). This work is described in "Short-term relationship between solar irradiances and equatorial peak electron densities" by X. Wang, R. Eastes, B. W. Reinisch, S. Bailey, C. E. Valladares, and T. Woods, *J. Geophys. Res.*, 112, A06310, doi:10.1029/2006JA012128.

4.11. Comparison of CHAMP and Digisonde Plasma Frequencies at Jicamarca

We compared in situ density measurements made by CHAMP and ionospheric plasma frequencies at the altitude of the CHAMP satellite deduced from ionosonde true-height profiles for Jicamarca. We found that the differences were well within the uncertainties associated with the ionosonde profiles. More specifically, we found that for satellite-ionosonde separations of less than 250 km and for satellite altitudes below the peak of the F_2 layer, the average discrepancy between the two plasma frequencies is 0.25 MHz or 4%. Based on these positive results, and using CHAMP passes at altitudes above the peak of the F_2 layer at Jicamarca, it was possible to confirm that the ionosonde plasma frequency profile can be extended quite reliably up to three scale heights above the F_2 peak by assuming a Chapman layer shape with a constant scale height equal to that derived for the profile just below the peak. A description of this work is contained in the paper entitled, "Comparison of CHAMP and Digisonde plasma frequencies at Jicamarca, Peru, " by L. F. McNamara, D. L. Cooke, C. E. Valladares, and B. W. Reinisch, *Radio Sci.*, 42, RS2005, doi:10.1029/2006RS003491.

10

4.12. Observation of Bottomside Sinusoids (BSS)

A second type of plasma irregularity different than plasma bubbles can grow in the nighttime equatorial ionosphere. This type of irregularity, known as bottomside sinusoids or BSS, can be distinguished by its almost monochromatic spectral characteristics centered near a 1-km wavelength, their association with frequency-type spread ionograms, and their confinement to the F-region bottomside. A correlative study between the occurrence of BBS-type irregularities and the latitudinal profiles of TEC was conducted compiling a list of 21 events, which presented low or high levels of frequency-type spreading. These cases were accompanied with weak, moderate or strong levels of UHF scintillations, absence of TEC depletions at all 15 GPS sites, and no JULIA coherent echoes at the height of the frequency spreading. Based on the multi-technique characteristics of these 21 events, we concluded that BSS-type irregularities developed near the 76° W meridian and that these structures originated the particular signatures seen by the digisonde, GPS and scintillation receivers. The TEC latitudinal profiles exhibit a strong asymmetry in the amplitudes of the crests. It consistently shows a prevailing northern crest exceeding the southern crest by 60 TEC units. This asymmetry implied the presence of a strong transequatorial meridional wind blowing northward that pushed the density profiles located north of the magnetic equator toward lower altitudes.

Figure 3 shows the TEC latitudinal distribution observed on November 10, 2002 when frequency-type traces originated near 0200 UT (lower frames) and strong UHF scintillations were seen at Ancon and Antofagasta. The simultaneous onset of UHF scintillations at 2 locations separated by 600 km gives a lower limit to the east-west extension of the unstable region.

4.13. The Dependence of Latitudinal Profiles of Zonal Drifts on the TEC Values

We conducted a comparative study of the zonal velocities measured by the spaced-antenna scintillation systems that are located at Ancon, Antofagasta and Bogota. The Ancon and Antofagasta systems are quite similar; both are formed by antennas separated by 110 m in the east-west direction, which are used to measure the zonal drift of the irregularities. These two systems are spaced by 11° in latitude and about 800 km in longitude. Both systems collect and analyze UHF signals from the same geostationary satellite. The system at Bogota consists of 2 GPS antennas separated by 50 m. This system is located about 15° north of Ancon under the crest of the anomaly. Based on visual inspection of several plots, we determined that the difference between the Ancon's zonal velocity and the one measured at Antofagasta ($V_{ancon} - V_{antofagasta}$) anti-correlates with the difference of TEC measured at the sub-ionospheric intersections.

We calculated the dependence of the differential zonal velocity, measured at 3 scintillation stations, upon the K_p index, the solar flux value, and the differential TEC. The differential velocity was defined as the difference in velocity measured simultaneously near and away from the equator, i.e., V(ancon) − V(antofagasta) and V(ancon) − V(bogota). The differential TEC corresponds to the difference in TEC between both observing sites. The TEC values were measured using the network of GPS receivers in South America. We used over 40,000 independent measurements, which are displayed in Figure 4a. Figure 4b shows the results of the best fit corresponding to a solar flux equal to 120 and K_p equal to 2. For these values, the differential velocity is almost independent of the local time of the measurements, but varies

linearly as a function of the differential TEC. The differential zonal drifts also exhibit a dependence upon the K_p index and the solar flux. High K_p values show high differential velocities between 20 and 24 local time. A large solar flux has the opposite effect and permits the development of large differential velocities after midnight.
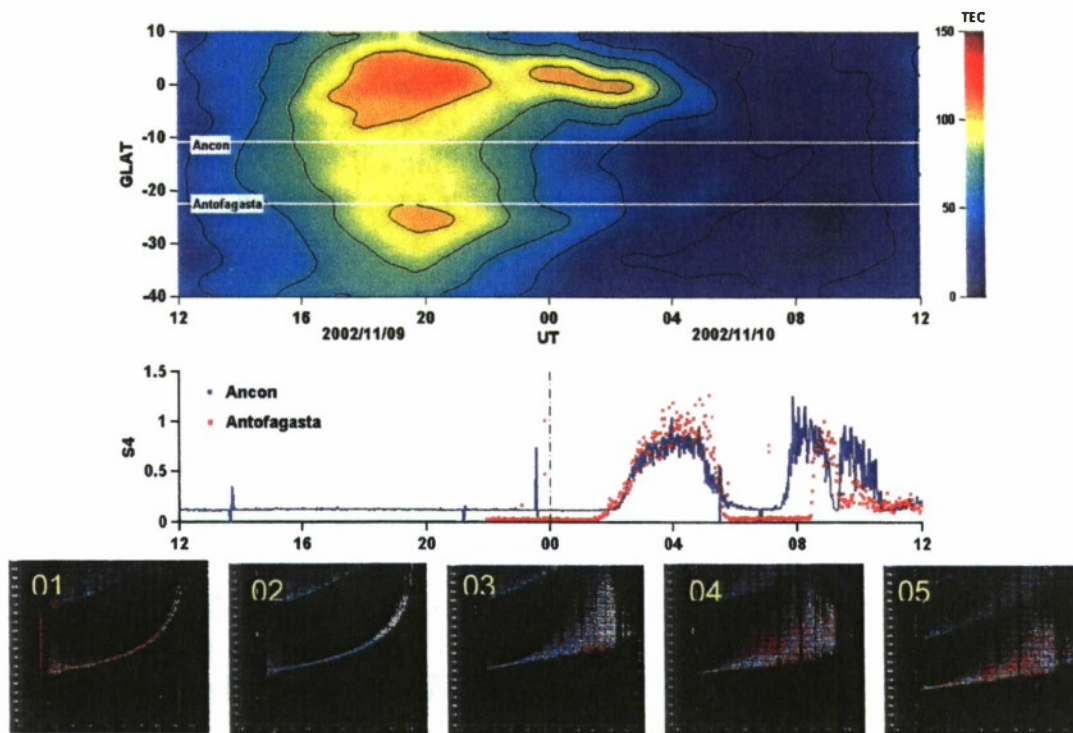

Figure 3. Top panel displays a map of TEC as a function of latitude. The middle panel displays scintillation measured at Ancon and Antofagasta. The lower panel displays ionograms from Jicamarca measured every hour between 01 and 05 UT.
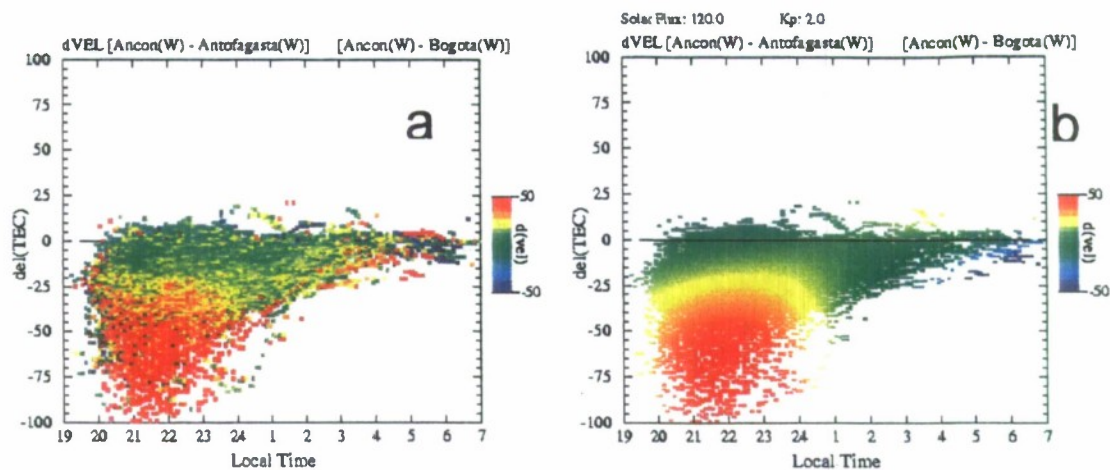
Figure 4. (a) Differential zonal drift velocity measured at 3 scintillation stations as a function of TEC and local time. (b) Best fit of the zonal velocity.

5. HIGH-LATITUDE PHENOMENA

5.1. Sondrestrom Campaign in January 2003

We participated actively in a campaign dedicated to study the formation of polar cap patches and their exit from the polar cap. The principal instruments used during the campaign were the Sondrestrom incoherent scatter radar, all-sky cameras at Sondrestrom and Qaanaaq, GPS receivers located at Sondrestrom and Qaanaaq, and several scintillation receivers. Data from other instruments, such as the global patterns of convection provided by the network of SuperDARN radars and the IMF values measured by ACE, were used as real-time displays and to guide the experiment. The IS radar operated during 6 daytime runs (January 1-6, 2003) and two nighttime runs (January 1 and January 6, 2003). During the times of the experiment, both B_z north and south conditions were observed. We detected several structures in the dayside F-region sometimes moving poleward into the polar cap. However, the structures were seen under both B_z north and south conditions. The SuperDARN velocities indicated the presence of large plasma jets and velocity surges at the time that plasma density structures were observed with the IS radar.

5.2. Observations at Vize Island Using an All-Sky Imager

Operations at Vize Island were carried out during two winters (2003-2004 and 2004-2005). During the second winter (2004-2005), the imager was able to conduct continuous measurements of the aurora between the months of October and March. A campaign was conducted with the Sondrestrom incoherent scatter radar between January 3 and January 10, 2005. During these radar runs, the imager at Qaanaaq performed observations of the polar cap aurora and patches. During the day, the IS radar conducted continuous 360° scans of the cusp and cleft ionospheres. During the night, more localized scans were conducted to measure drifts and densities associated with the passage of polar cap patches and displays of polar cap arcs. A complete description of the cusp aurora observed during the first and second winters of operation at Vize Island has been completed, and is included in this report (Appendix B). The report describes all periods of

interest in which cusp aurora was detected by the imager. We compared this database with other data sets such as the ACE IMF, particle and electric fields collected by the DMSP and POLAR satellites, images recorded at Ny Alesund, and convection patterns measured with the SuperDARN radars. Figure 5 displays the red (6300 nm) and the green (5577 nm) line emissions observed on December 18, 2003. On this day, a very distinct pattern of cusp aurora was observed. An arc was seen extending in the north-south direction connected to the cusp aurora at its poleward end and reaching magnetic latitudes as low as 72°.

5.3. Simultaneous Observations of North-South Aligned Arc and DMSP Large Electric Field

We investigated the origin of the north-south aligned arcs (NSAA) that was observed to grow equatorward of the cusp aurora. Seven events of N-S aligned arcs were identified in the data collected during the first winter campaign (2003-2004) conducted at Vize Island and five more in the second winter (2004-2005). IMF and solar wind information provided by the ACE satellite, particle and electric fields measured during DMSP overpasses near the site, and concurrent observations of the velocities measured by the SuperDARN radars were collected. Some of the NSAA events observed at Vize Island lasted for a few minutes. Others, as seen on December 27, 2003, lasted up to 150 minutes. Near 0623 UT, the DMSP-F13 satellite passed above the NSAA arc. The DMSP satellite crossed the site's field of view from the northeast to the southwest direction. Immediately after 0622 UT, the DMSP satellite intersected the NSAA arc observing simultaneously a large electron flux (Figure 6) and a prominent velocity. The particle data provided evidence of field-aligned acceleration as the high energy electrons were not exactly collocated with the ions. It was also significant that the precipitating electrons observed after the NSAA event exhibited characteristics proper of LLBL electrons. We have also acquired the images recorded at Ny Alesund during the NSAA event. Close inspection of these images revealed that only near the end of the NSAA event (0828 UT) did the Ny Alesund imager observe arcs closely aligned in the north south direction.
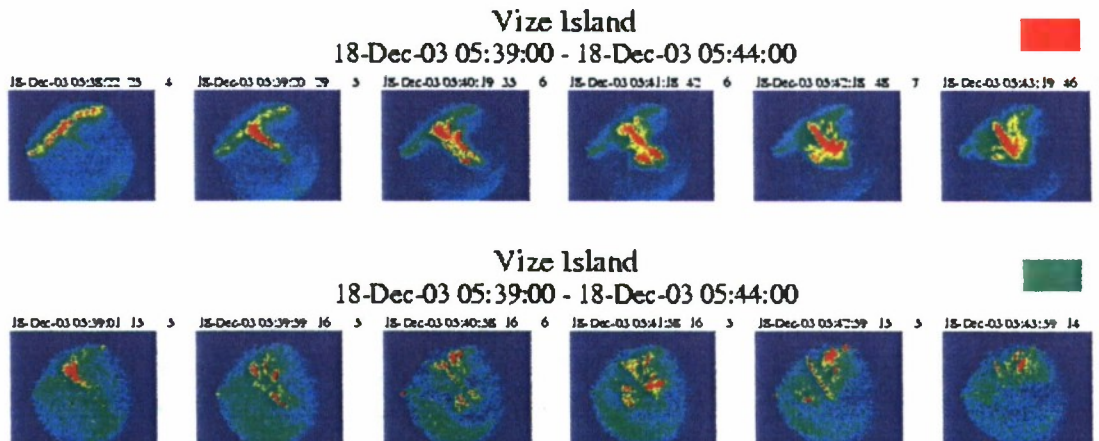
Figure 5. Red line (top) and green line (bottom) emissions observed at Vize Island during the first winter of operations at this site.

6. ENHANCEMENTS TO THE SCINDA NETWORK

6.1. Systems

Several efforts have been conducted under this contract in support of data acquisition for the SCINDA network to advance the aim of identifying and understanding low-latitude ionospheric structures. We have made improvements and upgrades to SDRS UHF systems operating in South America, Asia, and the Middle East that are part of the SCINDA network. These systems use dependable RACAL HF receivers to measure UHF scintillation levels after the received UHF signal is down-converted to HF. In older systems, the AGC output indicates signal strength, while newer systems provide more accuracy and stability by monitoring the IF stage signal level with a specially designed linear detector. The SDRS acquisition software has been continuously adapted to meet SCINDA requirements and conditions at various sites. It is designed to operate with little attention over long periods and has a (relatively) user-friendly graphic interface with controls to change options and displays. The common inputs uploaded for SCINDA are S4 and zonal drift velocity; spectrum and raw signal level data (optionally selected) are also recorded and backed-up at the local sites.
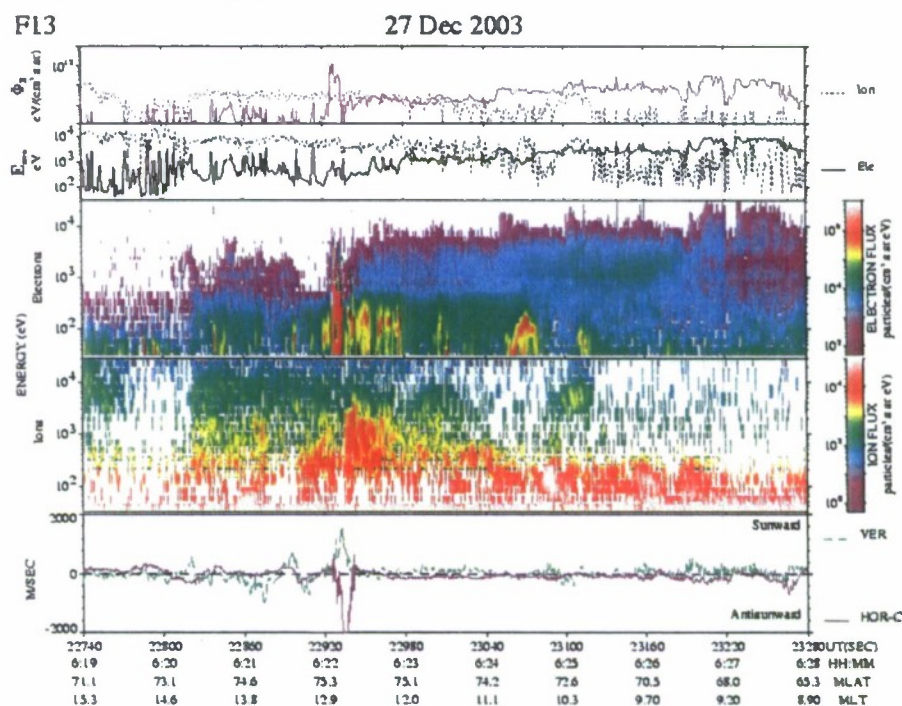
Figure 6. Electron and ion spectrograms and the vertical (green trace) and horizontal velocities (purple) measured by DMSP-F13.

Leica GPS receivers operated by Boston College in Columbia (Bogota, Popayan) and Peru (Iquitos) are also sending S4 data to the network, as well as a new Novatel GPS receiver in Lagos, Nigeria. Data uploaded to Boston College is rewritten in the SCINDA format and uploaded to the SCINDA server.

While the acquisition systems have become more reliable, everyday problems are now

generally about maintaining remote sites and transferring data over networks of varying quality. SDRS and Leica GPS files are either uploaded directly to the SCINDA server via secure ftp or to the Boston College server for re-formatting before relaying them to the SCINDA server.

6.2. Significant Items

1. The UHF scintillation system operating since 1994 at Ancon, Peru, was upgraded to replace the original running an old version of the acquisition software under Windows 3.1. This required a new PC with Windows 2000 SDRS software modified to handle 6 channels and an adapter to match the data cable to the new PC. A second PC running Linux was added to act as a firewall between the SDRS acquisition PC and the network gateway.

2. UHF systems in Guam and Bahrain were upgraded. Both are at U.S. military facilities and have encountered occasional network problems that required attention and were solved. A new PC was also sent to another important site, Ascension Island, to complement the existing GPS receiver. Depending on the network connection, the UHF can transfer data periodically to the Linux PC controlling the GPS receiver or upload directly to the SCINDA server.

3. A new SDRS UHF system installed in Taipei, Taiwan has operated smoothly except for episodes of interference from an unknown source, a situation found occasionally at other sites, as well. To avoid difficulties in computing the drift velocity caused by a short base line, cross-correlation lags near zero are ignored.

4. In preparation for the transition to a replacement UHF scintillation system, raw data collected by a system developed by Robert Livingston during the 2002 COPEX campaign in Brazil was processed with the on-line analysis software used by the SDRS UHF system. S4 and apparent drift velocities calculated by both systems were in general agreement, giving assurance that data comparisons can be viewed with some confidence.

5. A Novatel GPS receiver was recently installed in Lagos, Nigeria, and has uploaded data to the SCINDA server as part of the effort to increase the GPS coverage in Africa.

16

REFERENCES

Anderson, D., A. Anghel, E. Araujo, V. Eccles, C. E. Valladares, and C. Lin, Theoretically modeling the low-latitude, ionospheric response to large geomagnetic storms, *Radio Sci., 41*, 2006.

Basu, Su., S. Basu, J. J. Makela, R. E. Sheehan, E. MacKenzie, P. Doherty, J. W. Wright, M. J. Keskinen, D. Pallamraju, L. J. Paxton, and F. T. Berkey, Two components of ionospheric plasma structures at midlatitudes observed during the large magnetic storm of October 30, 2003, *Geophys. Res. Lett.*, 32, 2005.

Basu, S., Su. Basu, K..M. Groves, E. MacKenzie, M.J. Keskinen, and F.J. Rich, Near-simultaneous plasma structuring in the midlatitude and equatorial ionosphere during magnetic superstorms, *Geophys. Res. Lett.*, 32, 2005.

Basu, S., Su. Basu, F.J. Rich, K.M. Groves, E. MacKenzie, C. Coker, Y. Sahai, P.R. Fagundes, and F. Becker-Guedes, Response of the equatorial ionosphere to prompt penetration electric fields during intense magnetic storms, *J. of Geophys. Res.,* 112, 2007.

Basu, B., J. M. Retterer, O. de la Beaujardiere, C. E. Valladares, and E. Kudeki, Theoretical relationships between maximum value of the post-sunset drift velocity and peak-to-valley ratio of anomaly TEC, *Geophys. Res. Lett.*, 31, 2004.

Becker-Guedes, F., Y. Sahai, P. R. Fagundes, E. S. Espinoza, V. G. Pillat, W. L. C. Lima, Su. Basu, Sa. Basu, Y. Otsuka, K. Shiokawa, E. M. MacKenzie, X. Pi, and J. A. Bittencourt, The ionospheric response in the Brazilian sector during the super geomagnetic storm on 20 November 2003, *Ann. Geophys,* 25, 863-873, 2007.

Bowman, B. R., W. K. Tobiska, F. A. Marcos, and C. E. Valladares, The JB2006 empirical thermospheric density model, *J. Atm. and Solar-Terr. Phys.*, 70, 5, 774-793, 2008.

Burke, W. J., C.Y. Huang, C.E. Valladares, J.S. Machuzak, L.C. Gentile, and P.J. Sultan, Multipoint observations of equatorial plasma bubbles, *J. Geophys. Res.,* 108(A5), 1221, 2003.

Burke, W. J., L. C. Gentile, C. Y. Huang, C. E. Valladares, and S. Y. Su, Longitudinal variability of equatorial plasma bubbles observed by DMSP and ROCSAT-1, *J. Geophys. Res.*, 109, 2004.

Foster, J. C., et al. (2005), Multiradar observations of the polar tongue of ionization, *J. Geophys. Res., 110,* 2005.

McDonald, S. E., Su. Basu, S. Basu, K. M. Groves, C. E. Valladares, L. Scherliess, D. C. Thompson, R. W. Schunk, J. J. Sojka, L. Zhu, Extreme longitudinal variability of plasma structuring in the equatorial ionosphere on a magnetically quiet equinoctial day, *Radio Sci., 41*, 2006.

McNamara, L. F., D. L. Cooke, C. E. Valladares, and B. W. Reinisch, Comparison of CHAMP and Digisonde plasma frequencies at Jicamarca, Peru, *Radio Sci.*, 42, 2006.

Pallamraju, D., C. Chakrabarti, and C. E. Valladares, Magnetic storm-induced enhancement in neutral composition at low latitudes as inferred by $O(^1D)$ dayglow measurements from Chile, *Ann. Geophys.*, 22, 3241-3250, 2004.

Sheehan, R. and C. E. Valladares, Equatorial ionospheric zonal drift model and vertical drift statistics from UHF scintillation measurements in South America, *Annales of Geophys.*, 22, 3177 – 3193, 2004.

Valladares. C.E., J. Villalobos, M.A. Hei, R. Sheehan, Su. Basu, E. MacKenzie, P.H. Doherty, and V. H. Rios, Simultaneous Observation of traveling ionospheric disturbances in the northern and southern hemispheres, submitted to *Annales Geophysicae*, 2007.

Valladares, C. E., T. Pedersen, and R. Sheehan, Polar Cap Patches Observed during the Magnetic Storm of November 2003: Observations and Modeling, submitted to *J. Geophys. Res.*

Valladares, C. E., R. Sheehan, and J. Villalobos, A Latitudinal network of GPS receivers dedicated to studies of equatorial spread-F, *Radio Sci.*, 39, 2004.

Valladares, C. E., J. Villalobos, R. Sheehan, and M.P. Hagan, Latitudinal extension of low-latitude scintillations measured with a network of GPS receivers, *Annales of Geophys.*, 22, 3155 - 3175, 2004.

Wang, X., R. Eastes, S. Weichecki Vergara, S. Bailey, C. E. Valladares, and T. Woods, On the short-term relationship between solar soft X-ray irradiances and equatorial total electron content (TEC), *J. Geophys. Res.*, 111, 2005.

Wang, X., R. Eastes, B. W. Reinisch, S. Bailey, C. E. Valladares, and T. Woods, Short-term relationship between solar irradiances and equatorial peak electron densities, *J. Geophys. Res.*, 112, 2006.

A latitudinal network of GPS receivers dedicated to studies of equatorial spread *F*

C. E. Valladares and R. Sheehan

Newton Resource Center, Institute for Scientific Research, Boston College, Chestnut Hill, Massachusetts, USA

J. Villalobos

Department of Physics, Universidad Nacional de Colombia, Bogota, Colombia

[1] Five GPS receivers have been deployed near the 74°W longitude meridian to measure the variability of total electron content (TEC) latitudinal profiles and to study the relation of this variability with the onset and evolution of spread *F* plasma structures. These five GPS receivers, together with two others that form part of the International GPS Service (IGS) network, three more that belong to the South Andes Project network, and an additional receiver located at Ancon, Peru, provide TEC values between 8°N and 40°S geographic latitude. In addition, all five GPS receivers managed by Boston College give the amplitude scintillation on a near-real time basis. This fact allows us to know the maximum latitude to which the irregularities extend and to infer the maximum altitude of the plasma bubbles. We have calculated TEC latitudinal profiles using the TEC values obtained by all the receivers between 1998 and 2001. We found that during the equinoxes, UHF scintillations occur when the ratio of the crest to the trough of the anomaly is 2 or larger. During the December solstice the crest is not very pronounced, but a sharp decrease of TEC at the magnetic equator precedes the onset of 1-km scale irregularities. We have also examined a longitudinal variability of scintillations by partitioning the sky in two sectors separated at the 74°W meridian. We consistently observe a greater number of GPS scintillation events at the eastern longitudes over the Amazon rain forest. This intriguing finding could well be explained by a larger population of gravity waves at longitudes east of the Andes.   *INDEX TERMS:* 2415 Ionosphere: Equatorial ionosphere; 2439 Ionosphere: Ionospheric irregularities; 2471 Ionosphere: Plasma waves and instabilities; *KEYWORDS:* equatorial spread *F*, scintillations, equatorial anomaly, gravity waves, plasma bubbles

1. Introduction

[2] The equatorial spread *F* (ESF) phenomenon consists of the sudden advection of a region 100 to 500 km wide containing low-density plasma [*Woodman and LaHoz*, 1976]. This unstable plasma originates at the bottomside of the *F* region and rises, in most cases, up to the topside of the *F* layer. While ESF was initially used to describe plasma bubbles and the irregularities that grow within them, it is used now to denote other types of structures seen at low latitudes such as bottomside sinus-oids (BSS) [*Valladares et al.*, 1983] and bottomside and bottomtype traces [*Hysell and Burcham*, 1998].

[3] When a radio wave propagates through a medium containing plasma structures (equatorial spread *F*), the signal suffers amplitude and phase distortions. If the level of the structuring is low, only the phase and the angle of arrival are changed (thin phase screen). If the structuring level is strong, the amplitude of the signal also varies (thick phase screen). After crossing the phase screen, the electromagnetic wave is affected by strong interference, and a diffraction pattern in both intensity and phase develops at the ground. These fluctuations of the radio signals are known as scintillations; they are more common in the VHF, UHF, and L-band frequency range. Weak and strong levels of scintillations can

produce disruptions of the communication and navigation links that use low- or high-altitude orbiting satellites. Fadeouts of GPS signals cause, in some cases, an additional error in the location of the site, which could be as large as tens of meters. In other cases, a complete loss of the navigation capability may occur. The disruption of communication signals and the degradation of navigation capabilities constitute the main incentive to develop a forecasting capability of the onset of irregularities and to closely monitor the evolution of the spread F phenomenon.

[4] In the last two years, Boston College has installed five GPS receivers at different locations in Colombia and Peru. Two receivers were installed in Bogota and one in each of the cities of Iquitos, Pucallpa, and Cuzco. These new receivers are providing values of the S4 scintillation index, and together with the IGS and SAP GPS receivers, they give the latitudinal distribution of TEC. This paper presents the statistics of the latitude extension of GPS scintillations as seen by some of the GPS receivers operating near and north of the magnetic equator and the characteristics of the TEC latitudinal profiles as a function of ESF activity. The onset of ESF was determined on the basis of the appearance of UHF scintillations measured at Ancon near the magnetic equator. For a single case study we also compare the maximum latitude of scintillations to the altitude extension of radar plumes recorded with the JULIA radar.

2. TEC Latitudinal Profiles

[5] Figure 1 shows the location and the TEC field-of-view of the GPS receivers that belong to the IGS, the North Andes Project (NAP), and the South Andes Project (SAP) networks. At present the IGS stations (Arequipa and Santiago) and the SAP receivers (Iquique, Copiapo, and Antuco) produce data files that are made available to us on an off-line basis. The Boston College (BC) receivers measure the S4 index using the L1 frequency. Their scintillation field-of-view covers a latitudinal region extending between 21°S and 11°N geographic latitude (−9° and +23° magnetic latitude). An additional receiver, to be located at the northern boundary of Colombia, should allow us to detect the exceptional events when scintillations reach 15°N latitude (∼27° magnetic latitude) or plasma bubbles extending up to 2000 km. Figure 1 also displays the ground projection of a field line that passes above the Jicamarca station reaching an apex altitude of 1610 km.

[6] Figures 2, 3, and 4 display the result of subtracting the TEC distribution measured at 1800 LT and the values at 2000 LT. In mathematical form, this is expressed as

$$d\text{TEC} = \text{TEC}(1800) - \text{TEC}(2000).$$
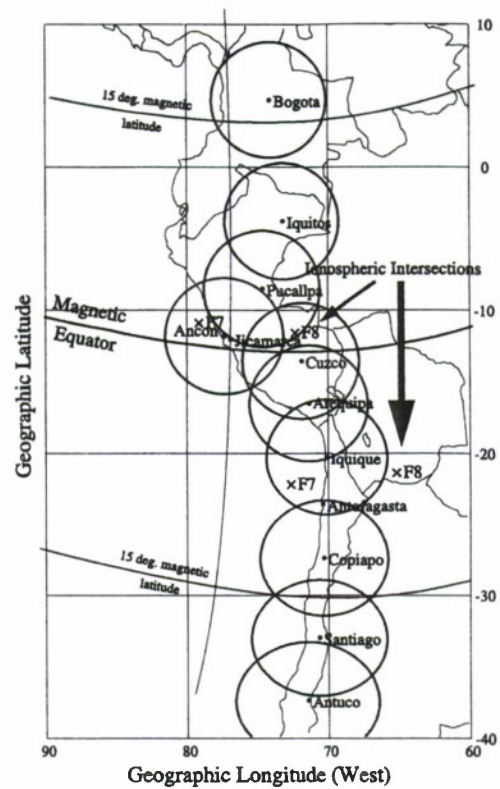
Figure 1. Geographic locations and field-of-views of several GPS receivers operating near the west coast of South America. The stations at Ancon, Cuzco, Pucallpa, Iquitos, and Bogota form the North Andes Project (NAP) network. The stations of Iquique, Copiapo, and Antuco form the South Andes Project (SAP), and the stations of Arequipa and Santiago form part of the IGS network of receivers. The fields-of-view encircling the stations are for 35° elevation angle and an altitude of 350 km. The near-vertical line that crosses the Jicamarca station corresponds to the ground projection of a field line with a 1610 km apex altitude and feet at 350 km altitude.

Positive values of d TEC indicate a temporal reduction of the TEC distributions; negative d TEC values indicate a temporal growth in TEC. Figure 2 shows d TEC values for all nights in 1999 when UHF scintillations are seen at both Ancon and Antofagasta stations. These curves show a strong latitudinal variability during all 8 months of scintillation activity. The d TEC values at latitudes near the magnetic equator (∼12°S geographic latitude) are 30 units or larger. On a few days during the months of March, October, and November, the TEC value at the magnetic equator reaches 50 units. At latitudes corresponding to the peaks of the anomaly (near 4°N and 28°S), the d TEC values are near zero and are in many

Figure 2. TEC latitudinal distribution of the difference of the curves corresponding to 1800 LT and the traces for 2000 LT. Only days when scintillations occurred at Ancon and Antofagasta are considered here.

cases negative. This variable pattern indicates that between 1800 and 2000 LT, the TEC value of the crests increase and the trough diminishes during days when ESF occurs. 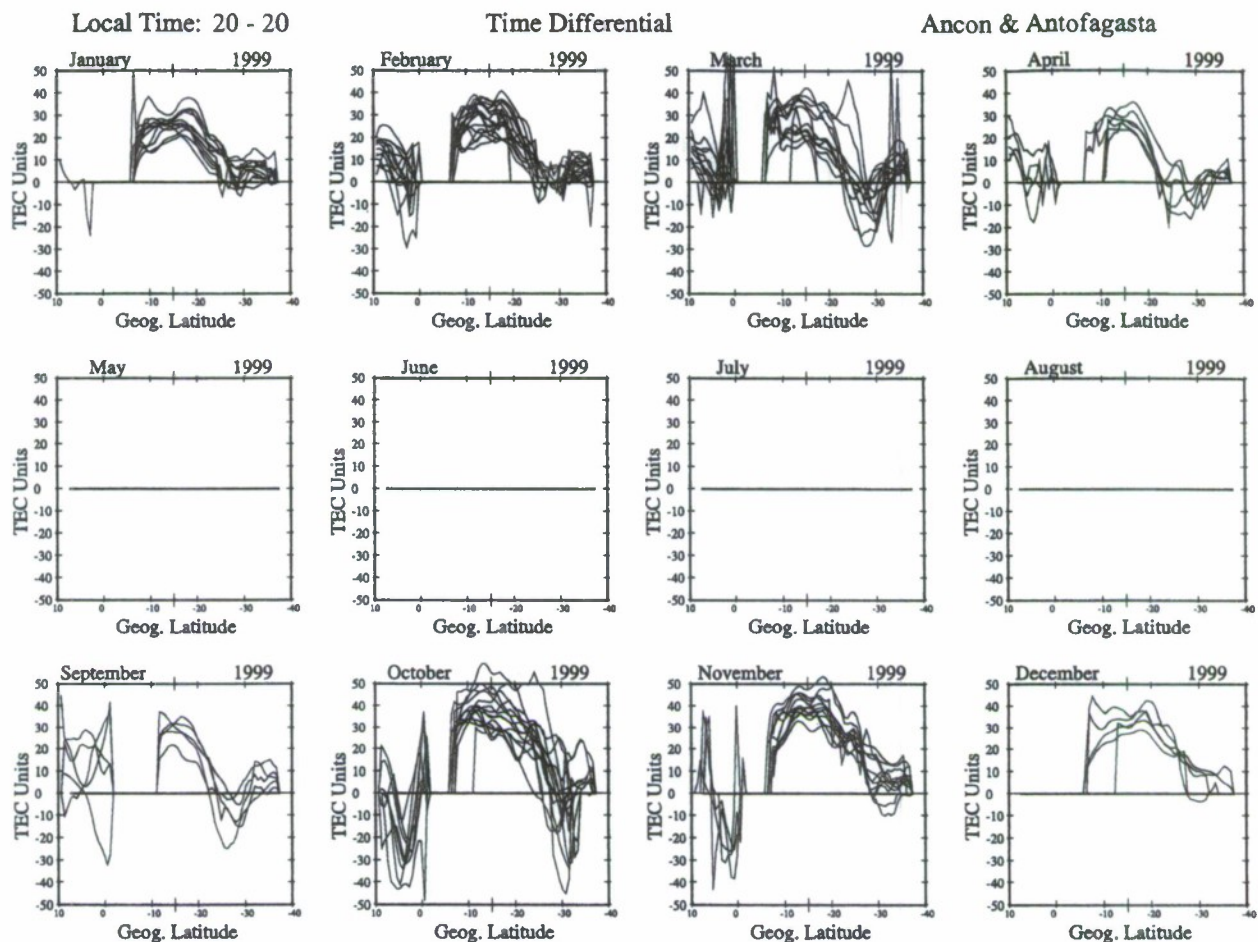This behavior reflects the changes in the F region that occur right after sunset. *Fejer et al.* [1999] introduced Jicamarca measurements that provided evidence for the appearance of a fully developed prereversal enhancement (PRE) of the vertical drift during nights of ESF activity. In agreement with this idea, *Valladares et al.* [2001] presented TEC latitudinal profiles obtained in 1998 indicating that the PRE is able to reenergize the equatorial fountain effect, deplete the density near the equator, and simultaneously increase the density near the crests of the anomaly. This plasma dynamics explains the general characteristics of the dTEC curves. However, the profiles corresponding to 1999 and 2001 (Figure 3) show an additional effect that was not seen in the latitudinal profiles of 1998 [*Valladares et al.*, 2001]. During the

months of January, February, November, and December, the negative dTEC values are seen only in the northern crest, while the southern crest shows values near zero. This is more evident in the frame corresponding to November 2001 (Figure 3), where dTEC values are near -50 TEC units at the location of the northern crest but near zero at latitudes typical of the southern crest. Figure 4 shows the dTEC profiles for days when no scintillations were seen at the Ancon and the Antofagasta sites. In this figure, all the curves are more uniform, displaying values less than 30 TEC units near the magnetic equator. At crest latitudes the dTEC values are in most cases near 20 units. Only two cases, one in October 1999 and the other in November 1999, show significant negative (less than -10 TEC units) dTEC values near the northern crest.

[7] Figure 5 displays a statistical distribution of the crest TEC value as a function of the trough TEC value for years 1999, 2000, and 2001. The red dots correspond
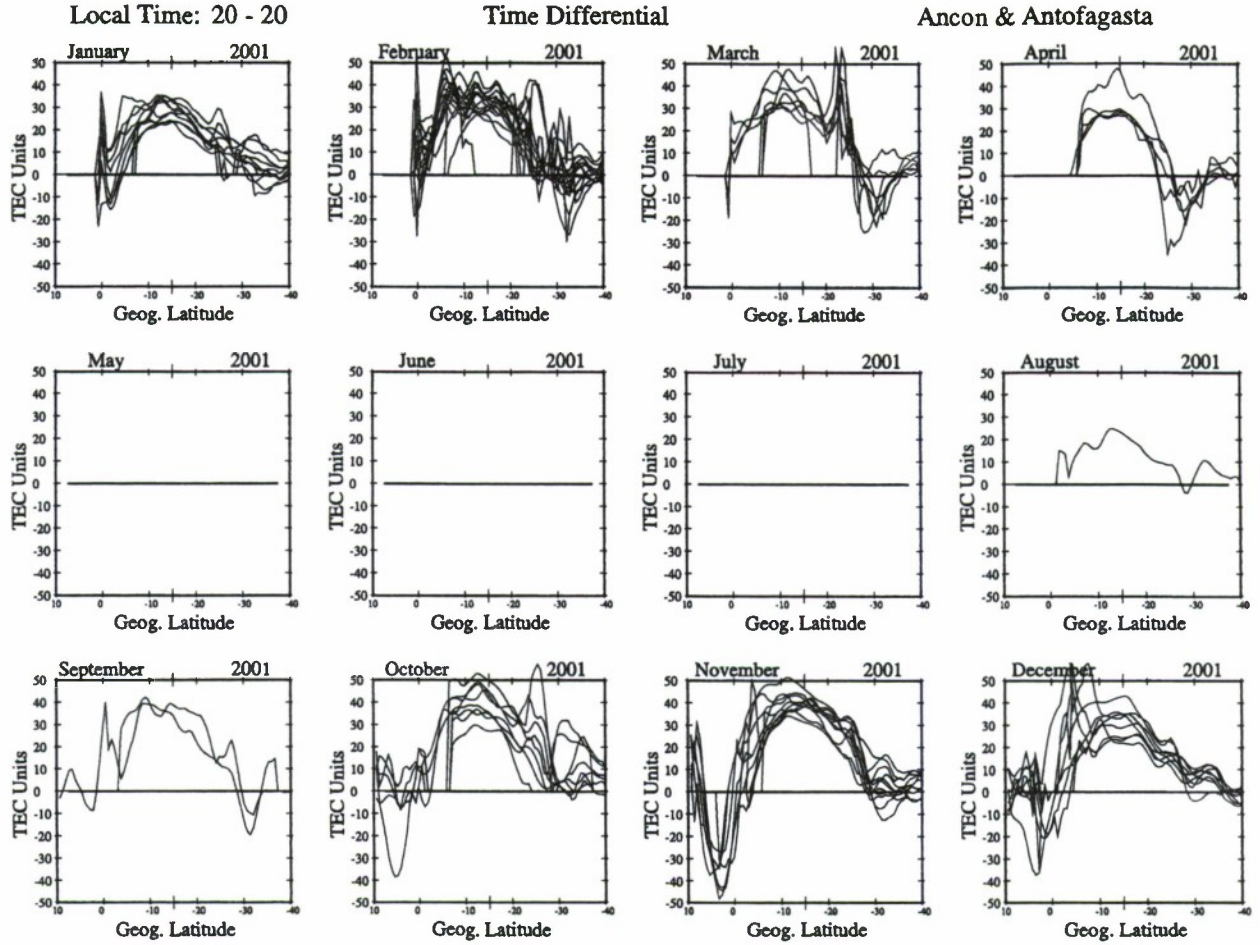
3 of 11

21

Figure 3. Same as Figure 2 but for year 2001.

to events when scintillations are present and the blue dots to times of no scintillation activity. The scintillation events are mainly restricted to small trough TEC values and large amplitude of the crests. The no-scintillation cases consist of large trough values and are placed in regions to the right but adjacent to the red dots. This figure also indicates that the peak value of the crests is the largest during the equinoctial months (March, April, October, and November). It is between 40 and 120 units during the months of January, February, September, and December and the smallest during the June solstice (May, June, July, and August). Figure 6 shows a mass plot of the peak-to-trough ratio as a function of local time for all the TEC latitudinal profiles that were obtained in 1999 during the nighttime hours (1900–0700 LT). The left panel exhibits the ratios for events of premidnight scintillations; the right panel displays all cases of no scintillations. Large color-coded dots are used to indicate the average value for every 1-hour bin. The scintillation events exhibit ratios above 1.5 and present a large

dispersion with most of the values larger than 2. The no-scintillation events have ratios less than 1.5, small spread, and 1-hour averages near 1.3. This prominent difference in the characteristics of the TEC profiles, which are highly dependent on the scintillation activity, points to an inherently different behavior of the drivers of the equatorial F region dynamics during nights when scintillations occur.

3. GPS Scintillation Latitudinal Profiles

[8] The top panels of Figure 7 show the scintillation S4 index measured by the Bogota, Iquitos, and Cuzco stations between 19 and 23 LT on 5 September 2002. The lower panel exhibits the coherent echoes measured by the JULIA radar during the same day. A single plume is observed at 2040 LT, extending up to 1610 km altitude. However, the westward tilt of the plume makes the topside part of the coherent echoes to be detected by JULIA near 2115 LT. GPS scintillations were observed
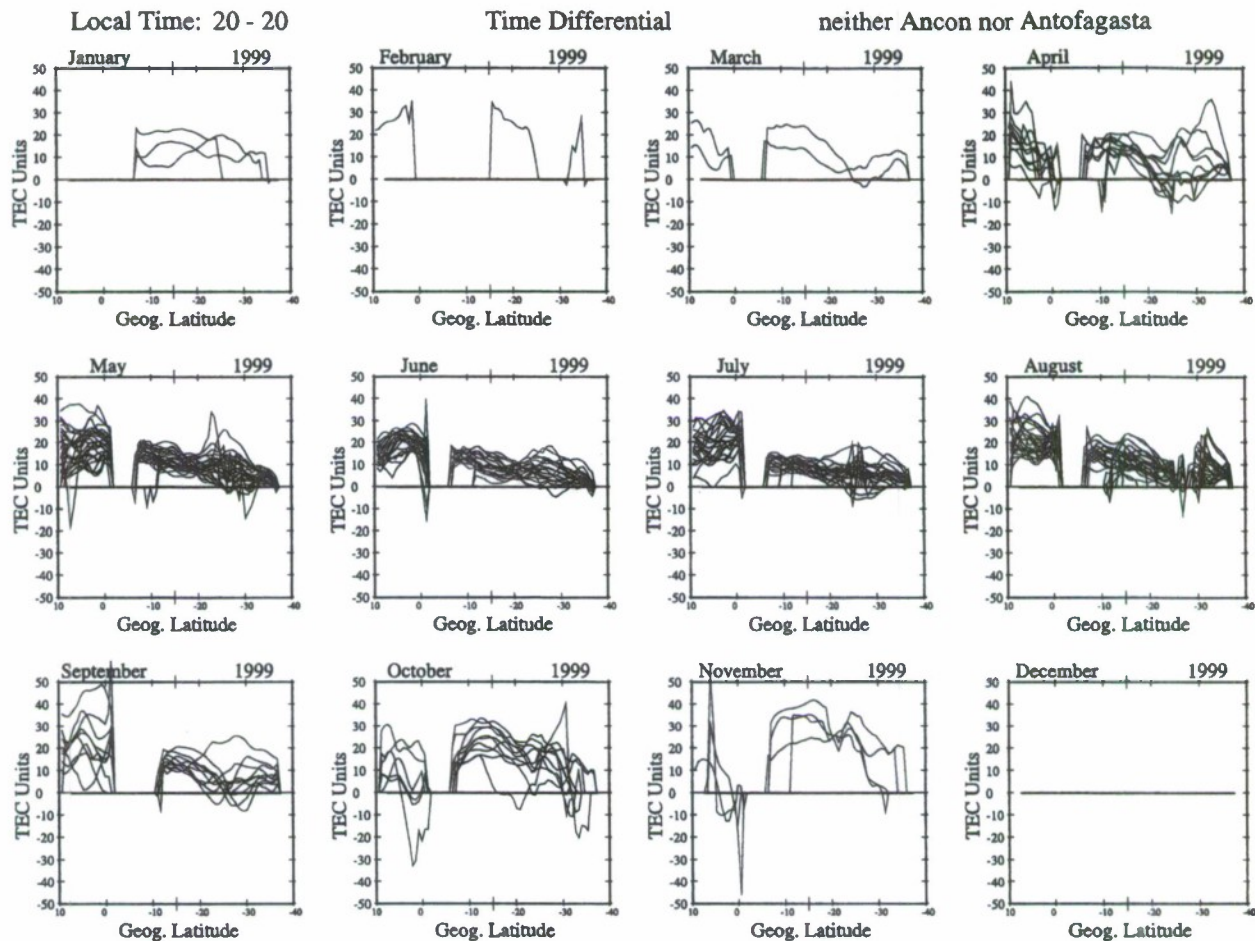
Figure 4. Same as Figure 2 but for days of no scintillations at both stations.

from Bogota reaching 11°N latitude (~23°N magnetic latitude) at the 78°W meridian between 2050 and 2130 LT (see arrow). As indicated in Figure 1, the field line over Jicamarca with an apex altitude of 1610 km intersects the F region at 11°N latitude. Consequently, the location and the local time of the GPS scintillations are in very good agreement with the observations of a plume reaching 1610 km altitude that was observed with the JULIA radar.

[9] On the basis of the excellent agreement that exists between the altitude of the plasma plumes observed with the JULIA radar and the maximum latitude of the scintillation S4 index measured with the GPS L1 band, we decided to use the maximum latitude of the GPS scintillation as a proxy for the altitude of the plasma plumes. Figure 8 shows the magnetic latitude distribution of the scintillations detected by the systems located at Bogota, Iquitos, and Cuzco between 28 August 2001 and 28 February 2002. We have used arrows that point to a small segment to indicate the maximum latitude at which

scintillations were observed during each individual day. We also divided the field of views of the three stations in two sectors. One sector, labeled west, included all the S4 values detected to the west of the 74°W meridian. The east observations indicated the scintillations seen to the east of the 74°W meridian. It is evident that more scintillation events exist on the east side, and for a larger number of cases the maximum latitude reached values up to 23° magnetic latitude (~11°N geographic latitude). It is important to mention that Bogota is located close to the 74°W meridian, and almost the same number of GPS satellites is seen to the west and east of each meridian. It is also evident that during several nights the maximum latitude (and the altitude of the plumes) exceeded the northern boundary of the field-of-view of the Bogota station that is limited at 12°N latitude.

[10] Figure 9 shows histograms of the number of days when scintillations reached the maximum magnetic latitude indicated on the horizontal axis. The histogram on the left side includes all the observations between
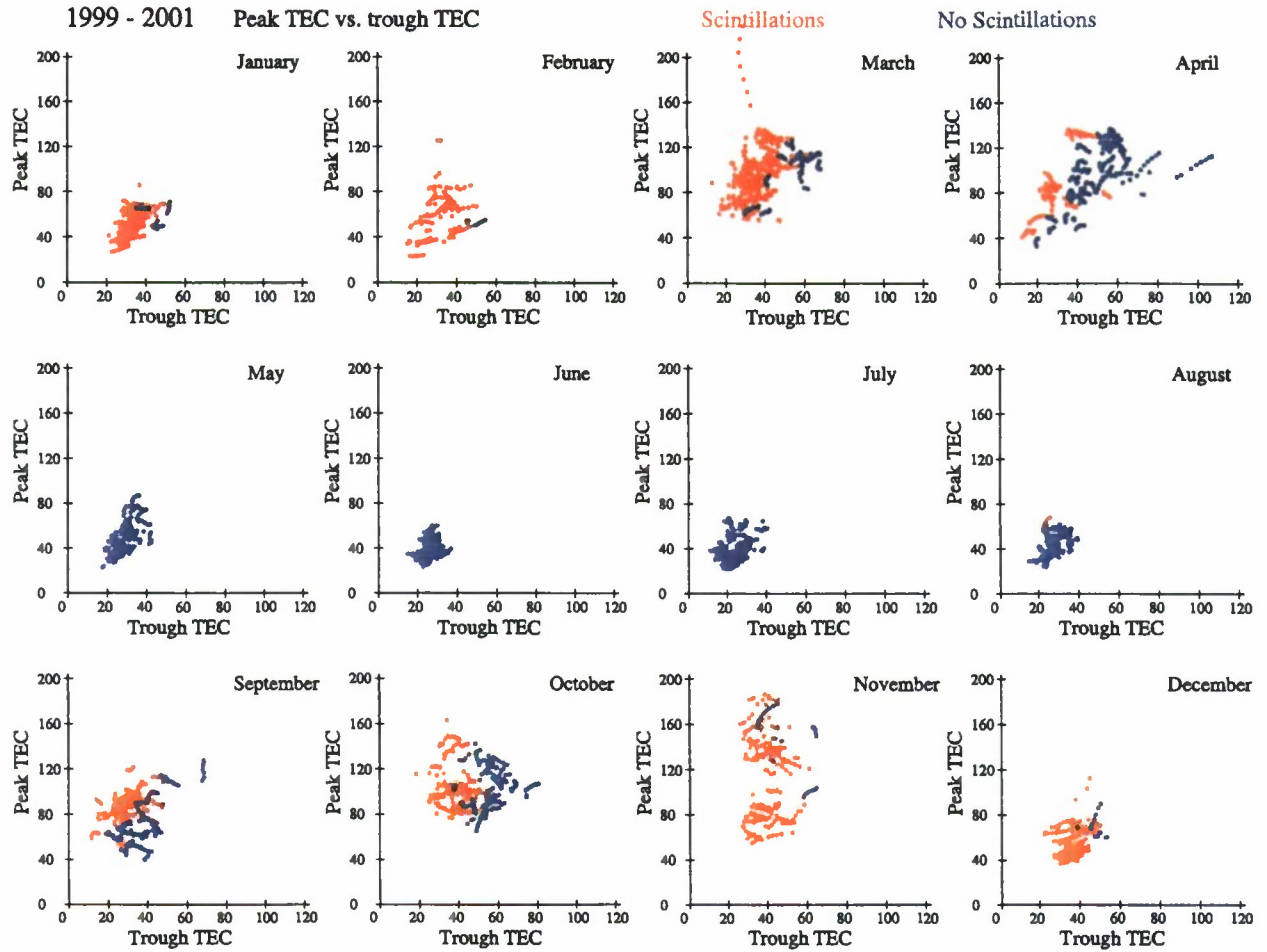
Peak TEC vs. trough TEC

Figure 5. Monthly mass plots of the crest TEC value as a function of the trough TEC value extracted from the latitudinal profiles for years 1999–2001. The red dots are coded for days of scintillations and the blue dots for days of no scintillations.

28 August 2001 and 28 February 2002. The histograms at the center and the right side correspond to the west and east sectors as defined above. Figure 9 explicitly indicates that more events are seen in the east sector than in the west side. In addition, the average maximum latitude is larger to the east than to the west. While prominent difference in scintillation activity have been seen by stations separated by few hundred kilometers [*Basu et al.*, 2001] during magnetically disturbed days, we did not expect to find that statistics of 180 days, most of them during quiet magnetic conditions, would give such different results.

4. Discussion

[11] Figure 2 indicates that during the equinoctial and December solstice months the fountain effect, which is driven by the upward vertical drift, is in effect when scintillations are simultaneously observed at both Ancon and Antofagasta. This evidence endorses the role of the vertical drift velocity as the controlling parameter in the generation of spread F irregularities [*Fejer et al.*, 1999]. These authors associated the occurrence of a large PRE with the initiation of equatorial spread F. We suggest that the same upward drift, which drives the F region to higher altitudes, creates a postsunset resurgence of the fountain effect. Thus Figures 2 and 3 are indirect proof of the control that the equatorial electrodynamics, and specifically the upward vertical drift velocity, exerts on establishing the right conditions for the development of ESF. This result agrees with data recently presented by *Valladares et al.* [2001]. This latter study presented latitudinal distributions of TEC obtained in 1998 to demonstrate that the temporal difference of TEC showed
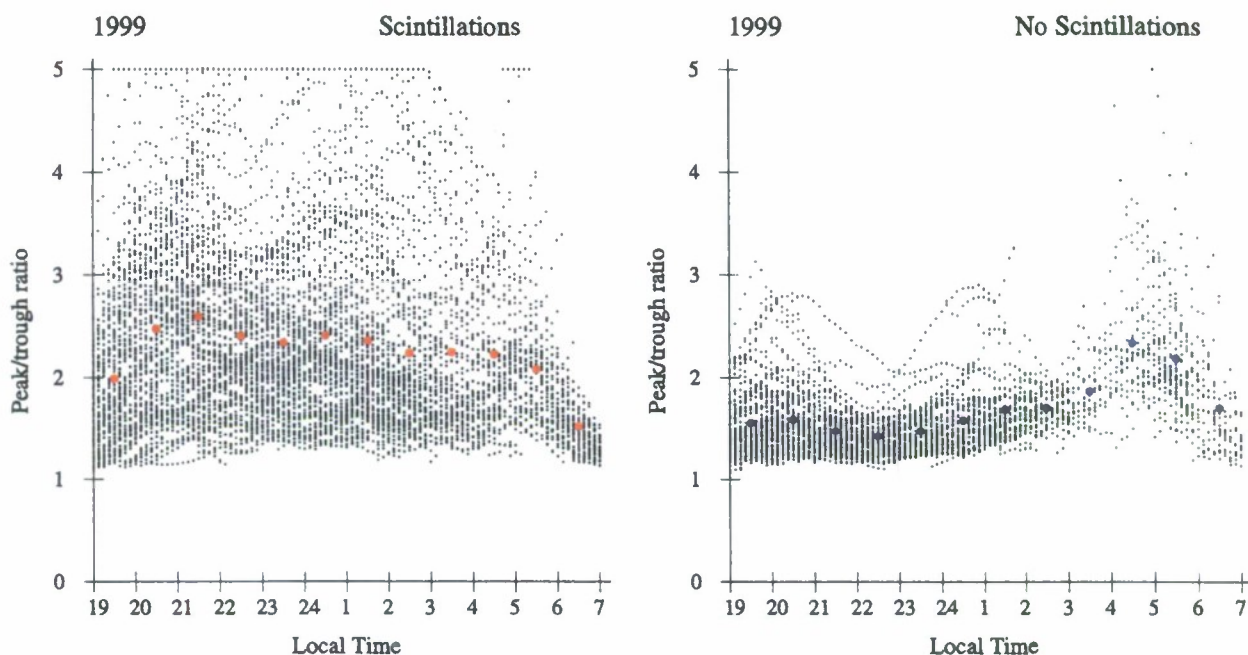
Figure 6. Scatterplot of the peak-to-trough ratio versus local time for all the TEC distributions in which scintillations were observed in 1999. The average value (large red dots) is above 2 between 2000 and 0600 LT. The right panel corresponds to nights of no scintillations. In this frame the average values (blue dots) are near 1.5 between 1900 and 0300 LT.

quite drastic increases of the crest values and sharp decreases near the trough during days when strong scintillations were observed. In addition, Figures 2 and 3 showed that during the solstice months (November through February) the dTEC distributions were clearly asymmetric. A large negative value of order 50 TEC units was seen near latitudes typical of the northern crest and small values ($\sim$0) around the southern crest. This fact indicates that between 1800 and 2000 LT the TEC profile developed into a highly asymmetric distribution with a prominent northern crest and a much smaller southern peak. This effect is probably caused by a strong northward directed meridional neutral wind. The appearance of asymmetrical distributions, mainly during the December solstice months, agrees well with the season of larger meridional winds and times when the low-latitude thermospheric wind blows toward the north.

[12] *Maruyama and Matura* [1984] suggested that the meridional wind was able to suppress the growth of the Rayleigh-Taylor instability (RTI) and hence to control the ESF activity. The numerical calculations of *Maruyama* [1988] indicated that the transequatorial wind was able to depress the F layer in the lee-side hemisphere and consequently change the field-integrated Pedersen conductivity [*Mendillo et al.*, 1992]. This evidence suggested that a southward wind was some-

what responsible for lowering the density contours and for making the whole flux tube more stable to the onset of the RTI. More recently, *Mendillo et al.* [2001] used measurements from a Fabry-Perot Interferometer (FPI) and an imager to conclude that during 8 days of a campaign in September 1998 the meridional wind did not influence the onset of ESF in the premidnight hours. Our finding reinforces this idea and indicates that for years of high solar activity the meridional wind may not be able to inhibit the growth of ESF irregularities. *Devasia et al.* [2002] have presented evidence suggesting that when $h'F$ is below 300 km, ESF may occur only for a thermospheric meridional wind directed equatorward and less than 60 m/s. The dTEC curves shown by *Valladares et al.* [2001] for a year of low solar activity did not display the asymmetry that was presented in the data corresponding to 1999 and 2001. Therefore the more symmetric curves of 1998 may confirm the need for the meridional wind to be small during years of low solar flux and to be unimportant during years of high solar activity.

[13] The consistent difference in scintillation activity between two adjacent longitudinal sectors suggests the presence of a suppressor (or intensifier) mechanism on the west (east) side of the 74°W meridian. Penetrating electric fields of magnetospheric origin have been suggested to be localized in longitude [*Basu et al.*, 2001] and do produce
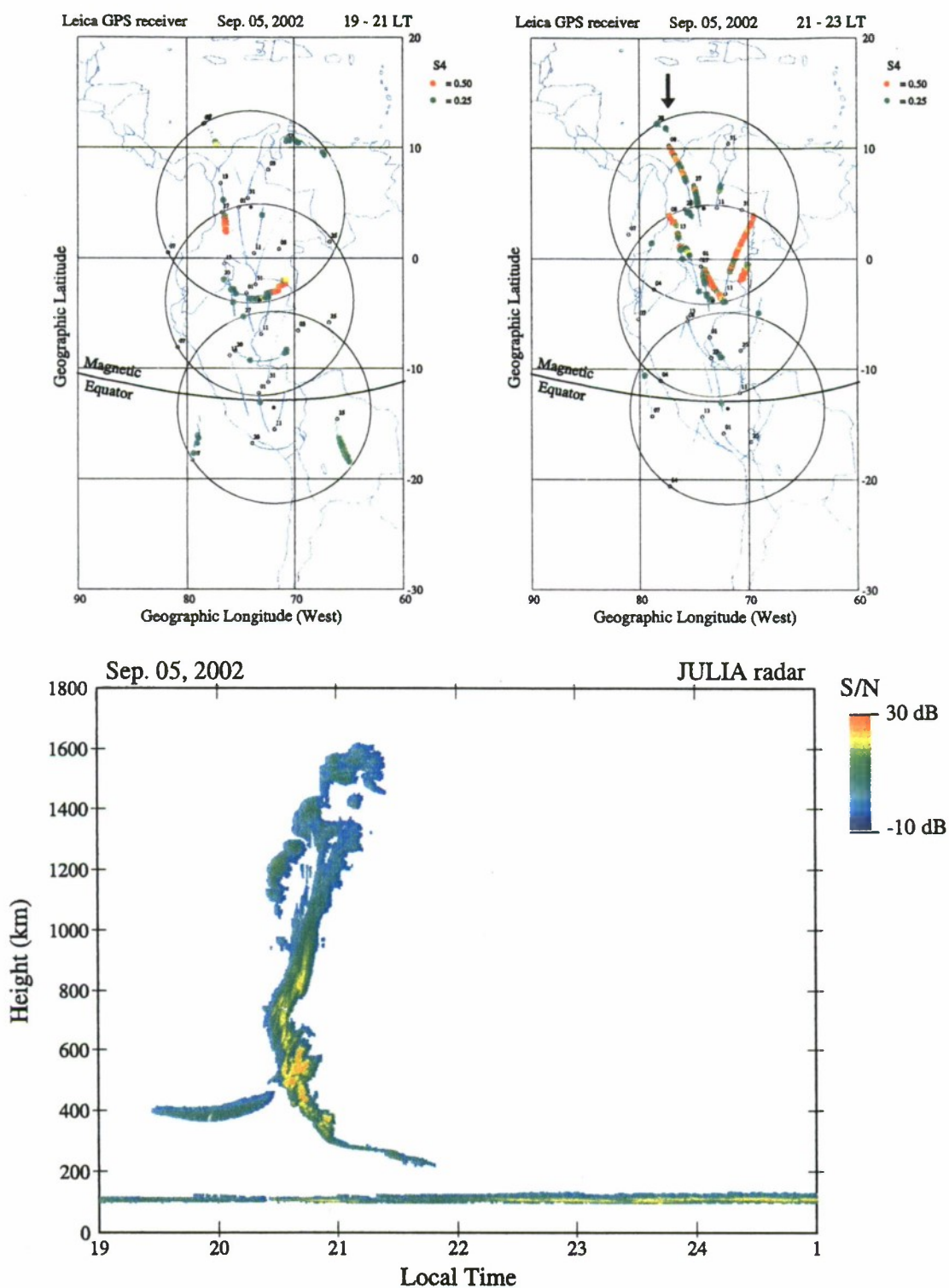
Figure 7. Top panels show the scintillation S4 index measured by the GPS receivers installed at Bogota, Iquitos, and Cuzco during two 2-hour periods. The lower panel displays a power map of coherent echoes detected by the Julia radar. Note that scintillations are seen up to 11°N latitude at the same time and location when the JULIA radar observed a plume extending up to 1610 km altitude.
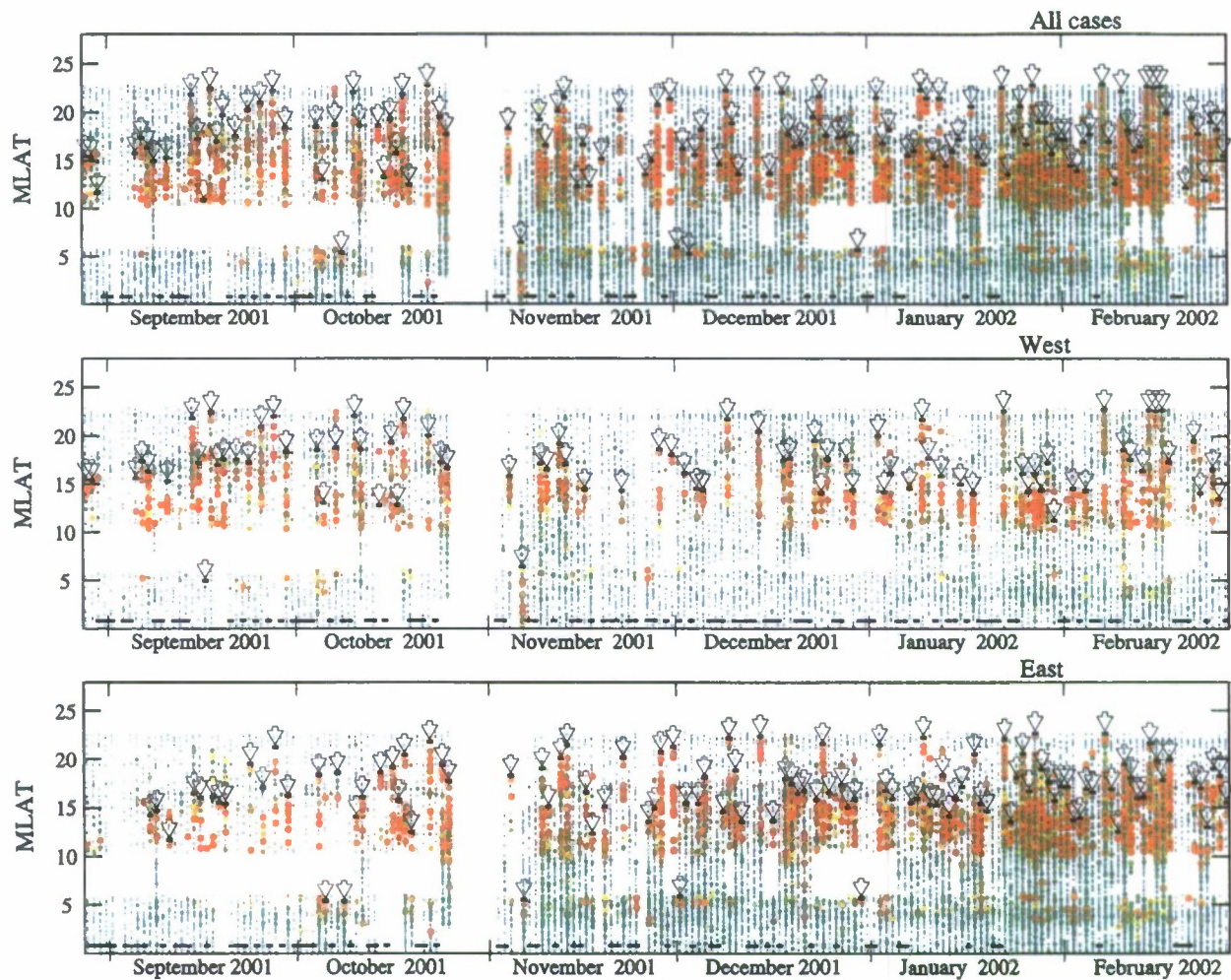
Figure 8. Map of scintillation activity for days between 28 August 2001 and 27 February 2002. The magnitude of the S4 index has been color-coded with red meaning values larger than 0.5, the green dots equal to 0.25, and the small blue dots indicate recording noise level. The vertical axis is the magnetic latitude at which the scintillations were observed. The arrows point to the latitude of the third polewardmost point of S4 values above the noise level (0.20).
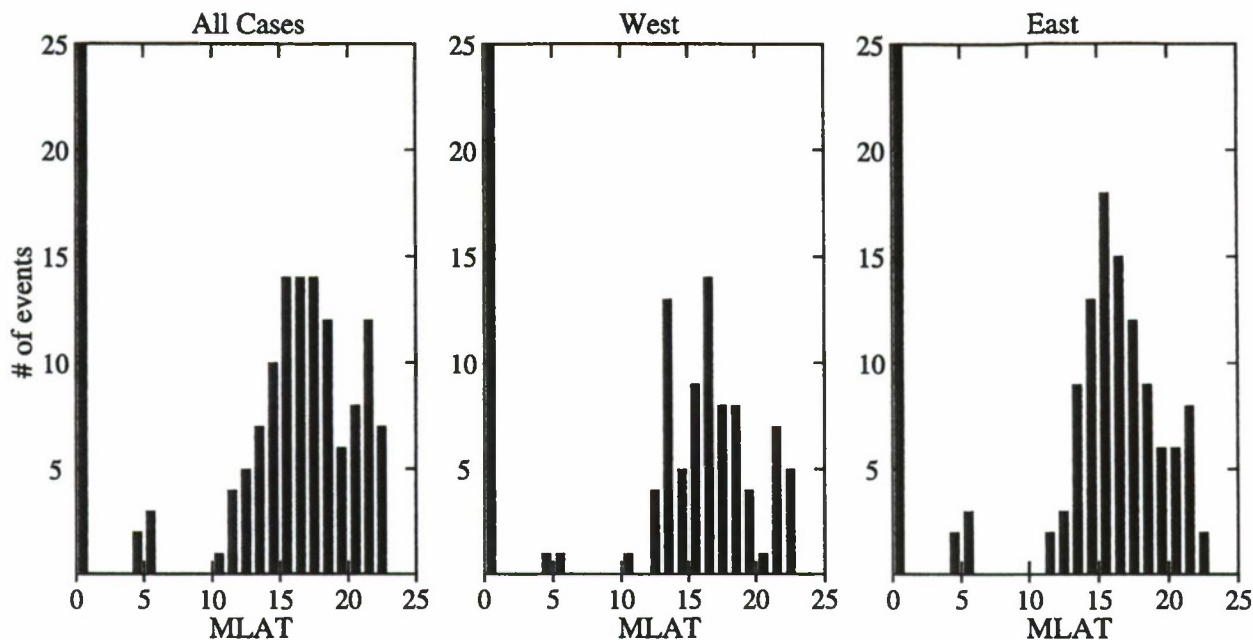
Figure 9. Statistical distribution of the number of days and the maximum latitude where scintillations (S4 > 0.20) were observed during the first 6 months of measurements at Bogota. The statistics have been separated into two regions called west (west of the 74°W meridian) and east to longitudes eastward of this meridian.

substantial differences in scintillation activity at regions separated by few hundred kilometers. However, they have been observed to operate during magnetically disturbed times and are nearly absent during quiet or moderate conditions. Other ionospheric effects such as a longitudinal variation in the altitude of the F layer or a limited spatial extension of the prereversal enhancement seem unlikely to occur on a regular basis. Instead, we suggest that the source of the longitudinal variability resides in the different behavior of the gravity wave activity at regions separated by few degrees in longitude. *Meriwether et al.* [1996, 1997] have presented solar maximum observations of elevated thermospheric temperatures in the directions over the Andes, suggesting that gravity wave energy from the surface penetrates into the thermosphere, where viscous dissipation causes the heating. In addition, there exists a general consensus that gravity waves of mesospheric origin initiate the development of the equatorial plasma bubbles acting as a "seed" of the RTI mechanism [*Kelley et al.*, 1981]. On the basis of these arguments, we suggest that a higher population of gravity waves may exist over the Andes and the Amazon forest regions, enhancing the production of plasma bubbles in a region situated to the east of the 74°W meridian.

References

Basu, S., et al. (2001), Ionospheric effects of major magnetic storms during the international space weather period of September and October 1999: GPS observations, VHF/UHF scintillations and in situ density structures at middle and equatorial latitudes, *J. Geophys. Res.*, *106*, 30,389.

Devasia, C. V., N. Jyoti, K. S. V. Subbarao, K. S. Viswanathan, D. Tiwari, and R. Sridharan (2002), On the plausible linkage of thermospheric meridional winds with the equatorial spread *F*, *J. Atmos. Sol. Terr. Phys.*, *64*, 111.

Fejer, B. G., L. Scherliess, and E. R. de Paula (1999), Effects of the vertical plasma drift velocity on the generation and evolution of equatorial spread *F*, *J. Geophys. Res.*, *104*, 19,859.

Hysell, D. L., and J. D. Burcham (1998), JULIA radar studies of equatorial spread *F*, *J. Geophys. Res.*, *103*, 29,155.

Kelley, M. C., M. F. Larsen, C. A. LaHoz, and J. P. McClure (1981), Gravity wave initiation of equatorial spread *F*, *J. Geophys. Res.*, *86*, 9087.

Maruyama, T. (1988), A diagnostic model for equatorial spread *F*: 1. Model description and application to electric field and neutral wind effects, *J. Geophys. Res.*, *93*, 14,611.

Maruyama, T., and N. Matuura (1984), Longitudinal variability of annual changes in activity of equatorial spread *F* and plasma bubbles, *J. Geophys. Res.*, *89*, 10,903.

Mendillo, M., J. Baumgardner, X. Pi, P. J. Sultan, and R. Tsunoda (1992), Onset conditions for equatorial spread *F*, *J. Geophys. Res.*, *97*, 13,865.

Mendillo, M., J. Meriwether, and M. Biondi (2001), Testing the thermospheric neutral wind suppression mechanism for day-to-day variability of equatorial spread *F*, *J. Geophys. Res.*, *106*, 3655.

Meriwether, J. W., J. L. Mirick, M. A. Biondi, F. A. Herrero, and C. G. Fesen (1996), Evidence for orographic wave heating of the equatorial thermosphere at solar maximum, *Geophys. Res. Lett.*, *23*, 2177.

Meriwether, J. W., M. A. Biondi, F. A. Herrero, C. G. Fesen, and D. C. Hallenback (1997), Optical interferometric studies of the nighttime equatorial thermosphere: Enhanced temperatures and zonal wind gradients, *J. Geophys. Res.*, *102*, 20,041.

Valladares, C. E., W. B. Hanson, J. P. McClure, and B. L. Cragin (1983), Bottomside sinusoidal irregularities in the equatorial *F* region, *J. Geophys. Res.*, *88*, 8025.

Valladares, C. E., S. Basu, K. Groves, M. P. Hagan, D. Hysell, A. J. Mazzella Jr., and R. E. Sheehan (2001), Measurement of the latitudinal distributions of total electron content during equatorial spread *F* events, *J. Geophys. Res.*, *106*, 29,133.

Woodman, R. F., and C. LaHoz (1976), Radar observations of *F* region equatorial irregularities, *J. Geophys. Res.*, *81*, 5447.

R. E. Sheehan and C. E. Valladares, Institute for Scientific Research, Boston College, 140 Commonwealth Ave., Chestnut Hill, MA 02647, USA. (valladar@bc.edu)

J. Villalobos, Department of Physics, Universidad Nacional de Colombia, Bogota, Colombia. (ionosfera2001@yahoo.com)

Annales
Geophysicae

Latitudinal extension of low-latitude scintillations measured with a network of GPS receivers

C. E. Valladares[1], J. Villalobos[2], R. Sheehan[1], and M. P. Hagan[1]

[1]Institute for Scientific Research, Boston College, Newton Center, Massachusetts, USA
[2]Department of Physics , Universidad Nacional de Colombia, Bogota, Colombia

Abstract. A latitudinal-distributed network of GPS receivers has been operating within Colombia, Peru and Chile with sufficient latitudinal span to measure the absolute total electron content (TEC) at both crests of the equatorial anomaly. The network also provides the latitudinal extension of GPS scintillations and TEC depletions. The GPS-based information has been supplemented with density profiles collected with the Jicamarca digisonde and JULIA power maps to investigate the background conditions of the nighttime ionosphere that prevail during the formation and the persistence of plasma depletions. This paper presents case-study events in which the latitudinal extension of GPS scintillations, the maximum latitude of TEC depletion detections, and the altitude extension of radar plumes are correlated with the location and extension of the equatorial anomaly. Then it shows the combined statistics of GPS scintillations, TEC depletions, TEC latitudinal profiles, and bottomside density profiles collected between September 2001 and June 2002. It is demonstrated that multiple sights of TEC depletions from different stations can be used to estimate the drift of the background plasma, the tilt of the plasma plumes, and in some cases even the approximate time and location of the depletion onset. This study corroborates the fact that TEC depletions and radar plumes coincide with intense levels of GPS scintillations. Bottomside radar traces do not seem to be associated with GPS scintillations. It is demonstrated that scintillations/depletions can occur when the TEC latitude profiles are symmetric, asymmetric or highly asymmetric; this is during the absence of one crest. Comparison of the location of the northern crest of the equatorial anomaly and the maximum latitude of scintillations reveals that for 90% of the days, scintillations are confined within the boundaries of the 50% decay limit of the anomaly crests. The crests of the anomaly are the regions where the most intense GPS scintillations and the deepest TEC depletions are encountered. In accord with early results, we observe that GPS scintilla-

tions/TEC depletions mainly occur when the altitude of the magnetic equator F-region is above 500 km. Nevertheless, in many instances GPS scintillations and TEC depletions are observed to exist when the F-layer is well below 500 km or to persist when the F-layer undergoes its typical nighttime descent. Close inspection of the TEC profiles during scintillations/depletions events that occur when the equatorial F-layer peak is below 500 km altitude reveals that on these occasions the ratio of the crest-to-equator TEC is above 2, and the crests are displaced 10° or more from the magnetic equator. When the equatorial F-layer is above 500 km, neither of the two requirements is needed, as the flux tube seems to be inherently unstable. We discuss these findings in terms of the Rayleigh-Taylor instability (RTI) mechanism for flux-tube integrated quantities. We advance the idea that the seeming control that the reverse fountain effect exerts on inhibiting or suppressing GPS scintillations may be related to the redistribution of the density and plasma transport from the crests of the anomaly toward the equatorial region and then to much lower altitudes, and the simultaneous decrease of the F-region altitude. These two effects originate a decrease in the crest/trough ratio and a reduction of the crests separation, making the whole flux tube more stable to the RTI. The correspondence between crest separation, altitude of the equatorial F-region, the onset of depletions, and the altitude (latitude) extension of plumes (GPS scintillations) can be used to track the fate of the density structures.

Key words. Ionosphere (Equatorial ionsphere; ionospheric irregularities; modeling and forecasting)

1 Introduction

Equatorial spread F (ESF) is a complex plasma phenomenon that develops almost exclusively during the nighttime hours. ESF consists of a turbulent gravitational overturn of the ionosphere in which plasma densities and electric fields develop irregular structures with scale lengths from hundreds

Correspondence to: C. E. Valladares
(valladar@bc.edu)

of kilometers down to sub-meter sizes. A basic understanding of ESF has been obtained due to insights from Jicamarca measurements (Woodman and LaHoz, 1976), satellite in-situ observations (McClure et al., 1977), and numerical modeling of the Rayleigh-Taylor instability (Ossakov et al., 1979; Zalesak and Ossakov, 1980). Woodman and LaHoz (1976), almost 3 decades ago, presented two-dimensional maps of coherent echoes to indicate that plume-like structures extend for hundreds of kilometers in altitude, connecting the unstable bottomside F-region with the spread F on the stable topside. The radar maps provided strong evidence for a plasma density depletion convecting upward, following a Raleigh-Taylor Instability (RTI) mechanism. McClure et al. (1977) used plasma composition measured by the RPA on board the AE-C satellite to demonstrate that the plasma biteouts or depletions, seen in the nighttime equatorial F-region, sometimes contained molecular ions. This fact implied that the plasma depletions had recently moved from the low bottomside. Numerical calculations of the RTI conducted by Ott (1978) provided the rising velocity of the plasma bubbles in the collisional and inertial regimes, well in accord with experimental values. Computer simulations of the nonlinear collisional RTI carried out by Ossakov et al. (1979) demonstrated the production of topside irregularities by the rising bubbles and the dependence of the instability growth rate on the altitude of the F-layer and the gradient scale-size. Zalesak et al. (1982) incorporated the zonal neutral wind and an underlying E-region conductivity in their simulations and were able to demonstrate that these processes produce a slow-down effect in the evolution of ESF. Satyanarayana et al. (1984) investigated the effect of a velocity shear in the RTI that tends to stabilize the small-scale irregularities and excite long wavelength modes. Zargham and Seyler (1987) used boundary conditions proper for the nighttime F-layer to show the inherently anisotropic state of the generalized RTI. According to their numerical results, they postulated that a predominant km-scale wavelength develops in the zonal direction for an eastward-directed effective electric field, and shocklike structures are formed along the vertical direction.

It is well accepted that near sunset, the dynamics of the equatorial ionosphere are dominated by the pre-reversal enhancement (PRE) (Woodman, 1970) of the vertical drift, and that the variability of this process may dictate the onset or not of ESF (Basu et al., 1996; Fejer et al., 1999; Hysell and Burcham, 1998). The rapid decay of the E-region conductivity produces polarization electric fields that vary greatly in local time and latitude. The PRE is originated by a response of the electric fields to maintain a curl-free nature near sunset (Eccles, 1998), but is modified, up to some extent, by the divergence of zonal Hall currents in the off-equatorial E-region (Farley et al., 1986) and/or the zonal Cowling conductivity gradients in the electrojet (Haerendel and Eccles, 1992). The maximum value of the PRE has been associated with the generation and evolution of ESF (Fejer et al., 1999). These authors found that during solar minimum conditions a PRE larger than 15–20 m/s implied the occurrence of radar plumes extending to the topside. During so-

lar maximum conditions, (>200) a PRE of 40–45 m/s was required for the generation of ESF. When the PRE is fully developed, the Appleton anomaly is seen to re-intensify after sunset, making the crests more prominent and displaced even further away (15°-20°) from the magnetic equator. This close relationship between vertical drifts, the location of the crests of the anomaly, and ESF has been noted by several researchers (Whalen, 2001; Valladares et al., 2001). Others have used the amplitude of the equatorial anomaly to define precursors of the occurrence of ESF (Raghavarao et al., 1988; Sridharan et al., 1994). Whalen (2001) used bottomside densities collected by a network of sounders that operated in September 1958 to demonstrate that strong bottomside spread F (BSSF) and bubbles occurred when the crest density exceeded 3.5×10^6 cm^{-3}, and the anomaly peak was located poleward of 15.4° dip latitude. Weaker BSSF was observed when the crest of the anomaly was smaller and closer to the equator. No BSSF was detected when the peak density was below 3.5×10^6 cm^{-3} or if the crest was non-existent. Valladares et al. (2001) used TEC values measured with 6 GPS receivers forming a latitudinal chain, to show that during the equinoxes a crest-to-trough ratio equal to 2 or larger always implied the onset of UHF scintillations and the presence of radar plumes in the JULIA maps.

In addition to the vertical drift and the altitude of the F-layer, a downward vertical wind makes the F-region unstable to the initiation of the RTI. The meridional wind can also influence the onset of irregularities, by making the F-region more stable and inhibiting ESF. Maruyama and Matura (1984) and Maruyama (1988) indicated that a transequatorial wind could depress the F-layer in the lee side hemisphere, changing the field-integrated Pedersen conductivity and, consequently, suppressing the growth of the RTI. Mendillo et al. (1992) presented measurements from the Altair incoherent scatter radar and all-sky optical images providing evidence that a southward wind was somewhat responsible for lowering the density contours and making the whole flux tube more stable to the onset of the RTI. More recently, Mendillo et al. (2001) have re-examined the importance of the meridional winds in suppressing ESF during a campaign in South America. These researchers concluded that during the eight days of the campaign in September 1998, the meridional wind did not influence the onset of ESF in the pre-midnight hours. However, Devasia et al. (2002) have presented evidence that suggests that when h'F is below 300 km, ESF may occur only for a thermospheric meridional wind directed equatorward and less than 60 m/s.

In spite of this formidable advance in the theory of ESF, we are not able to forecast with complete certainty the day-to-day variability of ESF, even less to predict the specific region that will become unstable or calculate in advance the maximum altitude that the plasma bubbles may attain. This apparent failure may be a sign of our inability to measure the great variability of several ionospheric parameters with the accuracy that is needed. Alternatively, it may indicate that one important ingredient of the physics of equatorial plasma bubbles is still missing.

This paper shows TEC values measured by a network of ten GPS receivers during ten months, spanning September 2001 and June 2002. We present GPS scintillations measured by three of these receivers in an effort to assess the latitudinal (and apex altitude) extension of the plasma bubbles. We also used information of TEC depletions, and range-time maps of coherent echoes collected with the JULIA radar, to indicate the spatial location of plasma biteouts and to infer that the GPS scintillations, in fact, correspond to plasma bubbles or depletions in the equatorial F-region. We also investigate the background conditions of the equatorial ionosphere, by providing the location of the crests and the trough. Three events are analyzed in detail and the statistics of the first 10 months of operations at Bogota are introduced to demonstrate that in most cases the plasma bubbles extend up to the poleward edges of the anomaly. Finally, we use measurements conducted with the Jicamarca digisonde to corroborate the relationship between the appearance of GPS scintillations and the altitude of the F-region.

2 Instrumentation

TEC measurements were gathered using 10 GPS receivers located near the west coast of South America, and spanning in latitude between 9° N and 40° S. Their fields-of-view are indicated in Fig. 1, using circles extending 45° in elevation. Five of these receivers are managed by BC. These receivers have been implemented with specially-designed software that makes real-time calculations of the amplitude scintillations. Four of the sites (Bogota, Iquitos, Pucallpa and Cuzco) are equipped with CRS 1000 Leica receivers running at 10 Hz. The last of the five sites (Ancon) possesses two GPS receivers, a Novatel that records GPS signals at 50 Hz, and an Ashtech receiver dedicated to measure TEC values. Figure 1 also displays the geographic location of the magnetic equator and the 15° magnetic latitude line. Note that the Bogota and Santiago stations are practically conjugate from the magnetic equator. These two receivers are able to measure, quite frequently, the TEC value in the northern and southern crests of the anomaly. Other systems, such as the UHF (~250 MHz) and L-band scintillation receivers, have operated at Ancon and Antofagasta since 1994 and 1996, respectively. These systems measure the S4 index, the spectra of the amplitude scintillation, and the zonal drift of the irregularities (Valladares et al., 1996), using the space-antenna technique. The ionospheric penetration points corresponding to the UHF systems are shown with the large crosses, and labeled F7 and F8. These points are the 350-km altitude intersection of the lines-of-sight directed to 2 geosynchronous satellites parked at the 100° W and 23° W meridians. A ground projection of the magnetic field line passing above the Ancon F8 ionospheric intersection has been traced to indicate that this point and the Antofagasta F7 intersection point are almost aligned along the same field line. The apex altitude of this field line is at 1200 km over the magnetic equator and is displayed ending in the F-region (350 km) near
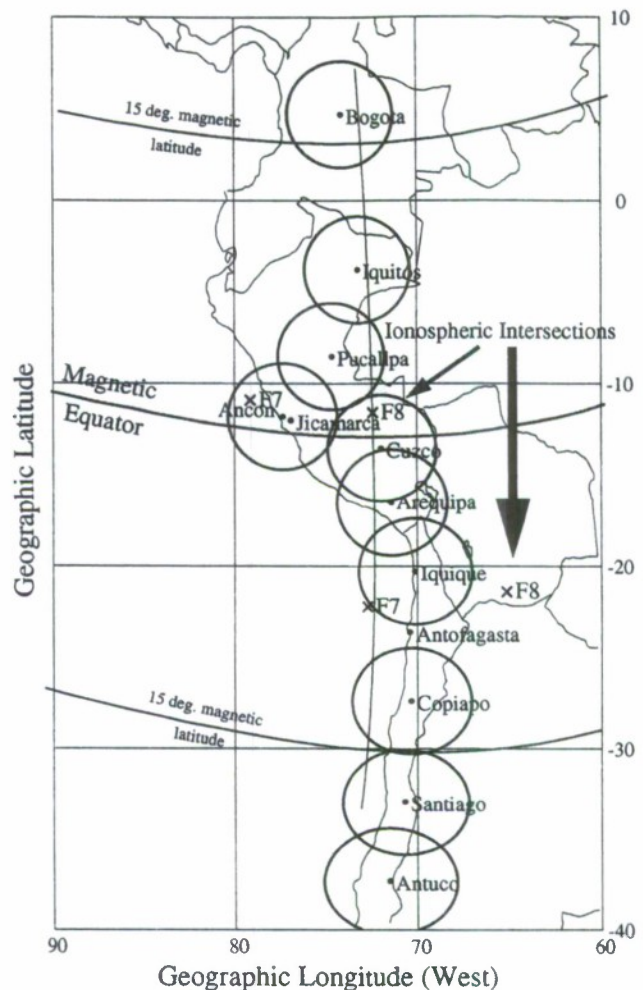
Fig. 1. Geographic locations of several GPS receivers operating near the west coast of South America. The stations at Ancon, Cuzco, Pucallpa, Iquitos and Bogota form the North Andes Project (NAP) network. The stations at Iquique, Copiapo and Antuco are part of the South Andes Project (SAP) network. The stations at Arequipa and Santiago correspond to the IGS network of receivers. The locations of the Jicamarca radar and the sub-ionospheric intersections of the lines-of-sight from the Ancon and Antofagasta UHF receivers to the F7 and F8 satellites are also included. The line crossing the F8 intersection point shows the ground projection of a field line with apex height equal to 1200 km that ends at 350 km altitude.

Bogota in the north and close to Santiago in the south. This paper also presents altitude-time maps of coherent echoes collected with the JULIA radar. A comprehensive description of this system can be found in the publication by Hysell and Burcham (1998).

3 TEC depletions

A TEC depletion consists of a sudden reduction of TEC followed by a recovery to a level near the TEC value preceding

Fig. 2. Values of absolute TEC measured at several sites using signals from 3 GPS satellites. In all of these passes TEC depletions are evident, sometimes exceeding 50 TEC units (10^{16} el/m^2). The additional sub-panel plotted below the Bogota, Iquitos and Cuzco TEC data corresponds to the S4 GPS scintillation index. Note that the minimum at Arequipa coincides w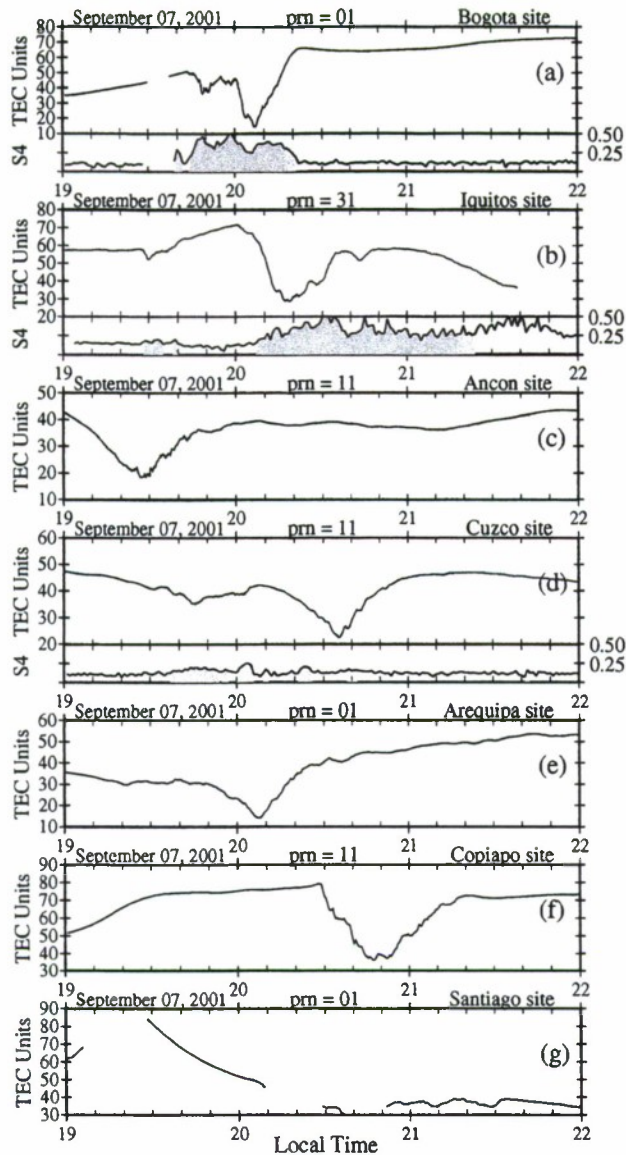ith the minimum at Bogota, which is located ~200 km to the west. As the bubbles move toward the east, TEC depletions should be observed at Bogota tens of min ahead of Arequipa. This discrepancy can be explained by the westward tilt of the plumes. See text for details.

the depletion. A TEC depletion originates when one or more plasma bubbles $E \times B$ drift across the satellite ray path. The general morphology of TEC depletions and their association with strong levels of VHF scintillations were described by DasGupta et al. (1983). More recently, Weber et al. (1996) have showed that there exists a strong correlation between TEC depletions and airglow 630.0 nm depletions, endors-

ing the view that TEC depletions are a manifestation of the equatorial plasma depletions (also called bubbles). In this section, we use the information about TEC depletions gathered by a network of GPS receivers to infer the presence and the north-south extension of plasma bubbles. Nevertheless, we are aware that other non-bubble-related processes could produce quick reductions in the TEC value, and lead to a mistaken identification of the TEC depletions. Processes such as the nighttime decay of the F-layer and the density re-distribution caused by the fountain effect also lessen the TEC value. However, these two types of processes result in shallow TEC slopes and an absence of the recovery segment. We have excluded these cases from our statistics of TEC depletions. Different than previous studies, the TEC depletions presented here were sequentially detected by several of the 10 receivers located at different longitudes, providing a glimpse of the temporal evolution of the plasma depletions. Due to the relatively slow east-west motion of the GPS satellites, it is fair to say that the plasma depletions are traversing a quasi-stationary receiver-satellite link. We also note that the temporal duration of the passage of TEC depletion is a function of the bubble width and the satellite elevation. A pass near zenith will provide a TEC depletion width almost equal to the true bubble cross section. As the line-of-sight elevation becomes lower the TEC depletion will appear much wider. We also note that the depth of the TEC depletion is more likely to be a function of the local F-region peak density, the value of the underlying equatorial bottomside, and the magnetic latitude of the observation point. Assuming that the density remains constant along the depleted flux tube (Hanson and Bamgboye, 1984), there may exist a more pronounced depletion at the crest of the anomaly than at the magnetic equator.

Figure 2 shows TEC depletions measured at several sites, using signals from three different GPS satellites. On this day, TEC depletions were observed at all stations except Antuco. In addition, the receiver at Santiago suffered a loss of signals caused by the strong fading which was likely associated with TEC depletions. Figure 2a shows the passage of a TEC depletion, 35 TEC units (10^{16} el/m^2) in depth, detected by the receiver at Bogota between 20:00 and 20:20 LT. Below the TEC curve, we display the S4 index that is calculated on-line using the signal received from each of GPS satellites. The gray shading indicates the times when the S4 index is above the noise level and the satellite elevation is above 20°. The TEC depletion of Fig. 2a is accompanied by high levels of GPS scintillations (S4=0.5) on both the east and west walls of the depletion. Figure 2b illustrates the same TEC depletion that was detected at Bogota 11 min earlier, but at Iquitos strong values (0.5) of the S4 index were seen only on the west wall and weaker scintillations on the east side (0.25) of the depletion. Due to the smaller look angle, the receiver at Iquitos observed the same TEC depletion that was seen at Bogota with an apparent wider width. The longitudinal separation between stations, and the time the TEC depletion takes to drift between them can be used to calculate the average zonal velocity of the plasma. We have used the transit time of TEC

depletions between Ancon and Cuzco (65 min) that are separated by 550 km in the magnetic east-west direction, and calculated a 140 m/s average zonal drift. Scintillations at Cuzco (Fig. 2d) were less intense, due to a smaller density that commonly prevails near the magnetic equator when the anomaly is fully developed. At Arequipa, the lowest value within the TEC depletion was observed at 20:08 UT. This is the same time that the minimum TEC was detected in Bogota (Fig. 2a), which is located 225 km west and several hundred kilometers north of Arequipa. This apparent discrepancy can be explained if we allow the bubbles to tilt westward at altitudes above the F-region peak (Woodman and LaHoz, 1976). The westward tilt will make the part of the TEC depletions that extends to higher latitudes to appear at slightly later times in a way similar to the plasma plumes seen with coherent radars. The Copiapo receiver (Fig. 2f) detected a 30 TEC units depletion spanning between 20:30 and 21:10 LT. As mentioned before, the receiver at Santiago was strongly affected by deep fades, likely associated with the turbulence within the depletions, suffered several data dropouts, and recorded only minor TEC disturbances.

Figure 3 displays the passage of two deep TEC depletions, which were observed by several of the receivers on 6 February 2002. Figures 3a–3i display TEC values collected from signals transmitted only by 2 GPS satellites. The subionospheric intersections between satellite 26 and the sites at Bogota, Iquitos, Pucallpa, Ancon and Cuzco varied in a south to north fashion, following a direction almost aligned with the local field line. The ionospheric penetration point from GPS satellite 09 passed south of Arequipa, Iquique, Copiapo, and Antuco, moving from west to east. Figure 3a shows that GPS scintillations at Bogota are equally intense on both sides of the depletion. However, at lower magnetic latitudes stations such as Iquitos and Cuzco (Figs. 3b and 3e), we observed that the west wall of the depletion possesses larger S4 values than the east side. Similar to Fig. 2 the plasma bubbles drift through the stations' fields-of-view at slightly different times. This means that a plasma bubble aligned with the B field and with no tilt in altitude will sequentially go through Ancon, Pucallpa, Bogota, Iquitos and Cuzco. If the bubble is tilted in altitude, as most of them are, then the station located further poleward, Bogota, may detect the TEC depletion after it has passed over a more equatorward station located further to the east, as Iquitos. This is the most likely physical scenario that can explain the TEC data recorded on 6 February 2002, as the first TEC depletion was seen at Iquitos at 20:25 LT, then at Bogota at 20:40 LT, and later at Cuzco ~20:45 LT. In addition, traces of the temporal variability of the sub-ionospheric intersections from different stations but toward the same GPS satellite display almost parallel curves separated by the distance between the stations. It is quite significant that the Ancon and Pucallpa stations did not observe any TEC depletion before 20:25 LT. The implication of the last statement is that the depletion, seen at Iquitos at 20:25 LT, appeared in a location between Pucallpa and Iquitos, near the 74° W meridian and was triggered approximately at 20:20 LT. A different TEC depletion was seen
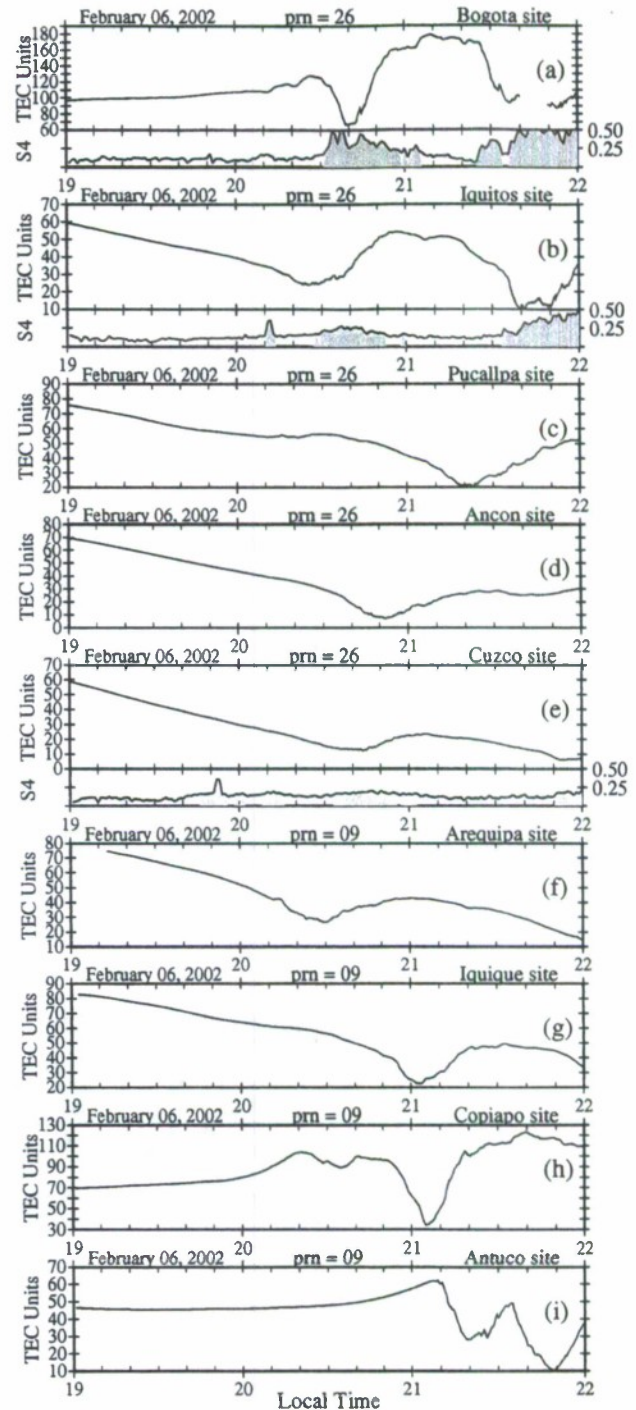
Fig. 3. Same as Fig. 2, but for 6 February 2002. Plasma bubbles drift through the stations fields-of-view at slightly different times. One TEC depletion was seen first at Iquitos at 20:25 LT, then at 20:40 LT at Bogota, and later at Cuzco ~20:45 LT. Ancon and Pucallpa did not observe the TEC depletion, suggesting that the depletion developed in a location between Pucallpa and Iquitos, near the 74° W meridian and approximately at 20:20 LT.
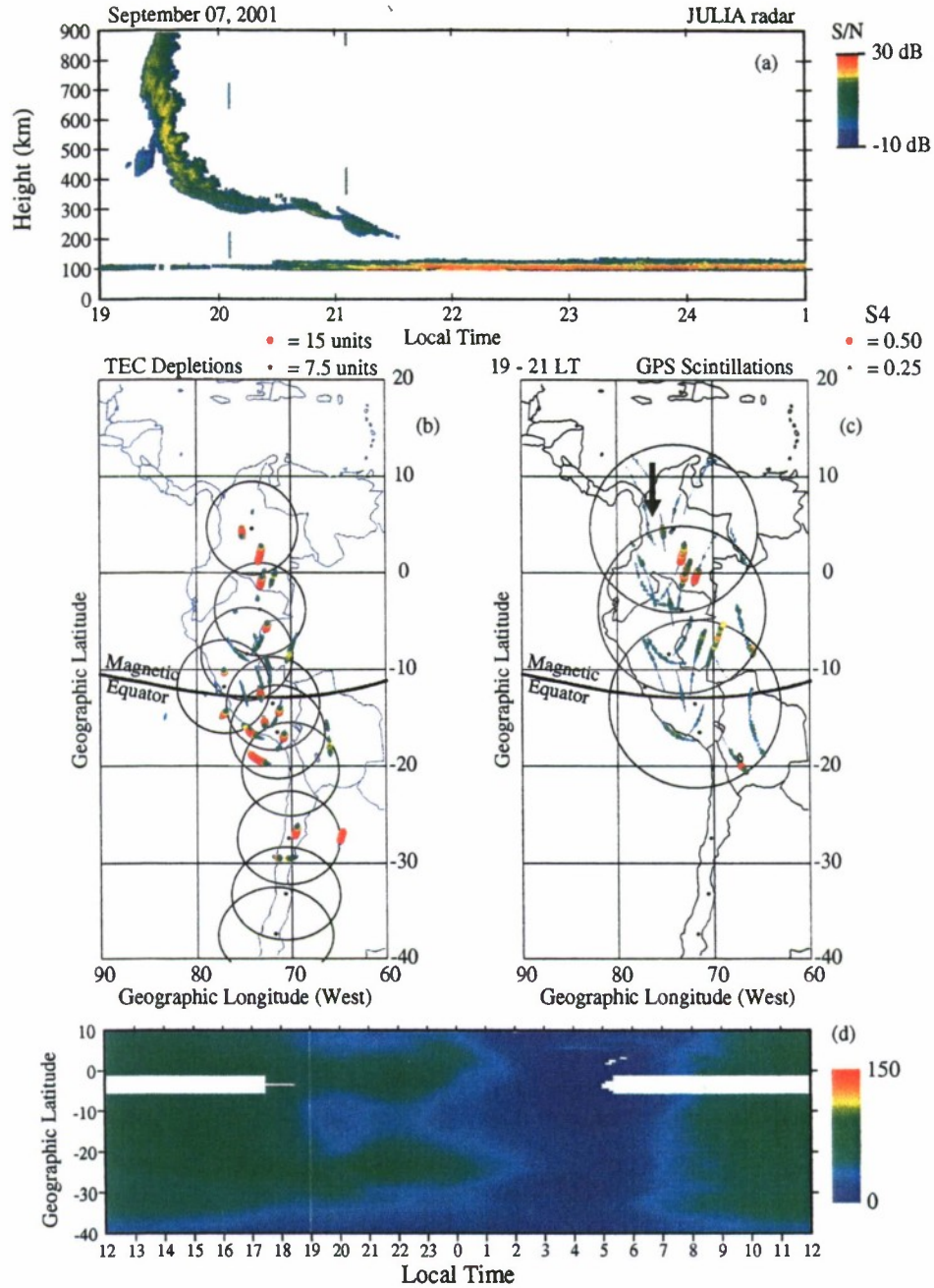
Fig. 4. The top panel shows range-time-intensity plot of a radar plume and a bottomside trace observed by the JULIA radar on 7 September 2001. The middle panels show maps of TEC depletions and GPS scintillations detected by the GPS receivers in South America. The lower panel displays absolute TEC latitudinal profiles measured between 12:00 LT on 7 September and 12:00 LT on 8 September 2001.

first in Ancon at 20:50 LT very close to the zenith direction. This depletion drifted through Pucallpa (21:20 LT), Bogota (21:38 LT), Iquitos (21:40 LT) and later Cuzco at 21:55 LT. The level of depletion in the northern crest (Bogota) was 60 TEC units. At Copiapo, near the southern crest of the anomaly the depletion was also 60 units, which indicates that the amount of depletion is approximately symmetric with respect to the magnetic equator. Nevertheless, as we will see in the following section, the TEC latitudinal profiles were

not well symmetric. Note that the TEC value at Copiapo is above 100 TEC units, which for this local time is indicative that the southern crest of the anomaly was situated close to this site. The Antuco site, located ~1000 km south of Copiapo, was likely located south of the southern crest. However, two deep depletions of 20 TEC units were seen here. This fact suggests that under some circumstances a TEC depletion can be located near the poleward limits of the anomaly and map to very high apex altitudes.

36

4 Case Studies

In Sect. 3 we presented TEC depletions observed near the anomaly crests that were as large as 60 TEC units in depth, but close to the magnetic equator the TEC depletions were only 20 TEC units or less. In this section, we introduce three case studies to confirm the inherent association between TEC depletions, GPS scintillations and radar plumes.

4.1 7 September 2001

Figure 4a shows the JULIA power map measured on 7 September 2001, in which we observed a single plume, extending at least 900 km altitude at 19:30 LT. The correspondence of this radar plume and a TEC depletion containing low density plasma is demonstrated in Fig. 2c by the presence of a 15-unit TEC depletion passing near Ancon, also at 19:30 UT. No additional plumes were seen at Jicamarca during the rest of the evening, although a bottomside trace was detected with JULIA lowering in altitude between 19:40 and 21:30 LT. In association with the bottomside trace, no TEC depletions were observed near the Jicamarca longitude. Nevertheless, other TEC depletions developed far to the east of the 76° W meridian. Also significant was the absence of UHF scintillations (not shown here) after 20:00 LT at the Ancon F7 sub-ionospheric intersection (see Fig. 1). This lack of UHF scintillations and the absence of TEC depletions larger than 2 TEC units, implied that the JULIA bottomside trace of 7 September 2001 was not associated with significantly large TEC depletions, and if 1-km irregularities existed, they were constrained to the bottomside F-region and probably generated a very low level of UHF scintillations below the detection threshold of the Ancon system.

Figure 4b displays the location and the magnitude of the TEC depletions that were identified in the TEC profiles for all stations and all satellites passes observed between 19:00 and 21:00 LT. This plot denotes three important features common to the three events presented in this section. First, the latitudinal extension of the TEC depletions is quite symmetric with respect to the magnetic equator. Secondly, the depth of the TEC depletion is less at the equator (<8 units) and larger at the crests (>30 units). Thirdly, the latitudinal extension of the depletions agrees quite well with the maximum latitude of scintillations.

Figure 4c shows the L1 GPS scintillations measured with the receivers deployed at Bogota, Iquitos and Cuzco between 19:00 and 21:00 LT. Scintillations from Pucallpa were not included due to the strong contamination of the S4 index produced by signal multi-paths. The magnitude of the S4 index has been color coded according to the scale indicated in the upper right corner. The S4 scintillation index is equal to 0.4 at the location of the northern crest where the density is the largest, but decreases to 0.2 at the trough. The scintillations associated with the radar plume are seen to reach 16° magnetic latitude (see arrow in Fig. 4c). A field line crossing the F-region at this latitude maps to an apex height of 1000 km. This maximum altitude inferred from the GPS scintillation

does not contradict the smaller apex altitude of the plume since the JULIA range-time plot was limited to 900 km.

Figure 4d shows a color-coded representation of the TEC values measured on 7 September 2001, plotted as a function of latitude and local time. At 19:00 LT, the TEC value near the magnetic equator (−12° geographic latitude) diminished rapidly and the amplitude of the crests increased slightly, indicating a re-energization of the fountain effect and the development of a more pronounced anomaly. The anomaly remained visible until 02:00 LT, when the TEC latitudinal profiles became more uniform and adopted a typical nighttime value of 15 units. On this day the anomaly was quite symmetric, centered at the magnetic equator, and with both crests possessing nearly the same width.

4.2 3 December 2001

Figure 5 shows the intensity of coherent echoes measured by JULIA on 3 December 2001, the locations of TEC depletions and GPS scintillations superimposed on a geographic layout, and 24 h of TEC latitudinal profiles centered on local midnight. The JULIA map indicates the existence of a 100-km thick bottomside layer, which starts right after sunset and lasts until 23;30 LT. A single radar plume appeared at 20:35 LT and extended up to 720 km altitude. GPS scintillations corresponding to this day (Fig. 5c) show that the latitudinal extension of scintillations has a strong variability as a function of longitude. It reaches 15° magnetic latitude (MLAT) at 73° W longitude, but only 13° MLAT near the Jicamarca longitude (see arrow). A plume rising to 720 km maps to 12.7° MLAT, which is in very good agreement with the maximum extension of GPS scintillations at the Jicamarca longitude. Figure 5b shows that on this day the TEC depletions have depths smaller than the depletions seen on 7 September 2001. The TEC depletions are 6 units near the equator and about 10 units at the anomaly, much smaller than 12 and >40 units that was seen at the equator and the crests on 7 September 2001. Notwithstanding, the GPS scintillations of 3 December 2001 are more intense, containing S4 values near 0.6 at the northern crest and 0.4 near the trough. Another important difference is the low level of UHF scintillations that was detected on 7 September 2001 (S4=0.3) and the more intense (S4=0.7) and long lasting event of 3 December 2001. On the latter day, a decreasing level of scintillations was seen between 20:00 LT and the early morning hours (06:00 LT).

Figure 5d shows the formation of the TEC anomaly that occurred right after sunset. Both the northern and southern crests are easily distinguishable after 19:30 LT. However, both crests are not symmetric, presenting different peak values, widths and lifetimes. It has been indicated that a northward directed meridional wind is able to reduce the amplitude of the southern crest and amplify the northern crest by transporting the plasma along field lines. The TEC distribution of 3 December 2001 can be well explained by this wind mechanism. Maruyama and Matuura (1984) have suggested that a meridional wind with this characteristic might
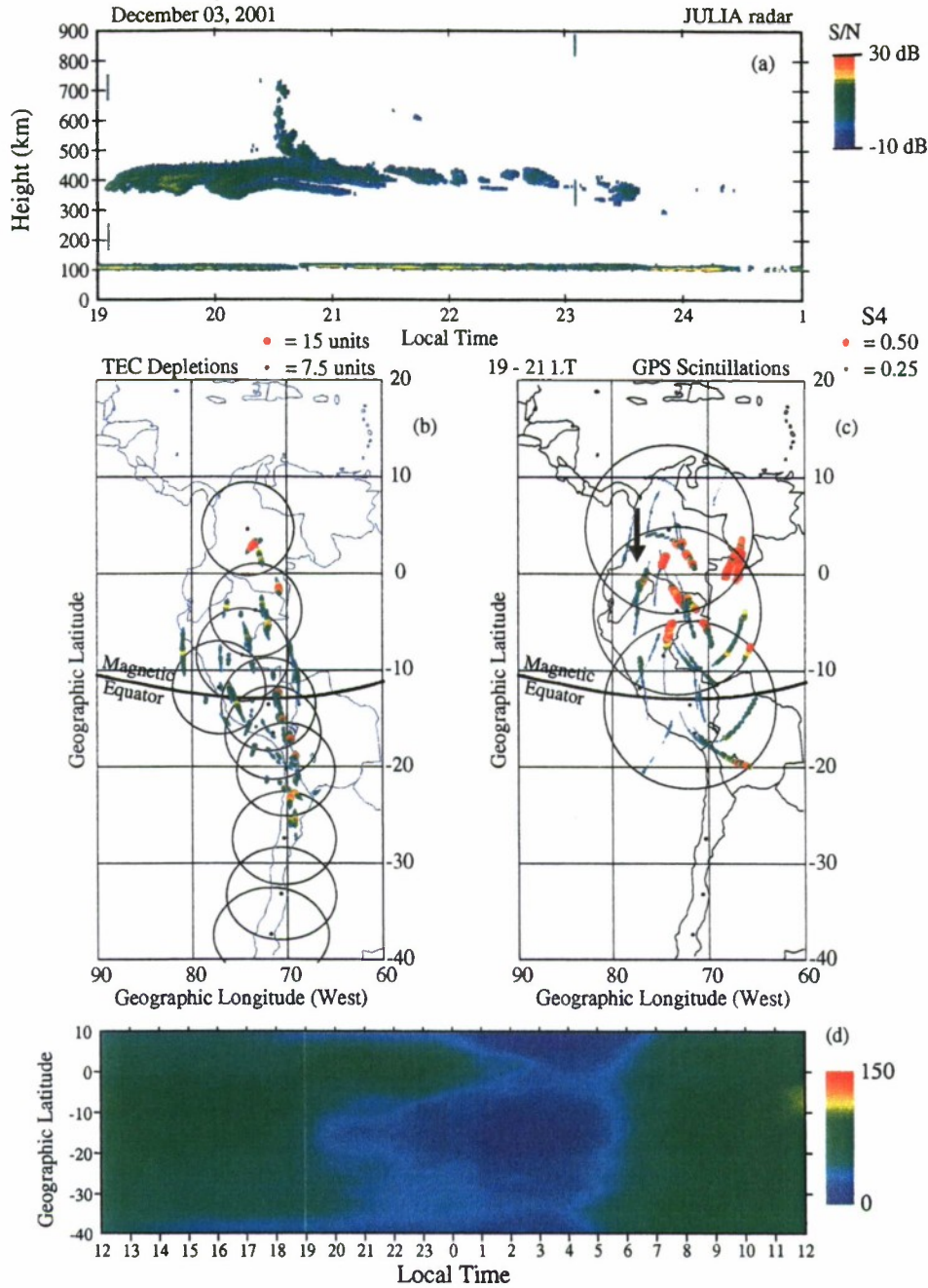
Fig. 5. Same as Fig. 4, but corresponding to 3 December 2001. The top panel shows a single radar plume developing at 20:40 LT, and reaching 700 km. The TEC depletion and the GPS scintillations, at locations near Jicamarca, extend up to 13° magnetic latitude. The TEC profiles seen near sunset are highly asymmetric. Nevertheless, strong scintillations were detected this day.

inhibit the growth of the equatorial plasma bubbles. However, we did not observe an inhibition of the irregularities on 3 December 2001 and on many other nights, which are presented below in Sect. 5. It has been recently suggested by Devasia et al. (2002) that the transequatorial wind may act as an instability suppressor but only when the F-region altitude is below a certain limit. This hypothesis could explain the maintenance of ESF during nights when the anomaly is

widely asymmetric. In Sect. 7, we put forth another hypothesis that might explain the variability of the TEC profiles that commonly exist during GPS scintillations events.

4.3 6 February 2002

Figure 6 shows a plot of JULIA coherent echoes, TEC depletions, GPS scintillations, and TEC latitudinal profiles recorded on 3 February 2002. The JULIA map illustrates the
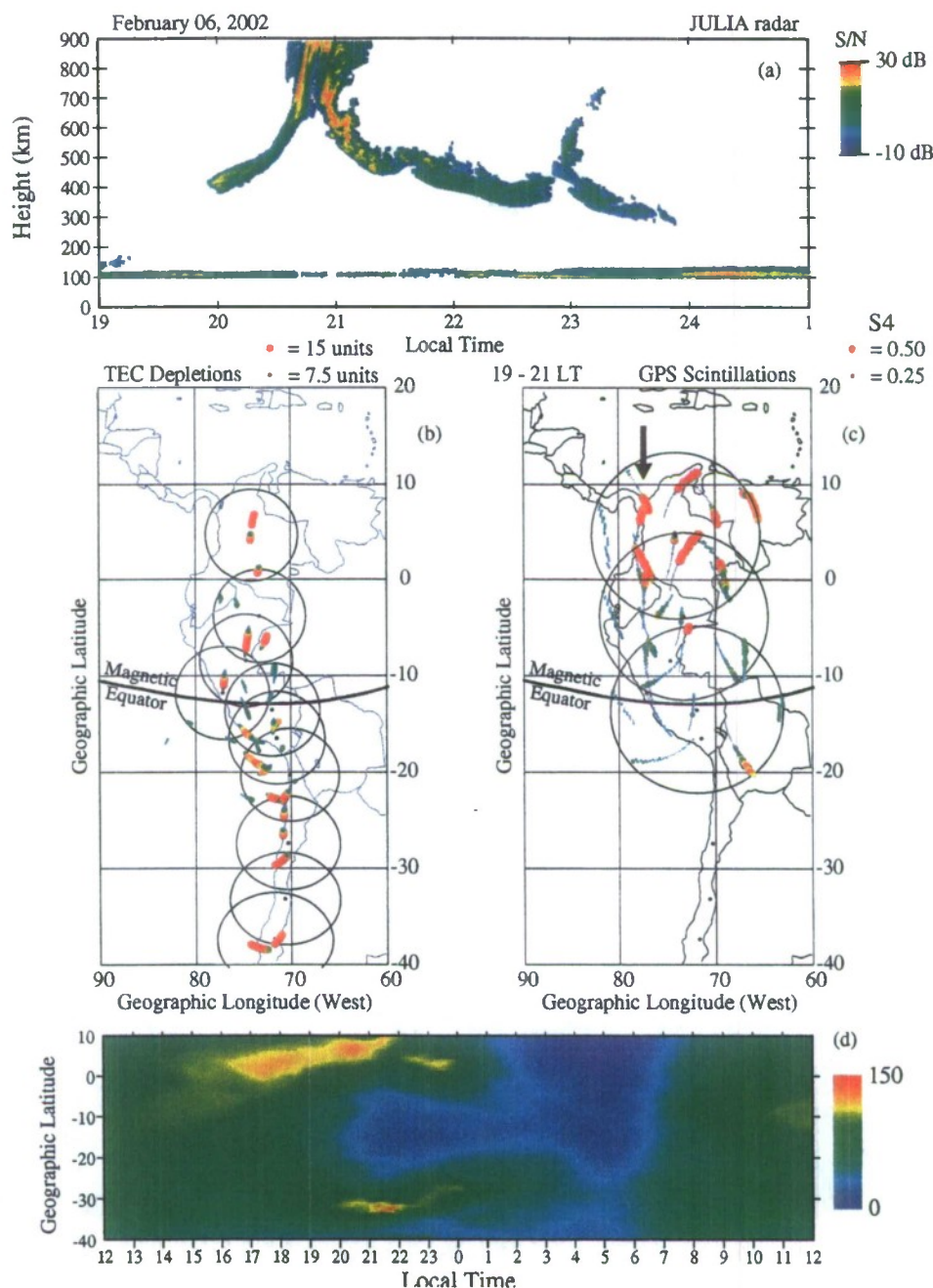
38

Fig. 6. Same as Fig. 4, but corresponding to 6 February 2002. The radar map shows two plumes. The first occurs between 20:40 and 21:10 LT and extends beyond 900 km. The TEC depletions and GPS scintillations detected at several sites extend up to 23 degrees magnetic latitude and indicate that the plasma bubbles extend up to 1400 km altitude.

extension of two radar plumes that developed from a bottomside trace that was seen to continuously decrease in altitude. The first plume was seen at 21:00 LT, when the F-region bottomside had raised up to 600 km altitude. The strength of the echoes suggested that this plume extended well beyond the 900 km altitude limit of Fig. 6a. The second plume was detected at 23:00 LT and reached 700 km altitude. Figure 6b displays the geographic location of several TEC depletions measured by all ten GPS receivers. Similar to the other

two case-events, the magnitude of the depletions increased at latitudes further away from the equator, but in this event the depletions were seen up to 20° N MLAT (8° geographic lat) and 25° S MLAT (38° S geographic lat). The depletions detected at the Ancon and Cuzco sites were 20 units, but reached 40–50 units near the crests of the anomaly. As expected the magnitude of the GPS scintillation index (Fig. 6c) is much larger during this day. S4 values as high as 0.8 were encountered at 23° MLAT, but only 0.3 near the magnetic
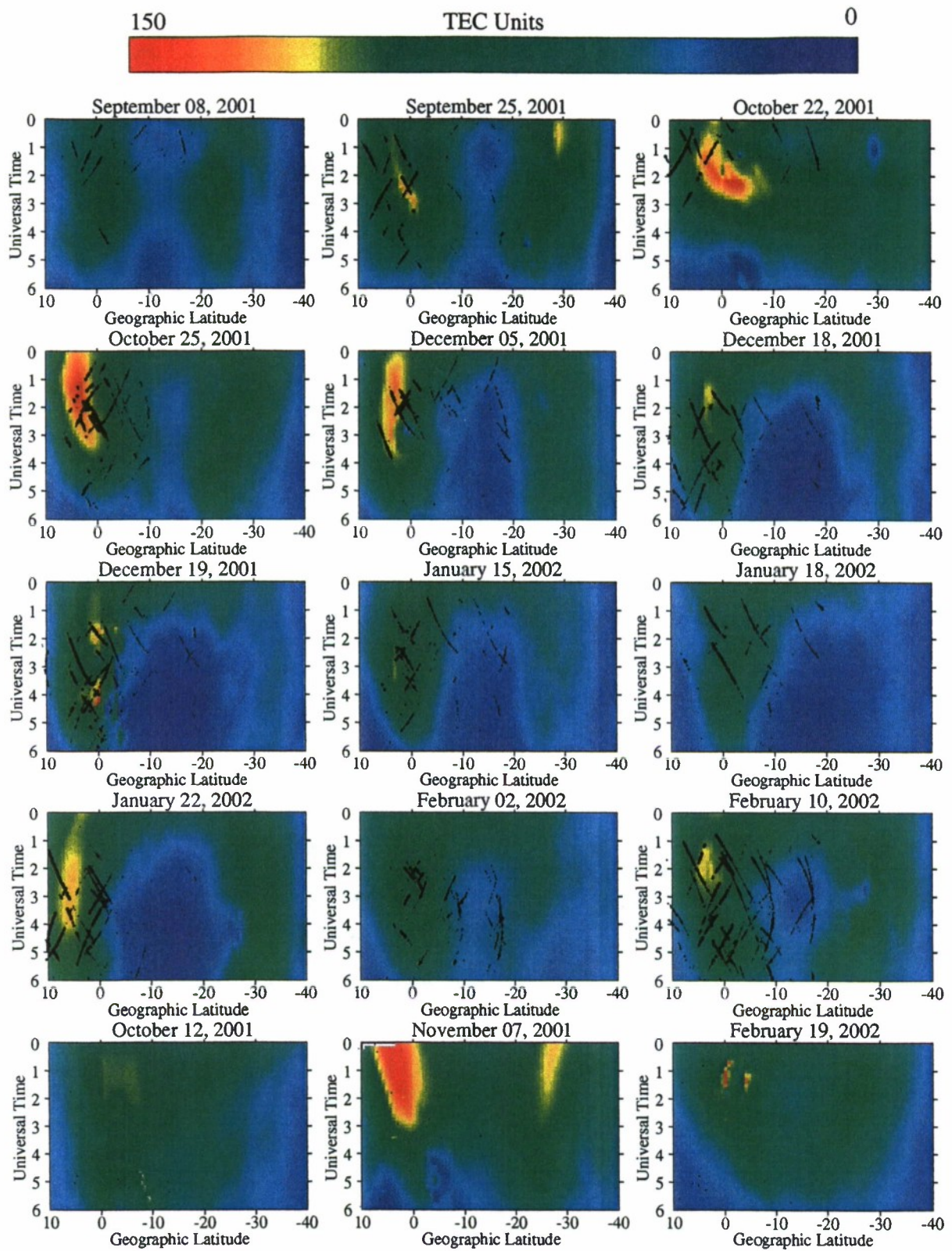
Fig. 7. Absolute TEC distributions for 15 case study events observed during the equinox and December solstice seasons. The first 12 cases correspond to days of GPS scintillations and the last 3 (the lower row) are for days with no scintillations. The black traces indicate the location, time and intensity of the GPS scintillations.

equator. UHF scintillations, measured at Ancon with the 250 MHz system, were also much stronger than the previous two cases. The UHF scintillations detected at both F7 and F8 sub-ionospheric penetration points contained several bursts of saturated values. The TEC profiles of Fig. 6d indicates that the TEC anomaly becomes more pronounced and separated from the magnetic equator at 17:00 LT. Both crests are displaced at least 19° MLAT away from the magnetic equator at 22:00 LT. This event displays one of the largest anomaly displacements that we have seen. The location of the crests 19° away from the magnetic equator correlates quite well with the largest latitudinal extensions of scintillations. Right after 22:00 LT, both crests retracted and moved closer to the magnetic equator until 01:00 LT when they faded. We interpret that this separation of the crests of the anomaly is the result of a strong fountain effect, driven by a large vertical drift that was most likely directed upwards until 22:00 LT when it reversed to a downward direction.

5 Simultaneous observations of TEC and GPS scintillations

Figure 7 shows the temporal evolution of the TEC profiles for 15 days selected between the months of September 2001 and February 2002. The TEC values presented in this figure correspond to the first 6 h of the evening, starting after local sunset (00:00 UT). The dark traces superimposed on the color-coded TEC data illustrate the scintillation S4 index measured at Bogota, Iquitos and Cuzco. They are placed at the latitude of the sub-ionospheric penetration point and at the times when the S4 index exceeded the noise level (0.20). The purpose of this figure is: 1) to demonstrate the close relationship between the location of scintillations and the latitudinal extension of the equatorial anomaly, and 2) to indicate the rapid response of GPS scintillations to the evolution of the TEC profiles. The 12 frames in the four upper rows show data for days with scintillation activity. The three frames in the bottom row are for nights with no scintillation activity. It is worthwhile to note that between 00:00 and 06:00 UT the nighttime F-region normally decays in a slow manner. In addition, during the early evening hours there commonly exists a rapid plasma re-distribution along the field lines: the fountain effect. An upward drift near the equator drives the direct fountain effect (Hanson and Moffett, 1966) by moving the plasma poleward, reinforces the amplitude of the crests, and reduces the density at the trough. A downward vertical velocity creates a reverse fountain effect (Sridharan et al., 1993; Balan and Bailey, 1995), moves both crests equatorward, diminishes the size of the crests, and increases the TEC value at the trough.

The frame labeled 8 September 2001 (7 Sept 2001 in local time), placed in the upper left corner, reproduces the TEC latitudinal profiles of Fig. 4d, but here we introduce the scintillation information within the context of the TEC variability. GPS scintillations appeared at 00:00 UT, when the TEC crest was fairly constant; the trough TEC value was small and the

crest/trough ratio close to 2. Scintillations ceased between 02:20 and 04:00 UT during a period when the TEC value at the trough increased from 35 to 45 units. This evolution of the TEC profiles follows the typical variability of the TEC latitudinal profiles when a reverse fountain develops. Scintillation activity resumed after 04:00 UT when the trough decreased and the TEC crest increased in amplitude, suggesting a late re-initiation of the fountain effect. The frame for 25 September 2001 presents a case when both crests of the anomaly were relatively wide and large. Scintillations persisted for almost two hours after both crests decreased due to the effect of a reverse fountain. Notice that for both days described above, and for most of the cases in Fig. 7, we detected high levels of GPS scintillations confined within the boundaries of the anomaly. A more dramatic case of the control that the variability of the anomaly exerts on the existence of GPS scintillations is shown in the frame corresponding to 22 October 2001, a day of intense magnetic activity. The rapid equatorward motion of the crest, seen at 02:00 UT, is again the manifestation of a large downward vertical drift that drives the reverse fountain. Similar to the frame for 8 September 2001, this example shows an excellent correlation between the equatorward displacement of the anomaly and the suppression of scintillations. The sub-frames in the second and third rows show events in which the amplitude of the anomaly was asymmetric. These events were seen during the December solstice when it is typical to have a meridional wind blowing northward during the afternoon and early evening hours (Meriwether et al., 1986). Notice that in two cases (19 December 2001 and 18 January 2002), the southern crest was almost non-existent. Nevertheless, high levels of GPS scintillations were detected on the northern part of the anomaly. We do not have records of GPS scintillations at regions south of the magnetic equator. However, we do indicate that the UHF system at Antofagasta (22° S latitude, 10° S magnetic latitude) recorded strong, followed by moderate levels of scintillations between 00:20 and 08:00 UT. These two cases also emphasize the notion that the regions of scintillations are limited poleward within regions where the anomaly is fully developed and prominent in comparison to the TEC trough. The 25 October 2001 event shows the northern crest moving inward toward the equator and the amplitude of the crest decaying very rapidly after 02:00 UT. GPS scintillations were observed to stay for 3 more hours after the start of the reverse fountain. During the event of 5 December 2001, scintillations decayed much rapidly after the crest amplitude diminished from 140 to 100 units at 03:50 UT. The following 2 frames, corresponding to 18 and 19 December 2001, display the northern crest slowly decaying with no apparent increase or decrease of the TEC value at the trough. During these two days of no apparent fountain effects between 00:00 and 06:00 UT, GPS scintillation persisted even after 06:00 UT. This is longer than the other cases when the reverse fountain was active. On these two days GPS scintillations lasted until the amplitude of the crest was below 40 TEC units. The 15 January 2002 TEC panel presents a case of moderate levels of GPS scintillations over
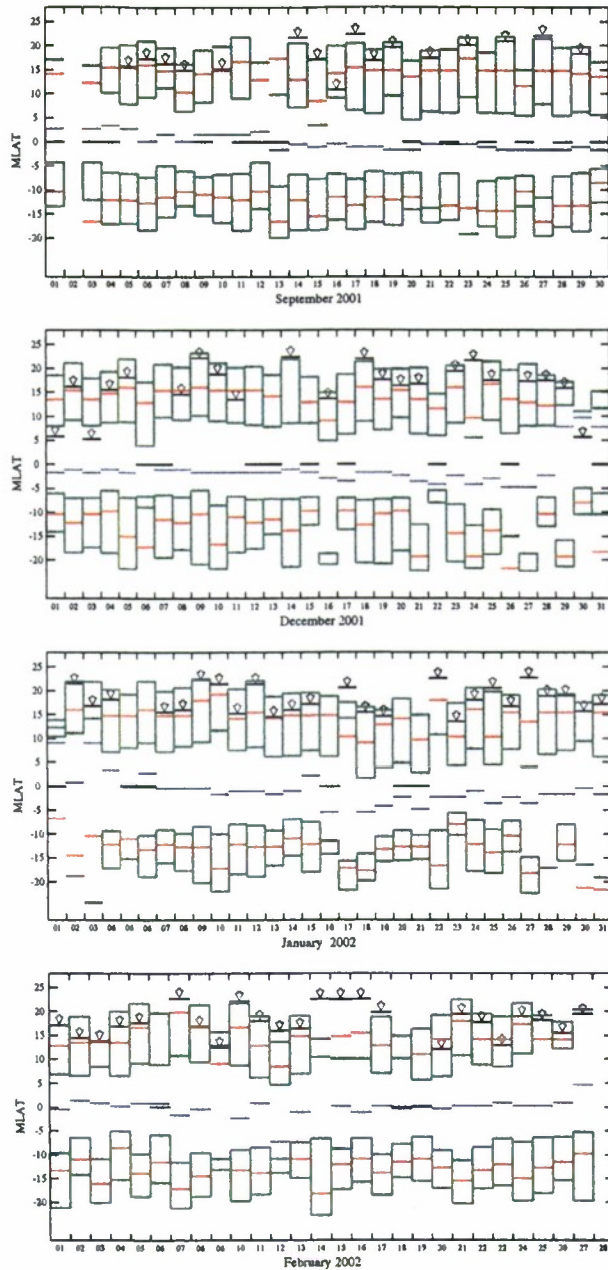
Fig. 8. Latitudinal distribution of the location of the anomaly for the months of September, December, January and February. The blue trace near 0° magnetic latitude indicates the location of the trough. The red lines are used to point out the locations of the anomaly crests. The green lines indicate the extension where the crests diminish 50%. The short black lines and the arrows seen near the northern boundary of the northern crest indicate the maximum latitude of GPS scintillations. Note that only in a few cases does the maximum latitude of scintillations extend beyond the limits of the anomaly.

the anomaly peak and weak scintillations within the trough region. The frame for 22 January 2002 shows the northern crest of the anomaly displaced up to 19° magnetic latitude and GPS scintillations extending beyond our latitudinal cov-

erage. The frame for 2 February 2002 shows the crests of the anomaly placed near 13° magnetic latitude and the GPS scintillations confined to a maximum latitudinal extension of 14° magnetic latitude. On this day scintillations ceased at 05:30 UT during a period when the reverse fountain was in effect. The frame corresponding to 10 February 2002 shows a pattern of strong scintillations that initiated at 01:00 UT. At this time, there is a re-initiation of the fountain effect, shown as a decrease of the TEC trough and an increase of the northern crest. Nevertheless, GPS scintillations persisted for several hours after the anomaly had started retracting equatorward. On this day, GPS scintillations were observed to extend beyond the limit of northern boundary of the northern crest (22° MLAT). However, the southern crest reached a larger magnetic latitude equal to 27°.

All three cases displayed in the bottom row were not associated with GPS and UHF scintillations at all the stations. The salient feature seen in all three panels is the relatively high level of TEC values at the magnetic equator ($\sim$12° S). The plot for 12 October 2001 shows a fairly uniform TEC latitudinal distribution. In this plot a modest TEC increase occurs between 0° and 6° S at 01:00 UT. The profiles for 7 November 2001 show two well-defined crests and a prominent northern peak, but the trough is quite broad with a TEC value above 70 TEC units. The event of 19 February 2002 shows a quasi-uniform TEC distribution with a narrow and short-lived crest. The cases presented in Fig. 7 summarize the great variability of the TEC profiles during 15 nights when all 10 GPS receivers were operating concurrently.

6 Statistics

Figure 8 presents the day-to-day variability of the extension of the equatorial anomaly measured at 20:00 LT. This time commonly corresponds to the initiation of ESF/scintillations. Figure 8 displays the magnetic latitude of the location of both crests of the anomaly (red traces), the trough (blue trace), and the 50% amplitude decay of the crests (green boxes). We also indicate the northern edge of the region subject to GPS scintillations using a bold line and an arrow. The scintillation information originates from real-time calculations of the S4 index based on the 10-Hz amplitude of the L1 GPS signal recorded at three of the stations (Bogota, Iquitos and Cuzco). Their combined scintillation-observing range stretches between 21° S and 12° N geographic latitude. Days without GPS scintillation activity are indicated by using a dark line placed at the magnetic equator. This study is restricted to display only the scintillation northern boundary, as we did not have access to scintillation information from GPS receivers located further south of the magnetic equator. The frames of Fig. 8 correspond, from top to bottom, to the months of September 2001, December 2001, January 2002, and February 2002. During days when insufficient TEC data prevented us from completely defining the boundary of the anomaly we left the green boxes incomplete, as can be seen at the northern poleward boundary on 1 and 3 September. The trough
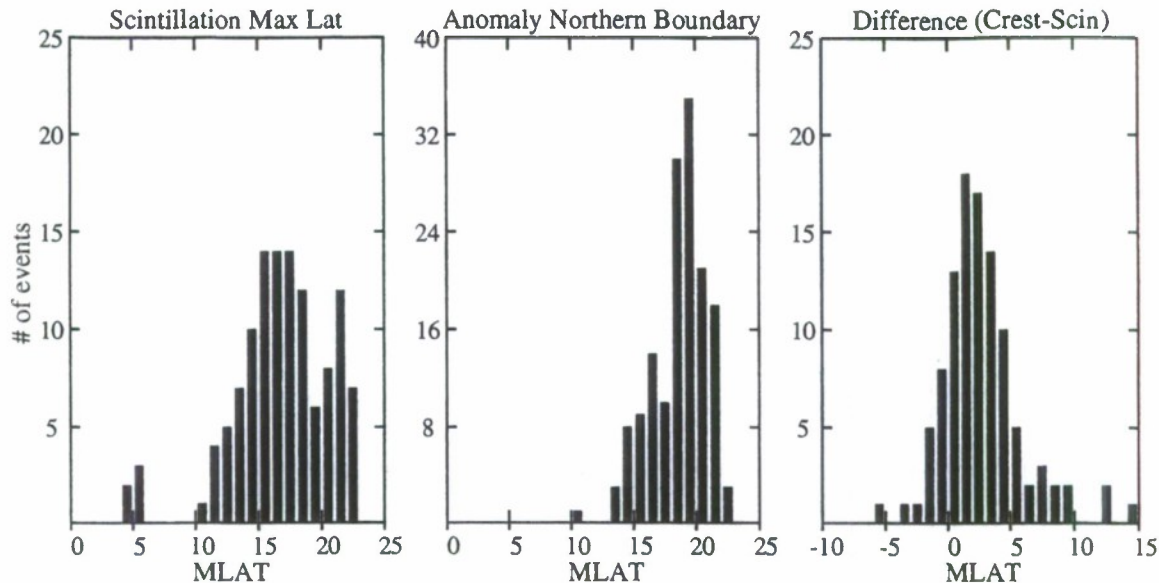
Fig. 9. The left histogram shows the maximum latitude of scintillations. The center panel displays the location of the northern boundary of the anomaly, defined as the poleward edge where the northern crest decreases 50% of its peak value. The right panel exhibits the distribution of the difference between poleward boundary of the anomaly and the maximum latitude of scintillations. Only in 9 cases out of 100 were GPS scintillations (and TEC depletions) seen poleward of the northern boundary of the anomaly.

was observed, most of the days, close to the magnetic equator. Exceptions are seen in early September, late December, 16–20 January and 12 and 27 February when the trough was displaced up to 7° from the magnetic equator. The location and width of the crests also show a large degree of variability. In some cases, both crests of the anomaly are close to 10° magnetic latitude, as seen on 8 and 26 September, 17 December, 23 January, and 12 February. But, on other occasions, they are nearly at 20°, as seen on 10 and 22 January and 7 February. The width of the crests were calculated by taking the difference between the crest and the trough TEC values, and recording the latitude where this difference falls off by 50%. It is evident that for most of the days the northern and southern crests are not placed symmetrically with respect to the magnetic equator and do not have the same latitudinal span. The maximum latitude of scintillations also shows a great variability; sometimes it is only 5° from the magnetic equator. But in other cases scintillations reach 23° magnetic latitude; this latitude corresponds to the poleward limit of the combined field-of-view of the GPS network. There is no doubt that, for some of these events, scintillations and the anomaly continue extending further poleward, but these regions were beyond the observing boundaries of the existing chain of GPS receivers. During the 6-month period presented in this paper, we found that on 40 nights (22% of all days) scintillations extended up to a latitude equal or greater than 20° away from the magnetic equator. We also observed that while the amplitude of the crests show a prominent seasonal variability, the latitudinal location and extension of the anomaly display no significant seasonal dependence. We have also detected that for all months involved in this study,

the northern crest was displaced toward more poleward latitudes than the southern peak of the anomaly.

Figure 9 illustrates the statistical distribution of the latitudinal extension of scintillations, the latitude of the anomaly northern boundary and a cross-comparison between them. The histogram on the left side reveals that for the majority of days, scintillations are confined to a magnetic latitude range that varies between 10° and 23°. Nevertheless, there exist a small number of days when scintillations appeared only at latitudes very close to the magnetic equator, and the disturbed region extended no more than 4° or 5° to both sides of the magnetic equator. The center panel displays the statistical distribution of the location of the northern boundary (50% decay) of the northern crest. This figure suggests that during the period that was analyzed in this study, the northern boundary of the anomaly varied between 14° and 22° magnetic latitude. The histogram on the right side shows the distribution of the difference between the northern boundary of the crests and the maximum latitude of GPS scintillations. Positive values correspond to cases when the anomaly boundary was located poleward of the region affected by scintillations. Then, we conclude that for most of the days scintillations are confined equatorward of the 50% fall off of the anomaly. This result suggests the existence of a relationship between the latitudinal extension of GPS scintillations (plasma bubbles) and the location of the crest of the anomaly. It is important to mention that on a few days, 8 days to be precise (~9%), we observed GPS scintillations located more than 1° poleward of the northern boundary (50% fall off) of the anomaly.
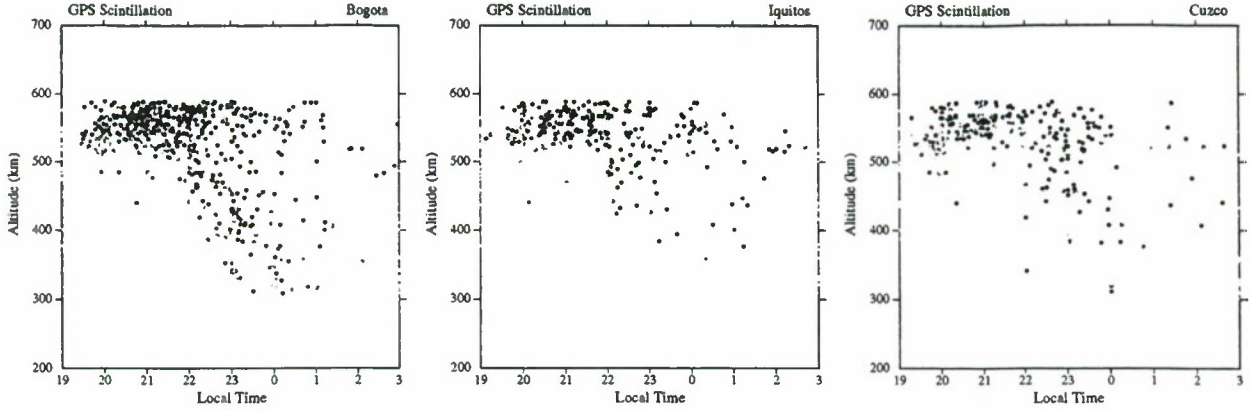
43

Fig. 10. hmF2 value of the equatorial ionosphere during the ten-month observational period presented in this study. The gray dots correspond to events when the GPS scintillation index was below 0.20. The black dots are for S4 levels above 0.20.

Figure 10 displays a mass plot of the altitude of the F-region peak measured by the Jicamarca digisonde between the months of September 2001 and June 2002. The peak altitude (hmF2) is plotted as a function of local time starting near local sunset. The hmF2 values are calculated with the Artist software that runs simultaneously with the data acquisition process. Different gray shading is used to distinguish between the absence (light gray) and presence (black) of GPS scintillation. Each panel of Fig. 10 shows the hmF2 values binned as a function of the scintillation activity measured by the receivers placed at Bogota, Iquitos and Cuzco. Similar to results published by other researchers, we found a well-defined dependence of the appearance of GPS scintillations and the altitude of the F-layer. Between 19:00 and 21:30 LT, scintillations mostly appear when the layer is located above 500 km altitude. Nevertheless, a small number of events occur when hmF2 is less than 500 km altitude. At local times later than 21:30 LT, the relative number of scintillation events with hmF2 below 500 km drastically increases, as it is common to observe scintillations at altitudes varying between 300 and 500 km. These events probably correspond to cases that outlived the descent of the F-region, and scintillations persisted during the nighttime decay. This feature is common to all three stations and usually starts near 21:30 LT. During the descent of the F-region, we found that the number of scintillation events detected at Cuzco, near the magnetic equator, was smaller than the number of events at other stations. This result is probably due to the much smaller density at the trough that makes the S4 level significantly close to the noise level. Figure 11 displays the altitude of the F-layer for all instances when TEC depletions were detected at the Bogota, Iquitos, Pucallpa, and Iquique stations. The red dots indicate cases when the depth of the depletions were larger than 30 TEC units. The blue dots are for depletions less than 30 units. The distribution of hmF2 is quite similar to the distributions of Fig. 10 for GPS scintillations. Figures 10 and 11 demonstrate that equatorial plasma bubbles can survive up to 2 hours after the nighttime F-layer starts descending. We also indicate that plasma bubbles and GPS scintillations rapidly

decay when the equatorial F-layer reaches 300 km altitude. For days when the hmF2 remains at altitudes above 500 km, scintillations and TEC depletions seem to last for longer periods and can be seen as late as 03:00 LT. The occurrence of GPS scintillations and TEC depletions when the F-region peak was below 500 km altitude warrants further study of the background conditions of the ionosphere during these cases.

A very informative statistics of the preferred ionospheric conditions that prevailed during the occurrence of scintillation/depletion events is presented in Fig. 12. This figure shows the hmF2 measured at Jicamarca as a function of two key representative parameters of the TEC profiles: the crest-to-trough TEC ratio and the latitudinal separation of the northern crest. The left panel shows the hmF2 versus the crest-to-trough ratio binned according to the presence (red and blue dots) and absence of scintillation (gray dots). The right panel displays the peak altitude as a function of the crest separation in degrees. Figures 12a and 12b were constructed by estimating the maximum level of scintillations every hour the Bogota and Iquitos GPS receivers operated between sunset ($\sim$19:00 LT) and 23:00 LT. Each scintillation value was paired with the corresponding F-region peak altitude measured at Jicamarca and the TEC latitudinal profile recorded with the GPS network. The red dots illustrate scintillation events observed before 22:00 LT, and the blue dots represent scintillation cases occurring before 23:00 LT. Figure 12 reveals that when the equatorial F-region peak is above 500 km, GPS scintillations are able to develop for TEC ratios as small as 1.25 or as large as 6.0, and crest separations between 6° and more than 20°. But as the peak altitude becomes less than 500 km the TEC ratio becoms restricted to values larger than a threshold number and to crest separations exceeding a minimum value. Figure 12 implies that the TEC ratio threshold and the crest minimum separation increase as the altitude of the F-region peak becomes smaller. For an F-region peak near 400 km the TEC ratio needs to be higher than 2.5 and the crest separation larger than 12°. We also divided all the scintillation events in nine altitude sectors and looked for the minimum ratio and crest separation in each altitude block.
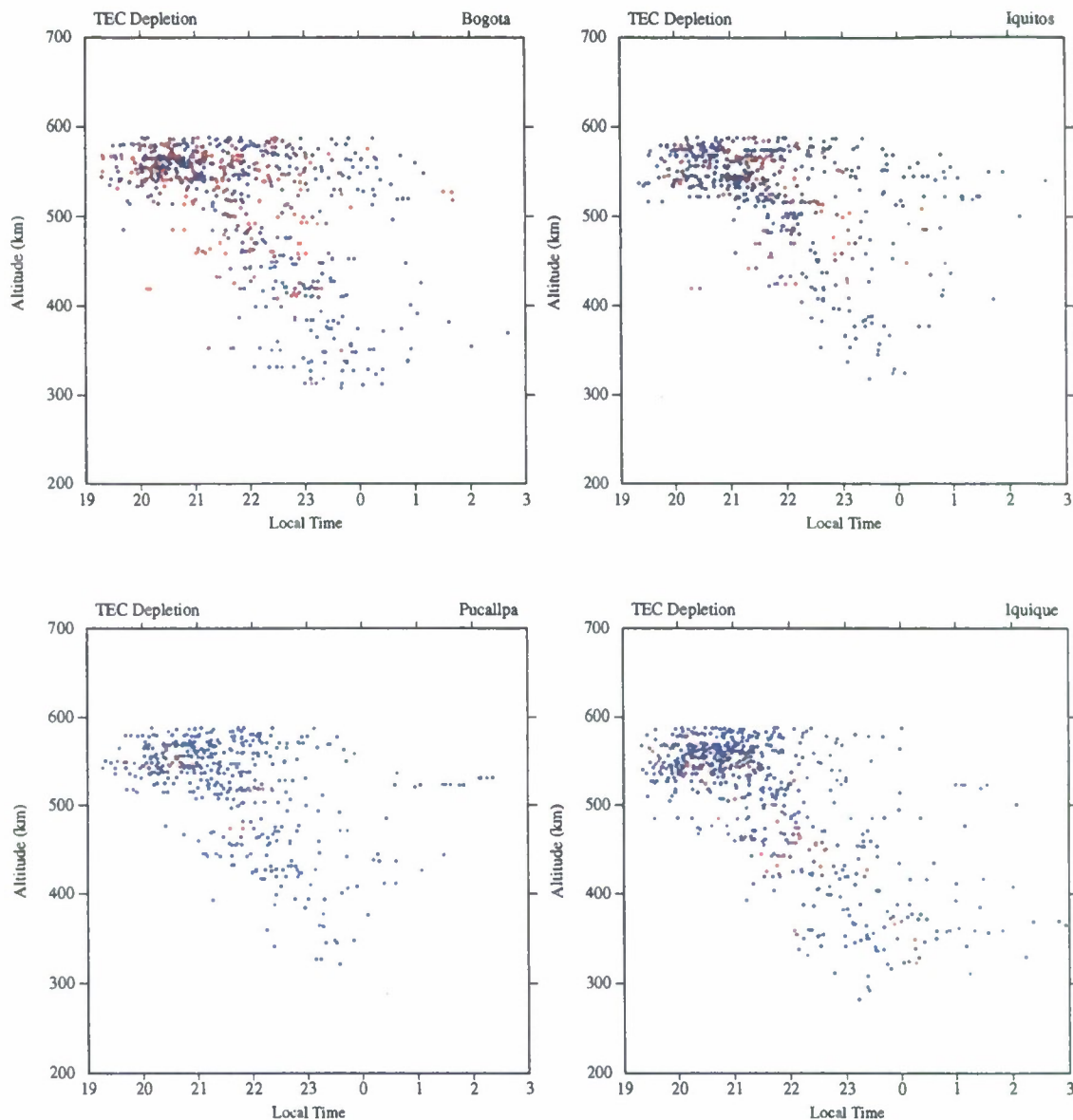
44

Fig. 11. *hm*F2 values measured during the occurrence of TEC depletions measured with the network of GPS receivers. TEC depletions larger than 30 TEC units are depicted as red dots; values smaller than 30 units are indicated by blue dots. Mass plots for only 4 stations are presented here.

The inclined line in each panel depicts the best fit to these minimum points. These traces also indicate the almost linear relationship between the minimum crest separation (and crest/trough ratio) and the altitude of the F-region for all the scintillations events that were observed at Bogota and Iquitos. It is important to mention that most of the gray dots (times of no scintillations) are observed bunched at TEC ratios less than 2.2. Based on this data, it is possible to conclude that an equatorial F-region peak below 500 km does not necessarily imply an inhibition of the onset or persistence of GPS scintillation, but it does require the crest/trough TEC ratio to be 2 or higher and the crest separation to exceed 8°. The lower the F-region peak, the higher that the TEC ratio

and the crest separation have to be for the flux tube to remain unstable to the initiation or persistence of GPS scintillations.

7 Discussion

TEC depletions provide precisely the total amount of plasma that is evacuated within a plasma bubble. In addition to this quantity, we have shown that other geophysical parameters can also be estimated if careful account of multiple sights of a plasma bubble are considered. These calculations are facilitated by the time progression of the ionospheric penetration points that look like nearly parallel curves when the
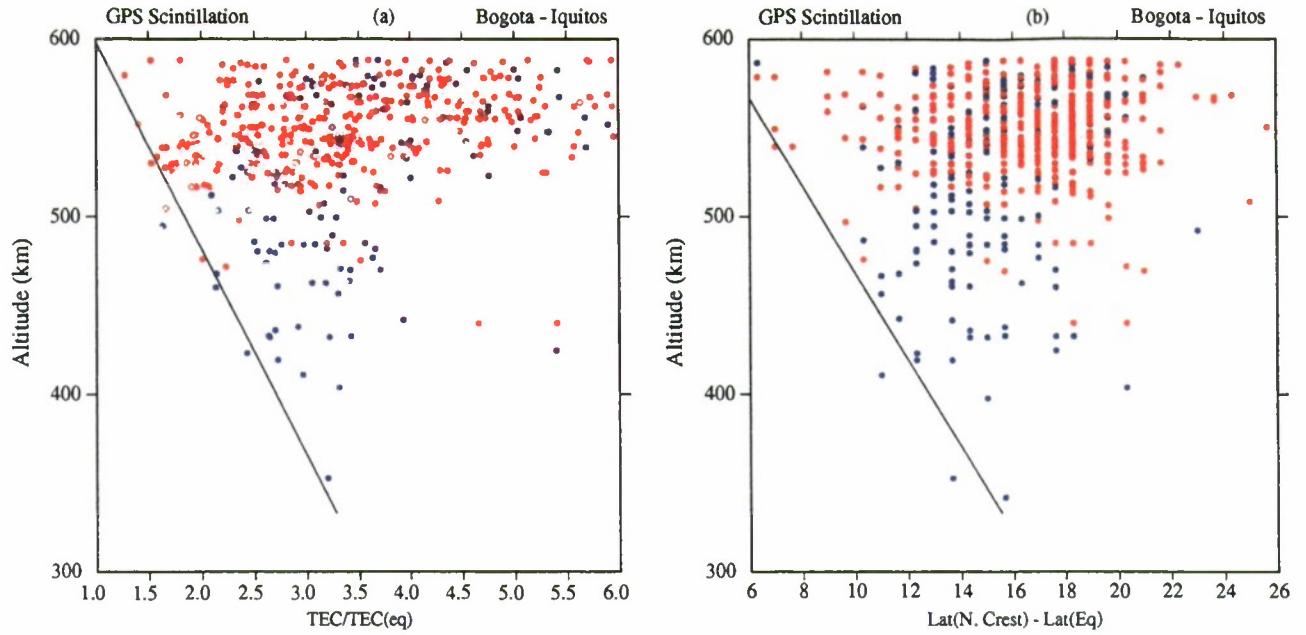
45

Fig. 12. Distribution of the *hm*F2 values as a function of the crest-to-trough ratio (panel (**a**) and vs. the crest separation (panel (**b**)), binned according to the presence (colored dots) and absence of GPS scintillations (gray dots). The inclined lines in the left part of each frame have been fitted to the minimum values of the crest/trough ratio (or crest separations) for different altitude sectors.

signal from the same GPS satellite is recorded at different stations. One of the physical properties inferred from the TEC data is the determination of the location where a bubble is triggered. Figures 3a, 3b and 3e (corresponding to Bogota, Iquitos and Cuzco) observed 2 TEC depletions between 19:00 and 22:00 LT; contrary to this, Figs. 3c and 3d (Pucallpa and Ancon) showed only one depletion. This fact indicated that the TEC depletion seen at Iquitos between 20:20 and 20:42 LT, which was also observed in Bogota between 20:30 and 20:53 LT, most likely originated in a location between Pucallpa and Iquitos. The depletion seen at Pucallpa between 21:08 and 21:47 LT could not be associated with the plasma bubble recorded much earlier at Iquitos and Bogota since the plasma depletions were drifting eastward. The average drift of the background plasma is another physical parameter that can be calculated using the arrival time of the TEC depletion as it moves from one station to another located further east. TEC observations from 2 stations located near the magnetic equator such as Ancon and Cuzco (Figs. 2c and 2d) show the passage of a TEC depletion crossing their ionospheric intersections with relatively small changes in the shape of the depletion. We determined a velocity equal to 140 m/s using the time elapsed between the TEC minima at Ancon and Cuzco and the east-west distance between the stations. In agreement with this value, the UHF spaced-receiver scintillation system that operates at Ancon (Valladares et al., 1996) measured a zonal drift equal to 160 m/s at 22:10 LT. The third geophysical parameter that we calculated was the westward tilt of the plasma bubbles. Comparison of the TEC curves measured at Cuzco, Iquitos and Bogota indicated the passage of a TEC depletion at times that were consistent with

plumes tilted westward at higher altitudes. We observed that the flux tubes that extended to larger magnetic latitudes (Bogota) lagged the flux tubes that ended closer to the equator (Cuzco). On both days the TEC depletions were observed almost overhead the sites. The tilt angles were calculated using precise estimates of the time and location of a TEC depletion detected at Bogota, an off equatorial site, and the time and location when the same depletion was observed at Cuzco or Arequipa, both near-equatorial stations. A zonal drift equal to 140 m/s was used on both days to "transport" the location of the TEC depletion to a common observational time. These locations were then mapped using the IGRF model of the magnetic field to determine their separation in altitude and the east-west distance. A tilt angle equal to 20° was observed on 7 September 2001 and 25° on 6 February 2002. These values are in accord with tilt angles recently calculated by Makela and Kelley (2003) using airglow images of plasma depletions recorded at Hawaii. Woodman and La-Hoz (1976) suggested that an altitude-sheared zonal drift of the ionosphere or a slip velocity between the neutrals and ionized medium could cause the tilt of the radar plumes. The numerical simulations of Zalesak et al. (1982) indicated that the westward tilt of the plumes was attributed to an incomplete coupling of the plasma motion to the neutral wind due to a finite conductivity of the E layer away from the equator.

We observed that at Bogota, which is typically located under the crest, both walls of the TEC depletions commonly presented intense levels of GPS scintillations. At Cuzco and Iquitos, the GPS scintillations were mainly restricted to the west side of the plasma bubbles. The latter can be understood in terms of the gradient-drift instability, which is able

to generate irregularities on the west wall of a plasma bubble. A zonal neutral wind U is also able to produce structures under the condition $U \cdot \nabla n < 0$, which for an eastward wind corresponds again to the westward wall. Based on their computer calculations Zalesak et al. (1982) indicated that the westward as well as the eastward wall could be subject to secondary instabilities. These authors included the tilt of the plumes and suggested that at high altitudes the normally stable east wall orients out of the purely vertical direction and becomes unstable to the gravitational and gradient-drift instabilities. More refined statistical analysis of these geophysical parameters will be exploited in the future to investigate the evolution and lifetime of the plasma bubbles and their associated scintillations.

By using data collected by the JULIA radar, along with TEC and GPS scintillations, we have constructed a very complete diagnostic of the background and the turbulent state of the nighttime low-latitude ionosphere for three different days. The radar coherent echoes, TEC depletions, GPS scintillations, and the TEC latitudinal profiles of Figs. 4, 5, and 6 portray the seasonal and day-to-day variability of the equatorial irregularities at different scale sizes. The following features were consistently observed in all three figures:

1) The location and the depth of the TEC depletions were approximately symmetric with respect to the magnetic equator, even when the background TEC was not symmetric. The absence of GPS scintillation measurements south the magnetic equator prevented us from investigating the symmetry of this parameter. 2) The depth of the TEC depletions and the intensity of GPS scintillations were larger at the crests of the anomaly than at the trough. 3) The latitudinal extension of the locations of the TEC depletions was equal to the extension of GPS scintillations. 4) Radar plumes were always collocated with TEC depletions and GPS scintillations. In addition, when the JULIA radar observed bottomside traces, these were not observed to be associated with GPS scintillations. The latter two experimental facts reaffirm the theoretical predictions of Costa and Kelley (1976) and previous observations conducted by Basu et al. (1986). The presence of the largest depletion depths at the crests of the anomaly is probably a consequence of the density along the depleted flux tubes being almost constant (Hanson and Bamgboye, 1984). Because the background undisturbed density is the largest at the crests, then a more dense region will be evacuated by the instability process, resulting in a much deeper depletion. Recently, Keskinen et al. (2003) have studied the three-dimensional nonlinear evolution of plasma bubbles and demonstrated that the sharpest density gradients exist at equatorial anomaly latitudes. We found that indeed GPS scintillations were more prominent near the crest, but when a single station was considered, we found no firm assurance that deeper TEC depletions correlate with more intense GPS scintillations. In fact, by comparing Figs. 4 and 5 the opposite correspondence seems to be valid. Figure 2 shows a 20-unit depletion that was observed at Cuzco on 7 September 2001. This depletion was accompanied with a S4 index near the noise level (0.20). In comparison, a smaller 12-unit depletion was seen on 3 December 2001, but on this day the GPS scintillations exceeded 0.3. LaBelle and Kelley (1986) have presented the spatial spectrum of irregularities, detected by two rockets launched into ESF, that exhibited a knee near the 1-km scale length. These authors suggested that two processes could affect the amplitude of km-scale irregularities: 1) the injection of km-scale turbulence at the steepened walls of plasma bubbles and 2) nonlocal effects of the underlying E region. While it is likely that density gradients with scale lengths of the order of a few hundred meters exist at the walls of the plasma bubbles, electric fields with these dimensions do not easily map to the E-region (Farley, 1960). In principle, the depth and width of TEC depletions, and also the TEC gradients within the TEC depletions, do not necessarily reflect the sharpness of the density gradients in the F-region, as TEC is an integrated measurement that heavily depends upon the satellite elevation, the tilt of the plasma bubbles, the zonal plasma drift, and even the satellite trajectory. Contrary to the uncertain relationship between TEC depletions and GPS scintillations, we observed that the intensity of coherent echoes seem to follow a proportional relationship with the depth of the TEC depletions. Figures 4, 5 and 6 suggested that the intensity of the coherent echoes recorded by the JULIA radar followed a proportional dependence with the depth of the TEC depletions. As a corollary, we state the lack of a proportional correspondence between the level of the GPS (1.6 GHz) scintillations and the intensity of the coherent echoes recorded by the JULIA radar. At 1.6 GHz, scintillations are caused by irregularities in the range 40–400 m in dimension. Therefore, we should not expect a one-to-one relationship with the 50 MHz backscatter, which is caused by 3-m irregularities. The different frames of Fig. 7 have illustrated the direct relationship that exists between the location and width of the crests and the latitudinal extension of the region where GPS scintillations (400-m scale length structures) occur. For 10 days (Fig. 7) scintillations were confined within the limits of the equatorial anomaly. This particular association can be understood by invoking the arguments employed by Sultan (1996) to derive the non-local linear growth rate of the RTI. This author used the magnetic flux tube formalism of Haerendel (1973) to numerically calculate the RTI growth rate, taking into account changes in physical parameters over the entire magnetic field tube. The flux-tube integrated parameters presented by Sultan (1996) showed the integrated Pedersen conductivity increasing up to 1000 km altitude and growth rates remaining positive even at 800 km. Under these circumstances, one expects to find radar plumes reaching the topside, or altitudes near 800 km. Field lines that cross the equatorial topside are unstable to the RTI because of the longer length of flux tubes that penetrate the crests of the anomaly and the much higher TEC and F-region density at the F-region ends of these field lines. Field lines with higher apex altitudes are even longer but will end poleward of the crests where the density is much reduced. On two other days, 10 February 2002 and 18 December 2001, GPS scintillations were observed at latitudes one or two degrees beyond the northern boundary of the anomaly. However, we

noticed that on these two days, the southern crest reached more poleward latitudes than the northern peak. This again reinforces the need to conduct the field line integration from end-to-end of the flux tube. We suggest that this relationship between the latitudinal width of the anomaly and the extension of GPS scintillations seems to be necessary conditions for all local times, all magnetic conditions, and probably all solar activity epochs. The bottom row of Fig. 7 has shown the TEC distributions for 3 days when no GPS scintillations were detected. The common feature on all 3 days was the large TEC value (>75 units) at the trough and the crest/trough ratio less than 2. This behavior of a stable equatorial ionosphere is in agreement with the conditions of the TEC profiles put forth by Valladares et al. (2001). Figure 7 also introduced the role of the reverse fountain effect, acting as a suppressor of plasma bubbles and GPS scintillations. The initiation of the reverse fountain was illustrated in Figure 4a in which a bottomside trace was observed to be moving rapidly downward after 19:30 UT. Simultaneously, the TEC latitudinal profiles indicated an increase in the TEC values near the magnetic equator. We have observed that GPS scintillations can be inhibited right after the start of the reverse fountain effect; but can also decay 1–2 h afterwards. Below we explain how the re-distribution of plasma along the field lines can make the equatorial ionosphere become stable to the RTI and are able to suppress or extinguish ESF irregularities. We did not expect to find the strong asymmetry of the TEC profiles that prevailed during the December solstice, even during days when the latitudinal distribution of the TEC depletions was symmetric with respect to the magnetic equator. On many days, GPS scintillations, TEC depletions, and radar plumes were detected even when the southern crest was absent. The main contributor to the asymmetry of the anomaly is the meridional wind that during the December solstice blows from south to north (Walker et al., 1994). Other factors may be an asymmetrical distribution of the O/N2 ratio or latitudinal gradients of the zonal or vertical neutral wind.

Figures 8 and 9 indicated that sometimes GPS scintillations could be detected poleward of the 50% decay of the northern crest. In fact, a total of 9 cases were found during the analysis of this limited data set. We noticed that during these nine days the poleward boundary of the southern crest was displaced to even higher magnetic latitudes than the poleward boundary of the northern crest. This will definitely augment the flux-tube integrated conductivity of the field line that intersects the poleward boundary of the GPS scintillations. In summary, Figs. 7, 8 and 9 reaffirm that the stability of the flux tube is a non-local phenomenon that depends on the density along the whole flux tube.

Figure 12 indicated that when the equatorial F-region peak is above 500 km, the low-latitude ionosphere is inherently unstable to the onset of the RTI. Then, if gravity waves (Kelley et al., 1981; Hysell et al., 1990) are present, GPS scintillations and plasma bubbles will develop. But as the F-region descends toward lower apex altitudes, the requirement for ESF turbulence becomes more stringent, and larger

crest/trough TEC ratios and more widely separated crests are needed for the ionosphere to remain unstable. Figure 13 presents the schematic representations of the ionospheric densities for two different scenarios in which the nighttime F-region can be considered disturbed. These plots display a north-south 36°-segment of the equatorial ionosphere centered at the magnetic equator. Four field lines with apex altitudes varying from 500 km to 2000 km are indicated in each of the two frames. Both plots have been properly scaled to depict horizontal and vertical distances proportionally. The circular segment near the lower boundary represents the surface of the Earth. The numbers under this curve show the geographic latitude at the 76° W meridian. The main differences between these two frames are the altitude of the F-region at the magnetic equator and the poleward extension of the anomaly. The left frame shows a density distribution that contains an equatorial F-region peaking at 750 km altitude and the crests separated by 8° from the magnetic equator. The right frame displays the F-region hmF2 at 400 km altitude, and the anomaly extending up to 15°. Although the latitude-altitude profiles of Fig. 13 look drastically different, their flux-tube integrated parameters, such as conductivities, density gradients, and probably their growth rates, will have a much closer resemblance. We suggest that both density distributions presented in Fig. 13 will be conducive to the development of ESF, favor the initiation of plasma bubbles and support the persistence of bubbles and GPS scintillations. However, we note that the larger latitudinal extension of the density distribution of the right frame will support taller plumes and GPS scintillations incursions to much higher latitudes. When the crest/trough ratio decreases, the crest separation becomes either small, or the peak altitude of the equatorial F-region reduces, thus the plasma depletions will be annihilated. The reverse fountain effect is a plasma redistribution process in which crest plasma is transported toward the magnetic equator due to pressure gradients along the field lines that are large enough to overcome the gravity force. The main driver of the reverse fountain is the downward motion of the plasma at equatorial latitudes. Previous studies that have used DMSP data (Sultan and Rich, 2000; Huang et al., 2001) concluded that the amplitude of the crest is associated with the occurrence pattern of ESF. Here, we have demonstrated that the crest/trough ratio, the crest separation, together with the altitude of the equatorial F-region, are the parameters that can be used to forecast the onset, the persistence, and the maximum altitude of the plasma plumes.

As final remarks we point out that it is conceivable that the proper conditions for bubble generation could be set, in some circumstances, even hours prior to sunset (e.g. a large daytime vertical drift). When this happens plasma bubbles would be triggered just after the decay of the underlying E region. During these events, it would be possible to define precursors of the ESF, as has been indicated by Raghavarao et al. (1988). We are aware that the TEC is an integrated quantity equal to the integral of the density between the lower boundary of the D region and the satellite altitude. As such, it does not reproduce all the variability of the density profiles.
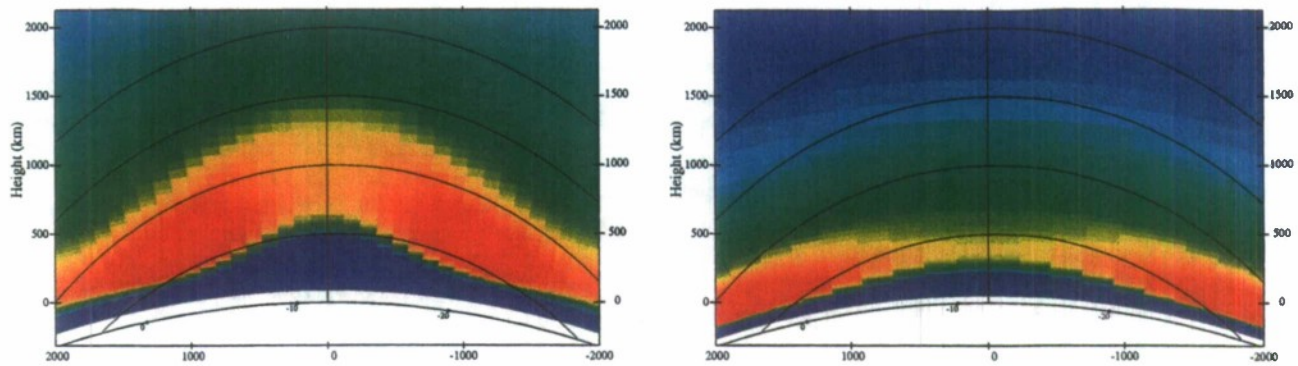
Fig. 13. Schematic representation showing two possible scenarios of the latitudinal distribution of the F-region densities during events that support the initiation and the development of plasma depletions. Note the difference in the altitude of the F-region near the magnetic equator and the locations of the Anomaly crests.

Nevertheless, after sunset the F-layer is reduced in depth and the TEC becomes a good representation of the density. We emphasize that the three parameters mentioned above can be used as a proxy for the initiation and persistence of equatorial plasma bubbles.

8 Conclusions

The investigation has led to the following:

1. We have shown that independent measurements of the same TEC depletion by two GPS receivers displaced in longitude can be employed to estimate the eastward motion of the background ionosphere. GPS receivers displaced in latitude can also provide the tilt of the plasma plumes. We demonstrated that in some instances GPS receivers indicate the place and time of bubble initiation.

2. The three case-study events presented here have demonstrated the temporal and spatial correspondence between radar plumes, GPS scintillations and TEC depletions. This fact supports the use of several GPS receiver sites to monitor the maximum altitude of the plasma bubbles.

3. We did not find a direct relationship between the depth of the TEC depletion and the intensity of GPS scintillations. Nevertheless, more intense coherent echoes were observed when deeper TEC depletions transited above the JULIA radar.

4. At Bogota, GPS scintillations were seen on both walls of the TEC depletions. At Iquitos and Cuzco scintillations mainly occurred in the west side of the depletions. This latitudinal distribution of scintillations is in accord with predictions presented by Zalesak et al. (1982) based on numerical simulations of the evolution of plasma bubbles.

5. We detected strong levels of GPS scintillation and deep TEC depletions when the TEC latitudinal profiles were symmetric, asymmetric, or even when one of the crests was absent. This fact indicates the importance of flux-tube integrated quantities to assess the stability of the equatorial F-region (Sultan, 1996).

6. There exists a prominent day-to-day variability in the location and width of the crest. The trough is principally located near the magnetic equator, but it contains a 2° dispersion with respect to the equator. The crests locations typically vary between 10° and 18° of magnetic latitude, but could be as small as 5° from the magnetic equator.

7. The poleward boundary of GPS scintillations and TEC depletions were bounded 90% of the days to the regions where the equatorial anomaly decreased 50% of the peak value. Weak level of scintillations were seen near the trough, but much higher values (>0.8) were observed at the crests during this period of solar maximum conditions.

8. In agreement with previous studies of the onset of ESF phenomena, we found that the majority of scintillation events start when the F-layer peak was above 500 km. We observed that scintillations and TEC depletions can persist during the descending phase of the F-region, but rapidly decay when the F-region peak is below 300 km altitude. TEC latitudinal profiles obtained simultaneously during scintillation events and equatorial F-region peak altitudes below 500 km indicate that these events occur when the crest-to-trough TEC ratios are larger than 2.2; and the crest separation is 10° or more. These limits apply to the onset as well as the persistence of GPS scintillations. This result is largely unexpected, as the persistence of GPS scintillations is mainly dominated by the electrical and magnetic properties of the plasma bubble.

49

9. The good correlation between the appearance of the reverse fountain and the inhibition of scintillations can be understood in terms of the redistribution of the plasma along the field lines, flowing from the crest toward the magnetic equator and then to lower altitudes. The development of the reverse fountain effect implies a decrease in the crest/trough TEC ratio and a reduction in the crest separation. We postulate that these two facts make the whole flux-tube more stable to the RTI.

10. We conclude that tracking the location, magnitude and extension of both crests of the anomaly can serve to infer the maximum latitudinal extension of scintillations, TEC depletions, and the maximum altitude of radar plumes. Precise measurements of TEC latitudinal profiles and bottomside density profiles can be used to predict the onset of plasma bubbles and to infer the evolution and decay time of the ESF phenomenon.

References

Balan, N. and Bailey, G. J.: Equatorial plasma fountain and its effects: Possibility of an additional layer, J. Geophys. Res., 100, 21 421, 1995.

Basu, S., Basu, S., LaBelle, J., Kudeki, E., Fejer, B. G., Kelley, M. C., Whitney, H. E., and Bushby, A.: Gigahertz scintillations and spaced receiver drift measurements during Project Condor equatorial F-region rocket campaign in Peru, J. Geophys. Res., 91, 5526, 1986.

Basu, S., E. Kudeki, Basu, Su., et al.: Scintillations, plasma drifts, and neutral winds in the equatorial ionosphere after sunset, J. Geophys. Res., 101, 26 795, 1996.

Costa, E. and Kelley, M. C.: Calculations of equatorial scintillations at VHF gigahertz frequencies based on a new model of the disturbed equatorial ionosphere, Geophys. Res. Lett., 3, 677, 1976.

DasGupta, A., Basu, S., Aarons, J., Klobuchar, J. A., Basu, S., and Bushby, A.: VHF amplitude scintillations and associated electron content depletions as observed at Arequipa, Peru, J. Atm. Terr. Phys., 45, 15, 1983.

Devasia, C. V., Jyoti, N., Subbarao, K. S. V., Viswanathan, K. S., Tiwari, D., and Sridharan, R.: On the plausible linkage of thermospheric meridional winds with the equatorial spread F, J. Atm. and Sol. Terr. Phys., 64, 111, 2002.

Eccles, J. V.: Modeling investigation of the evening prereversal enhancement of the zonal electric field in the equatorial ionosphere, J. Geophys. Res., 103, 26 709, 1998.

Farley, D. T.: A theory of electrostatic fields in the ionosphere at nonpolar geomagnetic latitudes, J. Geophys. Res., 65, 869, 1960.

Farley, D. T., Bonnelli, E., Fejer, B. G., and Larsen, M. F.: The prereversal enhancement of the zonal electric field in the equatorial ionosphere, J. Geophys. Res., 91, 13 723, 1986.

Fejer, B .G., Scherliess, L., and de Paula, E. R.: Effects of the vertical plasma drift velocity on the generation and evolution of equatorial spread F, J. Geophys. Res., 104, 19 859–19 869, 1999.

Haerendel, G.: Theory of equatorial spread F, unpublished report, Max Planck Instit für Extraterr. Phys., 1973.

Haerendel, G. and Eccles, J. V.: The role of the equatorial electrojet in the evening ionosphere, J. Geophys. Res., 97, 1181, 1992.

Hanson, W. B. and Moffett, R. J.: Ionization transport effects in the equatorial F-region J. Geophys. Res., 71, 5559, 1966.

Hanson, W. B. and Bamgboye, D. K.: The measured motions inside equatorial plasma bubbles, J. Geophys. Res., 89, 8997, 1984.

Huang, C. Y., Burke, W. J., Machuzak, J. S., Gentile, L. C., and Sultan, P. J.: DMSP observations of equatorial plasma bubbles in the topside ionosphere near solar maximum, J. Geophys. Res., 106, 8131, 2001.

Hysell, D. L., Kelley, M. C., Swartz, W. E., and Woodman, R. F.: Seeding and layering of equatorial spread F by gravity waves, J. Geophys. Res., 95, 17 253, 1990.

Hysell, D. L. and Burcham, J. D.: JULIA radar studies of equatorial spread F, J. Geophys. Res., 103, 29 155, 1998.

Kelley, M. C., Larsen, M. F., LaHoz, C. A., and McClure, J. P.: Gravity wave initiation of equatorial spread F, J. Geophys. Res., 86, 9087, 1981.

Keskinen, M. J., Ossakov, S. L., and Fejer, B. G.: Three-dimensional nonlinear evolution of equatorial ionospheric spread-F bubbles, Geophys. Res. Lett., 30, doi:10.1029/2003GL17418, 1855, 2003.

LaBelle, J., and Kelley, M. C.: The generation of kilometer scale irregularities in equatorial spread F, J. Geophys. Res., 91, 5504, 1986.

Makela, J. J. and Kelley, M. C.: Field-aligned 777.4 nm composition airglow images of equatorial plasma depletions, Geophys. Res. Lett., 30, doi:10.1029/2003GL17106, 1442, 2003.

Maruyama, T.: A diagnostic model for equatorial spread F, 1. Model description and application to electric field and neutral wind effects, J. Geophys. Res., 93, 14 611, 1988.

Maruyama, T. and Matuura, N.: Longitudinal variability of annual changes in activity of equatorial spread F and plasma bubbles, J. Geophys. Res., 89, 10 903, 1984.

McClure, J. P., Hanson, W. B., and Hoffman, J. H.: Plasma bubbles and irregularities in the equatorial ionosphere, J. Geophys. Res., 82, 2650, 1977.

Mendillo, M., Baumgardner, J., Pi, X., Sultan, P. J., and Tsunoda, R.: Onset conditions for equatorial spread *F*, J. Geophys. Res., 97, 13 865, 1992.

Mendillo, M., Meriwether, J., and Biondi, M.: Testing the thermospheric neutral wind suppression mechanism for day-to-day variability of equatorial spread F, J. Geophys. Res., 106, 3655, 2001.

Meriwether, J. W., Moody, J. W., Biondi, M. A., and Roble, R.

G.: Optical interferometric measurements of nighttime equatorial thermospheric winds at Arequipa, Peru, J. Geophys. Res., 91, 5557, 1986.

Ossakow, S. L., Zalesak, S. T., McDonald, B. E., and Chaturvedi, P. K.: Nonlinear equatorial spread-F: Dependence on altitude of the F peak and bottomside background electron density gradient scale length, J. Geophys. Res., 84, 17, 1979.

Ott, E.: Theory of Rayleigh-Taylor bubbles in the equatorial ionosphere, J. Geophys. Res., 83, 2066, 1978.

Raghavarao, R., Nageshwararao, M., Hanumath Sastri, J., Vyas, G. D., and Sriramarao, M.: Role of equatorial ionization anomaly in the initiation of equatorial spread-F, J. Geophys. Res., 93, 5959, 1988.

Satyanarayana, P., Guzdar, P. N., Huba, J. D., and Ossakow, S. L.: Rayleigh-Taylor instability in the presence of a stratified shear layer, J. Geophys. Res., 89, 2945, 1984.

Sridharan, R., Sekar, R., and Gurubaran, S.: Two-dimensional high-resolution imaging of the equatorial plasma fountain, J. Atm. and Terr. Phys., 55, 1661, 1993.

Sridharan, R., PallamRaju, D., Raghavarao, R., and Ramarao, P. V. S.: Precursor to equatorial spread-F in Ol 630.0 nm dayglow, Geophys. Res. Lett., 21, 2797, 1994.

Sultan, P.: Linear theory and modeling of the Rayleigh-Taylor instability leading to the occurrence of equatorial spread F, J. Geophys. Res., 101, 26 875, 1996.

Sultan, P. J. and Rich, F. I.: Observations and modeling of the seasonal and longitudinal occurrence pattern of equatorial spread-F, paper presented at Chapman Conference on Space Weather: Progress and Challenges in Research and Applications, AGU, Clearwater, Fla., March 2000.

Valladares, C. E., Sheehan, R., Basu, S., Kuenzler, H., and Espinoza, J.: The multi-instrumented studies of equatorial thermosphere aeronomy scintillation system: Climatology of zonal drifts, J. Geophys. Res., 101, 26 839–26 850, 1996.

Valladares, C. E., Basu, S., Groves, K., Hagan, M. P., Hysell, D., Mazzella Jr., A. J., and Sheehan, R. E.: Measurement of the latitudinal distributions of total electron content during equatorial spread-F events, J. Geophys. Res., 106, 29 133, 2001.

Walker, G. O., Ma, J. H. K., and Golton, E.: The equatorial ionospheric anomaly in electron content from solar minimum for South East Asia, Ann. Geophys., 12, 195, 1994.

Weber, E. J., Basu, S., Bullett, T. W., et al.: Equatorial plasma depletion precursor signatures and onset observed at 11° south of the magnetic equator, J. Geophys. Res., 101, 26 829, 1996.

Whalen, J. A.: The equatorial anomaly: Its quantitative relation to equatorial bubbles, bottomside spread F, and $E \times B$ drift velocity during a month at solar maximum, J. Geophys. Res., 106, 29 125, 2001.

Woodman, R. F.: Vertical drift velocities and east-west electric fields at the magnetic equator, J. Geophys. Res., 75, 6249, 1970.

Woodman, R. F. and LaHoz, C.: Radar observations of F region equatorial irregularities, J. Geophys. Res., 81, 5447, 1976.

Zalesak, S. T. and Ossakow, S. L.: Nonlinear equatorial spread F: Spatially large bubbles resulting from large horizontal scale initial perturbations, J. Geophys. Res., 85, 2131, 1980.

Zalesak, S. T., Ossakow, S. L., and Chaturvedi, P. K.: Nonlinear equatorial spread F: The effect of neutral winds and background Pedersen conductivity, J. Geophys. Res., 87, 151, 1982.

Zargham, S. and Seyler, C. E.: Collisional interchange instability, 1, Numerical simulations of intermediate-scale irregularities, J. Geophys. Res., 92, 10 073, 1987.

Annales
Geophysicae

Equatorial ionospheric zonal drift model and vertical drift statistics from UHF scintillation measurements in South America

R. E. Sheehan and C. E. Valladares

Institute for Scientific Research, Boston College, Chestnut Hill, Massachusetts, USA

Abstract. UHF scintillation measurements of zonal ionospheric drifts have been conducted at Ancon, Peru since 1994 using antennas spaced in the magnetic east-west direction to cross-correlate geo-synchronous satellite signals. An empirical model of average drift over a wide range of K_p and solar flux conditions was constructed from successive two-dimensional fits of drift vs. the parameters and day of year. The model exhibits the typical local time trend of maximum eastward velocity in the early evening with a gradual decrease and reversal in the early morning hours. As expected, velocities at all hours increase with the solar flux and decrease with K_p activity. It was also found that vertical drifts could contribute to the variability of drift measurements to the east of Ancon at a low elevation angle. The vertical drift at the ionospheric intersection to the east can be estimated when combined with nearly overhead observations at Ancon or a similar spaced-antenna site at Antofagasta, Chile. Comparisons on five days with nearly simultaneous measurements of vertical drift by the Julia radar at Jicamarca, Peru show varying agreement with the spaced-antenna estimates. Statistical results from 1997 to 2001 generally agree with radar and satellite studies.

Key words. Ionosphere (equatorial ionosphere; ionospheric irregularities; modeling and forecasting)

1 Introduction

A comprehensive understanding of the low latitude plasma electrodynamics is of great importance because of the controlling influence that plasma drifts and thermospheric winds exert on the number density distribution and on developing the favorable states conducive to the initiation of large-scale plasma bubbles. In general, the neutrals transfer momentum to the ions by collisions. In the F-region the ions move almost freely along the field lines; similarly, they create polariza-

Correspondence to: R. E. Sheehan
(sheehanp@bc.edu)

tion electric fields that transport the plasma perpendicular to the B-field. During quiet magnetic conditions, the E- and F-region neutral wind dynamos generate the equatorial electric fields (Rishbeth, 1970, 1981; Eccles, 1998). During magnetically disturbed periods, the penetration of E-field from high latitudes and the ionospheric disturbed dynamo can significantly modify the magnitude of the low latitude electric fields (Fejer and Scherliess, 1997).

At low latitudes the climatology of the zonal and vertical drifts has been defined based on measurements collected with incoherent scatter radars, satellites and scintillation receivers. Fejer et al. (1981, 1985) used measurements of drifts performed at Jicamarca to show that the zonal drift is westward and about 50 m/s during the day, and eastward and up to 130 m/s during the night. Coley and Heelis (1989) used drifts collected with the DE-2 satellite to show that these drifts coincided with the Jicamarca drifts. Their evening values of zonal eastward drifts peaking at 170 m/s were typical for solar maximum conditions. They also observed drift reversals from westward to eastward at 19:00 LT and to westward drifts at 04:30 LT. Recently, Fejer and Scherliess (1998) were able to extract the temporal evolution of the low latitude penetration zonal drifts that is driven by the magnetospheric E-field. They observed the largest effect on the dusk to midnight sector with an average duration of 2 h. Valladares et al. (1996) presented irregularity drifts observed during the first year of operations at Ancon. Their values were in agreement with the values measured at Jicamarca for solar minimum conditions.

More recently, Valladares et al. (2002) have compared the zonal drift measured with the scintillation technique at Ancon and the zonal wind measured by the FPI located at Arequipa. The drifts were close to the wind values;, with the drifts exceeding the winds by 15 m/s during the equinox and the opposite behavior was seen during the June solstice. They attributed the larger drift values to spatial variability of the zonal wind.

This paper presents statistical results of the zonal drifts measured using the spaced-antenna scintillation technique at
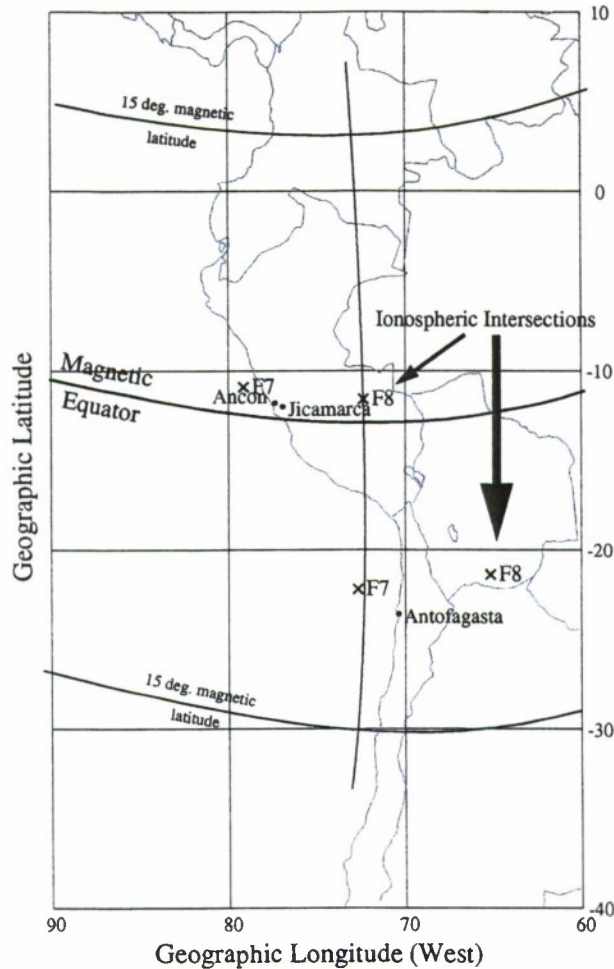
Fig. 1. Map of the west coast of South America showing the spaced-receiver sites at Ancon, Peru and Antofagasta, Chile, and the Julia radar at Jicamarca, Peru. F7 and F8 near Ancon indicate the 350-km ionospheric intersections of the Ancon-W and Ancon-E ray paths, respectively, to the F7 and F8 geostationary satellites. F7 and F8 near Antofagasta are the intersection points from Antofagasta to the same satellites.

two sites located near the west coast of South America. One of the sites, Ancon, Peru, is located near the magnetic equator, and the other is at Antofagasta, Chile (11° S magnetic latitude, 5° east of Ancon). The study constitutes a continuing effort to develop an empirical model of the climatology and day-to-day variability of the zonal irregularity drift as a function of local time, season, magnetic, and solar conditions. It also seeks to represent the spatial and altitude/latitude dependency of the zonal drifts during the nighttime hours.

In a related effort, spaced receiver measurements at Ancon from a low-elevation satellite to the east were combined with Antofagasta drifts to give estimates of vertical drift velocities near Antofagasta. The vertical drift is an important factor in the instability leading to equatorial spread F and plasma bubbles (Fejer et al., 1999). Several case studies compare the results with data from the Julia radar at Jicamarca.

2 Experimental setup

The spaced receiver system at Ancon described in Valladares et al. (1996) cross-correlates UHF signal level data at 50 Hz from two geo-synchronous satellites, one nearly overhead located at 100° west longitude (F7), the other low to the east at 23° west longitude (F8). Figure 1 shows the locations of Ancon and a similar spaced antenna system at Antofagasta, Chile, along with the 350-km ionospheric intersection points along the ray paths to the satellites. The intersection points F7 and F8 near Ancon will be designated Ancon-W, Ancon-E, respectively. Similarly, the points F7 and F8 near Antofagasta are the corresponding ionospheric intersections from Antofagasta. With the addition of Ancon-E in 1996, S4 and drift data have been collected nearly continuously up to the present.

Drift velocities at Ancon are calculated on-line using methods from Vacchione et al. (1987). This method uses quadratic approximations near the peaks of the cross- and autocorrelation functions to estimate both the drift velocity, V_0, and the random velocity, V_c, which is related to the amount of decorrelation over the sample time interval. When $V_c=0$ (maximum cross-correlation=1), V_0 is identical to the apparent drift velocity calculated from the lag of the maximum cross-correlation. V_0 decreases relative to the apparent velocity as V_c increases (maximum cross-correlation decreases).

3 Statistical results

Drift velocities measured at Ancon-W from 1994 to 2001 were sorted into solar flux bins and plotted against mean local time (LT=UT−5 h). Figure 2 summarizes the results for each season. Except for the June solstice when there were fewer points, there is a broad pre-midnight peak in eastward drift, followed by a slight post-midnight increase, or leveling off, and then a reversal to westward drift. Average drift velocities at all local times generally increase with solar flux, with the time of reversal occurring near local sunrise. The most pronounced post-midnight peak occurs during the March equinox, while during the December solstice the decline in eastward drift pauses before decreasing again and quickly reverses at about 05:00 local time. Similar trends are seen in Fig. 3 for Ancon-E drift data, although, as proposed in Sect. 5, vertical drifts contribute to the calculated drift because of the oblique ray path, and, since vertical drifts are predominantly downward after local sunset, the observed drifts appear consistently larger. The average drifts at Antofagasta (Fig. 4) are less consistent, and the pre-midnight peak tends to be somewhat earlier than at Ancon. The earlier peak is probably attributable to Antofagasta's location near the eastern border of the local time zone. These results were further broken into two broad categories of D_{st} index to separate the effect of magnetic storms. During active conditions ($D_{st} < -23$) at Ancon-W (Fig. 5a), the zonal drifts are generally 10–20 m/s slower in all seasons and solar flux levels,

compared to quiet conditions (Fig. 5b). The post-midnight enhancement, or leveling off, is seen in all seasons and conditions, but is most noticeable with active conditions during the vernal equinox.

To separate the influences of geomagnetic and solar conditions on the statistical distribution of zonal drifts, a two-step procedure was performed on the Ancon-W data from 1994 to 2002. Drifts were sorted into 12 local time bins, and a two-dimensional, second-order fit of the drift vs. K_p and the day of year was calculated in each bin. The drift data in each local time bin were then referenced to the model drift at a fixed K_p by subtracting the difference between the fit value of the drift and the fit value at $K_p=2$; $V_{0ref}=V_0-(V_{0fit}(K_p)-V_{0fit}(K_p=2))$, where V_0 is the measured drift and $V_{0fit}(K_p)$ is the fit value of drift. This in effect attributes the remaining dependence to the solar flux and other unspecified variables. A second two-dimensional fit was then carried out for V_{0ref} vs. solar flux and the day of year. A model drift for a given solar flux, K_p and day of year can be found by reversing the steps using a set of coefficients describing the two-dimensional fits. The Appendix gives the coefficients and a more detailed description.

Figures 6a–d illustrate the dependence of the empirical model zonal drift on K_p and the solar flux for each month. The K_p dependencies are shown for two extreme levels of solar flux, and also the solar flux dependencies for quiet and active levels of K_p activity. The drift dependencies are similar for all months, decreasing vs. K_p and increasing vs. solar flux. These, in turn, are superimposed on the dependence on the other parameter, as seen when comparing Figs. 6a and b, and Figs. 6c and d. Further refinements to the model are possible, but its main purpose is to provide a compact summary of zonal drifts at Ancon over a wide range of geophysical conditions.

4 Vertical drift

Drift velocities calculated from UHF scintillations along the low-elevation path to the east of Ancon are often larger and have more scatter than those from nearly overhead. Kil et al. (2000) noted that for ray paths at low elevation angles, vertical drifts contribute to the cross-correlation used for zonal drift calculations. Another effect is an overestimate of the zonal drift at low elevation angles caused by the Earth's curvature. Figure 7 depicts the geometry at Ancon, where vectors at 350-km altitude represent drifting irregularities directly overhead and at a 28° elevation angle to the east. The earth's curvature in this diagram is to scale, but the drift vectors have been exaggerated for clarity; the local horizontal and vertical components of the drift velocity are assumed to be the same at each location. An additional assumption is that scattering is only weak to moderate, so that an irregularity casts a shadow-like interference pattern on the ground along the continuation of the ray path from the satellite through the irregularity (dotted lines). As seen in the figure, the "shadow" looking to the east travels farther

in a unit time than the one overhead, leading to a larger calculated drift velocity, V_0. For purely horizontal drifts, the angular difference in local verticals due to the Earth's curvature causes an apparent downward vertical drift, as seen from Ancon looking toward the east. At an elevation angle of 28° and 350-km intersection altitude (ground distance ∼570 km) the difference in local verticals is ∼5°. Therefore, for zonal drifts, velocity measurements to the east should be multiplied by a correction factor of .86.

The vertical drift at the east intersection point can be determined from the measured V_0 and an independent measurement of the horizontal drift. Figure 8 depicts the geometry at the east intersection point. The angle θ is the difference between the local horizontals at Ancon and the east intersection point; ε is the elevation angle of the intersection point. The velocity perpendicular to the line of sight is the sum of the V_h and V_v components in that direction; $V_0 \sin(\varepsilon)=V_h \cos(\gamma)+V_v\sin(\gamma)$, where $\gamma=(90-\varepsilon-\theta)$ and V_0 is the measured drift at Ancon. The vertical drift V_v can then be determined from V_0 and V_h.

Because the Ancon-E (F8) and Antofagasta (F7) 350-km ionospheric intersection points are almost at the same magnetic longitude (Fig. 1), Antofagasta can provide the horizontal drift values needed to compute vertical drifts from Ancon V_0 measurements. Figures 9a–e are examples of vertical drifts calculated from Antofagasta and Ancon scintillations on 7 and 9 March and 3–5 April 1997. The top panels show horizontal drift velocities at Antofagasta and Ancon looking east; the bottom panels show calculated vertical drifts and Julia radar vertical drift velocities averaged over a 340–360 km altitude range in one-minute intervals, similar to the duration of scintillation samples. The Julia radar, located at Jicamarca near Ancon, detects drifting 3-m irregularities. Julia velocity points have been shifted 1.5 h, the time to travel the distance between the Julia and Antofagasta longitudes at a nominal 100 m/s zonal drift velocity. On 7 and 9 March the agreement between the scintillation and Julia velocities is poor, while on 3–5 April there is better agreement over extended periods. Given the uncertainty that the pattern of vertical drifts persists until it reaches the Antofagasta longitude, case by case agreement cannot be expected, especially during the dynamic growth phase of a plume. Also, because the Antofagasta intersection point maps to about 500 km apex altitude at the magnetic equator, height variations in horizontal drift are neglected (Pingree and Fejer, 1987; Basu et al., 1996). An alternative procedure is to use Ancon overhead V_0 to specify the horizontal drift. In this case the intersection points are at the same altitude over the magnetic equator but separated in longitude by 5° and 1 to 2 h in time.

Although individual case studies, like those in Fig. 9, show some agreement with radar measurements in the vicinity, statistical results over several years would lend more credibility if they exhibited trends seen in other studies. The panel for each year in Fig. 10a shows average vertical drift velocities, computed from Antofagasta and Ancon-E data, in one-hour bins, from 00:00 to 08:00 UT, during the months of February to April, when scintillation activity is common in South
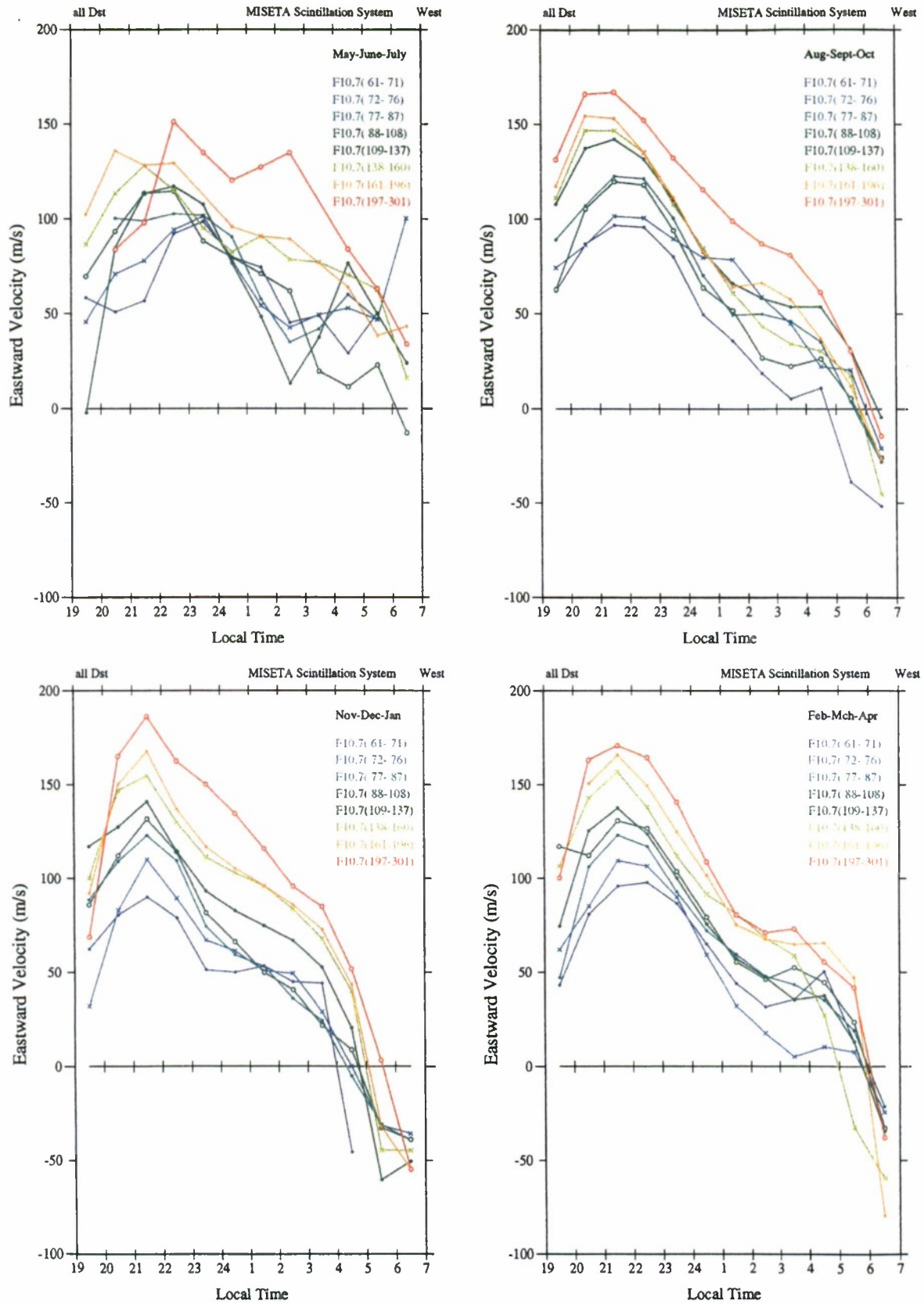
Fig. 2. Seasonal average zonal drifts for Ancon-W vs. local time (LT=UT−5 h) binned into 8 levels of solar flux activity.
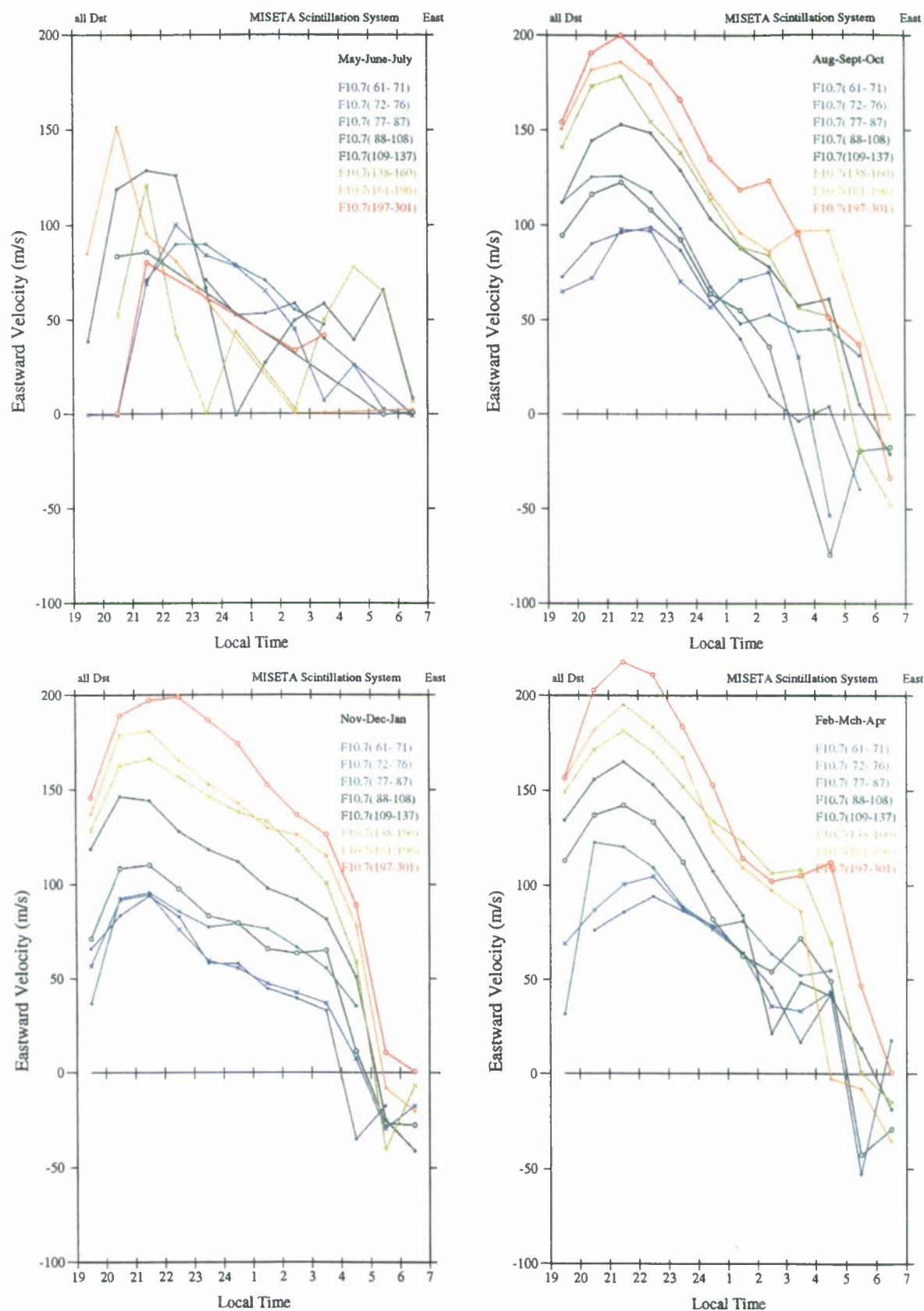
56

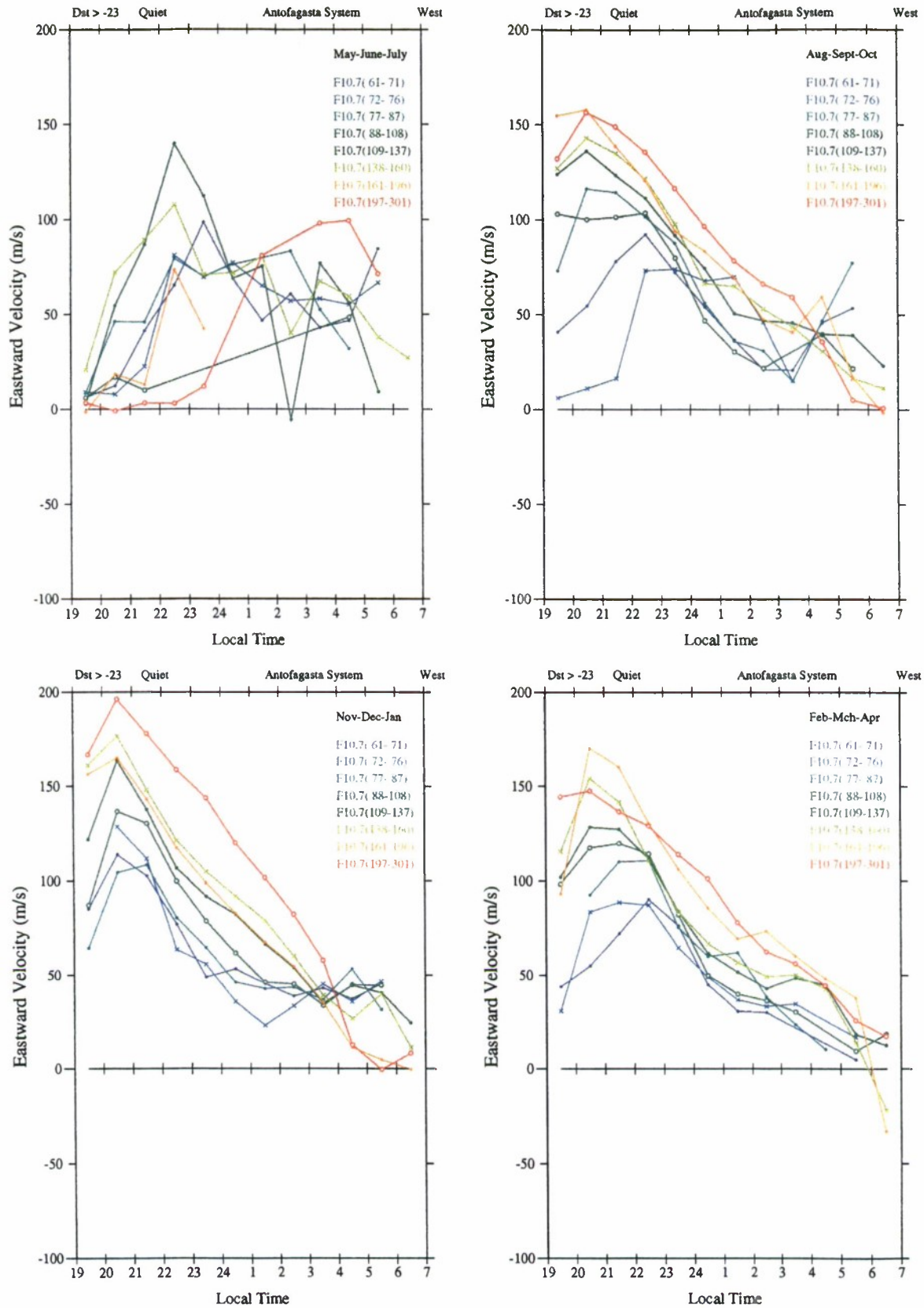**Fig. 3.** Seasonal average zonal drifts for Ancon-E.

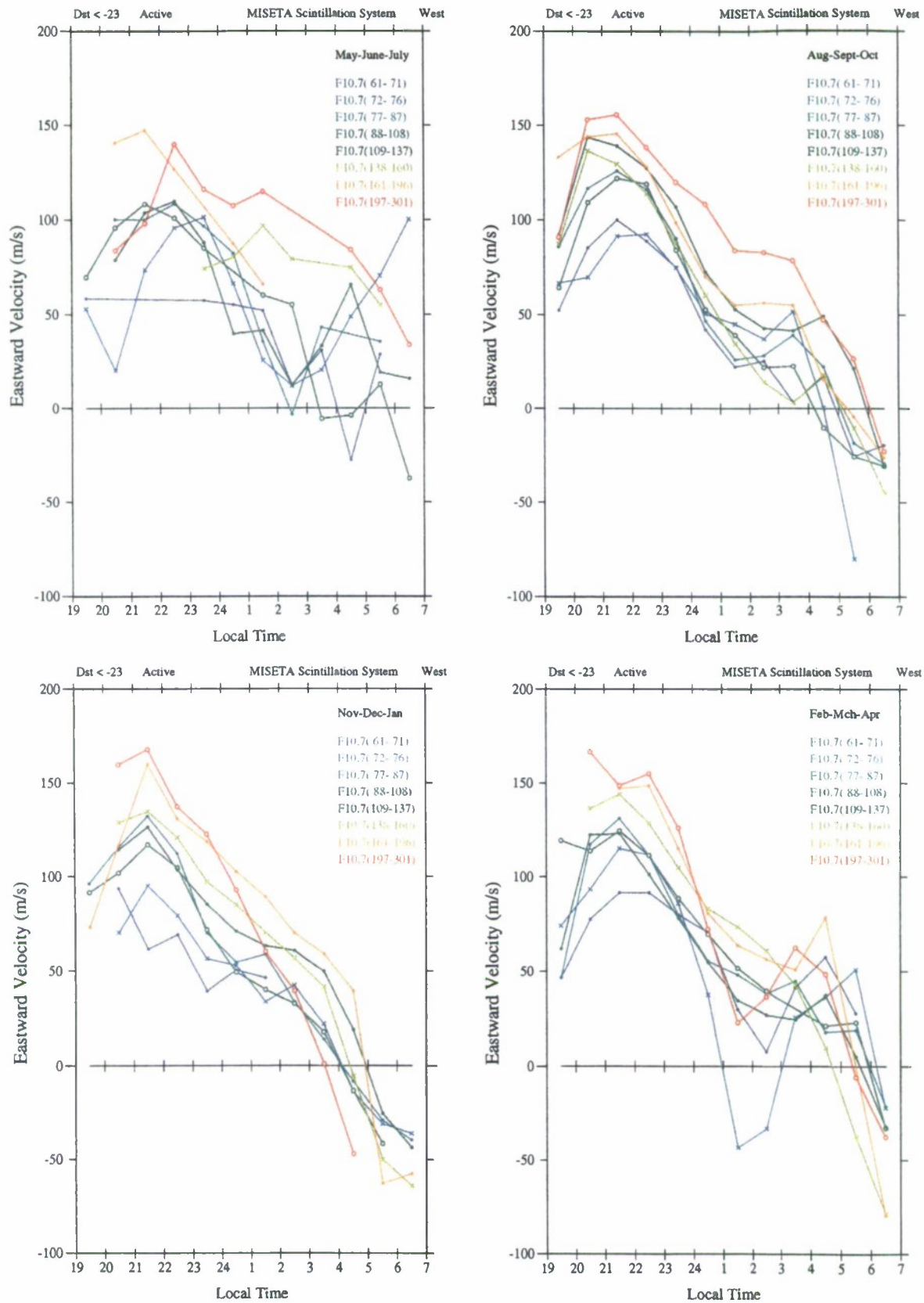**Fig. 4.** Seasonal average zonal drifts for Antofagasta.

Fig. 5. (a) Seasonal average zonal drifts for Ancon-W, active D_{st} (< -23).
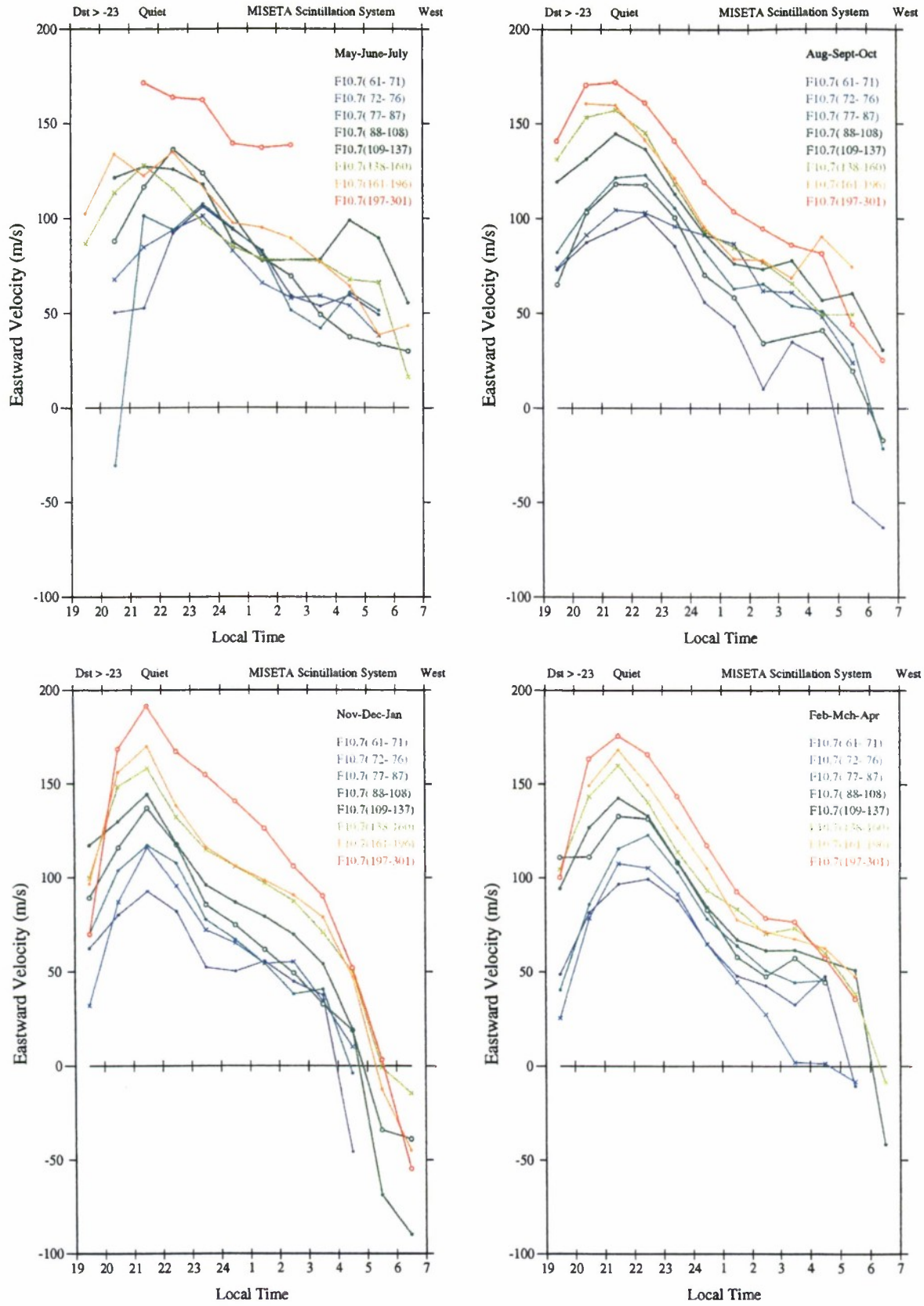
59

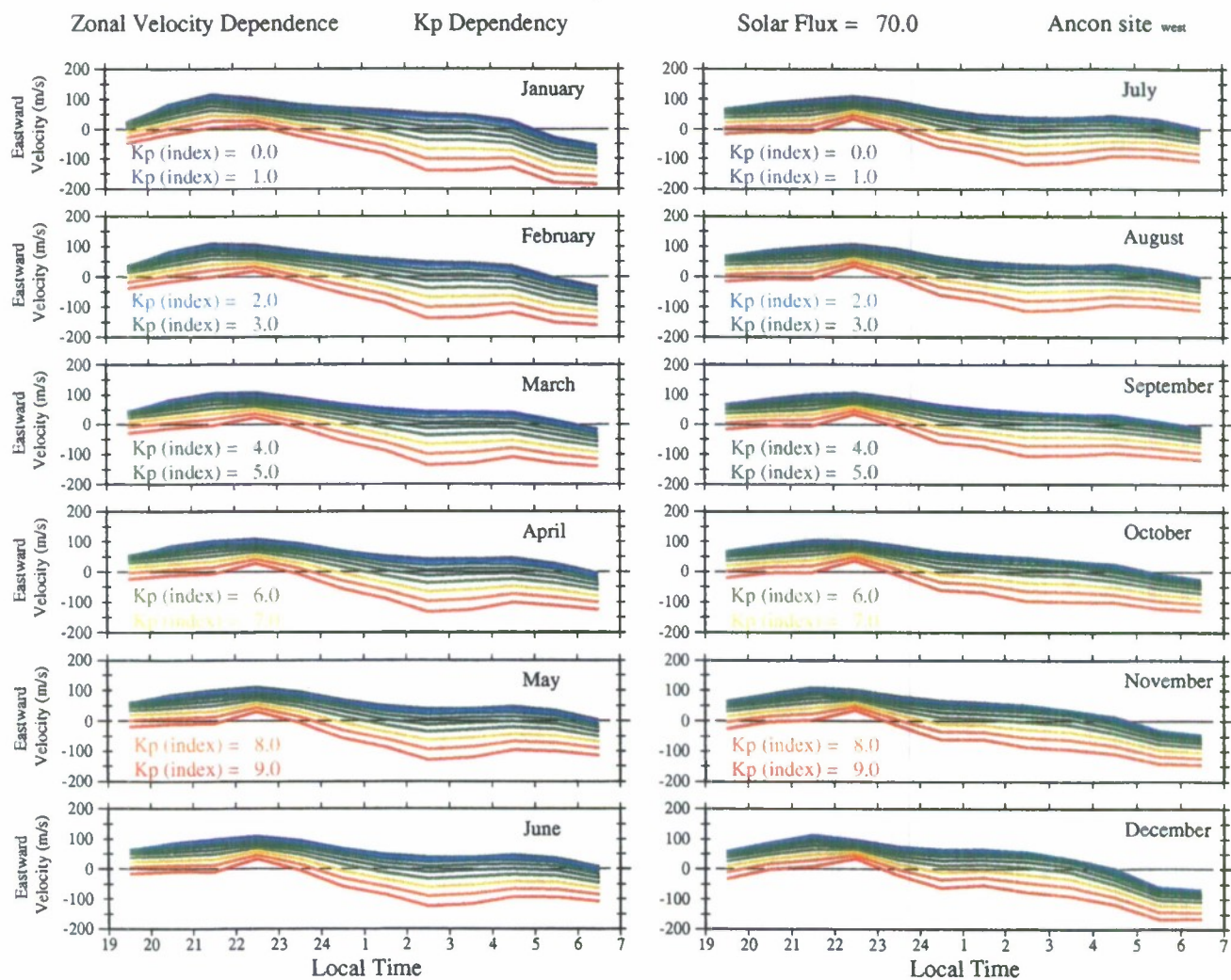**Fig. 5. (b)** Seasonal average zonal drifts for Ancon-W, quiet D_{st} (>-23).
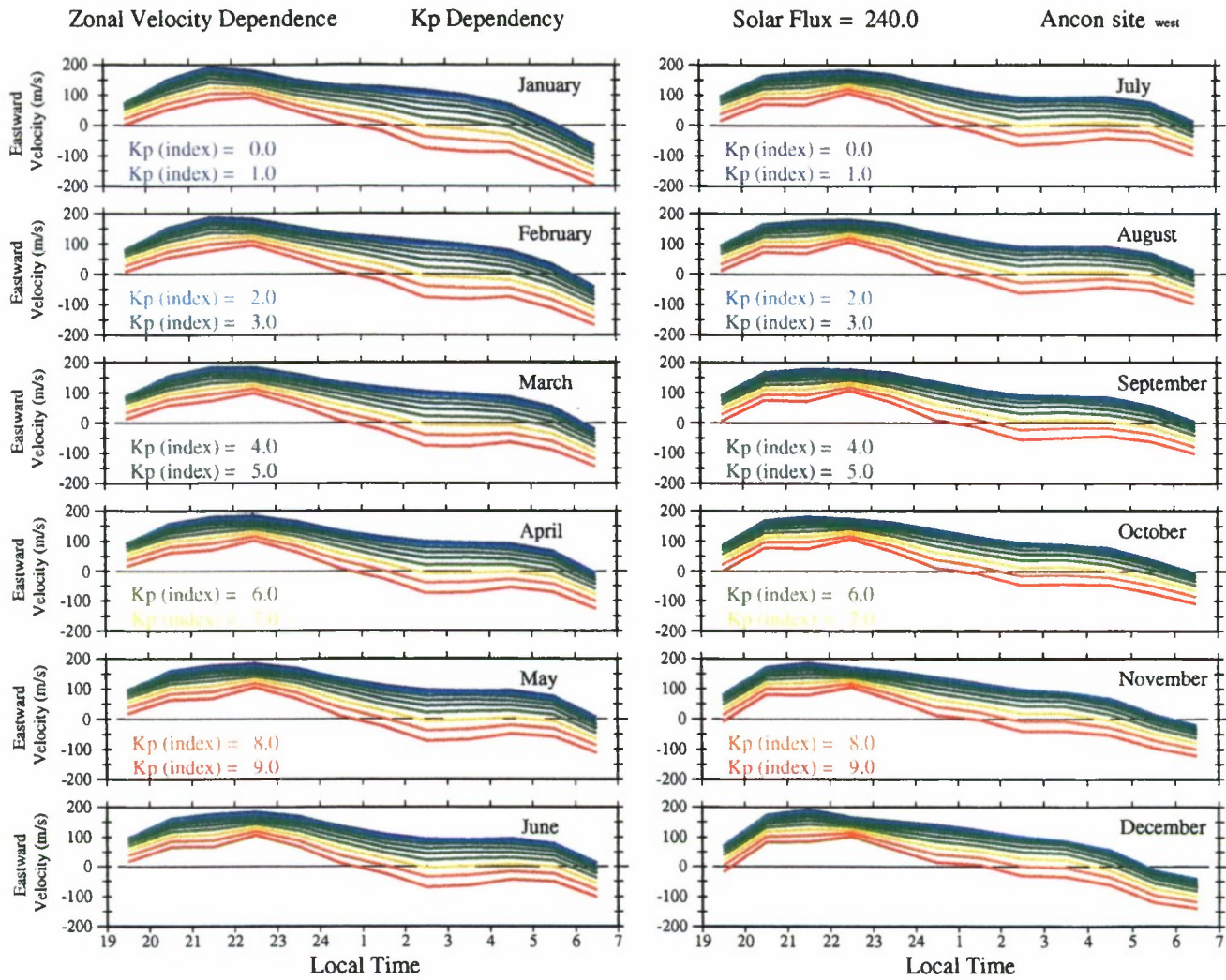
Fig. 6. (a) Ancon zonal drift dependence on K_p, solar flux=70.

61

Fig. 6. (b) Ancon zonal drift dependence on K_p, solar flux=240.
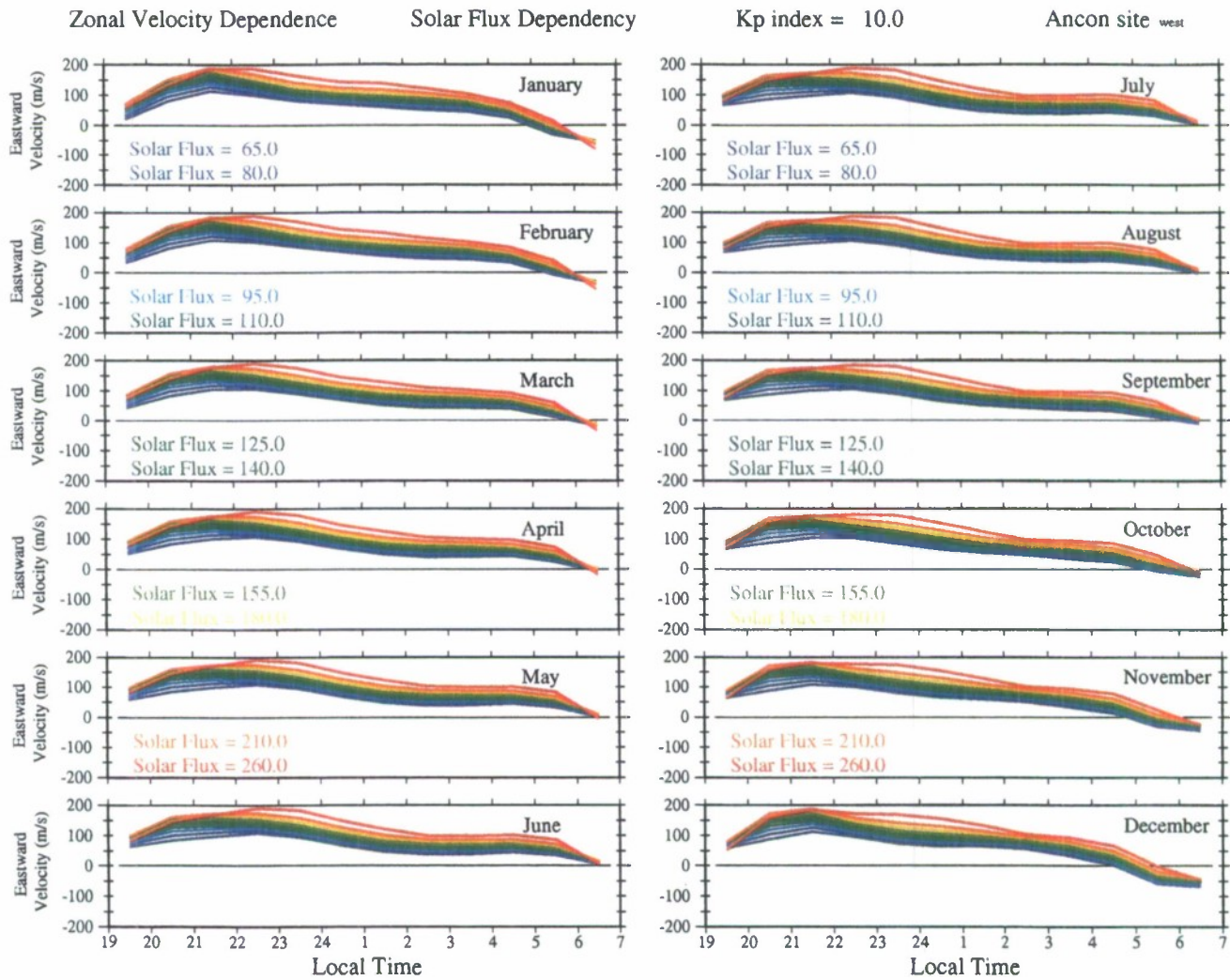
Fig. 6. (c) Ancon zonal drift dependence on solar flux, K_p=1.

63
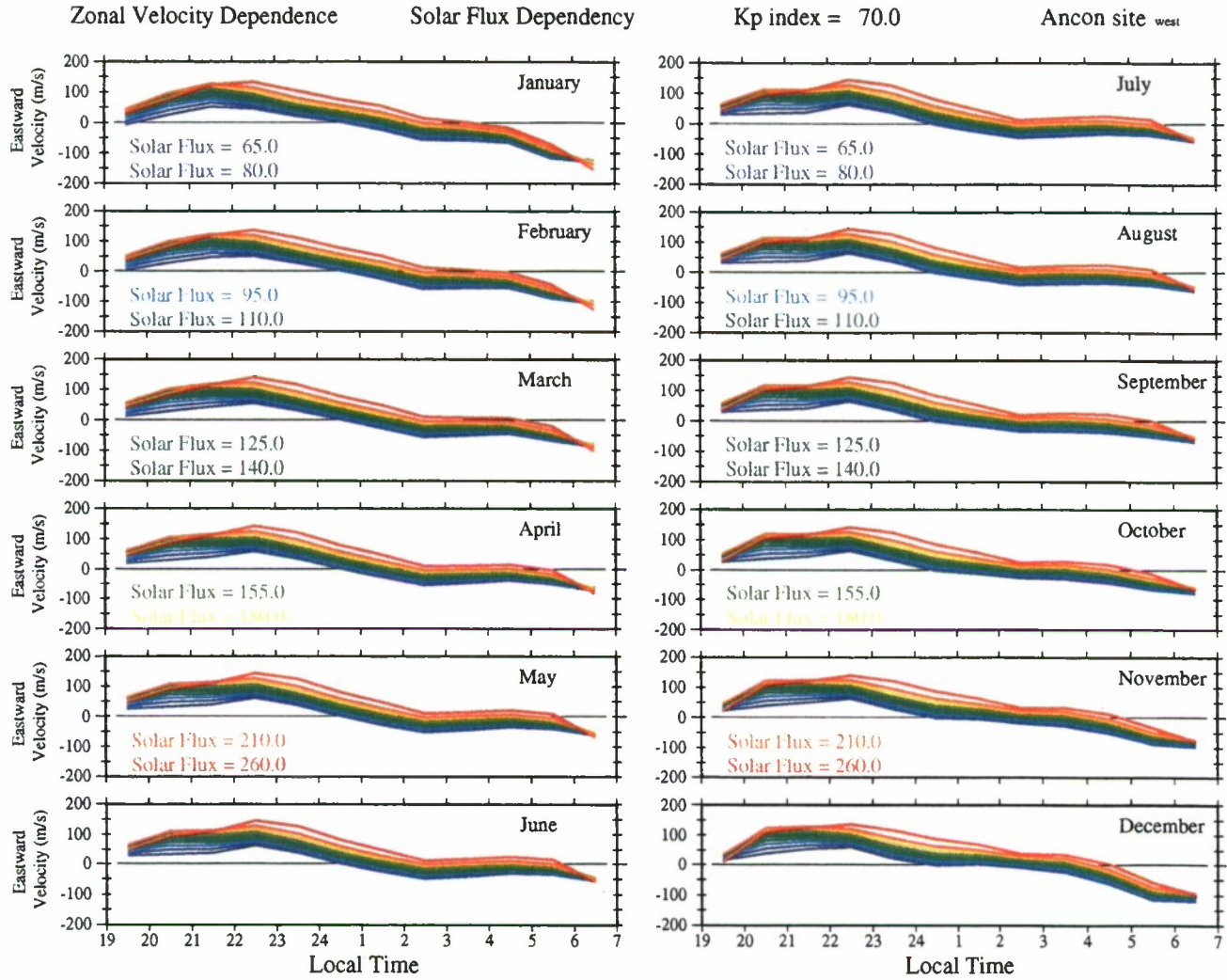
Fig. 6. (d) Ancon zonal drift dependence on solar flux, K_p=7.

64
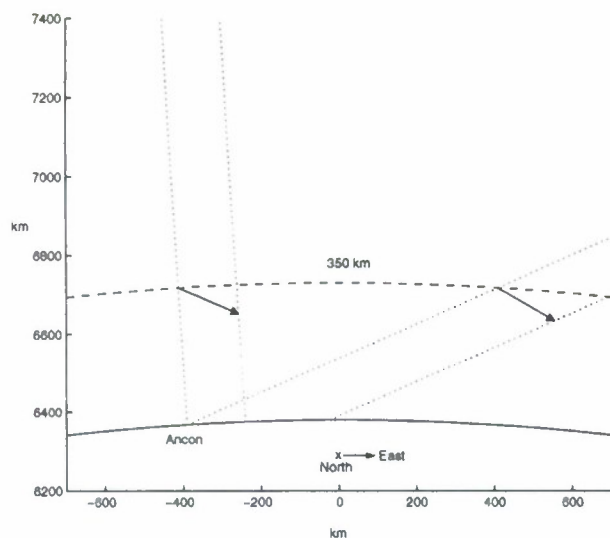
Fig. 7. View geometry from Ancon (approximately to scale). Dotted lines indicate ray paths intersected by drifting irregularities viewed nearly overhead and low to the east.
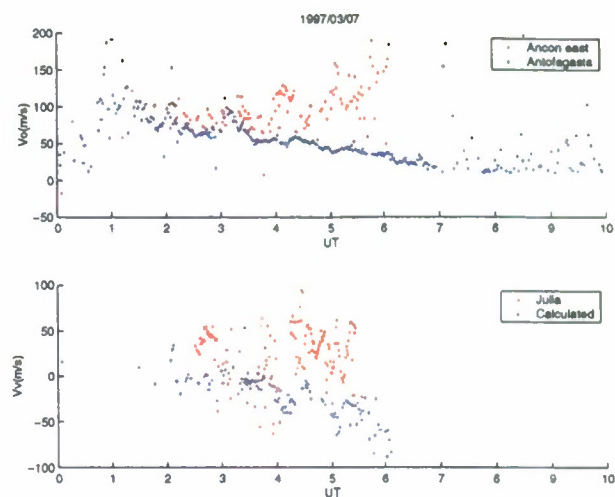

Fig. 9. (a) Top panel: Observed V_0 drift velocities at Ancon-E and Antofagasta on 7 March 1997. Bottom panel: Observed Julia radar vertical drifts and vertical drifts calculated from Ancon-E and Antofagasta V_0 in top panel. Julia data is displaced 1.5 h later to account for zonal drift.
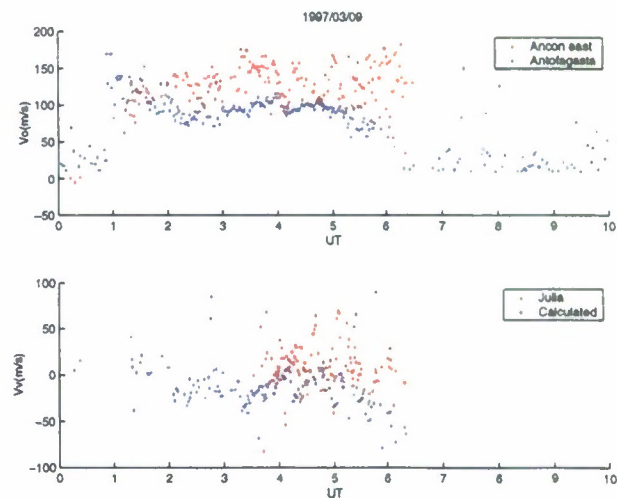

Fig. 8. Geometry at the Ancon-E ionospheric intersection point. Irregularities with horizontal and vertical drift components V_h and V_v, respectively, yield a calculated V_0 at Ancon-E.

Fig. 9. (b) Same as Fig. 9a for 9 March 1997.
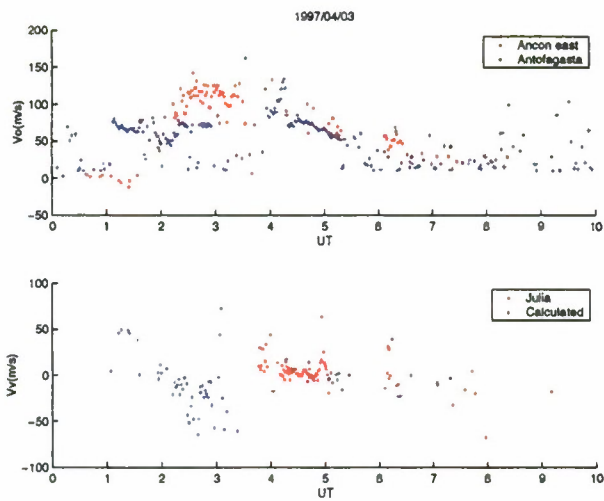
65

Fig. 9. (c) Same as Fig. 9a for 3 April 1997.
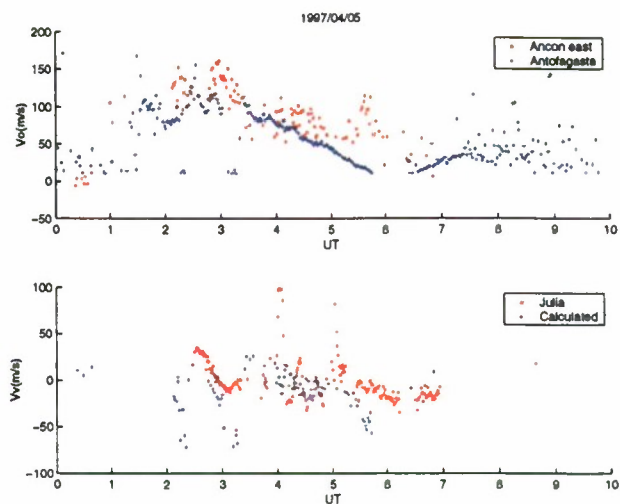

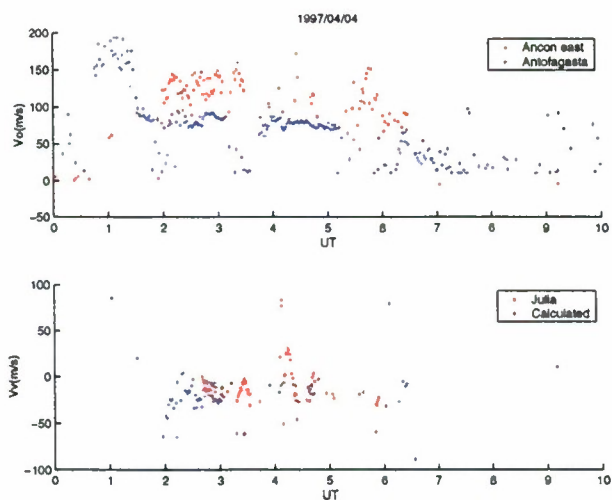**Fig. 9.** (e) Same as Fig. 9a for 5 April 1997.

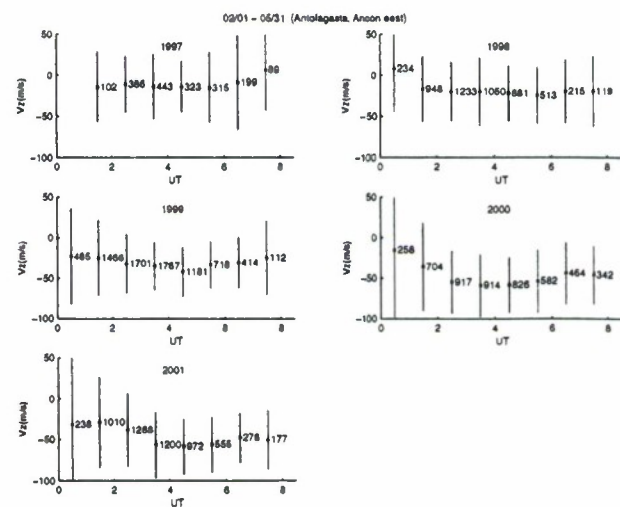**Fig. 9.** (d) Same as Fig. 9a for 4 April 1997.

Fig. 10. (a) Average vertical drift calculated from Antofagasta and Ancon-E V_0 data vs. UT for the months February–May from 1997 to 2001.
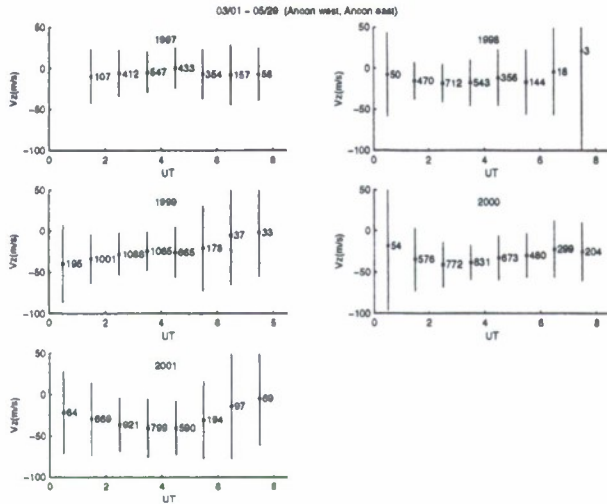
Fig. 10. (b) Same as Fig. 10a except data is from Ancon-W instead of Antofagasta.

Fig. 11. Linear fit to Ancon zonal drift measurements in 02:00 LT bin vs. solar flux during the equinoxes (all data 1994–2002).

America, and also including cases occurring in May. These results can be compared with equinox statistics from Fig. 1 in Fejer et al. (1991), which shows Jicamarca velocities that are generally negative (downward) from 20:00 to 03:00 LT (01:00 to 08:00 UT in Fig. 10a). In Fig. 10b Ancon-W supplies the horizontal velocity; the results are similar except that vertical drifts are somewhat less negative in 2000–2001. Since Ancon-E data is common to both figures, differences result from the horizontal drift data source, each of which suffers from its own drawback mentioned above. The Jicamarca data range from about −20 to −60 m/s for solar fluxes ranging from less than 100 to greater than 150, indicating that the more negative drifts in Figs. 10a and b around the year 2000 are consistent with increased solar activity. Valladares et al. (1996) found systematic differences between zonal drifts measured by incoherent radar and scintillation techniques which may apply to the vertical drifts as well. The vertical drift statistics include all geomagnetic and solar conditions and have rather large error bars that make the UT trend in each year suggestive but not definite.

5 Conclusions and discussion

The zonal drift statistics presented here update the first results of Valladares et al. (1996) through the current solar maximum. As noted by Fejer et al. (1985), eastward zonal drift velocities measured by the Jicamarca incoherent radar are generally slower than those seen by two spaced receivers. Figure 11 shows a linear fit of all the Ancon spaced-receiver zonal drift data (1994–2002) vs. solar flux during the equinoxes at 02:00 LT, generally the time of maximum eastward velocity. Each solar flux bin of 10 units has 1000 or more points up to flux=205 and over 200 points up to flux=245. A similar plot of the Jicamarca eastward peak velocity (Fig. 8 in Fejer et al., 1991) has comparable error bars,
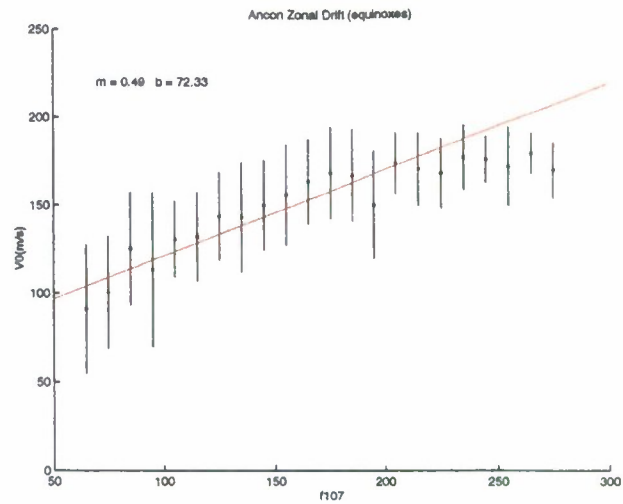
a slope of 0.45 and an intercept at 60.01 m/s. The higher intercept and slightly steeper slope in Fig. 11 confirm that average spaced-receiver drifts are about 10–20 m/s faster than the average Jicamarca drifts. In Fig. 11 the average drift stops increasing and remains at approximately 150 m/s when the solar flux exceeds 200, which indicates that the second-order fit in the empirical model presented here is a better approximation than a linear fit. However, the relatively large error bars for the solar flux and the K_p dependences mean that a broad range of drift velocities are associated with these global indices and the details depend more on local dynamic conditions.

After the installation of the Ancon-E antennas, it was noted that the measured drift velocities to the east were usually greater and more variable than the zonal drifts seen by Ancon-W nearly overhead. It was realized that, in addition to the longer path through the ionosphere, the viewing geometry could introduce contributions from real vertical drifts and an apparent vertical drift due to the Earth's curvature. This conclusion assumes mostly forward scatter of radio waves by km-scale irregularities that produce interference patterns on the ground and cause UHF scintillations. Furthermore, the km-scale ionospheric irregularities are assumed to drift both horizontally and vertically with the ambient plasma (frozen-in condition), the same drift that is seen by incoherent scatter radars. The characteristics of the zonal drift model presented here are well established and generally agree with the statistics of published radar data.

The results for vertical drifts from UHF measurements are encouraging, but tentative, and several questions remain. First, there is the applicability of the simple geometry used here, which should be compared with a full treatment of slant propagation through a real ionosphere. For low elevation angles, however, the approximations in propagation models like Costa and Basu (2002) and similar studies probably would not be valid. Second, Bhattacharyya et al. (2001) noted that

67

Table 1. Model coefficients for equation A2

				K_p*						
LT	C_1	C_2	C_3	C_4	C_5	C_6	XBAR	YBAR	SS
19:00–20:00	85.18	1.00	−5.15	−1.26	−1.32	−25.00	213.78	23.94	40.29
20:00–21:00	125.08	2.40	−19.74	0.12	0.55	−18.71	203.05	21.86	41.93
21:00–22:00	130.41	1.84	−23.81	1.68	0.28	−21.44	194.61	20.99	42.78
22:00–23:00	126.47	0.13	−23.57	0.20	1.71	−10.54	193.75	21.23	44.14
23:00–00:00	109.54	0.15	−24.09	−0.22	0.61	−19.15	193.25	21.03	43.63
00:00–01:00	82.34	1.10	−22.87	1.19	−0.15	−31.31	190.26	21.18	43.97
01:00–02:00	59.63	1.54	−27.13	2.25	1.81	−27.18	187.58	20.02	42.99
02:00–03:00	52.03	1.37	−29.78	2.27	4.06	−39.97	189.75	21.17	44.41
03:00–04:00	48.94	0.97	−28.19	1.52	4.58	−43.12	199.09	24.33	44.90
04:00–05:00	48.60	−2.31	−32.67	−0.92	2.02	−23.31	205.09	25.86	39.44
05:00–06:00	34.15	−6.49	−29.17	−3.44	2.12	−21.03	204.14	28.37	37.25
06:00–07:00	0.66	−4.34	−28.12	−3.33	1.56	−19.43	210.80	30.45	38.01

				Solar Flux						
LT	C_1	C_2	C_3	C_4	C_5	C_6	XBAR	YBAR	SS
19:00–20:00	92.72	0.77	23.28	−4.27	−2.99	−11.74	213.78	119.51	67.91
20:00–21:00	136.96	3.24	47.66	−0.24	1.64	−22.29	203.05	132.99	76.27
21:00–22:00	142.76	1.21	43.37	3.76	−0.07	−16.90	194.61	138.25	79.85
22:00–23:00	137.32	−1.79	36.54	−2.40	−1.04	−5.10	193.75	137.78	80.99
23:00–24:00	118.36	−1.81	35.47	−4.06	1.15	−0.24	193.25	136.35	81.44
00:00–01:00	92.67	−0.01	33.25	0.06	1.71	−0.74	190.26	138.99	81.98
01:00–02:00	70.76	1.77	30.09	3.93	−0.94	−1.09	187.58	144.99	82.90
02:00–03:00	64.78	1.96	26.66	3.82	−2.39	−4.50	189.75	150.70	83.70
03:00–04:00	64.40	−1.03	26.49	0.14	0.15	−4.05	199.09	147.60	81.91
04:00–05:00	60.15	−7.42	23.00	−6.58	1.42	−1.59	205.09	141.71	75.73
05:00–06:00	44.12	−14.05	17.84	−13.92	0.71	−0.43	204.14	133.40	68.85
06:00–07:00	10.83	−8.78	7.16	−10.90	2.94	−4.76	210.80	135.80	66.02

spaced antenna drift velocities might not reflect the ambient plasma drift during the turbulent early stage of plasma bubble development, which typically occurs before 22:00 LT. In fact, the top panels of Figs. 9a–e show that the drift measured by Ancon-E fluctuates considerably more than the zonal drift at Antofagasta at all local times, which indicates that the vertical motion of the irregularities is generally more variable than the zonal drift. The variability, as seen in the lower panels of Figs. 8a–e, is similar to the Julia data at most times. Finally, the horizontal velocities used in the calculations are not at the Ancon-E ionospheric intersection point, but either at a higher altitude, when coming from the Antofagasta data, or at a different longitude, when coming from the Ancon-W data.

Appendix A

The model drift at Ancon for a desired solar flux and K_p* is given by

$$V_{model} = V_{fit}(solar\ flux) + (V_{fit}(K_p*) - V_{fit}(K_p* = 20)),$$ (A1)

where $K_p* = 10\,K_p$ and $K_p = 0., 0.33, 0.67, 1.00, \ldots$. Each velocity term, V_{fit}, is expressed in terms of the row of coefficients for a local time in the appropriate table.

$$V_{fit} = C_1 + C_2X + C_3Y + C_4X^2 + C_5XY + C_6Y^2$$ (A2)

X=(DOY–XBAR)/SS, where DOY = day of year (1–365). Y=(GPH–YBAR)/SS, where GPH = geophysical parameter (solar flux or K_p*).

References

Basu, S., Kudeki, E., Basu, S., Valladares, C. E., Weber, E. J., Zengingonul, H. P., Bhattacharyya, S., Sheehan, R., Meriwether, J. W., Biondi, M. A., Kuenzler, H., and Espinoza, J.: Scintillations, plasma drifts, and neutral winds in the equatorial ionosphere after sunset, J. Geophys. Res., 101, 26 795–26 809, 1996.

Bhattacharyya, A., Basu, S., Groves, K. M., Valladares, C. E., and Sheehan, R.: Dynamics of equatorial F-region irregularities from spaced receiver scintillation observations, Geophys. Res. Lett., 28, 119–122, 2001.

Coley, W. R. and Heelis, R. A.: Low-latitude zonal and vertical ion drifts seen by DE 2, J. Geophys. Res., 6751, 1989.

Costa, E. and Basu, S.: A radio wave scattering algorithm and irregularity model for scintillation predictions, Radio Sci., 37, 10.1029, 2002.

Eccles, J. V.: A simple model of low latitude electric fields, J. Geophys. Res., 103, 26 699–26 708, 1998.

Fejer, B. G., de Paula, E. R., Gonzalez, S. A., and Woodman, R. R.: Average vertical and zonal F-region plasma drifts over Jicamarca, J. Geophys. Res., 96, 13 901, 1991.

Fejer, B. G., Farley, D. T., Gonzales, C. A., Woodman, R. F., and Calderon, C.: F-region east-west drifts at Jicamarca. J. Geophys. Res., 86, 215, 1981.

Fejer, B. G., Kudeki, E., and Farley, D. T.: Equatorial F-region zonal plasma drifts, J. Geophys. Res., 90, 12 249–12 255, 1985.

Fejer, B. G. and Scherliess, L.: Empirical models of storm time equatorial zonal electric fields, J. Geophys. Res., 102, 24 047–24 056, 1997.

Fejer, B. G. and Scherliess, L.: Mid- and low latitude prompt-penetration ionospheric zonal plasma drifts, Geophys. Res. Lett., 25, 3071, 1998.

Fejer, B. G., Scherliess, L., and de Paula, E. R.: Effects of the vertical plasma drift velocity on the generation and evolution of equatorial spread F, J. Geophys. Res., 104, 19 859–19 869, 1999.

Kil, H., Kintner, P. M., de Paula, E. R., and Kantor, I. J.: Global positioning system measurements of the ionospheric zonal apparent velocity at Cachoeira Paulista in Brazil, J. Geophys. Res., 105, 5317–5327, 2000.

Pingree, J. E. and Fejer, B. G.: On the height variation of the equatorial F-region vertical plasma drifts, J. Geophys. Res., 92, 4763, 1987.

Rishbeth, H.: Polarization fields produced by winds in the equatorial F-region, Planet Space Sci., 19, 357–369, 1971.

Rishbeth, H.: The F-region dynamo, J. Atmos. Terr. Phys., 43, 387–392, 1981.

Scherliess, L. and Fejer, B. G.: Radar and satellite global equatorial F-region vertical drift model, J. Geophys. Res., 104, 6829–6842, 1999.

Vacchione, J. D., Franke, S. J., and Yeh, K. C.: A new analysis technique for estimating zonal irregularity drifts and variability in the equatorial F-region using spaced receiver scintillation data, Radio Sci., 22, 745, 1987.

Valladares, C. E., Meriwether, J. W., Sheehan, R., and Biondi, M. A.: Correlative study of neutral winds and scintillation drifts measured near the magnetic equator, J. Geophys. Res., 107, A7, 10.1029, 2002.

Valladares, C. E., Sheehan, R., Basu, S., Kuenzler, H., and Espinoza, J.: The multi-instrumented studies of equatorial thermosphere aeronomy scintillation system: Climatology of zonal drifts, J. Geophys. Res., 101, 26 939, 1996.

Polar Cap Patches Observed during the Magnetic Storm of November 2003
Observations and Modeling

C.E. Valladares[1], T. Pedersen[2], and R. Sheehan[1]

[1]Institute for Scientific Research, Boston College, Chestnut Hill, Massachusetts
[2]Space Vehicle Directorate, Air Force research Laboratory, Hanscom Air Force Base, Massachusetts

Abstract

This paper presents multi-instrument measurements conducted early during the recovery phase of the major magnetic storm of November 20, 2003 aiming to diagnose the full dynamics and further structuring of intense polar cap patches. The Qaanaaq imager observed elongated, rounded, and small-scale break off patches within the polar cap. The Qaanaaq digisonde also detected abrupt N_mF_2 fluctuations and, more surprisingly, sharp h_mF_2 variations. The Sondrestrom incoherent scatter (IS) radar, located 12° south of Qaanaaq, measured additional patches placed close to but poleward of the auroral oval-polar cap boundary. The DMSP-F13 satellite, passing near Qaanaaq and Sondrestrom, intersected topside density enhancements which coincided with the imager, digisonde, and IS patches. Sudden changes in the patch airglow brightness were observed at times when the F-region altitude descended. These observations suggested that a downward motion of the plasma along B may produce the illusory view of a patch density being enhanced. Consecutive red-line images were used to compute the plasma drift velocity using a 2-D cross correlation analysis. The magnitude and direction of the patch velocity were in very good agreement with the SuperDARN convection patterns and velocities. We have also developed a trajectory analysis technique able to step backward in time the location of the patches to investigate the origin of the polar cap patches. It was concluded that most of the patches seen between 2000 and 2400 UT were part of the tongue-of-ionization (TOI) presented by *Foster et al.* [2005]. However, the patches observed by the Sondrestrom radar near the polar cap boundary were probably circulating along a reduced afternoon cell, producing elongated and stretched density enhancements. To investigate the origin of the polar cap patches, the outlines of patches observed between 2041 and 2129 UT were traced back to 1941–1951 UT with the purpose of inspecting the SuperDARN velocities at the time patches were entering the polar cap. There was spatial and temporal agreement between a narrow channel of enhanced SuperDARN velocities and a sector of reduced densities. We concluded that the polar cap patches were formed by a large plasma jet that was confined to a narrow longitudinal band. To investigate the variability of patch brightness, we have used the GTIM code to conduct numerical simulations of the polar cap ionosphere using as inputs the SuperDARN convection patterns and a variable upward/downward component of the neutral wind as has been observed within the polar cap during the transit of large-scale gravity waves (GW) [*Johnson et al.* 1995]. The numerical results indicate that variations in the airglow intensity of about 450 Rayleighs can be produced by a constant 75 m/s downward vertical wind. It is concluded here that airglow images collected deep inside the polar cap, together with a robust trajectory analysis and Super DARN measurements can be used to discern different formation mechanisms of polar cap patches.

1. INTRODUCTION

Early measurements of polar cap patches were conducted at Thule, Greenland (86° mlat) suggesting that enhanced ionization regions occur preferentially during magnetically disturbed periods (B_z south conditions) [*Buchau et al.*, 1983]. The newly-discovered patches were then diagnosed more fully using imagers, digisondes, scintillation receivers, and nearby satellites providing information on their typical horizontal dimensions (between 100 and 1000 km) [*Weber et al.*, 1984], on their prevailing motion (antisunward), and on their variety of shapes with a preference for cigar-shaped forms containing a major axis aligned in the dawn-dusk direction. During the 80's, it was found that the density enhanced patches reached 10^6 el/cm^3 at 250 km altitude; while outside the patches the ionization dropped below 10^5 el/cm^3 at 400 km altitude. Month-long experiments indicated that the hourly pattern of patch occurrence coincided with the universal time that the dayside auroral oval moves further down to lower geographic latitudes. This was an indication that the solar-produced sub auroral ionosphere was probably the source region of the patches [*Buchau et al.*, 1985]. Previous measurements at Chatanika and Sondrestrom conducted by *Foster and Doupnik* [1984] and *Kelly and Vickrey* [1984] had confirmed that sub-auroral densities intrude through the dayside throat region forming a continuous and long tongue-of-ionization (TOI). However, the patchy nature of the large-scale polar cap density enhancements implied the presence of a formation mechanism able to fragment the TOI and form discrete entities.

The first patch-formation mechanisms consisted of sudden reversals of the B_y and/or B_z IMF components [*Tsunoda*, 1988]. Shortly afterwards, numerical simulations confirmed that varying the convection pattern due to the migration of the reconnection point and a consequent redirection of the tension force [*Sojka et al.*, 1993] or a resizing of the polar cap [*Anderson et al.*, 1988], as commonly occurs when B_z switches sign, could result in a fragmented TOI resembling the observed polar cap patches. However, the observational fact that patches commonly occur in a succession of several polar cap patches separated by time intervals as short as 10 min raised some doubts about the efficiency of these mechanisms. More comprehensive measurements were conducted in the 90's combining instruments placed at the center of the polar cap and observatories located at the boundary of the auroral oval and polar cap, such as the Sondrestrom and EISCAT incoherent radars. These investigations demonstrated that large plasma jets are effective in creating a region of depleted densities across the TOI by enhancing the O+ recombination coefficient and transporting less dense plasma from later local times [*Rodger*, 1994, *Valladares et al.*, 1994, 1996]. Observations gathered mainly from EISCAT, and also from the EISCAT Svalbard radar (ESR) have confirmed the important role of sporadic transient reconnection in bringing plasma into the polar cap [*Carlson et al.*, 2002, 2004, 2006]. More recently, *MacDougall and Jayachandran*, [2007] used f_0F_2 values from several stations located in the Canadian Arctic to propose a mechanism for patch generation in which density enhancements were produced by low-energy electron precipitation as the plasma returns from midnight around the dawn convection cell. *Bust and Crowley* [2007] also concluded that a sequence of patches observed at Svalbard on December 12, 2001 had been transported toward noon from the morning and afternoon sectors. These authors introduced a trajectory analysis method and an assimilation scheme to demonstrate that the origin of the patch densities was at 62° geographic latitude. *Bust and Crowley* [2007] also indicated the need to use first–principles numerical models to associate ionospheric measurements conducted at separate locations to investigate the patch origin, and to forecast the decay of the large–scale enhanced densities.

New information on patch morphology was provided by *Coley and Heelis* [1998] who processed densities measured by the DE satellite in both polar caps to demonstrate that in the northern hemisphere (NH) the occurrence probability maximized during the winter solstice in a broad time interval between 12 and 22 h UT, when 4-5 patches are seen per hour. This time interval of patch occurrence is consistent with previous ground-based observations and the time the oval occupies its most dayward location. For the southern hemisphere (SH) *Coley and Heelis* [1998] indicated that the patches occur again in the local winter solstice, with a sharp maximum at about 1230 UT, and another smaller broad maximum around 1900-2200 UT. Note that there exist two important distinctions between the northern and southern hemispheres. In the SH, the cusp is at its most sunlit location at about 0400 UT, a time of minimum patch

occurrence. The second difference is the number of patches in the southern hemisphere, which is 10 per hour; this is twice as large as the occurrence seen in the northern hemisphere. To explain this discrepancy *Basu and Valladares* [1999] suggested that the greater offset of the magnetic pole in the southern hemisphere of 15° makes a large portion of the polar cap in sunlight near 0400 UT, smoothing the polar cap densities, reducing the patch intensity, and increasing the difficulty for patch identification. In spite of the large number of processes that can produce polar cap patches, we are still uncertain of the dominant mechanism, if a single one really exists, or if different mechanisms are more effective at different universal times, at different locations, or even in different hemispheres.

This paper presents observations of polar cap patches conducted at Qaanaaq, Sondrestrom, and ancillary data collected by the SuperDARN radars and DMSP satellites during the recovery phase of the major magnetic storm of November 20, 2003. We present observations of 630.0 nm airglow, digisonde bottomside densities, and UHF scintillations conducted near the center of the polar cap at Qaanaaq, Greenland in which series of polar cap patches were detected moving with the global convection (section 3). The goals of this paper are to document the morphology and dynamics of polar cap patches during extremely disturbed conditions, to demonstrate that the patch density under these conditions originate at the TOI, and to postulate that cusp-related dynamics was responsible for the patch fragmentation. This paper also introduces a method of determining the patch velocity using a 2-D cross correlation analysis of the 630.0 nm images detected at Qaanaaq (section 4), a backward tracing trajectory analysis (section 5) and a time–forward modeling of the patch densities (section 6).

2. EXTREME SPACE WEATHER CONDITIONS

The largest geomagnetic storm of solar cycle 23 occurred on November 20, 2003 caused by a fast and wide CME. The storm started at 0728 UT with the arrival of the shock and reached a minimum D_{st} value of –472 nT at 2000 UT [*Gopalswamy et al.*, 2005]. During the storm, the IMF B_z was the dominant component decreasing to –52 nT at 1500 UT. The IMF B_y was positive and large during the early part of the storm main phase, reversed to negative at ~1600 UT and became about –20 nT after 1800 UT. The IMF B_z became less negative after 1700 UT, remained constant near –20 nT between 1900 and 2100 UT, and then increased almost linearly attaining a value equal to –10 nT at 2400 UT. During major magnetic storms, the interaction between the solar wind and the magnetosphere causes a change in the region 1 and 2 currents. Under these conditions, the shielding characteristics are varied, allowing an instantaneous penetration of an electric field from high latitude to the mid and low latitudes. Recently, several authors have described the characteristics of the ionosphere and atmosphere that prevailed during the main and recovery phases of the 20 November 2003 geomagnetic storm [*Foster et al.*, 2005, *Meier et al.*, 2005; *Crowley et al.*, 2006; *Basu et al.*, 2007]. *Foster et al.* [2005] presented global displays of the ionospheric TEC to demonstrate that the dayside source of the TOI is the plume of storm enhanced densities (SED) that is transported from lower latitudes in the post-noon sector by the sub-auroral electric field. *Meier et al.* [2005] introduced images obtained by the TIMED/GUVI FUV imager that showed regions of depleted and others of enhanced integrated O/N_2 ratios that extended to equatorial latitudes during the peak of the storm. *Crowley et al.* [2006] studied the response of the thermosphere-ionosphere system using the NCAR TIMEGCM model and suggested that neutral thermospheric winds drive the ionospheric plasma to greater altitudes leading to enhanced plasma densities in the sunlit hemisphere. *Basu et al.* [2007] investigated the response of the equatorial ionosphere at dusk to the intense penetration electric field.

As mentioned above, a prominent effect that develops during a large geomagnetic storm is the formation of a narrow region containing storm enhanced densities (SEDs). *Foster*, [1993] and *Foster and Vo*, [2002] used measurements from the Millstone Hill ISR to characterize the SED as a narrow plume of large densities extending from mid latitudes up to the midday throat. *Foster and Burke* [2002] found intense flows that they called sub-auroral polarization streams (SAPS) commonly occurring in the region equatorward of the two-cell convection. It was then suggested that SAPS produce erosion of the outer layers of the plasmasphere and the channel of poleward moving SEDs in the ionosphere [*Foster et al.*, 2002]. During the major geomagnetic storm of November 20, 2003 a pronounced SED entered the polar

cap in the America sector near 1800 UT [*Foster et al.*, 2005]. These authors presented 2-D maps of equivalent vertical TEC from a network of GPS receivers to demonstrate that in fact SEDs penetrate the polar caps forming a tongue of ionization (TOI) containing plasma densities with h_mF_2 and N_mF_2 values typical of the mid-latitude ionosphere. They indicated that the SED density was transported from low latitudes by the subauroral disturbance electric field acting in the postnoon sector. This paper shows that the continuous subauroral TOI presented by *Foster et al.* [2005] breaks off into polar cap patches when it enters or is about to enter into the polar cap. We have used drifts measured by the SuperDARN radars and time-reversed trajectory tracing of the patches observed at Qaanaaq to demonstrate that the TOI fragmentation (i.e. patch formation) occurs in the early afternoon sector. However, we also show that during this time of extreme magnetic disturbances further patch splitting can occur even at the center of the polar cap.

3. OBSERVATIONS OF THE POLAR CAP IONOSPHERE

Optical, radar, and scintillation observations were carried out in the central polar cap at Qaanaaq, Greenland, (77.47° N 69.27° W, ~86° magnetic latitude) using a high-sensitivity all-sky imager, a digisonde and a system of UHF receivers, respectively. The imager consists of an all-sky lens telecentrically coupled to a 4" (100mm) filter wheel containing narrow-band (~2nm) filters. In the mode used, light passing through the filters was re-imaged onto a thermoelectrically cooled bare-CCD detector operated at -40C. Data was corrected for instrument vignetting and Van Rhijn brightening and converted to units of Rayleighs based on a laboratory calibration of the instrument against a calibration source traceable to the National Institute of Standards and Technology. The Sondrestrom ISR (67.0° N, 50.9° W, 75° magnetic latitude) observed electron densities and ion drift velocities and the northern-hemisphere SuperDARN radars recorded coherent drifts, which were used to infer the origin and formation of the patches. The characteristics of the electron and ion particle populations and the direction of the cross track drift velocities measured by the DMSP satellites at 850 km altitude were used to identify the boundaries of the polar cap.

3.1. Qaanaaq Observations

Figure 1 shows the value of 630.0 nm airglow emissions, the S4 scintillation index, the peak density of the F region, and density profiles of the F-region bottomside. The last two observables were measured by the Qaanaaq digisonde operating in a 5-min cadence time. The bottom panel also displays two iso-density contour traces corresponding to 10^5 and 10^6 cm^{-3}. A prominent feature in this plot is the rapid variability of the peak altitude and the pronounced changes in the maximum number density that is observed during the main and recovery phases of the storm. Between 2000 and 2100 UT the F-region peak descended from 500 to 400 km altitude and a series of patches was detected as the digisonde peak density varied between 2×10^5 and 2×10^6 cm^{-3}. After 2100 UT, and during the recovery phase of the storm, the number density continues displaying rapid altitude variations, but its magnitude becomes nearly constant at 2×10^5 cm^{-3}. Several authors [*Weber et al.*, 1984; *Crowley*, 1996] have defined polar cap patches to be 2-10 larger than the background density in the polar ionosphere. Patches are always accompanied by discrete regions of intense airglow and high levels of scintillations. However, altitude variations are seldom seen and much less fluctuations of order 100 km.

On November 20, the Qaanaaq imager started operations shortly after 2000 UT. Panel a displays absolute values of 630.0 nm intensities taken overhead the station. These values as well as other images presented here have the background intensity removed and are expressed as a function of the standard deviation (σ) of the emission intensities. Nevertheless, we found that σ was almost equal to 80 R after 2040 UT. The dotted line placed at ½ σ (40 Rayleighs) indicates our designated threshold values for patch detections. Values above this line are defined as enhanced airglow produced by patches transiting across the imager field of view. The 3 large positive excursions observed between 2000 and 2100 UT correspond to the transit of 3 patches; their airglow signatures correlate well with increases in the number

density. A fourth airglow patch is seen between 2140 and 2210; this is flanked by increases in the S4 index, occurring at the leading and trailing edges of the patch. No density enhancement is apparent during this period. Panel b shows 5-min averaged scintillation measurements obtained at Qaanaaq by the use of 250 MHz transmissions from quasi-stationary beacon satellites [*Basu et al.*, 1998]. Saturated levels of scintillations are commonly seen during the main phase of the magnetic storm. However, on this day saturated S4 values were observed even an hour after the start of the recovery phase of the storm. After 2040 UT, the scintillation S4 intensities decay as the number density decreases. Two smaller S4 peaks are seen at 2145 and 2215 UT during the passage of the fourth and longer polar cap patch event. After 2000 UT, the 350 km altitude sub-ionospheric intersection of the scintillation link was located at 77.6° N, 77° W and ~200 km west of the Qaanaaq site.

3.2. Qaanaaq Images

Figure 2 shows two selected 630.0 nm images obtained early during the observations of November 20, 2003. Date and time information is printed on the top left side of each image. The average and σ values are included in the right upper side. The two black lines intersecting at 90° in the center of the image indicate the direction of geographic north and east. Two white dots are used to indicate the center of the image field of view and the sub-ionospheric intersection of the scintillation measurements. At the time of the observations, the sunward direction is toward geographic west and the dawn-dusk meridian almost aligned to the north-south axis. The black stripes seen in the northern side of the image corresponding to 2009:03 UT were produced by clouds. A small number of clouds and some haze were present during the early period of the observations. However, after 2020 UT, the sky was devoid of tropospheric interferences.

The image of 2009 UT shows a large region of enhanced airglow extending across the southern part of the image. This region is the origin of 3 north-south (nearly dawn-dusk) elongated patches extending almost perpendicular to the sunward direction. The eastern patch extends further north reaching the poleward end of the image. This configuration of 3 closely spaced and elongated patches that are joined in their southern end is quite different from previous observations of patches that have been carried out at Qaanaaq [*Weber et al.*, 1984]. *Fukui et al.* [1994] and *Valladares et al.* [1998] have indicated that near the center of the polar cap, the patches are preferentially elongated and quite often adopt a cigar-shaped form with the major axis closely aligned in the dawn-dusk direction. This type of patch configuration is seen in the image of 2021 UT where a long and elongated patch, closely aligned to the magnetic north-south direction, is observed extending across the imager field of view. Two other smaller airglow enhancements are detected on the west half of the image.

Each of the 630.0 nm images of Figure 3 was processed by removing the average value of all pixels within the imager field of view and normalizing the intensity with respect to the image σ value. To avoid systematic effects a constant σ value equal to 80 Rayleighs was employed to normalize the images presented in Figures 3 and 4. Three contour levels serve to indicate the locations where airglow intensities reach the relative levels of 50 R (blue), 80 R (green), and 110 R (blue) values. Note also that the contour levels have been restricted to elevations larger than 20°. The image sequence of Figure 3 shows several polar cap patches with non-typical morphological characteristics. It displays the "appearance" of new patches, and sudden changes of the patch brightness that have never been reported before. The first image of the sequence (2023:03 UT) trails by 2 minutes image (b) of Figure 2. This image shows that the north-south elongated patch has drifted eastward and is now located ~200 km east of zenith. Two additional patches are also present in this image: (1) A small patch placed in the northern side adjacent to the elongated patch, and (2) a bright east-west segment located near the southern edge of the arc. The subsequent 3 images (2025 – 2029 UT) show the elongated eastern patch moving antisunward (eastward) and its width decreasing accordingly as it moves toward lower elevation viewing angles that have coarser spatial resolution. Images recorded between 2023 and 2047 UT display the growth, brightening and exit of the northern small patch as it transits across the imager field of view. As time progresses, the small northern patch is seen to extend further south and occupy a much larger area

75

(2035 UT), then move continuously toward the east, and reach the eastern edge of the imager (2047 UT). It is important to note, as it is demonstrated below, that during this time the SuperDARN convection velocity was directed antisunward (eastward). Nevertheless, the patch growth was in the southward direction. The images of 2037:03 and 2039:03 UT show the appearance and brightening of a "new" patch that intensifies near the western side of the patch that developed minutes before. Two additional observations endorse our hypothesis that the 630.0 nm emissions detected overhead the station at 2037 UT correspond in fact to a polar cap patch: (1) Before the appearance of the "new" patch, very faint emissions were observed close to where the patch develops (see image for 2035 UT). (2) The lower frame of Figure 1 indicated that at 2035 UT the F-region peak was descending and the lower part of the F-region bottomside decreased from 280 to 240 km altitude just before 2035 UT. Another faint patch is observed to brighten from 2051:03 to 2053:03 UT as the southern end of the eastward convecting patch seems to rotate clockwise.

Figure 4 shows a sequence of 16 images in which the patches display non-typical configurations. Here, we present break off events, circular patches, and others elongated in the sunward-antisunward direction. At 2127 UT an L-shaped patch is observed at Qaanaaq at times when the digisonde density profiles indicate pronounced variations in altitude. Opposite ends of the patch seem to be moving in opposite directions as the lower branch drifts eastward and the north-south aligned side intensifies and recedes westward. The images of 2129 and 2131 UT provide evidence for the lower side to continue drifting eastward, becoming a small rounded structure and then breaking off from the westward patch. After the small structure gets disconnected, the newly-formed patch rapidly moves to the edge of the imager field of view (2137 UT). Simultaneously, the northern part of the patch continues moving westward and shows a series of transformations that last for tens of minutes. At 2135 UT the patch widens and brightens, then becomes well elongated (2143 UT), later dims and becomes much thinner (2149 UT), and finally widens again and drifts toward the east side of the imager (2157 UT). Another series of polar cap patches (not shown here) was detected by the imager between 2209 and 2239 UT, along with a string of faint patches near the end of the observing period (2329 and 2359 UT).

3.3. Sondrestrom Densities

On November 20, 2003 the Sondrestrom radar conducted a series of composite scans along two parallel planes. The AZ and EL angles for both composite scans were properly selected to keep a constant height line almost parallel to the magnetic meridian (-27° from geographic north). Figure 5 presents the electron number density and the line-of-sight velocities collected during two consecutive scans corresponding to the periods of 200156-200504 and 200857-201205 UT. In this figure the density contours have been projected to a plane in which the vertical axis is the true height and the horizontal line is the north-south distance along the geographic meridian. The spacing between density contours is constant with the initial value and the spacing between consecutive levels both equal to 10^5 cm^{-3}. Figure 6 shows the ground projection (green line with dots) of the 300 and 500 km constant altitude for both scans. Note that the top frame corresponds to the western scan and the bottom panel shows measurements conducted during the eastern scan. Due to the nature of the composite scans the spatial (latitudinal) and height variability of the density are intermixed. However, the main features of the polar cap patches can be recovered based on the main property of the patches extending for hundreds of km. The western scan shows a patch with a peak number density almost equal to 10^6 cm^{-3} at 450 km altitude. This patch is placed between 0 and 400 km to the north and extends up to 850 km altitude. The eastern scan, conducted 7 min later, displays two density enhancements. The patch closer to the radar site has a peak value near 7×10^5 cm^{-3} at 500 km altitude and resides ~300 km north from the radar site. The second patch is seen in the northern part of the eastern scan containing densities near 10^6 cm^{-3} at 700 km north of the Sondrestrom site extending further north toward the direction of Qaanaaq. Figure 5 also shows the line-of-sight velocities using blue (toward the radar) and red (away) arrows of different lengths according to the magnitude of the plasma velocity. The fact that the velocities are all blue (toward) in the west scan and all red (away) in the east scan indicates that the plasma velocity was mainly directed toward magnetic

east and closely parallel to the boundary of the auroral oval and the polar cap. This interpretation is based on the nature of the composite scans in which the radar antenna is directed toward the west on the western scan and point toward the east on the eastern scan.

Figure 6 shows again some of the density contours presented in Figure 5, but here the contour lines have been projected to a ground plane. The contours corresponding to 5×10^5 and 10^6 cm^{-3} indicate that the radar bisected the patch, measuring the cross section of a long and east-west elongated patch. Figure 6 also includes the 630.0 nm emissions measured by the Qaanaaq imager, and the DMSP-F13 satellite trajectory (red line) mapped along the B lines from 850 km altitude to the F region and then projected to the ground plane. The right panel shows in-situ densities measured by the DMSP satellite and plotted according to the satellite trajectory as the satellite moved along in the geographic plot. Four density enhancements are displayed in the right frame clearly corresponding to the ISR density and airglow enhancements that were observed at Sondrestrom and Qaanaaq respectively. Notice that the DMSP intersected the Sondrestrom east scan at 2006 UT and later the Qaanaaq imager at 2008 UT. It is evident that the first patch detected by DMSP-F13 at 2006:10 UT corresponds to the density enhancement observed 350 km north and during the radar scan of 2008:57 UT. The DMSP density enhancement of 2007:20 UT is probably related to the density enhancement seen 700 km north of the radar site. And, the long density enhancement of 2008:30 UT is associated with the airglow enhancement seen by the imager. A fourth patch detected by the DMSP satellite was almost outside and northward of the field-of-view of the Qaanaaq imager.

3.4. DMSP Measurements

Figure 7 shows several parameters measured during the dusk-to-dawn DMSP-F13 pass whose trajectory is displayed on Figure 6. The top panel shows the four density enhancements that were mentioned above and were measured in the dusk side of the polar cap. A fifth density enhancement is seen in the dawn side of the polar cap at 2012:10 UT presenting a factor of 2 enhancement ratio. The dusk poleward boundary of the ion and electron precipitation are seen near 72° magnetic latitude at 2005 UT marking the boundary of the auroral oval and the polar cap regions. Figure 6 suggests that this boundary (see DMSP trajectory at 2005 UT) is placed about 200 km south of the radar site and clearly equatorward of the density enhancements detected by the IS radar. The DMSP drift velocities reverse from a sunward to an antisunward direction in a region equatorward of the particle boundary and are clearly antisunward within the polar cap. *Foster et al.* [2005] presented in-situ measurements spanning 1814 – 1844 UT collected by the DMSP D13 satellite on November 20, 2003. They indicated that during the main phase of the geomagnetic storm the oval boundary was placed at even lower latitudes. The DMSP data provide conclusive evidence for the presence and transit across the polar cap of the density and airglow enhancements that were observed at Qaanaaq and Sondrestrom.

4. PATCH DRIFT VELOCITIES

We calculated the drift velocity of the polar cap patches by using an algorithm based on a 2-D cross correlation analysis of two consecutive images. We have validated our results comparing the magnitude and direction of the velocities with the SuperDARN potential patterns downloaded from the JHU/APL web site. We recognize that when computing the patch velocity, it is necessary to overcome changes of the patch shape that may be occurring constantly due to actual changes of the plasma density distribution produced by nonuniform plasma flows, large-scale instability processes or even changes in the altitude of the F region due to vertical winds associated with atmospheric gravity waves.

Earlier estimations of the patch drift velocities using 630.0 nm images indicated very good agreement between the patch velocities and plasma drifts measured by a digisonde [*Fukui et al.*, 1994]. More recently, an automated estimation of the patch drift velocity conducted by *Hosokawa et al.*, [2006] has reproduced the close control of the IMF B_z component on the magnitude of the patch motion, and the B_y dependence on the direction of the patch drift. *Fukui et al.* [1994] derived the patch drift velocities by

tracking the location of the patch center of gravity. In general, the magnitude of the patch drift and the digisonde plasma drifts followed each other well, with differences rarely larger than 20%. These authors determined that the patch velocity did not deviate from the antisunward direction more that 150 m/s during the transit of 43 patches. *Hosokawa et al.* [2006] analysis consisted of a 2-D cross-correlation algorithm employing grids of 80×80 pixels to make precise estimations of the speed and direction of the polar cap patches.

Our algorithm is similar to the method employed by *Hosokawa et al.* [2006], but rather our grid size is equal to 32×32 pixels. By making the grid size smaller than the typical patch extension, we allow for multiple drift vector derivations within a single patch. This method takes advantage of the spatial structures and gradients within and at boundaries of the polar cap patches that remain coherent between consecutive images. We have restricted the drift calculations for cases when the enhancements occur above 30° elevation and consider a reliable estimation of the patch drift when the correlation factor is above 0.95. Figure 8 shows the 630.0 nm image and the patch drifts corresponding to 2037:03 UT displayed in a geographic (left panel) and Corrected Geomagnetic coordinate systems (right panel). The left frame shows the patch vectors directed eastward that are transformed into nearly antisunward directed vectors when they are displayed in a CG coordinate system. The average magnitude of the vector amplitudes is ~630 m/s. This frame also includes the SuperDARN potential pattern corresponding to 2030 UT and for latitudes poleward of 80°. Close comparison between the direction of the patch vectors and the SuperDARN flows indicate an additional constant 25° clockwise rotation of the patch vectors. Nevertheless, it is seen that the SuperDARN flows also rotate about 25° just outside the imager field of view at later CG local times. Figure 9 shows 4 images, the SuperDARN patterns, and the patch vectors superimposed in CG systems. These frames display the variability of the magnitude of the patch vectors that have average values of 560, 600, 730, and 460 m/s. Very good agreement between the vector directions and the SuperDARN contours is seen especially in the last two frames. The sudden decrease of the magnitude of the patch vector in the last frame is also reflected by the SuperDARN pattern as an increase in the separation of the potential contours. Between 2049:03 and 2053:03 UT, the patch vectors rotate about 45° in a counter-clockwise direction when the SuperDARN potentials show a similar variability. We believe that the magnitude and direction of the patch velocities derived here are in excellent agreement with the convection velocities provided by the SuperDARN radars. We have also observed that on several occasions, when the altitude of the bottomside F region is varying, the correlation factor diminishes and the calculated velocities lack spatial coherence.

5. THE TRAJECTORY ANALYSIS TECHNIQUE

Trajectory analysis is a numerical technique that consists of transporting, backward or forward in time, the ground location of quasi-vertical field lines based on the best estimate of the ionospheric E×B velocity field [*Crowley et al.*, 2000]. No calculation of the ionospheric density within the flux tube is conducted. *Bust and Crowley* [2007] used a trajectory analysis based on maps of ionospheric convection, obtained from the assimilative Mapping of Ionospheric Electrodynamics (AMIE), to indicate that some of the patches detected by the EISCAT Svalbard radar on 12 December 2001 formed part of the TOI. Bust and Crowley's trajectory analysis demonstrated that the patches originated in several different locations either in the morningside or afternoon sectors at geographic latitudes near 60–70°. They also indicated that no patch was formed at mid latitudes and conceded that the resolution of the technique limited them on identifying the patch formation mechanism.

We have used a similar trajectory analysis technique to step backward in time the location of the patches observed at Qaanaaq to times when they were formed and then we inspect the characteristics of the SuperDARN velocities at these new locations. Our trajectory analysis is similar to the technique described by *Bust and Crowley* [2007], but uses the SuperDARN convection patterns to provide the drift velocities. In this paper, we present two events. The first trajectory analysis starts with the precise location of patch boundaries calculated by the image contouring program and back traces the patch locations until it reaches times when the patches are entering the polar cap. We have used the contours

corresponding to 80 Rayleighs airglow enhancements to define the patch boundaries (green traces in Figures 3 and 4). It is also the goal of the trajectory analysis technique to inspect the characteristics of the velocities and the nature of the coherent echoes recorded by the SuperDARN radars at the time and location where the polar cap patches were formed. The second trajectory analysis relies on inputs provided simultaneously by the Qaanaaq imager, the Sondrestrom ISR, and the DMSP satellite to characterize all the patches that were transiting the polar cap across the 0600–1800 magnetic local time line near 2009 UT.

5.1. Trajectory Analysis of 630.0 nm Airglow Patches

Figure 10 shows the results of a trajectory analysis in which the images of 2041:03, 2101:03, and 2129:03 UT, were used to define 2-D maps of the patch boundaries. The top frames of Figure 10 show the location of the patches at two instances separated by ten minutes displayed in a Corrected Geomagnetic coordinate system. The lower panels show the location of the same patches in a geographic frame. The patches elongate and stretch as they turn from the afternoon cell into the polar cap. Several important facts are evident: (1) the red and blue patches seem to be part of a much longer and elongated TOI that seems to be broken up in two smaller pieces. (2) The patches originate from the afternoon sector and may be connected to the SED presented by *Foster et al.* [2005] that originated at mid latitudes. (3) The patches were probably formed between 1941 and 1951 UT when a sector of the TOI was crossing near the cusp region. The ground projection of the patches indicates that they entered the polar cap near Hudson Bay, Canada at ~1941 UT.

Figure 11 shows the line-of-sight velocity measured by the Kapuskasing radar for the periods of 1940–1941:32 and 1942–1943:32 UT on November 20, 2003. Both panels indicate the presence of velocities directed poleward (antisunward) at all locations over Hudson Bay (yellow traces). The important feature in these two plots is the small channel of enhanced velocities (~1.7 km/s, green) seen near the center of the radar scan. The left frame shows the velocity channel to be below 70°, and to coincide with the location of the gap that is observed between the patches of Figure 10. The next frame, starting at 1942 UT, displays a much longer and slightly wider channel that is placed close to the region between the red and blue patches. We also inspected the velocities from the adjacent frames to conclude that the channel of large velocities was restricted to three (~6 min) consecutive scans. It decayed before 1946 UT. Figures 10 and 11 provide evidence for a channel of large flows, a plasma jet [*Rodger et al.,* 1994; *Valladares et al.,* 1994] to split the TOI and form two smaller discrete entities. The magnitude of the plasma jet is smaller than the value reported by *Valladares et al.* [1994]; however, 1.7 km/s velocities should be able to form a channel of reduced densities and more efficiently if the direction of the velocity has a small divergent component. It is important to mention that another patch, although very faint, was observed at 2111 UT. In the discussion section, we elaborate on the causes of the high variability of the patch airglow intensity that was observed on November 20, 2003 during one of the strongest geomagnetic storms of the solar cycle.

5.2. Trajectory Analysis of Polar Cap Patches Observed Near 2009 UT

Each frame of Figure 12 depicts the time evolution of the four patches seen by the DMSP-F13 satellite near 2009 UT. The outline of the patch detected by the Qaanaaq imager at 2009 UT is displayed in red; the 5×10^5 cm^{-3} density enhancements seen during the west (east) scan of the Sondrestrom ISR are in blue (green), and a circular representation of the 4th and larger patch observed by the DMSP-F13 satellite is in black. The in-situ DMSP data indicated that this patch extended at least for 600 km (see Figure 6), but it was not completely imaged at Qaanaaq as it was situated further dawnward and practically outside the imager FOV. Figure 6 suggested that the two patches seen closer to the oval-polar cap boundary and represented here by a blue and a green contour correspond to the same patch that was noon-midnight elongated and placed almost parallel to polar cap boundary. Radar scans performed by the Sondrestrom ISR before and after the scans of Figure 5 indicated that this patch was continuously moving

equatorward and toward the auroral oval at 15 km/min. The SuperDARN convection patterns indicated the existence of a small duskward velocity component near the patch location at 1949 UT. When the patch reached the location of the Sondrestrom site at 2026 UT, the antenna was in an up-B dwell configuration and able to detect a peak density enhancement close to 10^6 cm^{-3}. The patch that was observed during the eastern scan of Figures 5, placed further north, is also partially displayed in each of the frames of Figure 12 and likely corresponds to a second patch that is aligned parallel to the polar cap boundary. The sequence of snapshots suggests that these two patches, which are located near the polar cap boundary, may have had a common origin. It is also indicated that these two patches may have been circulating along the afternoon cell, which at this time was more rounded, did not extend to late local times, and closed at magnetic latitudes as low as 60°. The other two patches presented much larger sizes, reached the center of the polar cap and according to the trajectory analysis originated at lower latitudes. The trajectory analysis suggests that these two patches were indeed part of the TOI and entered the polar cap between 1919 and 1929 UT.

6. MODELING

We have used the Global Theoretical Ionospheric Model (GTIM) of the high latitude ionosphere (GTIM) to investigate the effect that a vertical wind associated with a propagating gravity wave has on the amount of airglow emissions. GTIM is based in the numerical code initially developed by *Anderson* [1971, 1973] for the low-latitude ionosphere. This model was later extended to include several physical process of the high-latitude ionosphere and was used to correctly simulate the effect on the TOI density produced by a variable polar cap size [*Anderson et al.*, 1988]. GTIM has also reproduced highly structured densities as observed at Sondrestrom, Greenland [*Decker et al.*, 1994], defined the role of large plasma jets and traveling vortices on patch formation [*Valladares et al.*, 1996], and modeled boundary blobs [*Anderson et al.*, 1996]. The GTIM model is a 1-D high-latitude ionospheric model that calculates the ion density by numerically solving the time-dependent O^+ continuity equation. The model includes the effect of ionization by solar EUV radiation and electron precipitation loss through charge exchange with N_2 and O_2 transport by diffusion, neutral winds, and ExB convection drifts. The model solves the continuity equation along a fluxtube defining all the quantities in a direction parallel to B. The MSIS and Hedin's wind models supply neutral densities and winds, respectively; an option to specify a value for the vertical wind was added to see its effect on model profiles. We also modified the GTIM model by including a parameterized model of soft electron precipitation, a calculation of the ExB plasma drift based upon the SuperDARN convection patterns, and a first-order approximation of the NO^+ density based on chemical equilibrium. For this study, SuperDARN data at 10-minute intervals provided the electric potentials needed to trace convection paths. Figure 13 shows paths lasting 80 minutes that lead to the vicinity of the Qaanaaq site at 5 minute intervals from 2000 to 2055 UT on November 20, 2003. The trajectory analysis algorithm is quite similar to the one used in section 5, but here the progression is forward in time. Convection paths ending at 2000 - 2040 UT originated between 12 and 14 LT near 63° CGLAT; paths ending after 2040 LT started later in the afternoon near 60° CGLAT. The initial density profile that was used in all the simulation events correspond to the Millstone Hill (53° CGLAT) observations reported by *Foster et al.* [2005]. This initial vertical density profile was measured near the cusp region at 1730 UT (their Figure 8) and characterized the SED/TOI plasma containing densities above 10^6 cm^{-3} near 500 km altitude. Although the path calculation is restricted to the limits of the SuperDARN data (60° - 90° CGLAT), this initial profile is probably a reasonable one given the overall magnetic storm condition and the fact that we are not trying to closely reproduce the densities observed at Qaanaaq, but to study the effect that a vertical wind makes on the emission rates associated with patch (or TOI) densities. However, we noticed that doubling the amount of atomic oxygen provided by the MSIS model increased the F-region peak altitude to values closer to the values measured by the Qaanaaq digisonde.

Johnson et al. [1995] presented Dynamic Explorer-2 observations of neutrals and ions showing distinct vertical velocity distributions. These were interpreted as gravity waves propagating in the neutral

atmosphere. These disturbances were characterized by vertical velocities perturbations of the order of 100 m/s and horizontal wavelengths along the satellite path of ~ 500 km. The profiles of Figure 14 were calculated assuming a 75 m/s downward vertical neutral wind that last between 2000 and 2040 UT. This wind produces a downward component parallel to the nearly vertical magnetic field lines and causes the profile peak to descend from 460 km to 400 km at 2040 UT. Note also that the number density at 300 km altitude increases from 10^4 to 10^5 cm^{-3} and the shape of the F-region bottomside varies when the vertical wind is applied. These profiles were used to estimate the 630.0 nm column emission rate, J_{6300}, in Rayleighs due to dissociative recombination using the expression (1) derived by *Tinsley and Bittencourt* [1975].

$$J_{6300} = \int \frac{A_{6300} \gamma_1 n(O_2) n(O^+) \, dz}{A(1 + d(z)/A)}$$

(1)

Where γ_1 is the O$^+$ and O$_2$ rate coefficient, A is the radiative transition coefficient for the ^{1}D term, and $d(z)$ is the quenching frequency given by:

$$d(z) = S_{N_2} n(N_2) + S_e n(e)$$

(2)

S_{N_2} and S_e are the quenching coefficients for quenching on N$_2$ and electrons, respectively.

Figure 15 shows the count rate as a function of time calculated using expressions (1) and (2) and the density profiles of Figure 14. A maximum increase equal to 450 Rayleighs was obtained during the time the peak altitude lowered and the peak density nearly doubled. When no vertical neutral wind was applied the emission rate stayed nearly constant at 200 Rayleighs. The calculated 630.0 nm airglow emission increase is much higher than the ~160 R that was measured within the patches. This discrepancy may be produced by several factors such as the initial density profile, the O/N$_2$ ratio and the value of the vertical wind.

7. DISCUSSION

We have presented a comprehensive description of the measurements and analysis of the polar cap patches that developed during the recovery phase of the November 20, 2003 magnetic storm. The imager and digisonde that operate at Qaanaaq, the Sondrestrom IS radar, the SuperDARN radars, and the DMSP F13 satellite provided time-continuous observations of their dynamics and structuring. We have also applied a trajectory analysis technique, a 2-D cross-correlation algorithm, and modified the GTIM model of the high-latitude ionosphere to investigate the formation mechanism of polar cap patches and the effect that a vertical neutral wind produces on the patch airglow intensity. We believe that several aspects of the polar ionosphere during these extreme conditions have a pronounced effect, as discussed below, on the dynamics of the polar cap patches, their evolution, their airglow intensity and the level of structuring that was observed on that day.

Before discussing in detail the origin and development of the polar cap patches of November 20, 2003, we review several aspects of the polar ionosphere during major magnetic storms. On these occasions, the TOI becomes a dense stream of cold plasma that has a source in the SED density transported from much lower latitudes by the SAPS electric field [*Foster et al.,* 2005]; there exists severe disruptions of the thermosphere composition as regions of depleted O/N$_2$ ratios extend from high latitudes to the equator [*Meier et al.,* 2005; *Crowley et al.,* 2006]; at the same time large-scale internal gravity waves propagate from the nightside to the dayside [*Johnson et al.,* 1995]; and there is a penetration of the interplanetary electric field reaching the equatorial ionosphere.

The relationship that we observed on November 20, 2003 between enhanced patch densities, airglow, and UHF scintillations was largely unexpected. Early observations of the scintillations associated with polar cap patches have pointed out that the gradient drift instability (GDI) is responsible for the onset of km-scale irregularities [*Weber et al.,* 1986; *Basu et al.,* 1988]. While the linear GDI is

only unstable on the trailing edge of the patch, in the non-linear regimen GDI predicts structures that propagate from the unstable edge, through the patch and reach the stable edge [*Gondarenko et al.,* 2003; *Gondarenko and Guzdar,* 2004]. Similarly, if a velocity reversal or plasma stirring occurs along the patch trajectory then other sides of the patch could develop plasma structures. In fact, in-situ measurements have revealed the existence of 4 groups of patches containing different structuring characteristics: (1) fully structured patches, (2) structures only on the edges, (3) only one structured edge, and (4) unstructured patches [*Kivanc and Heelis,* 1997]. Some of the large S4 values follow predictions of the classical GDI mechanism, others do not. For example, the density spikes of Figure 1c seen at 2033 and 2057 UT have corresponding high airglow enhancements and significant levels (>0.7) of UHF scintillations. They seem to be the response of the GDI due to steep horizontal gradients (Figure 1d). It is noted that when comparing the peak density trace and the S4 index (Figure 1b), it is necessary to consider a small time lag due to the offset of the scintillations sub-ionospheric penetration point and the zenith direction.

A different relationship was observed between 1950 and 2020 UT when the number density was only half (10^6 cm^{-3}) of the density observed at 2033 UT and the scintillation S4 index was saturated. During this period, the F layer was rapidly moving upward and then downward in association with the passage of a GW. It is quite likely that shear instabilities, or E×B turbulence operated in this region in association with the vertical motion of the plasma. We believe that a similar scenario occurred near 2140 UT when the digisonde reported a rapid increase in the F-region altitude in association with the patch break up event of 2131 UT (Figure 4).

Images of the polar cap patches obtained during the major geomagnetic storm have shown several characteristics that have never been documented before. We have presented patch brightenings (2037 UT), a patch break up event (2131 UT), patch fading (2149 UT), and distortions (2127 and 2141 UT). We believe that several aspects of the patch evolution on November 20, 2003 are attributed to the change in altitude of the F region due to the passage of a large-scale gravity wave. These waves have been observed by *Johnson et al.* [1995] (W.B. Hanson personal communication, 1993) during magnetically disturbed periods. However, the break up event of 2131 UT and the sudden increase of the S4 values that occurred a few minutes later could only be explained if a region containing large flow develops inside the polar cap. We have no direct proof that such a large flow existed, only a suggestion made by the Super DARN and Sondrestrom radars that measured large southward plasma drifts, several hundred km to the south of the Qaanaaq site.

We conducted numerical simulations of the polar ionosphere incorporating into the 1-D equation of continuity and momentum a vertical thermospheric wind. A 75 m/s downward wind was applied for 40 minutes to mimic the behavior of the gravity wave passing above the station. We selected a 40 min semi-period of the GW to be in agreement with the variability of the density contours of Figure 1d. We obtained an airglow enhancement near 450 Rayleighs that was about a factor a 2 larger than the airglow brightening of Figure 3. The lowering of the simulated F region (50 km) was also smaller than the actual descent of the h_mF_2 measured by the Qaanaaq digisonde between 2000 and 2040 UT (100 km). The lack of quantitative agreement was probably due to several unknown factors such as the O/N2 ratio, initial density, and value of the downward wind. More precise calculations should consider assimilating the digisonde, airglow images, and a model of the polar ionosphere. We also examined the possibility that the F region height variations were reflecting the passage of a large structure that was modulating the bottomside polar ionosphere and was frozen in space. The fact that the patch airglow intensity increased by ~150 R between 2035 and 2043 UT (see Figure 3) does not support this contention.

This is the first time that the trajectory analysis has been applied to images from a polar cap station to investigate the origin and the formation mechanism of polar cap patches. *Bust and Crowley,* [2007] backtracked observations from the EISCAT Svalbard radar to conclude that some of the patch density had originated in the morning side. *MacDougall and Jayachandran* [2007] also suggested that the origin of the patches observed inside the polar cap could be in the dawn cell. Our trajectory analysis helps us to conclude that the majority of the patches observed on November 20, 2003 – during a major magnetic storm – were originated in the TOI, transported into the polar cap by the polar convection, and formed

(broken up) by processes related to the cusp electrodynamics. Two consecutive scans conducted by the Kapuskasing radar have indicated the existence of a channel containing a flow near 1.7 km/s that coincides, considering a small offset due to uncertainties of the trajectory analysis, with the region that is in between the patches. We imply that at 1941 UT a continuous TOI was about to enter the polar cap when a narrow channel of 1.7 km/s velocities, which probably was originated in association with the cusp, increased the Joule heating, the ion temperature, and the O^+ recombination rate. The temporal and spatial collocation between the large flow and the patch gap imply a relationship between these two structures and confirms that the patches of 1941 UT (Figure 10) were formed by the large plasma jet mechanism. The Qaanaaq images support the idea that the TOI presented by *Foster et al.* [2005] is not continuous inside the polar cap, but becomes segmented in a series of polar cap patches. We also indicate that the patches, detected by the Sondrestrom radar close but poleward of the polar cap boundary, were probably continuously circulating along a reduced dusk cell. The SuperDARN patterns of Figures 10 and 12 show that in fact between 1850 and 2010 UT the dusk cell is much smaller than the dawn cell and bounded inside the 12–18 LT quadrant. The Sondrestrom composite scans suggest that the density enhancement seen 150 north (west scan) and 300 km north (east scan) belong to the same patch that is aligned in the magnetic east west direction and extends for hundreds of km. A second patch, partially shown in Figure 5b, is located ~700 km north of the site. This patch is probably east-west aligned and largely elongated as the previous patch. The trajectory analysis (Figure 12) indicated that the latter two patches merge into a single patch near 1850 UT, but they keep a constant separation of a few degrees with respect to the TOI. We believe that the elongated patch is probably the result of a patch (or auroral blob) that entered and exited the polar cap at much earlier times and was trapped in the dusk cell.

We have used 630.0 nm images of polar cap patches and the principle that polar cap patches drift almost unchanged with the background E×B convection to derive the magnitude and direction of the underlying convection. We obtained vector velocities which were in very good agreement with measured SuperDARN drifts when the altitude of the F region was constant. We concluded that under normal conditions (no large-scale gravity waves) these velocities could be assimilated to increase radar coverage in regions where it is limited.

8. CONCLUSIONS

This study has led to the following:

(1) Polar cap patches observed during the geomagnetic storm of November 20, 2003 present characteristics different than patches seen under normal conditions. We found patches with non-typical shapes, striking variable airglow intensities, saturated S4 values, and even patch break up events occurring well inside the polar cap.

(2) The development of a trajectory analysis algorithm allows us to investigate the origin of the polar cap patches. We concluded that most of the patches originated from the TOI discussed by *Foster et al.* [2005]. Others were confined to circulate along a reduced dusk cell.

(3) Continuous routine measurements conducted by the SuperDARN radars, the imager, and the digisonde at Qaanaaq have provided conclusive evidence for a narrow channel of enhanced velocities (>1.7 km/s), a plasma jet, to be the formation mechanism of some of the patches observed at Qaanaaq on November 20, 2003. These types of measurements should be able to provide the statistics of the different mechanisms that can produce polar cap patches.

(4) The GTIM code was modified to accept Super DARN derived polar convection patterns and a variable value of the vertical component of the thermospheric wind. We were able to corroborate that a 75 m/s downward vertical wind acting on a field line for 40 min could produce a substantial increase (450 R) of the airglow emissions.

(5) A new method to calculate plasma drift velocity has been developed that uses a 2-D cross correlation algorithm based on the property of the patches to drift with the background polar cap convection. The Super DARN polar convection was used to validate our results and to demonstrate the usefulness of this technique for cases when the altitude of the F layer is constant.

(6) The algorithms developed in this study can be applied to other events to study patch formation mechanisms when the ionosphere is in non-storm conditions.

REFERENCES

Anderson D. N., Daily variation of the ionospheric F2 equatorial anomaly in the American and Asian sectors, cooperative thesis, 24pp. 1-144, *Natl. Cent. Atmos. Res.*, Boulder, Colo., 1971.

Anderson D. N., A theoretical study of the ionospheric F region equatorial anomaly, 1, Theory, *Planet. Space Sci.*, 21, 409, 1973.

Anderson, D.N., J. Buchau, and R.A. Heelis, Origin of density enhancements in the winter polar cap, *Radio Sci.*, 23, 513, 1988.

Anderson, D., D. Decker, and C. Valladares (1996), Modeling Boundary Blobs Using Time Varying Convection, *Geophys. Res. Lett.*, 23(5), 579-582.

Basu, Su. and C. E. Valladares, Global aspects of plasma structures, *J. of Atmos. and Solar-Terr. Phys.*, 61, 127-139, 1999.

Basu, Su., S. Basu, E. MacKenzie, P.F. Fougere, W.R. Coley, N.C. Maynard, J.D. Winningham, M. Sugiura, W.B. Hanson, and W.R. Hoegy, Simultaneous density and electric field fluctuation spectra associated with velocity shears in the auroral oval., *J. Geophys. Res.*, 93, 115, 1988.

Basu, S., E. J. Weber, T. W. Bullett, M. J. Keskinen, E. MacKenzie, P. Doherty, R. Sheehan, H. Kuenzler, P. Ning, and J. Bongiolatti (1998), Characteristics of plasma structuring in the cusp/cleft region at Svalbard, *Radio Sci.*, 33(6), 1885–1899.

Basu S., Su. Basu, F. J. Rich, K. M. Groves, E. MacKenzie, C. Coker, Y. Sahai, P. R. Fagundes, F. Becker-Guedes (2007), Response of the equatorial ionosphere at dusk to penetration electric fields during intense magnetic storms, *J. Geophys. Res.*, 112, A08308, doi:10.1029/2006JA012192.

Buchau, J., B.W. Reinisch, E.J. Weber, and J.G. Moore, Structure and dynamics of the winter polar cap F region, *Radio Sci.*, 18, 995, 1983.

Buchau, J., E.J. Weber, D.N. Anderson, H.C. Carlson, Jr., J.G. Moore, B.W. Reinisch, and R.C. Livingston, Ionospheric structures in the polar cap: their origin and relation to 250- Mhz scintillation, *Radio Sci.*, 20, 325, 1985.

Bust G. S., G. Crowley (2007), Tracking of polar cap ionospheric patches using data assimilation, *J. Geophys. Res.*, 112, A05307, doi:10.1029/2005JA011597.

Carlson, H.C., et al., ESR mapping of polar cap patches in the dark cusp, *Geophys. Res. Lett.*, 29 (10),1386, doi:10.1029/2001GL014087, 2002.

Carlson, H. C., Jr., K. Oksavik, J. Moen, and T. Pedersen, Ionospheric patch formation: Direct measurements of the origin of a polar cap patch, *Geophys. Res. Lett.*, 31, L08806, doi:10.1029/2003GL018166, 2004.

Carlson, H. C., J. Moen, K. Oksavik, C. P. Nielsen, I. W. McCrea, T. R. Pedersen, and P. Gallop (2006), Direct observations of injection events of subauroral plasma into the polar cap, *Geophys. Res. Lett.*, 33, L05103, doi:10.1029/2005GL025230.

Coley, W.R., and R.A. Heelis, Seasonal and universal time distributions of patches in the northern and southern polar caps, *J. Geophys. Res.*,103, 29229, 1998.

Crowley, G. (1996), Critical review of ionospheric patches and blobs, in *The Review of Radio Science,* p. 1, Oxford Univ. Press, New York.

Crowley, G., A. J. Ridley, D. Deist, S. Wing, D. J. Knipp, B. A. Emery, J. Foster, R. Heelis, M. Hairston, and B. W. Reinisch (2000), Transformation of high-latitude ionospheric F region patches into blobs during the March 21, 1990, storm, *J. Geophys. Res.*, *105*(A3), 5215–5230.

Crowley, G., et al. (2006), Global thermosphere-ionosphere response to onset of 20 November 2003 magnetic storm, *J. Geophys. Res.*, *111*, A10S18, doi:10.1029/2005JA011518.

Decker, D., C. Valladares, R. Sheehan, S. Basu, D. Anderson, and R. Heelis (1994), Modeling daytime F layer patches over Sondrestrom, *Radio Sci.*, 29(1), 249-268.

Foster, J.C., Storm time plasma transport at middle and high latitudes, *J. Geophys. Res.*, 98, 1675, 1993.

Foster, J., and J. Doupnik (1984), Plasma Convection in the Vicinity of the Dayside Cleft, *J. Geophys. Res.*, 89(A10), 9107-9113.

Foster, J. C. ., and W. J. . Burke (2002), SAPS: A new categorization for sub-auroral electric fields, *Eos Trans. AGU*, *83*(36), 393

Foster J. C., and H. B. Vo, Average characteristics and activity dependence of the subauroral polarization stream, *J. Geophys. Res.*, 107 (A12), 1475, doi:10.1029/2002JA009409, 2002.

Foster J. C., P. J. Erickson, A. J. Coster, J. Goldstein, and F. J. Rich, Ionospheric signatures of plasmaspheric tails, *Geophys. Res. Lett.*, 29 (13), doi:10.1029/2002GL015067, 2002.

Foster, J. C., et al. (2005), Multiradar observations of the polar tongue of ionization, *J. Geophys. Res.*, *110*, A09S31, doi:10.1029/2004JA010928, 2005.

Fukui, K., J. Buchau, and C. E. Valladares (1994), Convection of polar cap patches observed at Qaanaaq, Greenland during the winter of 1989–1990, *Radio Sci.*, *29*(1), 231–248.

Gondarenko N. A., P. N. Guzdar, J. J. Sojka, and M. David, Structuring of high latitude plasma patches with variable drive, *Geophys. Res. Lett.*, 30 (4), 1165, doi:10.1029/2002GL016437, 2003.

Gondarenko N. A., P. N. Guzdar (2004), Density and electric field fluctuations associated with the gradient drift instability in the high-latitude ionosphere, *Geophys. Res. Lett.*, 31, L11802, doi:10.1029/2004GL019703.

Gopalswamy N., S. Yashiro, G. Michalek, H. Xie, R. P. Lepping, R. A. Howard (2005), Solar source of the largest geomagnetic storm of cycle 23, *Geophys. Res. Lett.*, 32, L12S09, doi:10.1029/2004GL021639.

Hosokawa K., K. Shiokawa, Y. Otsuka, A. Nakajima, T. Ogawa, J. D. Kelly (2006), Estimating drift velocity of polar cap patches with all-sky airglow imager at Resolute Bay, Canada, *Geophys. Res. Lett.*, 33, L15111, doi:10.1029/2006GL026916.

Johnson, F., W. Hanson, R. Hodges, W. Coley, G. Carignan, and N. Spencer (1995), Gravity Waves Near 300 km Over the Polar Caps, *J. Geophys. Res.*, 100(A12), 23993-24002.

Kelly, J., and J. Vickrey (1984), F-Region Ionospheric Structure Associated with Antisunward Flow near the Dayside Polar Cusp, *Geophys. Res. Lett.*, 11(9), 907-910.

Kivanç, Ö., and R. Heelis (1997), Structures in ionospheric number density and velocity associated with polar cap ionization patches, *J. Geophys. Res.*, 102(A1), 307-318.

MacDougall J., P. T. Jayachandran (2007), Polar patches: Auroral zone precipitation effects, *J. Geophys. Res.*, 112, A05312, doi:10.1029/2006JA011930.

Meier, R. R., G. Crowley, D. J. Strickland, A. B. Christensen, L. J. Paxton, D. Morrison, and C. L. Hackert (2005), First look at the 20 November 2003 superstorm with TIMED/GUVI: Comparisons with a thermospheric global circulation model, *J. Geophys. Res.*, *110*, A09S41, doi:10.1029/2004JA010990.

Rodger, A.S., M. Pinnock, J.R. Dudeney, K.B. Baker, and R.A. Greenwald, A new mechanism for polar patch formation, *J. Geophys. Res.*, 99, 6425, 1994.

Sojka, J.J., M.D. Bowline, R.W. Schunk, D.T. Decker, C.E. Valladares, R. Sheehan, D.N. Anderson, and R.A. Heelis, Modeling polar cap F region patches using time varying convection, *Geophys. Res. Lett.*, 20, 1783, 1993.

Tinsley, B. A., and J. A. Bittencourt (1975), Determination of F Region Height and Peak Electron Density at Night Using Airglow Emissions from Atomic Oxygen, *J. Geophys. Res.*, *80*(16), 2333-2337.

Tsunoda, R. (1988), High-Latitude F Region Irregularities: A Review and Synthesis, *Rev. Geophys.*, 26(4), 719-760.

Valladares, C.E., Su. Basu, J. Buchau, and E. Friis-Christensen, Experimental evidence for the formation and entry of patches into the polar cap, *Radio Sci.*, 29, 167, 1994.

Valladares, C.E., D.T. Decker, R. Sheehan, and D.N. Anderson, Modeling the formation of polar cap patches using large plasma flows, *Radio Sci.*, 31, 573, 1996.

Valladares, C. E., K. Fukui, R. Sheehan, H. C. Carlson Jr., and T. Bullett (1998), Simultaneous observations of polar cap patches and Sun-aligned arcs during transitions of the IMF, *Radio Sci.*, 33(6), 1829–1845.

Weber, E.J., J. Buchau, J.G. Moore, J.R. Sharber, R.C. Livingston, J.D. Winningham, and B.W. Reinisch, F layer ionization patches in the polar cap, *J. Geophys. Res.*, 89, 1683, 1984.

Weber, E. J., J. A. Klobuchar, J. Buchau, H. C. Carlson Jr., R. C. Livingston, O. de la Beaujardiere, M. McCready, J. G. Moore, and G. J. Bishop (1986), Polar Cap *F* Layer Patches: Structure and Dynamics, *J. Geophys. Res.*, 91(A11), 12,121–12,129.
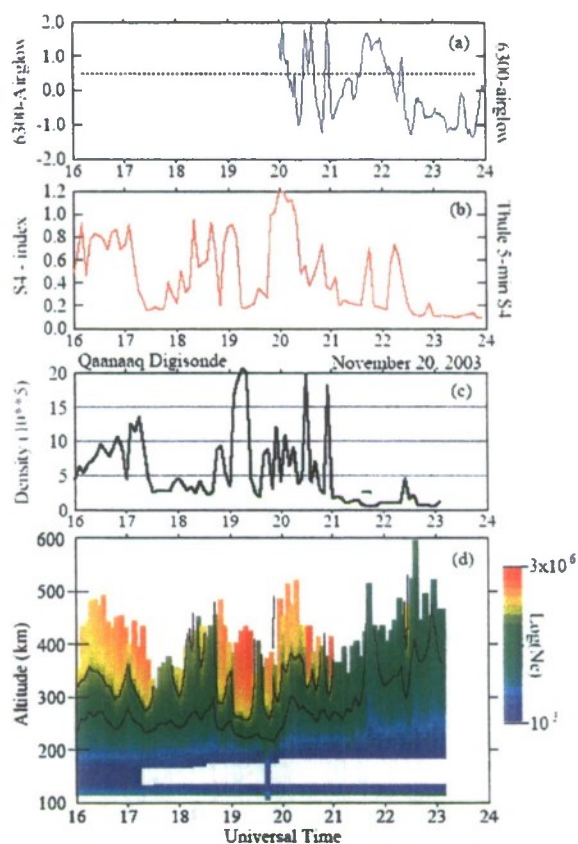
Figure 1. Panels from top to bottom show relative values of 630 nm airglow emissions, UHF S4 scintillation index, peak density measured by the digisonde and color-coded bottomside density profiles.
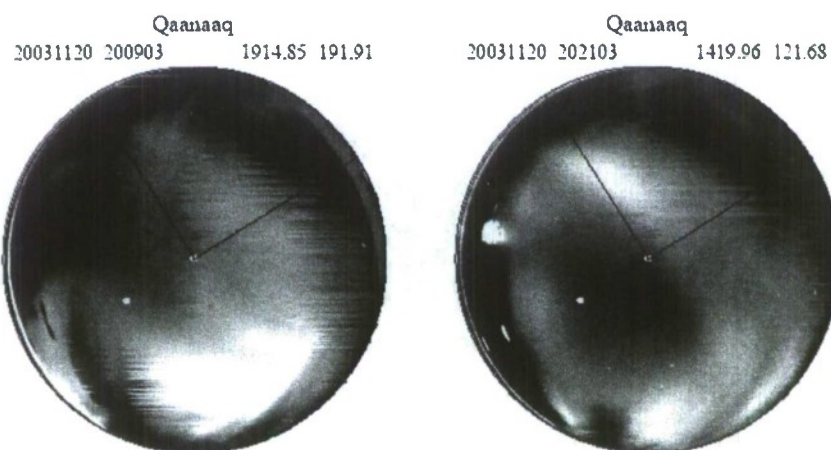
Figure 2. Two 630.0 nm airglow images from Qaanaaq, Greenland observed at 2009 UT and 2021 on November 20, 2003. The white dots correspond to the zenith direction and the sub-ionospheric intersection point of the scintillation system.

87
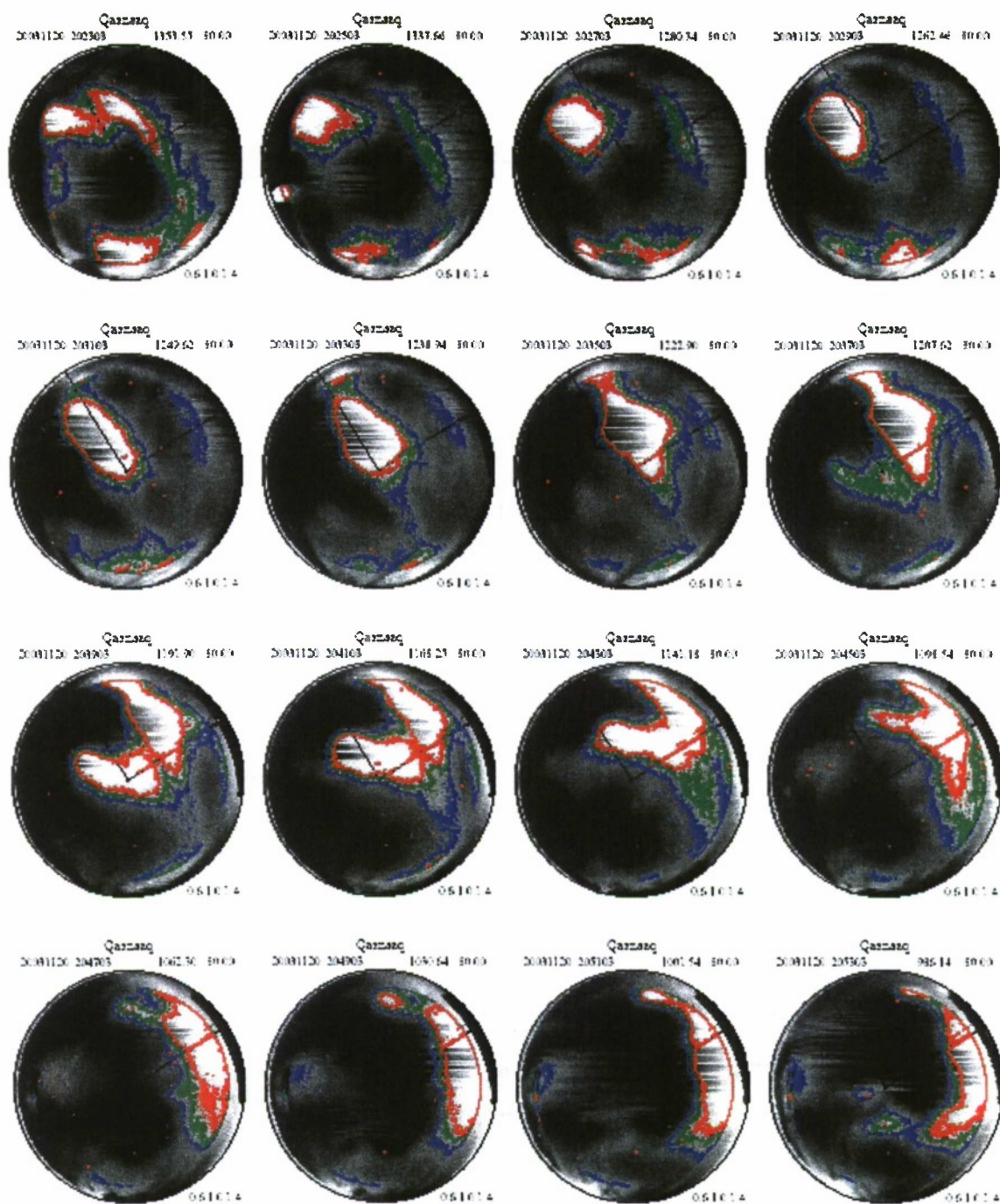
Figure 3. Sequence of images gathered at Qaanaaq, Greenland between 2023 and 2053 UT during the recovery phase of the magnetic storm of November 20, 2003.
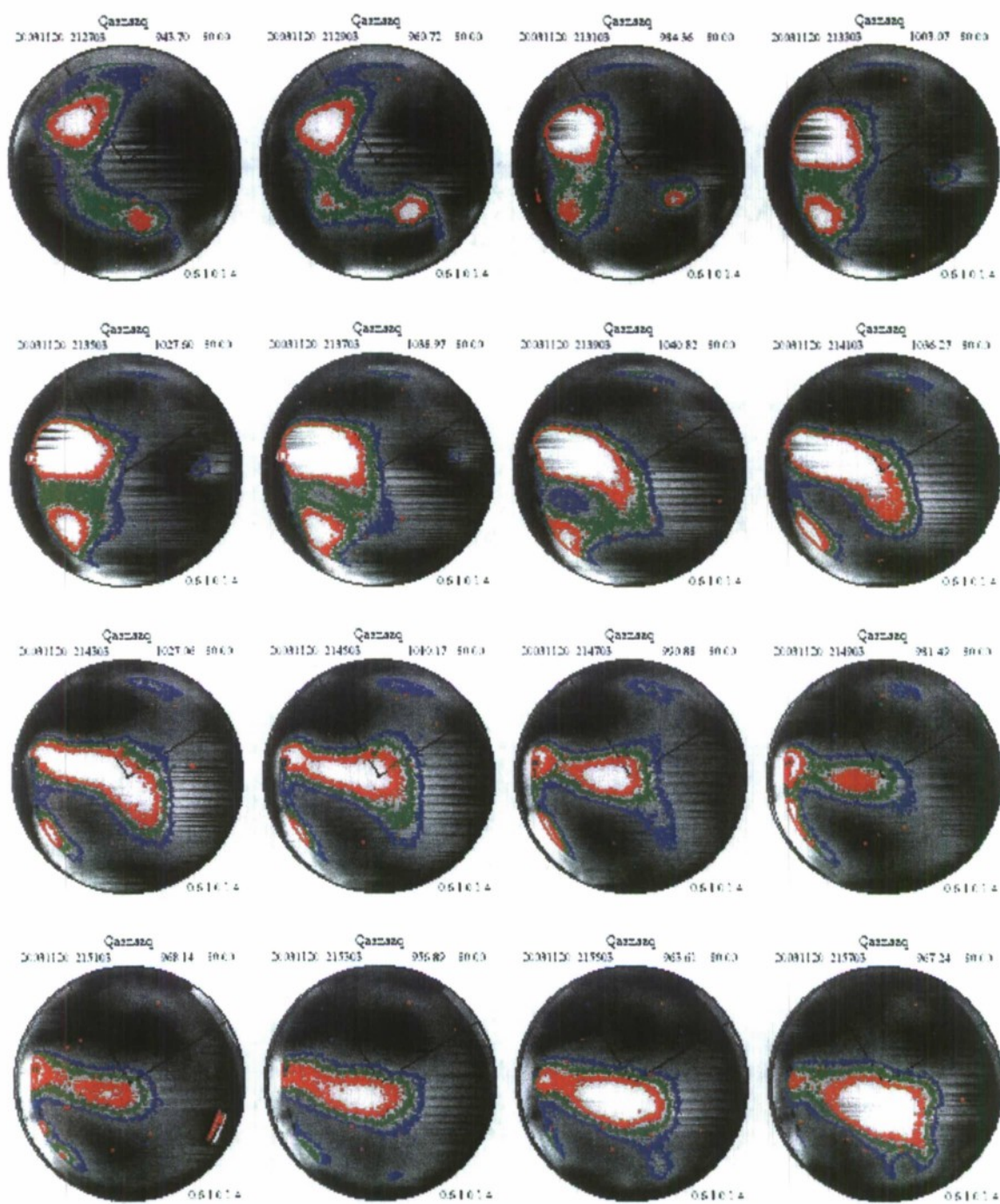
Figure 4. Same as Figure 3 but corresponding to period between 2127 and 2157 UT.
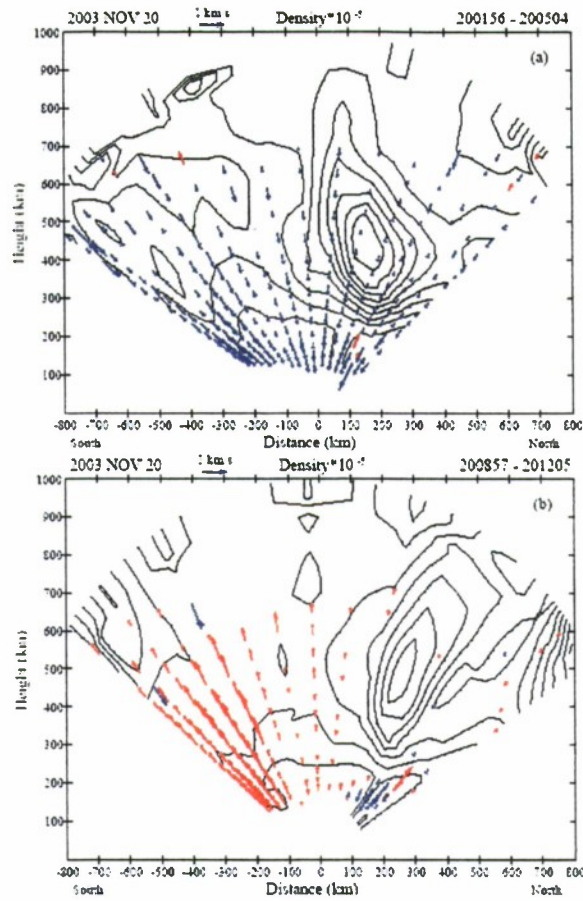
Figure 5. Number density and line-of-sight velocities measured by the Sondrestrom ISR on November 20, 2003, and during the time interval from 2001 and 2012 UT. The radar antenna conducted composite scans in which azimuth and elevation were varied to keep the scan plane almost parallel to the magnetic meridian.
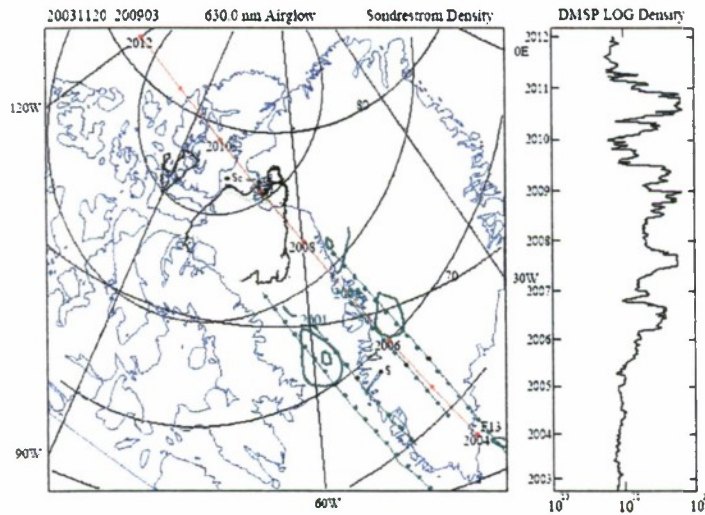
Figure 6. 630.0 nm airglow emissions from Qaanaaq, Greenland observed at 2009 UT on November 20, 2003 projected to 250 km altitude. The trajectory of the DMSP-F13 pass is plotted in red. The red dots indicate the minute at which the satellite passed near Qaanaaq. The density measure by F13 is shown in the right panel. Densities measured by the Sondrestrom radar during two consecutive composite scans are indicated in green.

90
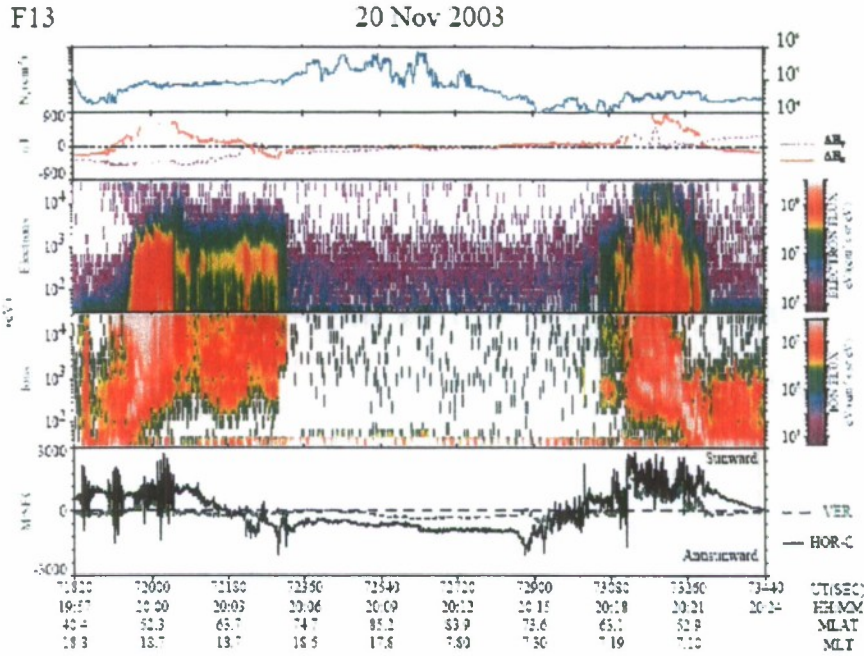
Figure 7. Density, magnetic field, electron and ion fluxes, and drift velocities measured by DMSP-F13 satellite on November 20, 2003. Note the density enhancements observed within the polar cap after 2006 UT.
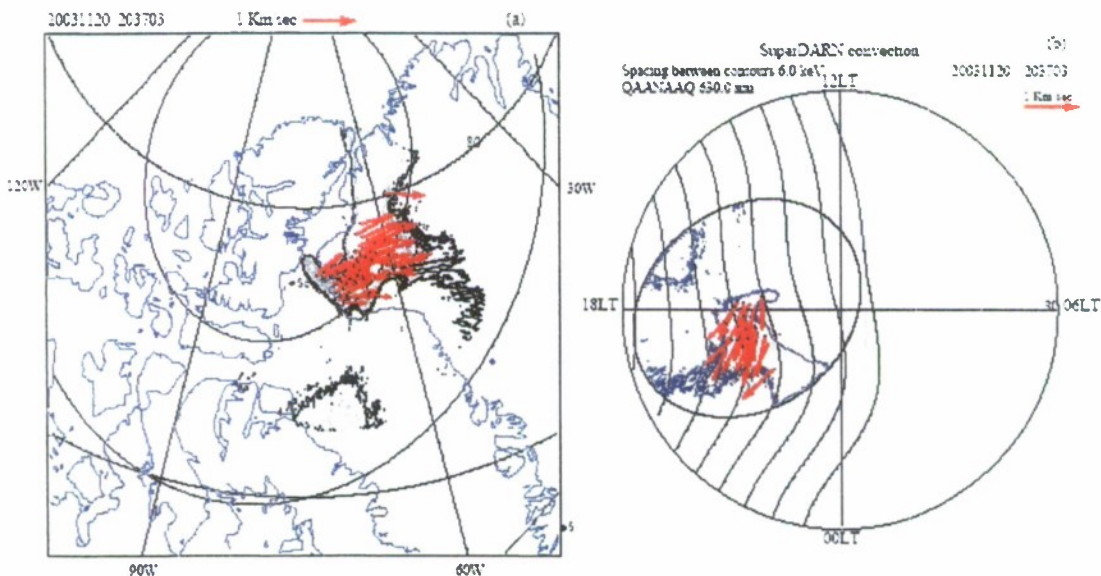
Figure 8. Airglow images and vectors of the patch drift velocities plotted in a geographic frame (left panel) and CG polar plot (right frame). Notice the SuperDARN convection pattern corresponding to 2030 UT is also included. Vectors were obtained by using a 2-D cross correlation analysis that includes images for 2035 and 2037 UT.
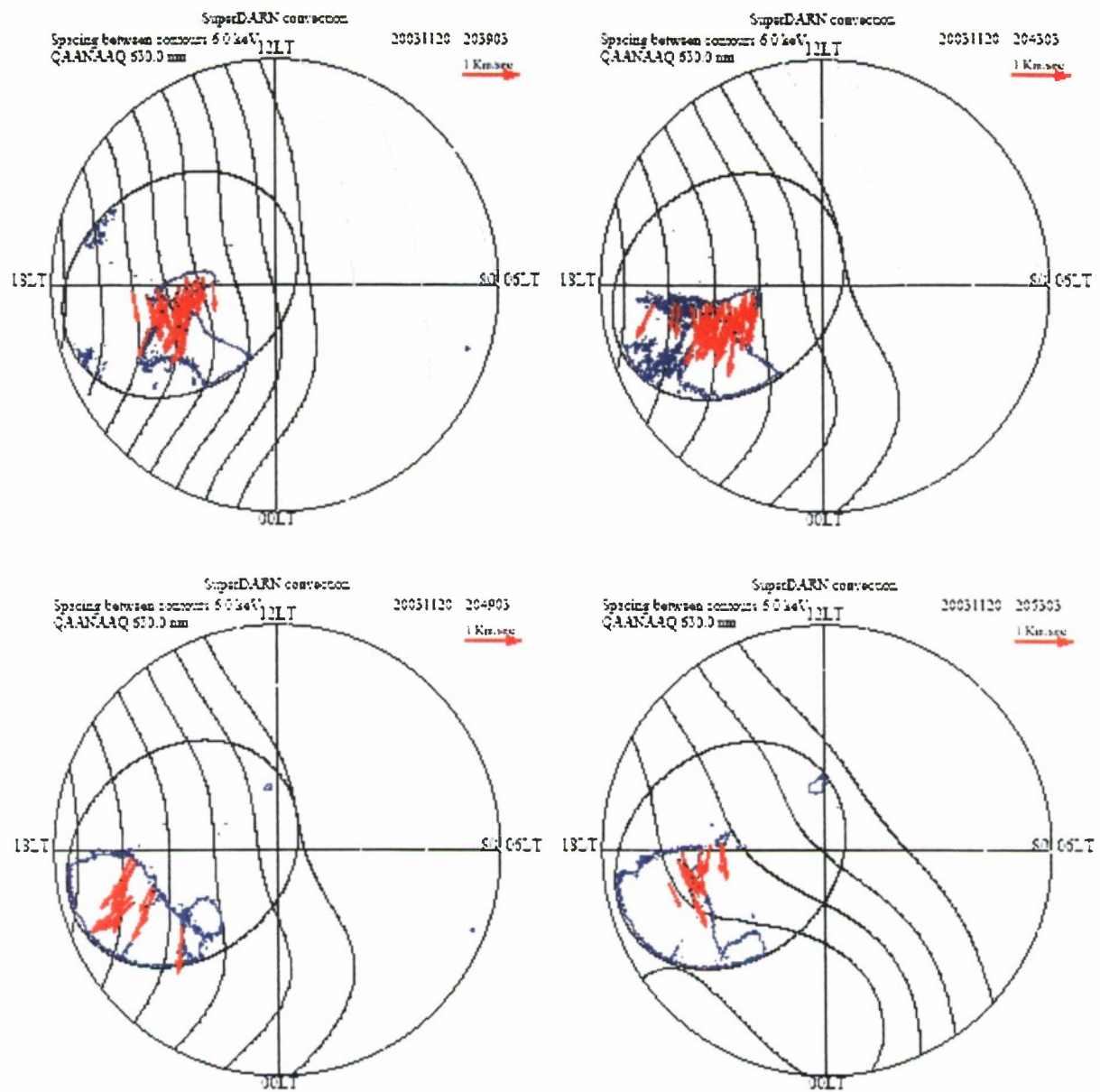
Figure 9. Series of polar cap patches and the patch drift velocity presented in a polar display of CG latitude versus CG local time coordinates. The format of each frame is similar to Figure 8b.
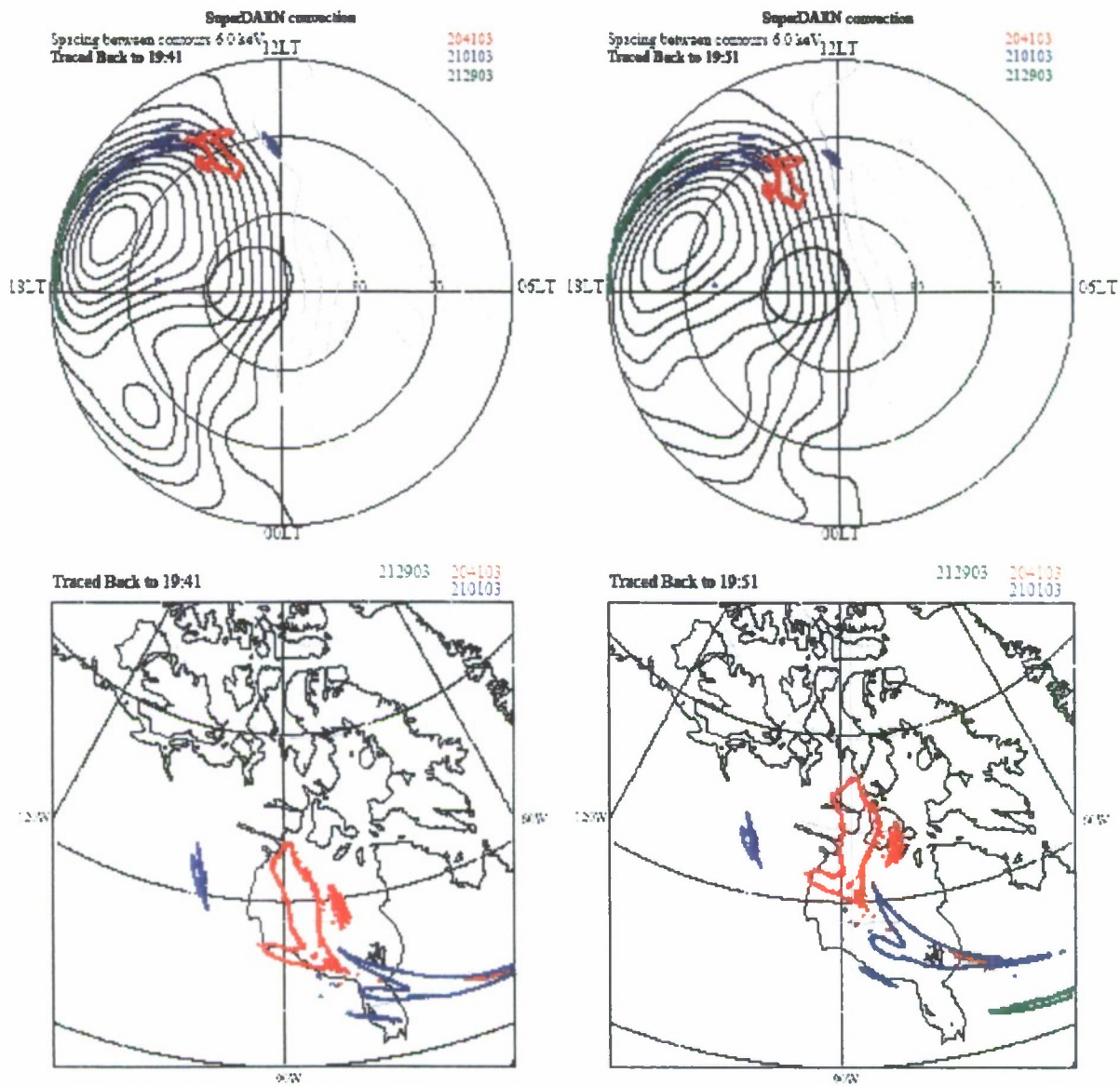
Figure 10. Trajectory analysis of the patches observed at Qaanaaq on November 20, 2003 at 2041, 2101, and 2129 UT. The images were traced backward in time to 1941 and 1951 UT. The top panels show the patches in a CG system. The lower panels show the same information in geographic coordinates. The grey lines in the lower panels indicate constant magnetic latitudes between 85° and 70°.
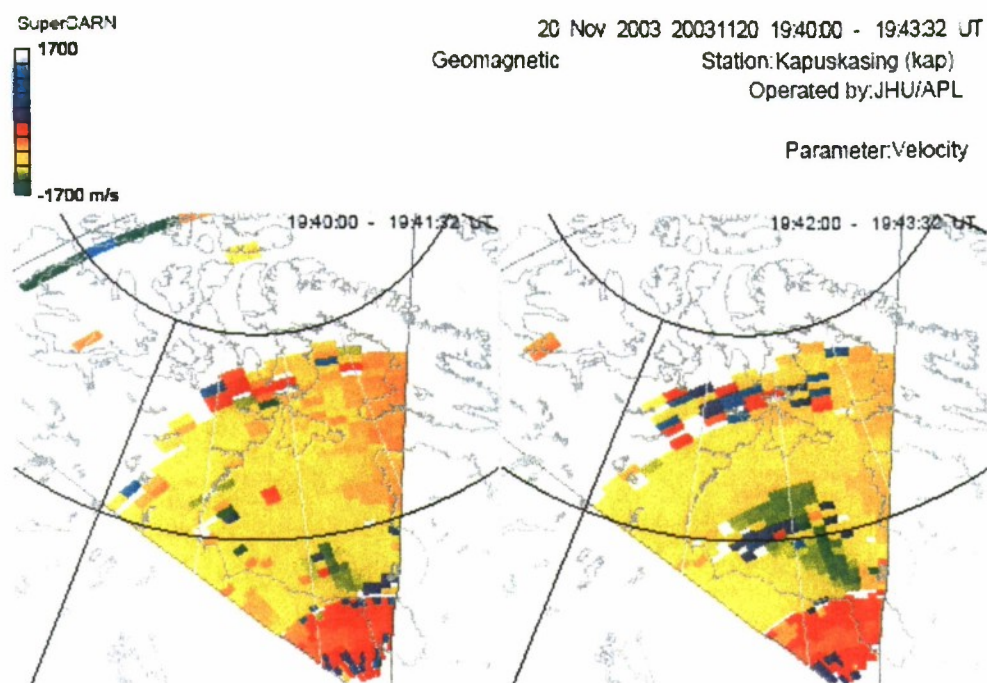
Figure 11. Distance-time plots of Doppler velocity (defined positive toward the radar) observed by the Kapuskasing radar. Note the channel of large negative values (~1700 m/s) seen in the frame of 1942-1943:32 UT.
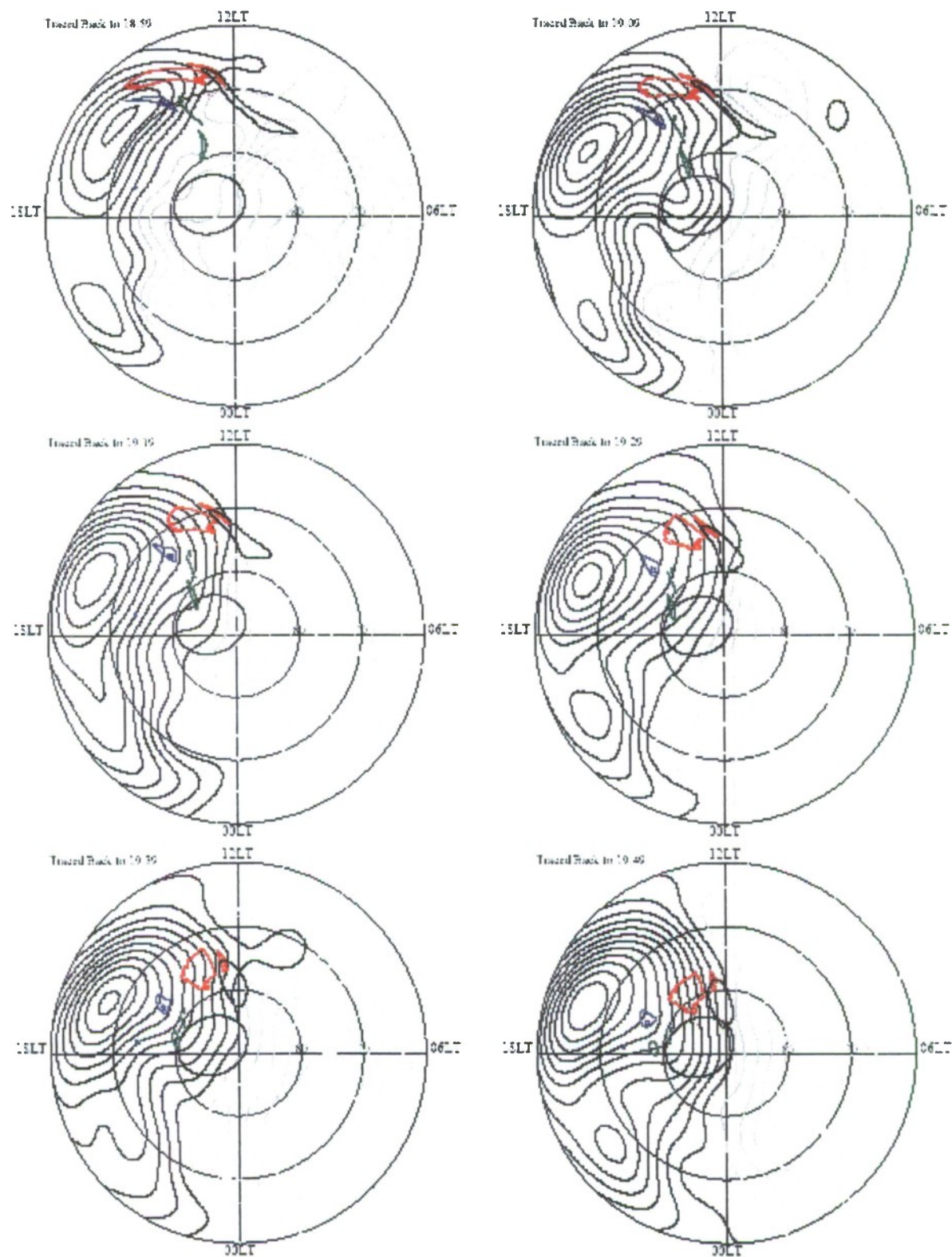
Figure 12. Trajectory analysis of polar cap patches observed at Qaanaaq, Sondrestrom, and the DMSP satellite on November 20, 2003 near 2009 UT. The images have been traced backward in time to the time indicated at the top left side. The fourth patch observed by the DMSP satellite has been depicted as a large circular contour.

95
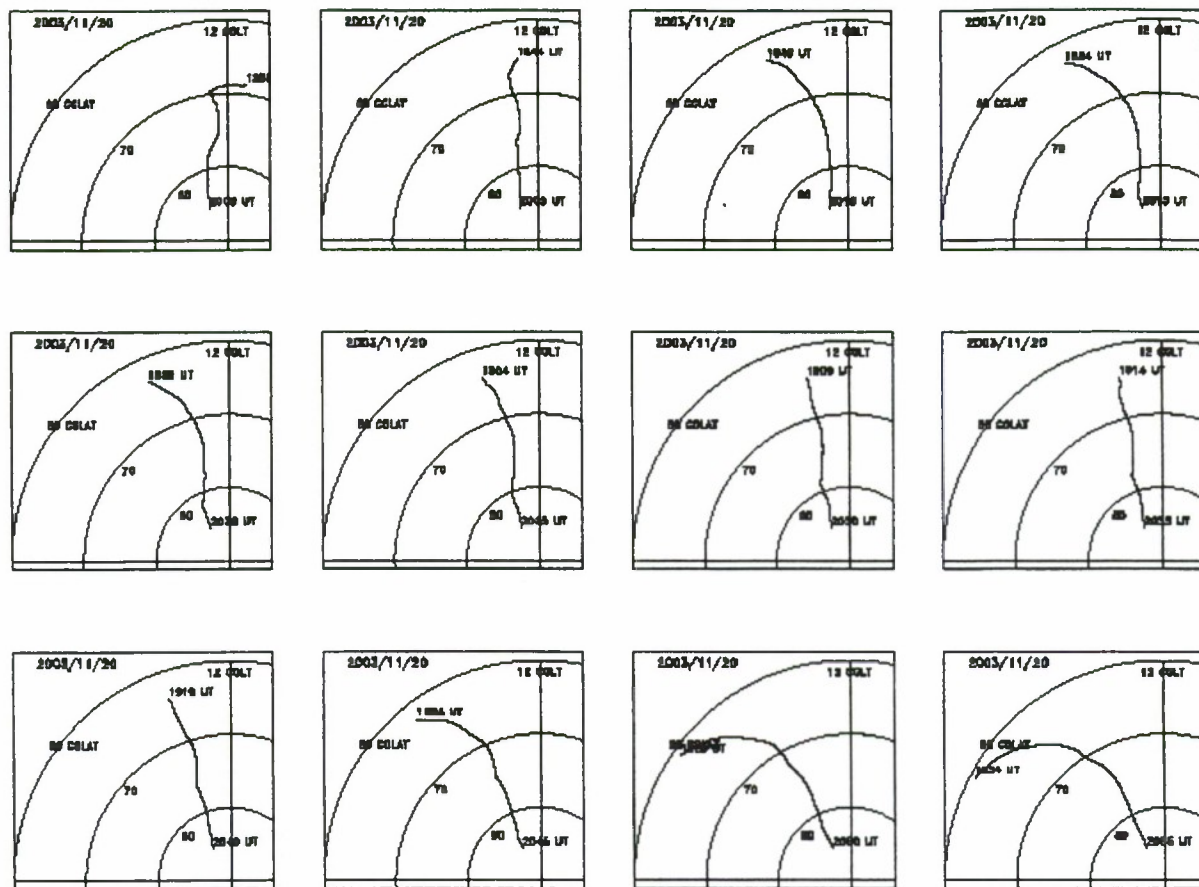
Figure 13. Trajectories in the polar cap of modeled densities shown in Figure 14. SuperDARN high latitude convection patterns were used to calculate the plasma velocities. End point for all the trajectories corresponding to the CG location of the Qaanaaq site.
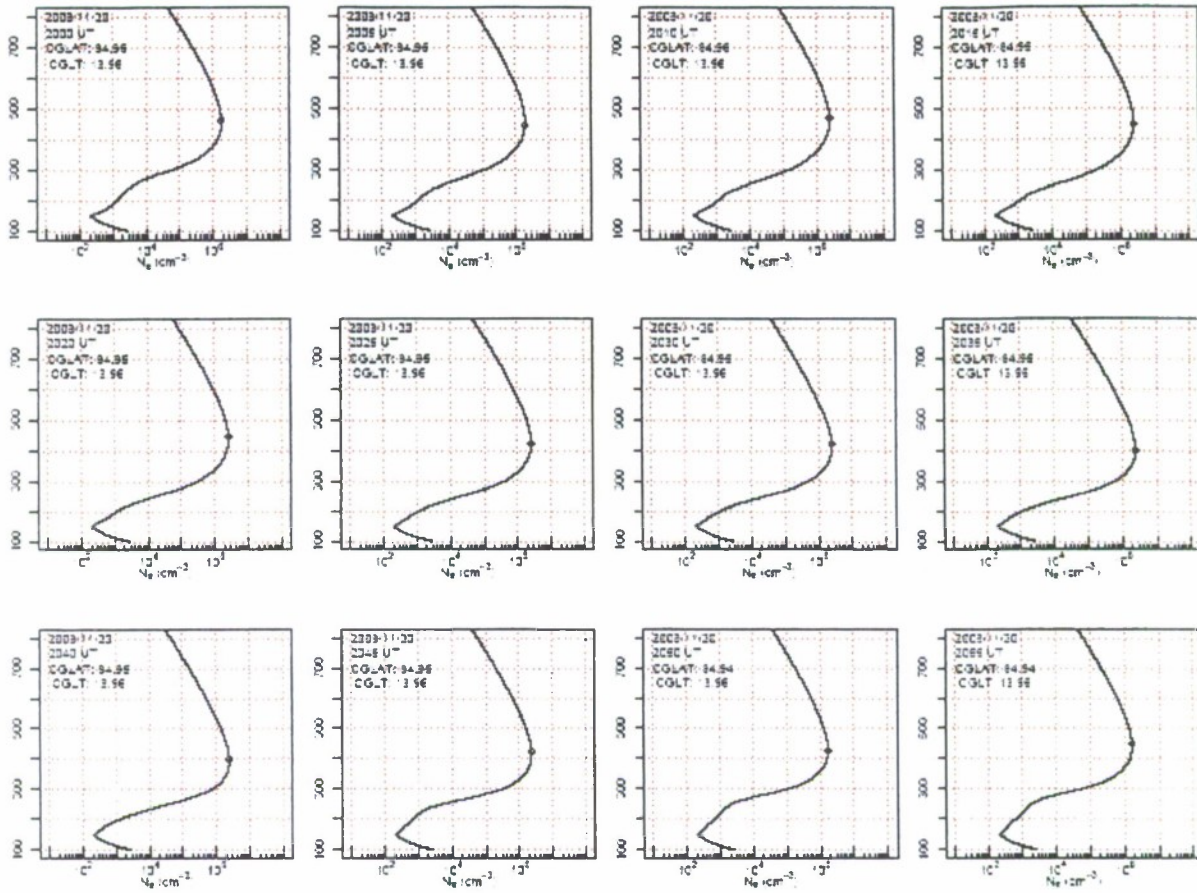
Figure 14. Modeled densities calculated by the GTIM model using MSIS, the Hedin wind model, and SuperDARN high latitude convection patterns. Densities were calculated for the Qaanaaq location every 5 min between 2000 and 2055 UT. A downward wind was introduced between 2000 and 2040 UT.
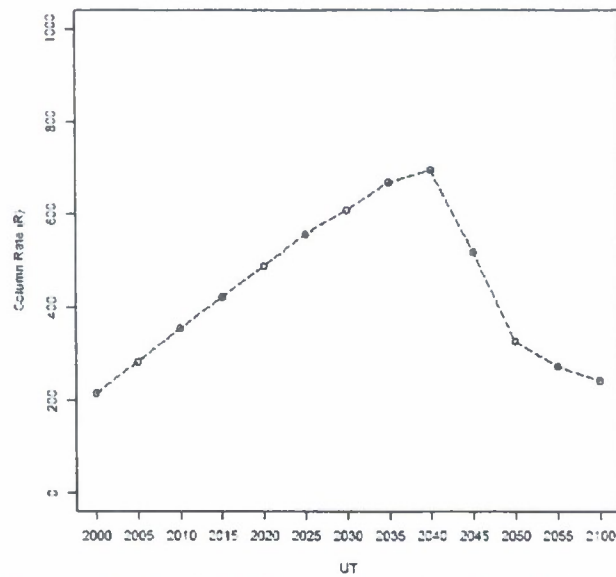
Figure 15. Vertical column emission rates of atomic oxygen arising from radiative recombination. Densities of Figure 14 were used to obtain the column rates. See below for details.

Simultaneous Observation of Traveling Ionospheric Disturbances in the Northern and Southern Hemispheres

C.E. Valladares[1], J. Villalobos[2], M.A. Hei[1], R. Sheehan[1], Su. Basu[3], E. MacKenzie[1],
P.H. Doherty[1] and V.H. Rios[4]

[1]Institute for Scientific Research, Boston College, Chestnut Hill, MA 02467
[2]Department of Physics, Universidad Nacional de Colombia, Bogota, Colombia
[3]Center for Space Physics, Boston University, Boston, MA 02215
[4]Department of Physics, Universidad de Tucuman, Tucuman, Argentina

Abstract

Measurements of total electron content (TEC) using 263 GPS receivers located in the North and South America continents are presented to demonstrate the simultaneous existence of traveling ionospheric disturbances (TID) at high, mid, and low latitudes, and in both northern and southern hemispheres. The TID observations pertain to the magnetically disturbed period of October 29-30, 2003 also known as the Halloween storm. The excellent quality of the TEC measurements makes it possible to calculate and remove the diurnal variability of TEC and then estimate the amplitude, wavelength, spectral characteristics of the perturbations, and the approximate velocity of the AGW. On October 29, 2003 between 17 and 19 UT, there existed a sequence of TEC perturbations (TECP), which were associated with the transit of atmospheric gravity waves (AGW) propagating from both auroral regions toward the geographic equator. A marked difference was found between the northern and southern perturbations. In the northern hemisphere, the preferred horizontal wavelength varies between 1500 and 1800 km; the propagation velocity is near 700 m/s and the perturbation amplitude about 1 TEC unit (TECu). South of the geographic equator the wavelength of the TECP is as large as 2700 km, the velocity is about 550 m/s, and the TECP amplitude is 3 TECu. Concurrently with our observations, the Jicamarca digisonde observed virtual height traces that exhibited typical features that are associated with TIDs. Here, it is suggested that differences in the local conductivity between northern and southern auroral ovals create a different Joule heating energy term. The quality of these observations illustrates the merits of GPS receivers to probe the ionosphere and thermosphere.

1. INTRODUCTION

During the last decade, it has become evident that a vast network of GPS receivers is a superb diagnostic of space weather due to its ability to resolve spatial-temporal ambiguities. Recently, GPS TEC measurements have detected the passage of atmospheric gravity waves (AGW) at mid and high latitudes [*Ho et al.* 1998a, *Saito et al.* 1998, *Shiokawa et al.* 2002], improved understanding of the dynamics of the magnetically-disturbed mid-latitude ionosphere [*Basu et al.,* 2005], and helped the forecast of the onset of equatorial plasma irregularities [*Valladares et al.,* 2001]. The first studies of AWG using GPS receivers employed 150+ globally distributed receivers to indicate the existence of small TEC enhancements developing simultaneously at both north and south auroral regions [*Ho et al.* 1998a, 1998b]. These TEC enhancements moved toward lower latitudes and from the night side into the dayside. Later, *Saito et al.* [1998] used a denser network of over 900 receivers in Japan to reveal the spatial and temporal evolution of TIDs. The amplitude of the perturbation structures was found to be 1 TEC unit (TECU), the wavelengths up to 300 km, and with a phase velocity of order 100 m/s. *Shiokawa et al.* [2002] used

1000+ GPS receivers, an all-sky imager, a scanning photometer, and three sounders, all installed in Japan, to study the dynamics, propagation and source of large-scale TIDs (LSTID). *Shiokawa et al.* [2002, 2003] concluded that the 630.0 nm airglow intensifications, f_oF2 and TEC perturbations were the response to an enhancement of the poleward neutral wind associated with an equatorward propagating gravity wave. However, their data did not resolve conclusively whether the source of the gravity waves was the high latitude Joule heating or the Lorentz force associate with substorms. Joule or frictional heating of the neutral gas is produced by the difference in velocity between neutrals and ions. The Lorentz forcing consists of momentum transfer to the ions that is passed to the neutrals by collisions (ion drag) [*Balthazor et al.,* 1997]. Joule heating is a dominant mechanism at higher altitudes producing large–scale gravity waves with velocity ~640 m/s that can propagate to lower latitudes whereas Lorentz forcing predominates at lower altitudes generating medium-scale gravity waves with ~320 m/s velocity .

It has been demonstrated that during magnetically active days large-scale waves generated in the auroral zone propagate equatorward; in contrast medium-scale GW generated by tropospheric weather systems travel mainly in the zonal direction [*Hocke and Schlegel,* 1996]. Theoretical considerations by *Hines* [1967] have indicated that GWs propagate with velocities near ~700 m/s and have periods that increase with travel distance from mid to low latitudes. The numerical model of *Richmond* [1978, 1979] suggested that the thermospheric response to a substorm consisted of disturbances propagating equatorward with a speed of about 750 m/s. *Mayr et al.* [1984a, b] developed a linear transfer function model to describe the different gravity wave modes and impulsive penetrations due to Joule heating. *Nicolls et al.* [2004] used TEC data from a network of GPS receivers in North America and vertical density profiles collected at Arecibo to examine the 3-D structure of LSTIDs. The TEC perturbations were of order 1 TEC unit and were associated with wind pulses that drove the mid-latitude F layer up and down. On the modeling side, *Balthazor and Moffett* [1997] used a global fully-coupled thermosphere-ionosphere-plasmasphere model to simulate the transit of gravity waves originated from a high-latitude electric field enhancement. The thermospheric disturbance propagated toward the equator from both poles and interfered constructively at the equator producing TEC and density variations that were larger than the mid latitude perturbations.

In this paper, we present TEC perturbations observed during the major storm of October 2003 by 263 GPS receivers distributed in the North and South Americas. The TEC perturbations were generated by large-scale AGWs traveling from auroral latitudes toward the geographic equator. In the northern hemisphere the dense network of GPS receivers made it possible to determine the wavelength, propagation direction, and phase velocity of the LSTID. In the southern hemisphere, GPS receivers are installed more sparsely. Nevertheless, the south-American TEC perturbations indicate TID-related fluctuations with slightly different characteristics than their northern hemisphere counterpart. We also point out that the propagating waves seem to meet in a location north of the geographic equator.

2. THE SUPERSTORM OF OCTOBER-NOVEMBER 2003

Between late October and early November 2003 a series of solar eruptions occurred from 3 regions of the Sun, producing a total of 80 coronal mass ejections (CMEs). During this period, the fastest CME (~2700 km/s) recorded in 30 years was observed on 4 November 2003 at 1954 UT. The solar flux of October 28, 2003 was the fourth most intense in recent history, and produced the largest TEC enhancement (25 TEC units) at the sub-solar point [*Tsurutani et al.,* 2005]. On October 30, shortly after 1800 UT, a tenfold enhancement in the TEC was observed over the US mainland. During this time, steep gradients were seen in the poleward boundaries of a storm-enhanced density (SED) eroded by strong sub-auroral polarization stream (SAPS) electric fields. *Foster and Rideout* [2005] indicated that the enhanced TEC resulted from a rapid poleward redistribution of equatorial plasma responding to the storm-time eastward electric fields. *Mannucci et al.* [2005] suggested that a combination of prompt penetration electric fields and diffusion along field lines driven by a super fountain effect were responsible for the peak mid-latitude density distribution.

3. OBSERVATIONS

Our primary data set consists of TEC values measured by 263 GPS receivers that routinely operate in North and South Americas. Equivalent vertical TEC values were calculated independently for each of the GPS receivers using an analysis code that was developed at Boston College. This computer software uses the satellite biases as reported by the University of Bern and calculates the receiver bias minimizing the TEC variability observed between 2 and 6 LT. TEC curves corresponding to each satellite pass and for each of the 263 receivers were then fitted to a 4th order polynomial to filter out the diurnal variability and to evaluate TEC perturbations (TECP) containing time scales of 3 hours or less. Our method is different than the algorithm used by *Shiokawa et al.* [2002] that estimates the unperturbed TEC level by removing a 2-hour running average, or the procedure employed by *Nicolls et al.* [2004] that calculates the unperturbed TEC value using a 4-hour running average for several latitude-longitude bins. We claim that our derivation of the TEC perturbations reflects quite well the variability of the integrated number density due to the transit of large-scale gravity waves.

Figure 1 shows four TECP traces corresponding to two stations located in the Northern Hemisphere (Ensenada and Darlington) and two sites placed in the southern hemisphere (Ancon and Cuzco). The prominent feature of panels (a) and (b) is the pronounced level of coherence that starts at 1700 UT. The latitudinal displacement of these 2 GPS stations produces a small time offset of a few minutes. We demonstrate later that the apparent motion of the TECP is southward in the northern hemisphere with an initial phase front almost aligned with the geographic east west. The TECP traces of Figures 1c and 1d display an almost perfect correlation, but show no offset as these stations (Ancon and Cuzco) are placed at nearly the same geographic latitude. The right side panels of Figure 1 display the spectral power of the TECP as a function of the period. The spectra (frames a and b) of the northern hemisphere stations are wide and centered at 100 minutes. Conversely, the southern hemisphere TECP spectra are much narrower and centered at slightly larger time scales (150 min).

Figure 2 shows 2-min snapshots of the TEC perturbations observed on four instances separated by 10 min. They have been color coded according to the sign of the perturbation to emphasize their latitudinal extension. Each color pixel has been placed at the geographic location of the assumed 350-km altitude piercing point. Figure 2a reveals the existence of up to 5 latitudinal bands alternating between positive (blue) and negative (red) TEC perturbations. The northernmost band coincides with the US-Canada border. This is followed by negative and positive bands extending across the continental US. A fourth band is seen over Florida and Mexico only to be interrupted by lack of data over the Caribbean Sea. Further south, we observe a fifth band filling Central America. It is important to note that in Central and South America GPS receivers are installed quite sparsely, hindering the identification of TECP bands. Figure 2b, obtained 10 min later, shows that the location of each band has shifted southward by ~4°, and a new band of positive TEC perturbations originates near the southern Canadian border. The apparent velocity of the TECP features approximates 700 m/s. Figures 2c and 2d confirm the persistence of TECP, the apparent southern motion of the TIDs, and the continuous formation of new TECP bands in the northern part of North America. Note that the TECP over Florida change colors every 15-20 min as northern TECP values apparently displace south. We also note that the phase front shows a small rotation as the perturbation "propagates" equatorward.

Figure 3 shows TECP values recorded by 10 GPS stations located near the west coast of South America. Although the apparent propagation of the TECP bands seems quite similar to the TEC perturbations observed in North America, their amplitude, wavelength, and velocity are very different. Also note that the frame-to-frame time difference in this sequence is 30 min. The symbols that are used to depict TEC perturbations are circles with radii dependent on the amplitude of the TECP. The size of the perturbations seems to grow as the perturbations are observed closer the geographic equator. A 3 TECu perturbation is seen near the magnetic equator at 1854 UT, and values ~1 TECu at a distance 20° away from the equator. In spite of the low number of points, it is evident that the southern hemisphere perturbations move northward with an average speed equal to 550 m/s. The latitudinal extension of the

southern TECP bands is evidently larger than the northern hemisphere bands. They extend ~13° in the southern hemisphere and only 8° in the northern.

Figure 4 shows a pictorial representation of both northern and southern hemisphere TEC perturbations; it serves to infer the equatorward motion of the underlying AGWs. This plot is framed in a coordinate system of geographic latitude versus universal time. This figure was obtained by integrating all the pixels measured between 60° and 90° W longitude and placing a blue or orange point depending on the sign of the result. Before 15 UT, a random distribution of average TECP values was obtained. Between 15 and 17 UT, the integrated perturbations display a good degree of coherence only at high and mid latitudes. These perturbations seem to fade at ~20° geographic latitude. After 17 UT, a new band seems to be propagating from the north and another from the south that meet near the geographic equator at 1845 UT. The black lines that reach the equator at 1845 and 1945 UT emphasize our interpretation of the locations of the negative perturbations and the equatorward propagation of the northern and southern TECP. A second band of TEC perturbations likely originates almost simultaneously from both high latitude regions between 1820 and 1830 UT. They are observed to merge near the geographic equator at 1950 UT. No propagation into the opposite hemisphere is evident during these events.

4. DISCUSSION

During the first two days of the Halloween storm we detected TEC perturbations, similar to the ones presented here, on 2 other occasions. These two periods correspond to 06-09 UT on Oct 29, and 17-21 UT on Oct 30, 2003. All three events developed during times of cross polar cap potential larger than 150 KV (DMSP F13 and F15). Similarly, the AE index of Figure 5 indicates that during the TIDs of October 2003 electrojet currents were enhanced at auroral latitudes. *Shiokawa et al.* [2002] have associated energy deposited in the auroral oval with the initiation of meridionally propagating gravity waves. These authors calculated the amount of high latitude Joule heating and Lorentz force. However, neither term had the necessary strength to generate a gravity wave. These authors concluded that a single wave large-scale TID was associated with the termination of the equatorward wind. The TIDs present here have characteristics that differ from the TIDs shown by *Shiokawa et al.* [2002]. During the October 2003 Halloween storm, we observed a train of gravity waves likely generated by repetitive pulses of energy that were deposited at auroral latitudes. We believe that intense Joule heating being deposited at auroral latitudes likely produced the GWs associated with the observed TIDs. *Balthazor et al.* [1997] have indicated that Joule heating is associated with gravity waves containing mean velocity near 640 m/s, whereas Lorentz forcing produce waves with a lower velocity about 320 m/s. The large velocity that was observed in both hemispheres, close to 600 m/s, support the idea that intense Joule heating, as seen in the large auroral currents of Figure 5, is likely responsible for the generation of the AGWs. Joule heating ($J \cdot E$) being proportional to the Pedersen conductivity could be different in opposite auroral zones due to differences in the number density. Additionally, Hajkowicz [1992] found that during magnetic storms, stronger TID signatures are created in the nighttime sector than in the sunlit region. The fact that the TEC perturbations interact at the geographic equator, instead of the magnetic equator as predicted by *Balthazor and Moffett* [1997], can be explained by the large difference in the gravity wave velocity in opposite hemispheres and/or the timing that the impulsive energy is released in opposite auroral zones. We are not able to resolve the time that the energy flux is deposited at high latitudes due to the limited number of observations near the auroral ovals.

We have also examined ionograms collected by the Jicamarca digisonde (not shown here) looking for signatures of TIDs. Two distinct features in the ionograms corroborate our contention that TIDs were simultaneously observed in South America. (1) The ionogram for 1730 UT shows a clear change in the shape of the virtual height trace between 4.5 and 13 MHz. (2) The ionogram color-coded Doppler profile exhibits a shift from positive to negative as a function of frequency. The ionogram height profile indicates that the density disturbance was limited to the height range between 225 and 380 km altitude,

corresponding to a half wavelength size equal to 155 km. Analysis of atmospheric wave propagation provides a dispersion relation of the form:

$$\lambda_z^2 = \left(\frac{\tau_g^2}{\tau^2 - \tau_g^2} \right) \lambda_x^2 \qquad (1)$$

where λ_x is the horizontal wavelength, λ_z is the vertical wavelength, τ is the period and τ_g is the Brunt-Väisälä period (~15 min). Using the values measured in the southern hemisphere, we obtained a vertical wavelength equal to 270 km. This value is in good quantitative agreement with the vertical wavelength measured by the Jicamarca digisonde.

It is necessary to mention that the perturbation spectra are mildly affected by the motion of the GPS satellites. The velocity of the sub-ionospheric penetration point of the GPS satellites is about 80 m/s. However, this effect does not change our conclusions about the time scale of the TID perturbations because the velocity of the GW is about an order of magnitude larger.

5. CONCLUSIONS

We have presented experimental evidence which indicates that the TEC perturbations are of order 1 TEC unit, that they coexist in both northern and southern hemispheres, propagate equatorward, and have wavelength, phase velocities, and amplitudes that differ between hemispheres.
Our results agree with findings of theoretical simulations by *Balthazor and Moffett* [1997] in which the TEC perturbations interact constructively near the equatorial line. However, our observations suggest that the TEC perturbations unite close to the geographic equator instead of the magnetic equator.

REFERENCES

Balthazor, R.L., and R. J. Moffett, A study of atmospheric gravity waves and travelling ionospheric disturbances at equatorial latitudes, *Ann. Geophys.*, 15, 1048, 1997.

Balthazor, R.L., R. J. Moffett, and G. H. Millward, A study of the Joule and Lorentz inputs in the production of atmospheric gravity waves in the upper thermosphere, *Ann. Geophys.*, 15, 779, 1997.

Basu, Su., et al., Two components of ionospheric plasma structuring at midlatitudes observed during the large magnetic storm of October 30, 2003, *Geophys. Res. Lett.*, 32, L12S06, doi:10.1029/2004GL021669, 2005.

Foster, J. C., and W. Rideout, Midlatitude TEC enhancements during the October 2003 superstorm, *Geophys. Res. Lett.*, 32, L12S04, doi:10.1029/2004GL021719, 2005.

Hajkowicz, L. A., Universal time effect in the occurrences of large-scale ionospheric disturbances, *Planet. Space Sci.*, 40, 1093-1099, 1992.

Hines, C. O., On the nature of traveling ionospheric disturbances launched by low-altitude nuclear explosions, *J. Geophys. Res.*, 72, 1877–1882, 1967.

Ho, C.M., A.J. Manucci, L. Sparks, X. Pi, U.L. Lindqwister, B.D. Wilson, B.A. Iijima, and M.J. Reyes, Ionospheric total electron content perturbations monitored by the GPS global network during two Northern Hemisphere winter storms, *J. Geophys. Res.*, 103, 26409, 1998a.

Ho, C. M., A. J. Mannucci, U. J. Lindqwister, X. Pi, B. T. Tsurutani, L. Sparks, B. A. Iijima, B. D. Wilson, I. Harris, and M. J. Reyes, Global ionospheric TEC variations during January 10, 1997 storm, *Geophys. Res. Lett.*, 25(14), 2589–2592, 1998b.

Hocke, K., and K. Schlegel, A review of atmospheric gravity waves and travelling ionospheric disturbances: 1982–1995, *Annales Geophys.*, 14, 917. 1996.

Mannucci, A. J., B. T. Tsurutani, B. A. Iijima, A. Komjathy, A. Saito, W. D. Gonzalez, F. L. Guarnieri, J. U. Kozyra, and R. Skoug, Dayside global ionospheric response to the major interplanetary events of October 29–30, 2003 "Halloween Storms", *Geophys. Res. Lett.*, 32, L12S02, doi:10.1029/2004GL021467, 2005.

Mayr, H.G., I. Harris, F. Varosi, and F. A. Herrero, Global excitation of wave phenomena in a dissipative multiconstituent medium, 1, Transfer function of the Earth's thermosphere, *J. Geophys. Res.*, 89, 10929, 1984a.

Mayr, H.G., I. Harris, F. Varosi, and F. A. Herrero, Global excitation of wave phenomena in a dissipative multiconstituent medium, 2, Impulsive perturbations in the Earth's thermosphere, *J. Geophys. Res.*, 89, 10961, 1984b.

Nicolls, M. J., M. C. Kelley, A. J. Coster, S. A. González, and J. J. Makela, Imaging the structure of a large-scale TID using ISR and TEC data, *Geophys. Res. Lett.*, 31, L09812, doi:10.1029/2004GL019797, 2004.

Richmond, A. D., Gravity wave generation, propagation, and dissipation in the thermosphere, *J. Geophys. Res.*, 83, 4131, 1978.

Richmond, A. D., Large-amplitude gravity wave energy production and dissipation in the thermosphere, *J. Geophys. Res.*, 84, 1880, 1979.

Saito, A., T. Iyemori, and M. Takeda, Evolutionary process of 10 kilometer scale irregularities in the nighttime midlatitude ionosphere, *J. Geophys. Res.*, 103(A3), 3993–4000, 1998.

Shiokawa, K., Y. Otsuka, T. Ogawa, N. Balan, K. Igarashi, A.J. Ridley, D.J. Knipp, A. Saito, and K. Yumoto, A large-scale traveling ionospheric disturbance during the magnetic storm of 15 September 1999, *J. Geophys. Res.*, 107, 1088, doi:10.1029/2001JA000245, 2002.

Shiokawa, K., C. Ihara, Y. Otsuka, and T. Ogawa, Statistical study of nighttime medium-scale traveling ionospheric disturbances using midlatitude airglow images, *J. Geophys. Res.*, 108(A1), 1052, doi:10.1029/2002JA009491, 2003.

Tsurutani, B. T., et al., The October 28, 2003 extreme EUV solar flare and resultant extreme ionospheric effects: Comparison to other Halloween events and the Bastille Day event, *Geophys. Res. Lett.*, 32, L03S09, doi:10.1029/2004GL021475, 2005.

Valladares C.E., S. Basu, K. Groves, M.P. Hagan, D. Hysell, A. Mazzella, R. Sheehan, Measurements of equatorial spread-F ionospheric conditions using a latitudinal chain of GPS receivers, *J. Geophys. Res.*, 106, 29133, 2001.
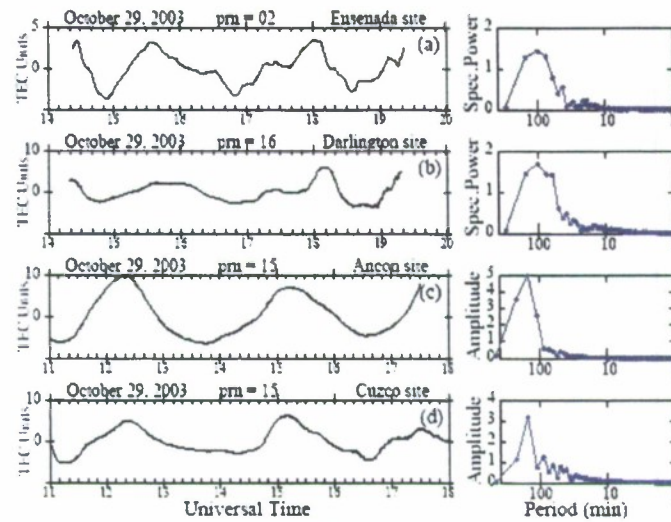
Figure 1. The left panels show the values of the TEC perturbations observed at two stations located in the northern hemisphere (Ensenada and Darlington) and two stations situated in the southern hemisphere (Ancon and Cuzco). The right-hand panels display the power spectra of the TEC perturbations.
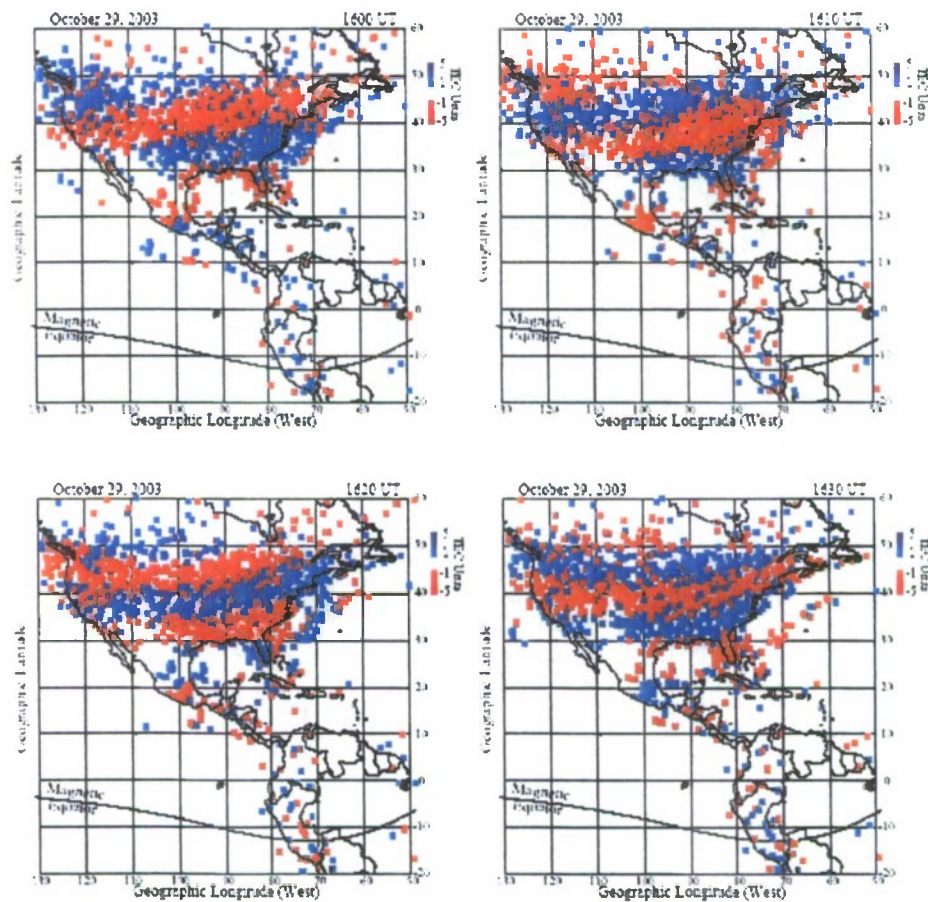
Figure 2. Set of geographic displays of the distribution of TEC perturbations recorded in North America and the Caribbean region. Blue pixels indicate positive variations of the perturbations and red negative TECP values. Time interval between frames is 10 min. See text for details.
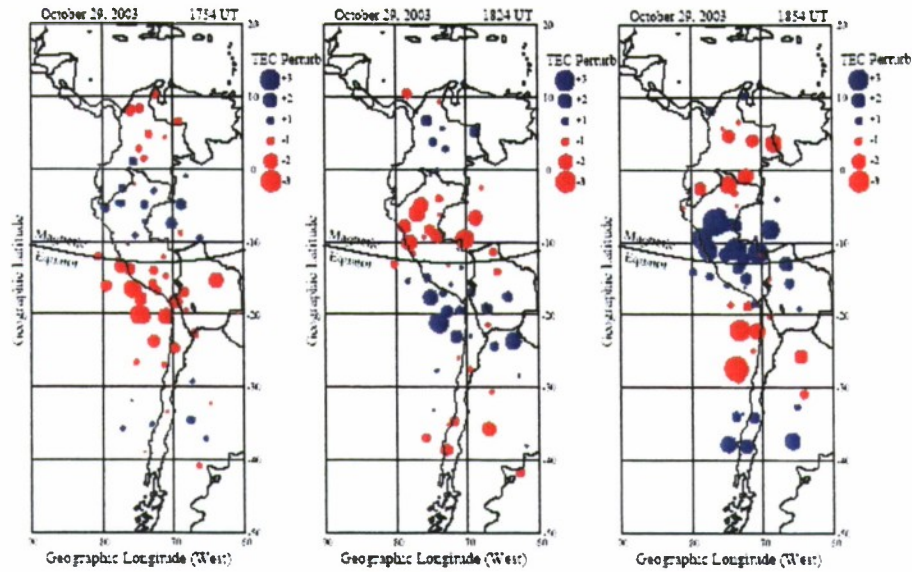
Figure 3. Similar to Figure 2 but for TEC perturbations observed in South America for 3 instances separated by 30 min. Note the size of the small circles indicate the amplitude of the TEC perturbations that vary between –3 and 3 TECu.
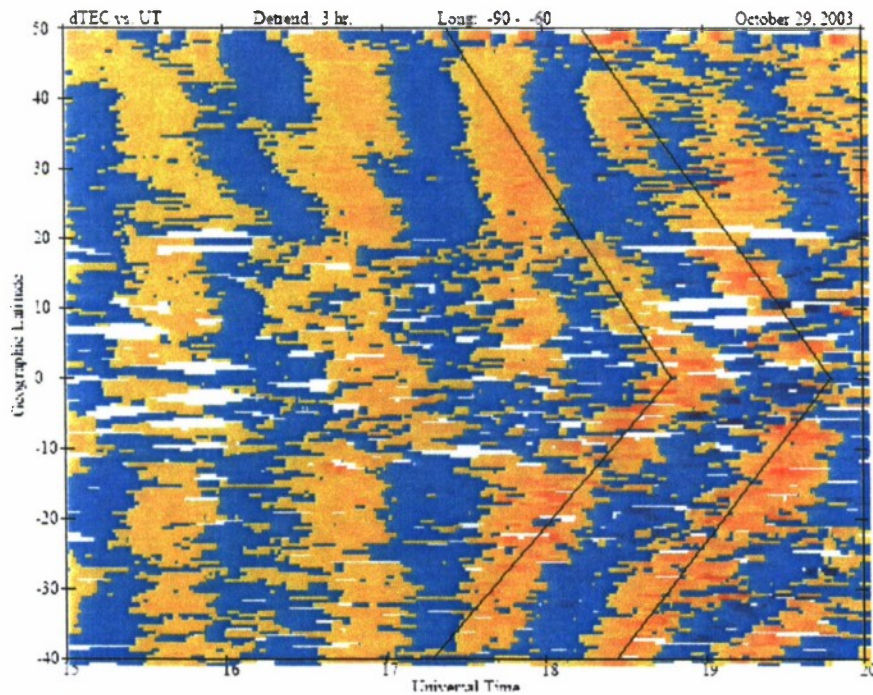
Figure 4. Color-coded representation of the TEC perturbations in a reference frame of geographic latitude versus universal time. Each pixel indicated here corresponds to the average of the perturbations that were observed in longitude between 90° W and 60°W at the latitude and time indicated in the figure.

106
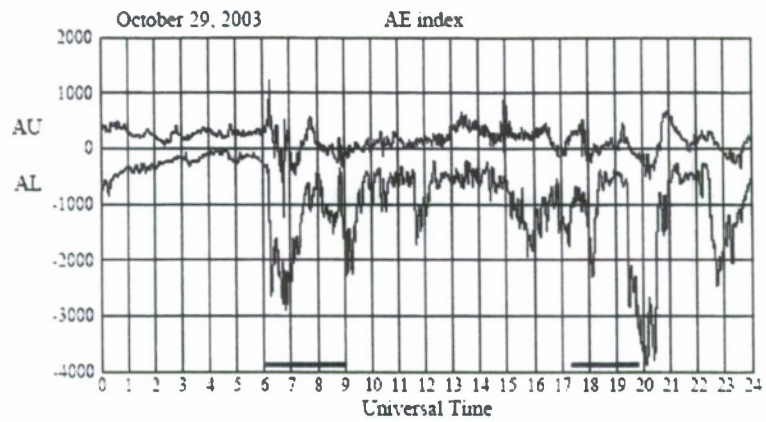
Figure 5. This figure presents the AE index corresponding to October 29, 2003. The lines near the bottom indicate the times when TEC perturbations were detected by our analysis program.

Vize Island Cusp Aurora Records, Winter: 2003-2004

November 25, 2003

On this day the aurora is highly mobile and drifting west. After 0800 UT the aurora disappears for awhile, then returns in a series of brightenings. At 0700, the aurora moves from a location north of the site to the south.
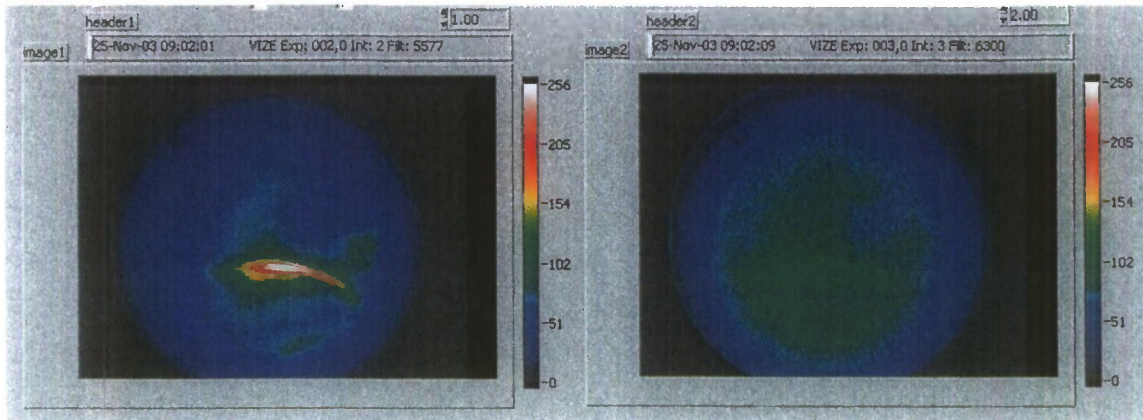
November 27, 2003

The "crew-cut" aurora moves from east-to-west in a few minutes. Two arcs, one located to the north and the other south, are seen after 0505 UT. An arc connected to the north is seen intersecting the southern arc (0605 UT). At 0636 the northern aurora dominates and several rays and spots are visible. After 0800 UT there exists only a stable northern arc.
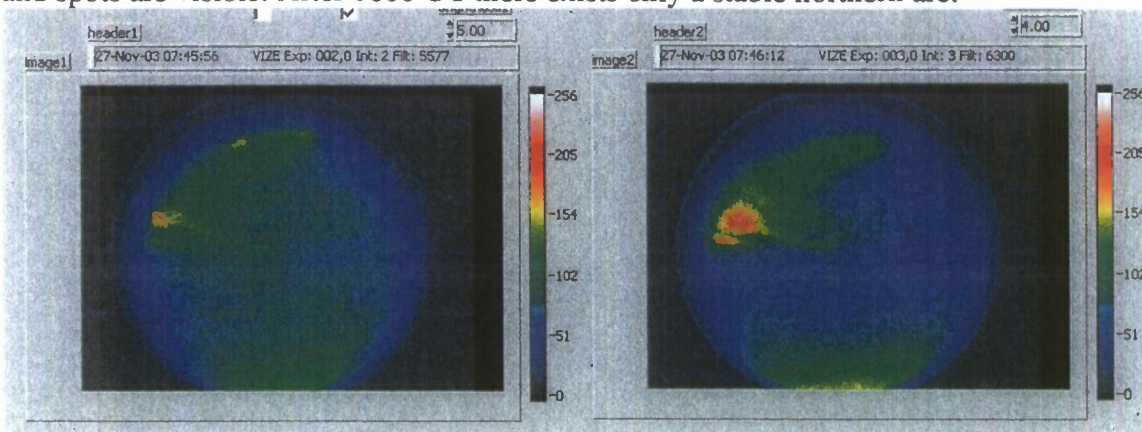
November 28, 2003

A cusp aurora is located to the north for few hours. A faint northern aurora was seen before 0645 UT, with some haze to the south. Auroral activity was high after 0715 UT. It becomes spotty and rayed after 0930 UT. Cusp aurora seems to last up to 1000 UT.
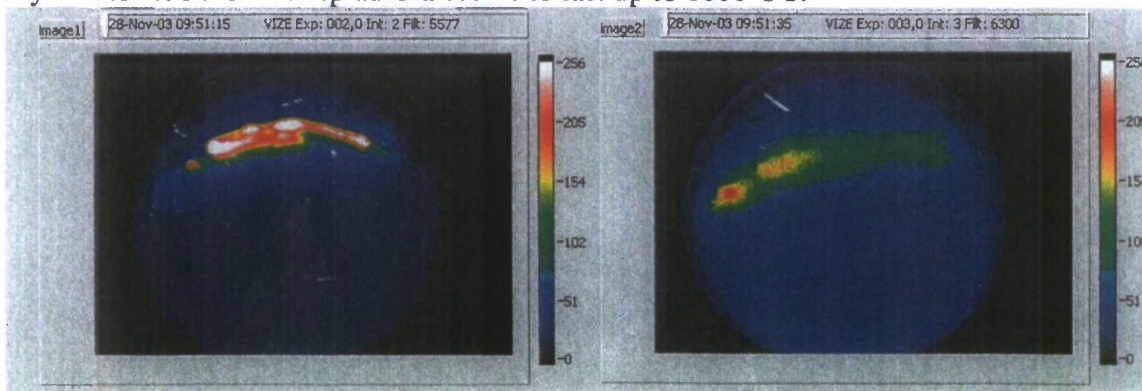
November 29, 2003

Haze or clouds occurred before 0650 UT. Some faint arcs were seen before the images shown below. This type of rays move very fast toward the west and disappear. After a succession of highly mobile arcs and structured aurora, a northern aurora forms that moves southward and stays overhead for a while. The rest of the night has clear skies.
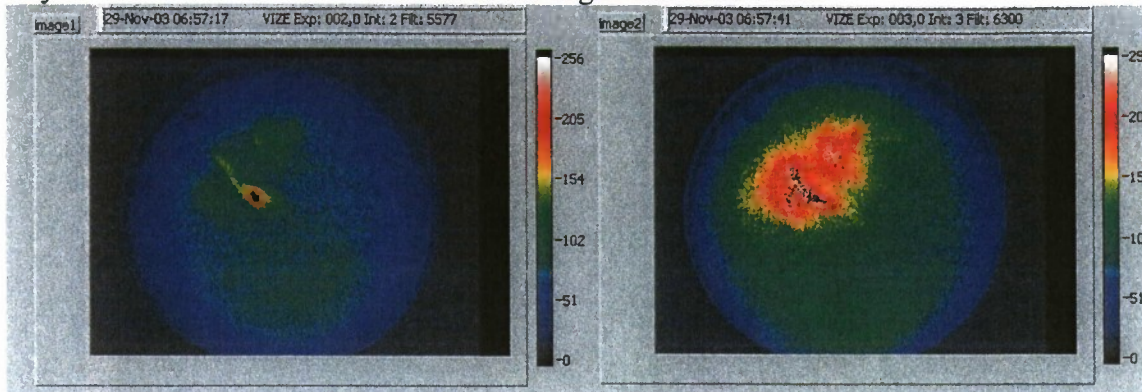
December 02, 2003

At 0500 UT there was a very dynamic corona. Near 0740 UT a more steady and elongated arc appears north of the site. Near 0830 UT there appears a more typical north B_Z aurora, however it is dynamic with rays developing and moving quite rapidly. Near 0900 UT, there is a 20-30 minute segment in which there were 2 (or more) bands in the green line. Near 1000 UT, the aurora moves equatorward, stays overhead and develops into a corona.
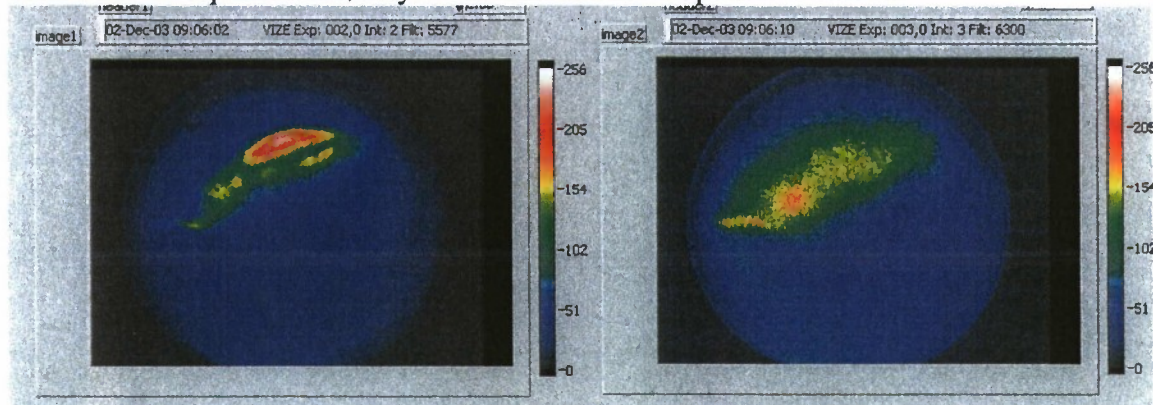
December 16, 2003

No data before 0800 UT. At 0800 UT there is an arc nearly overhead that splits in 2 (or 3), and sometimes an additional arc appears. It changes in minutes. The narrow arcs seen in the figure below were very dynamic as they changed in less than a minute.
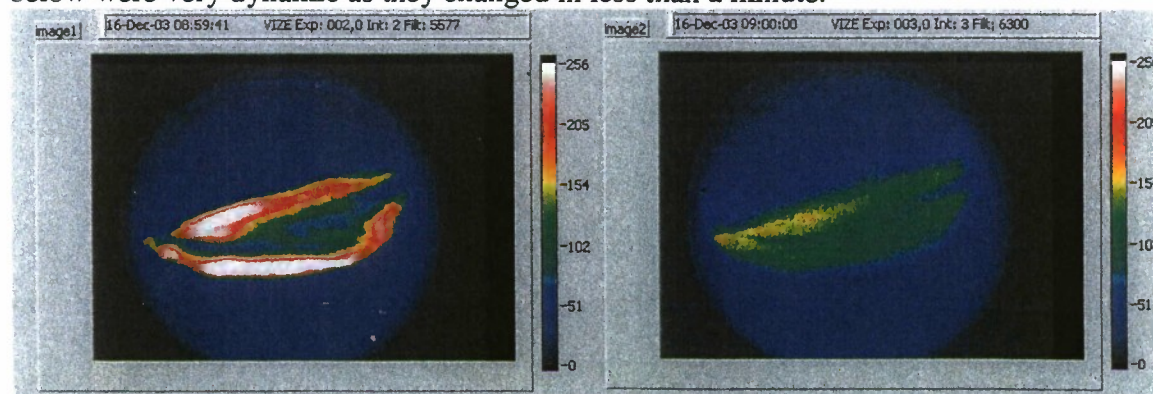
December 18, 2003

Since 0500 UT, a steady arc located north of the site is seen in both red and green lines. At 0537 UT appears a cusp aurora that displays an arc perpendicular to the main cusp aurora. This arc, as seen in the Figure below, lasts until 0543 UT when it develops many rays. The aurora remained north, but there were some haze after 0800 UT.
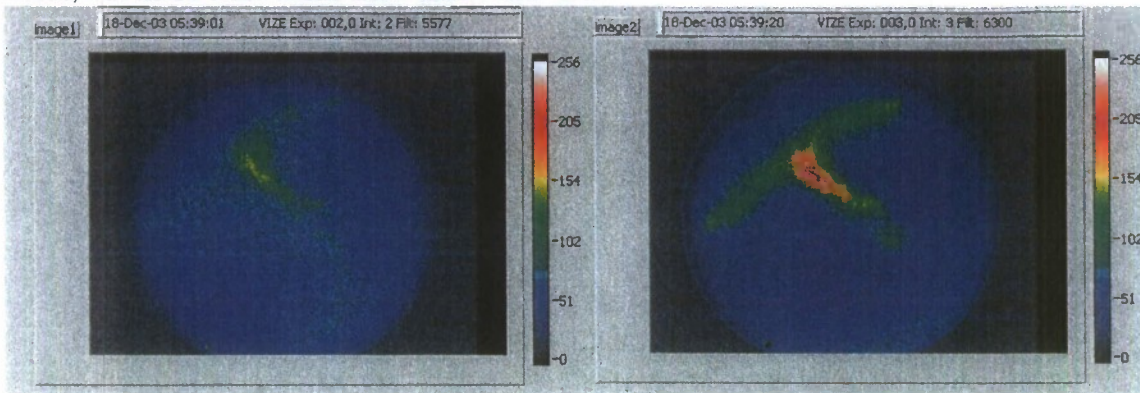
December 21, 2003

It is overcast until 0700 UT. Afterwards there is an overhead aurora as seen below that last only a few minutes. It is very dynamic and moves to the south. Later the aurora disappeared from the eastern side. The cusp remained south of the site and several features were seen moving poleward. The cusp drifted poleward for a while.
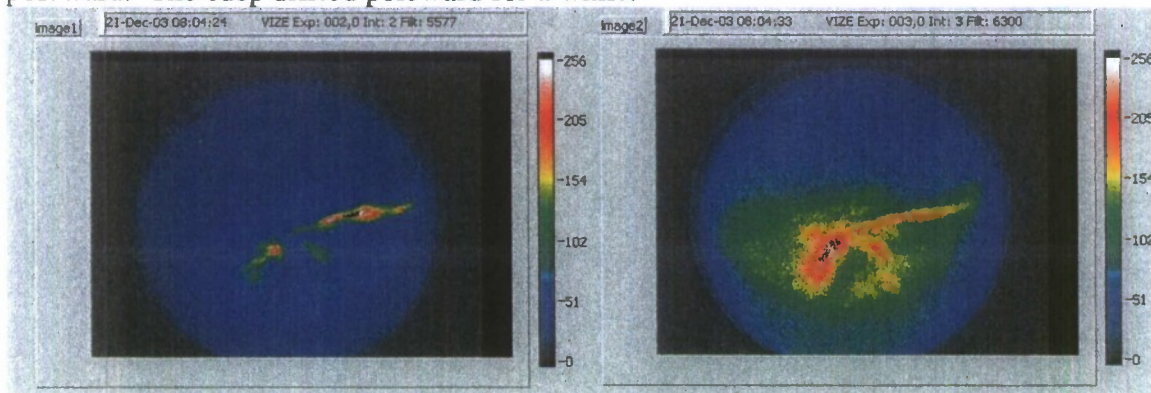
December 22, 2003

Near 0500 UT there existed an arc overhead from horizon to horizon. It developed structures for about an hour around 0600 UT. A very dynamic aurora lasts for more than 1 hour. It becomes more elongated and multi-layered as seen in the figure below. The aurora moves south and then at 0805 UT drifts back overhead. Then it drifts back southward containing poleward surges.
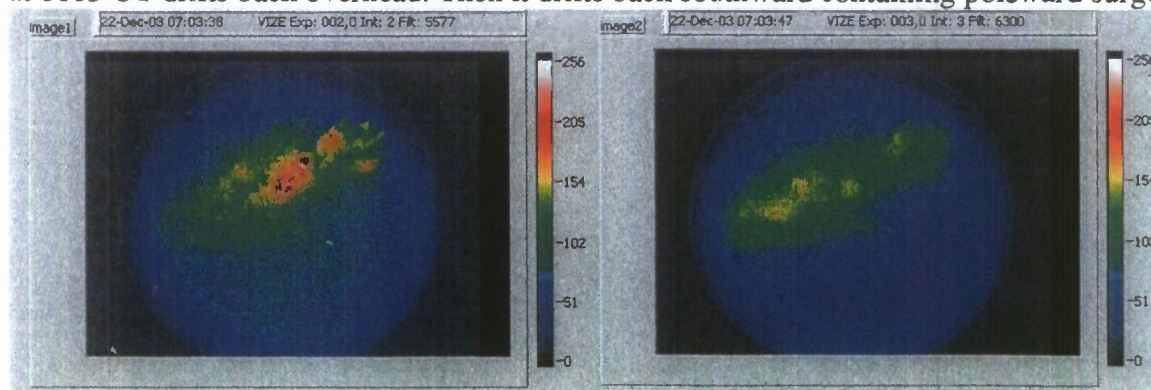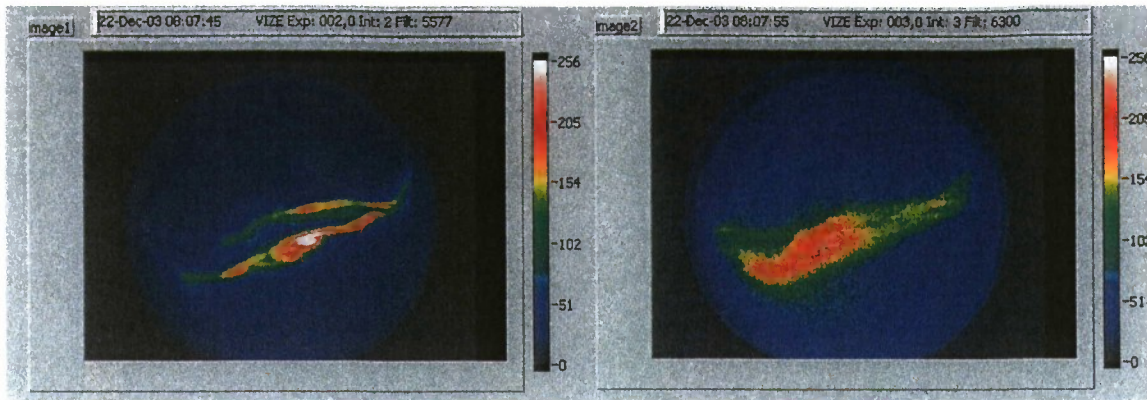
December 23, 2003

Some haze at the beginning of the cusp window. Then, a data gap between 0600 and 0700 UT. At 0700 the sky seems to be clear and there is a well-defined arc to the north that last for more than an hour. There are also some equatorward directed aurora, faint but visible in these images. At 0830 UT the aurora starts retracting equatorward; there is a thick auroral trace at this time. The images displayed below show a sequence of north and then south motions of the aurora. The aurora stays almost overhead and displays a series of brightening until 1020 UT.
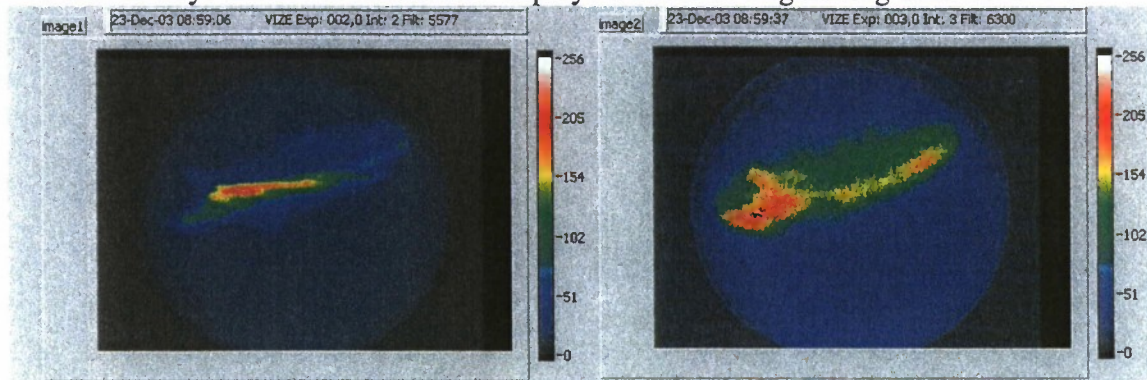
December 24, 2003

Since 0500 UT there are a series of equatorward directed arcs, some of them are short and do not last for many minutes. The main cusp is located poleward of the site. The arcs before noon show lots of rays and are very dynamic, as seen in the figure corresponding to 0556 UT. Equatorward elongated aurora (e.g. crewcut) connect to the cusp aurora. This configuration has been seen few times during this season. Later, more elongated arcs in the red and green lines appeared. These features are similar to the display of 0753 UT seen below. The westward-drifting, equatorward-elongated aurora remains until 0900 UT, but the main cusp aurora stays longer.
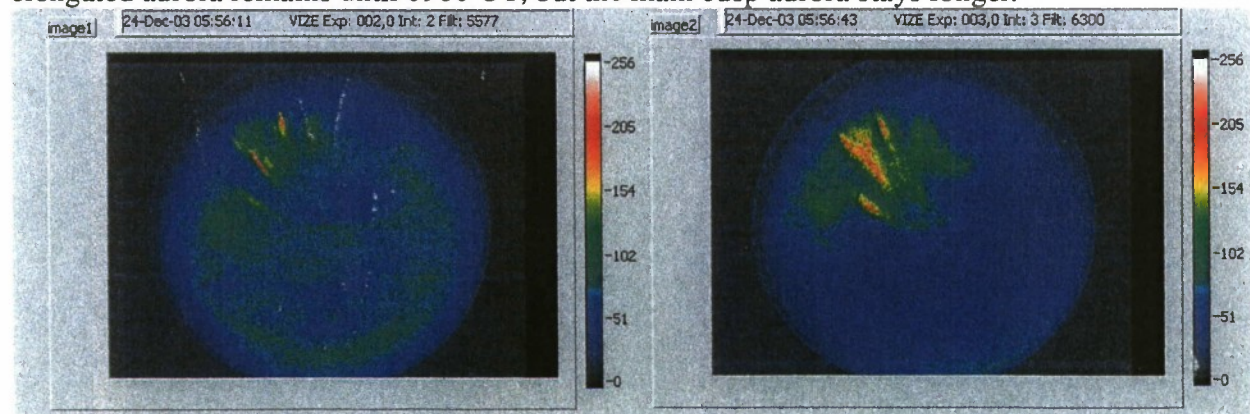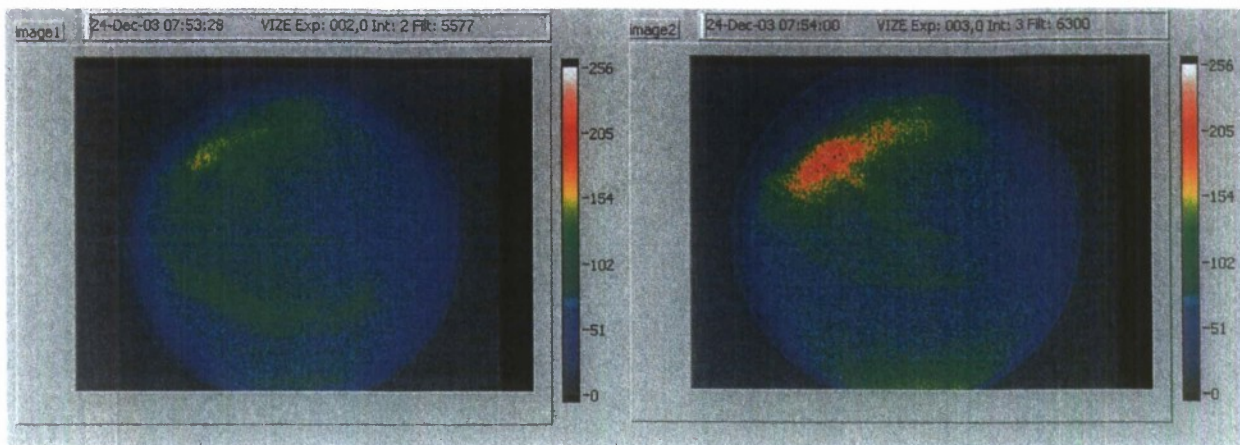
December 26, 2003

East-west aligned aurora starts at 0500 UT. This moves poleward and after 30 min seems to reach the poleward edge of the field of view. There is a period between 0700 and 0828 UT, when the sky apparently becomes hazy. There is also a period of no aurora (sort of uncommon). When the aurora displays resume, a north-south directed arc appeared in the east side and moved toward the west. A snapshot of this display is seen below. A series of arcs persisted after 1000 UT. Later they became more east-west aligned.
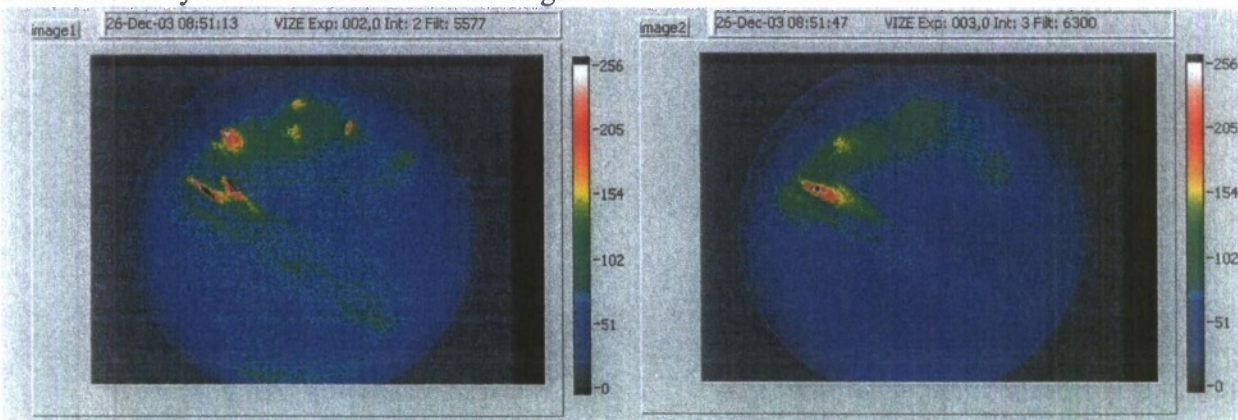
December 27, 2003

At 0500 UT there is an overhead aurora that develops into several bands. Starting at 0559 UT there is an equatorward aurora that moves eastward, opposite to all the other cases seen before during this season. At 0620 UT there appears in the east side of the imager an equatorward elongated arc that moves westward very slowly, and at 0659 it is overhead as shown in the figure More equatorward aurora is seen until 0850 UT. Later the arcs are more east-west aligned.

113
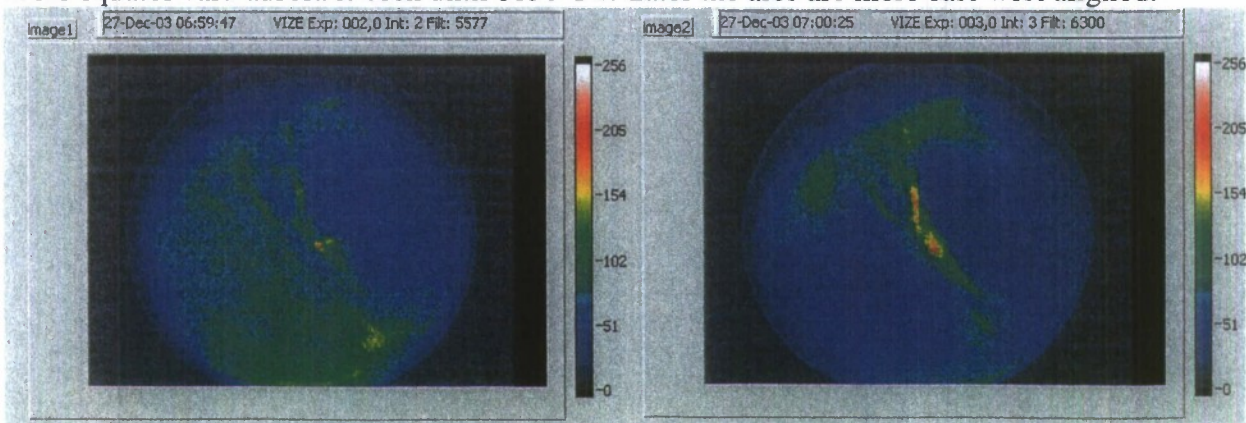
January 14, 2004

On this day, observations started at 0915 UT. Initially the aurora was placed north of the site. There occurred a succession of bright rays that developed to the south of the main aurora. As seen in the figure below a southern arc develops, forming a 45° angle with the main arc. This arc sometimes is brighter than the northern one, in other cases is weaker. At 0935 UT the northern arc becomes more prominent and splits into a multi-arc configuration. After 0950 UT, 3 or more arcs are seen near overhead. The latter arcs may not correspond to cusp aurora.
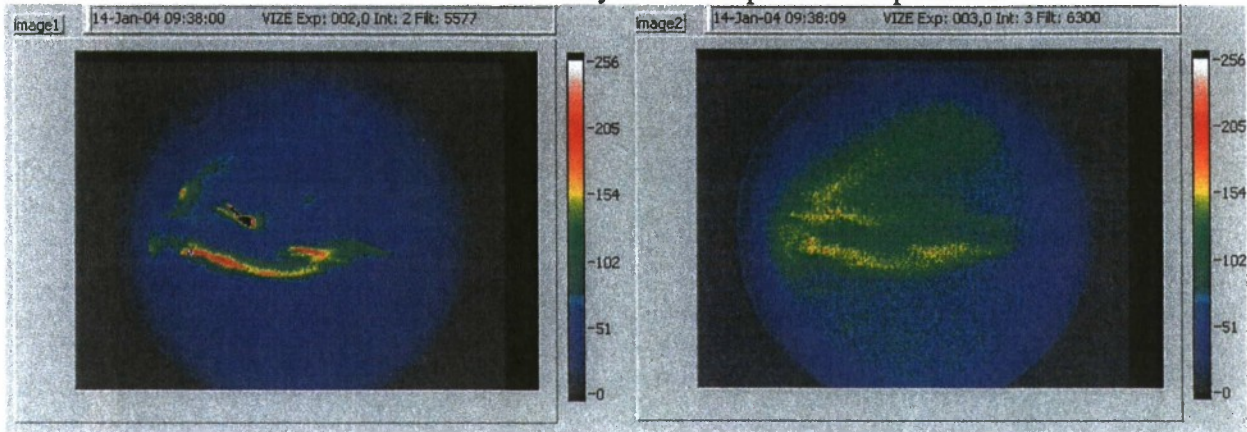
January 15, 2004

The first arc is seen at 0512 UT; it is faint but extends from horizon-to-horizon in the NE to SW direction. There is also an arc placed far to the north that is seen in the red line. The arc becomes very faint until 0600 UT, but it remains for more than an hour. The image of 0729, displayed below, shows a single green line arc extending from NE to SW. The arc lasts for ten minutes drifting to the west. Rays and spots develop after 0840 UT as seen in the figure for 0846 UT. During this day several arcs were seen in the green line with no corresponding arcs in the red.
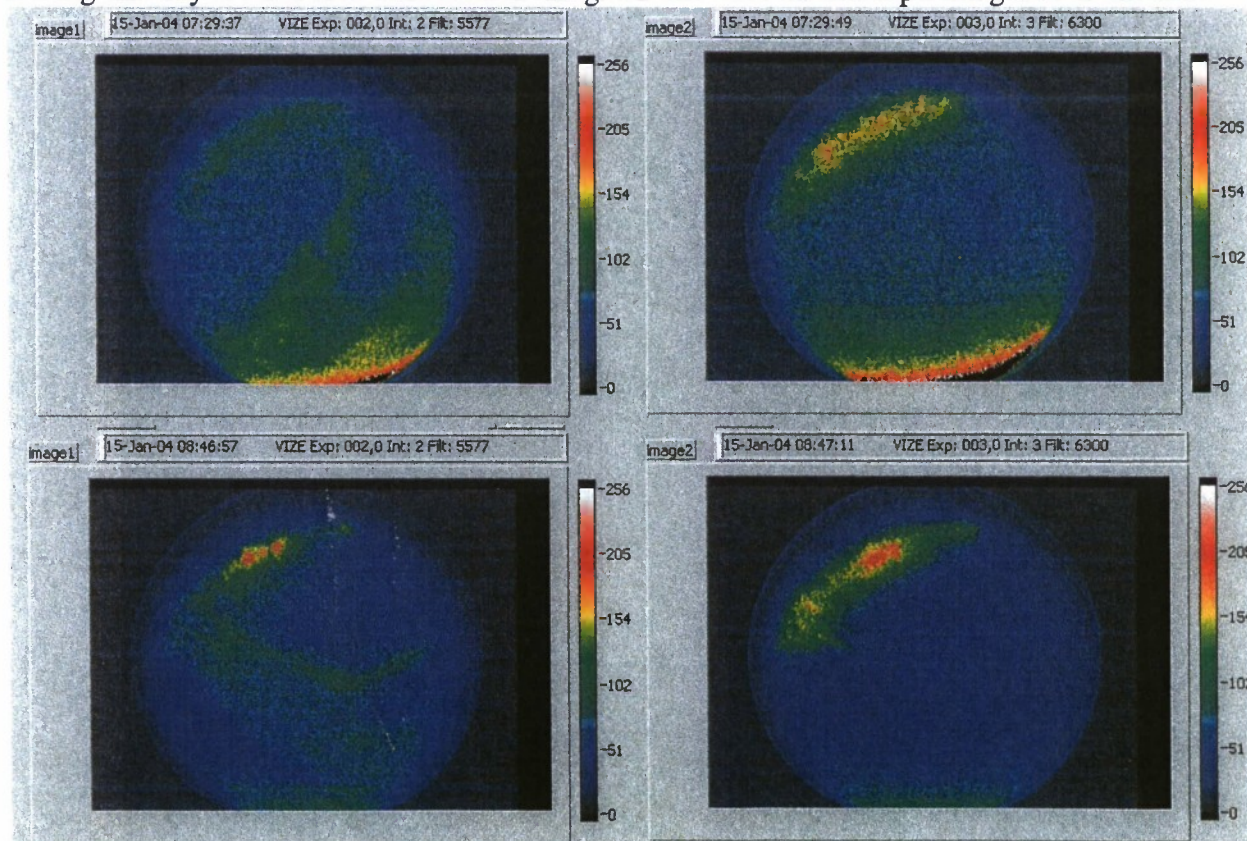
January 16, 2004

IMF B_x is the dominant component during this event. Near 0500 UT, several bands exist slightly south of overhead. Sometimes a single green line arc appears north as seen at 0509 UT. The aurora recedes south at 0520 UT, but several bands are displayed. At 0540 UT the cusp aurora moves poleward and new arcs form north of the existing arcs. By 0610 UT, the main arc is well north of the site. Sometimes small rays develop extending equatorward of the main aurora. There is a corona at 0620 UT. At 0650 UT there exists equatorward-directed arcs (crewcuts) and an undulated main aurora. A series of north-south arcs are seen drifting westward as shown in the 3 panels below. The aurora drifts slowly and a second north-south arc appears (see image for 0707 UT) that coincides with the first arc; both vanish in few minutes. The main cusp arc moves overhead and develops into a corona. It remains in this location for 30 min, displaying several brightenings. By 0800 UT there are several bands that move poleward. The main band moves to the south of the site and remains there for a while. Then it moves back to overhead. During this time it always develops rays that are prominent in the green line. By 0910 UT, the aurora is located far to the south near the southern edge of the FOV. At this time it looks more like an oval aurora than a cusp aurora.
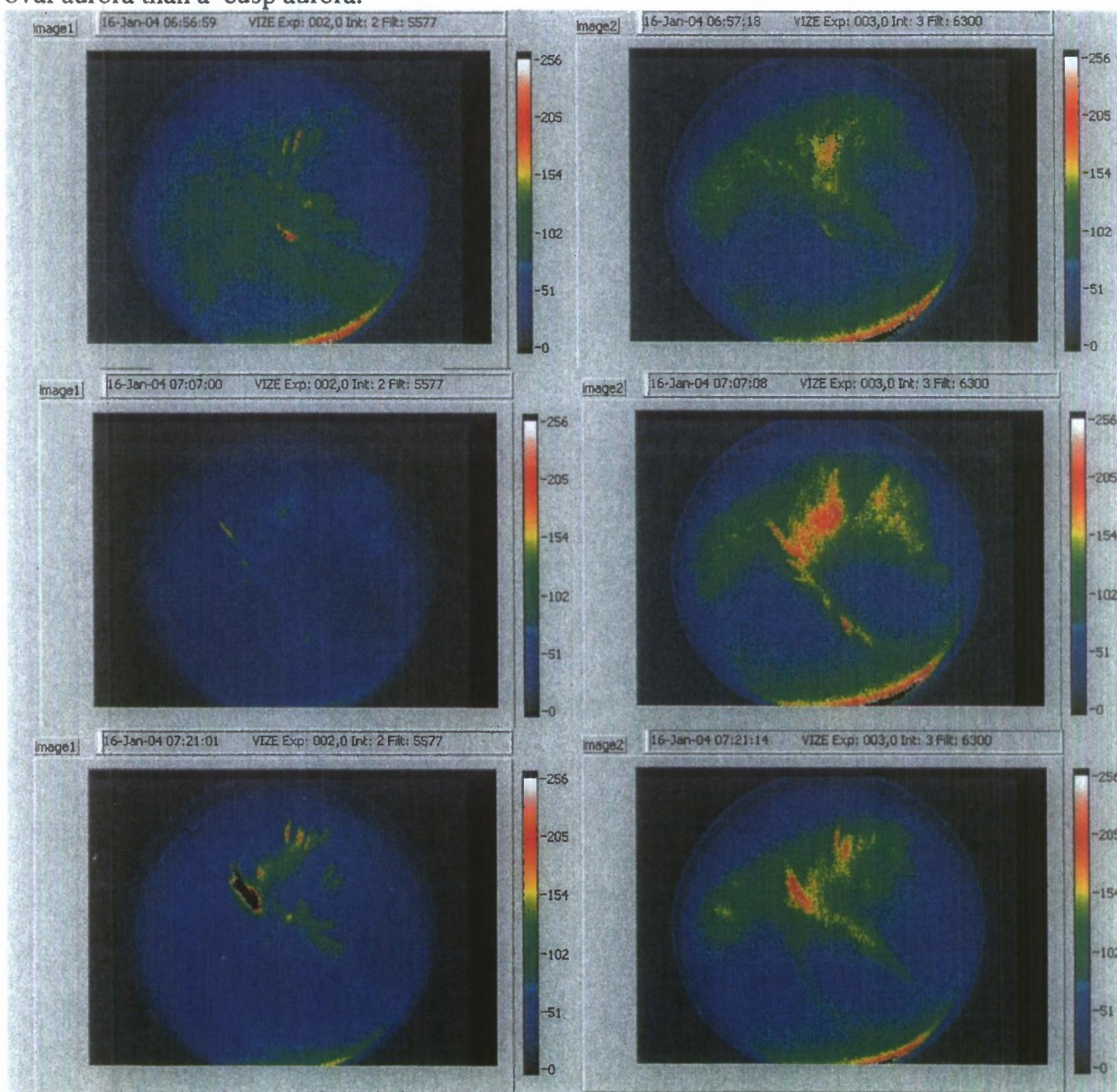
January 17, 2004

Near 0500 UT there is a series of overhead arcs. Some of them qualify as corona events. The arcs are elongated east to west but there are several small segments that drift quite rapidly. The green line shows quite narrow arcs. The red line looks more diffuse implying the presence of some haze. Bright arcs located poleward of the site appear at 0545 UT. The first image that is shown below displays an auroral event similar to previous day, but moving more rapidly. The arcs are seen moving westward. This display lasts for 10 min and then changes to east-west directed arcs. Starting at 0830 UT, it moves south reaching the southern boundary of the FOV at 0940 UT.
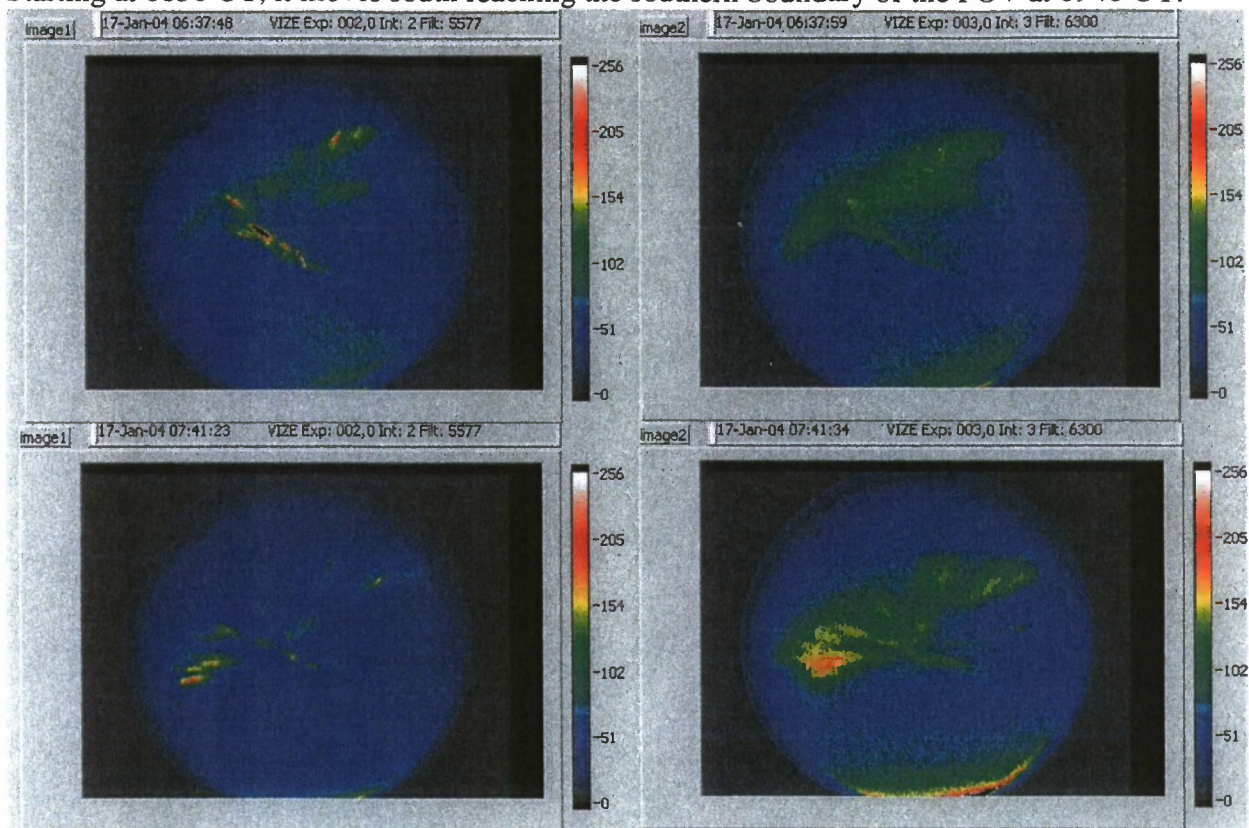
January 19, 2004

Observations started at 0814 UT. At this time there were rayed aurora located poleward of the site. The aurora is highly mobile and dynamic; it changes shape quite rapidly. Most of the time, the aurora is elongated in the east-west direction. There are some poleward moving auroral forms that seem to grow and detach from the main arc. There are also some loops and horse-shoe auroras that are formed like the configuration displayed below. There exist at least 2 arcs that are sometimes very thin. At 0940 UT several arcs form extending away from the main arc.
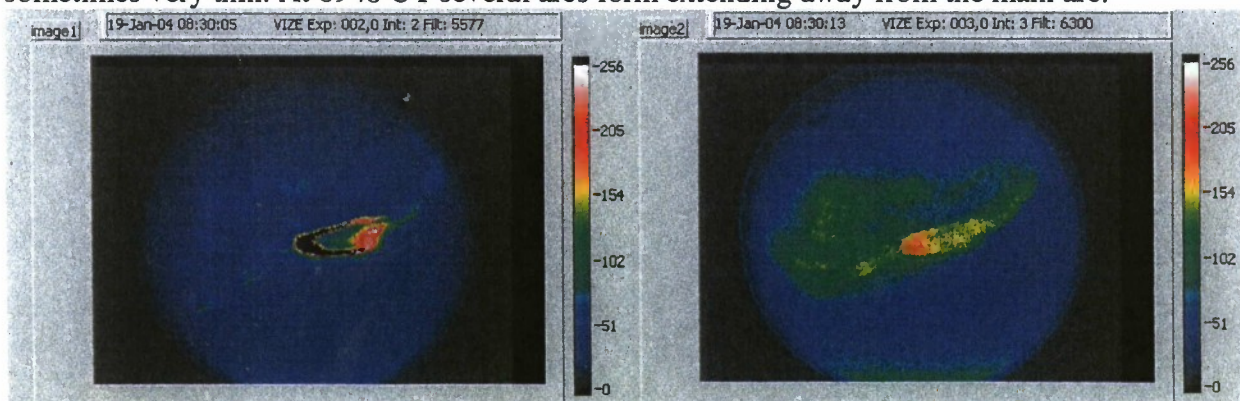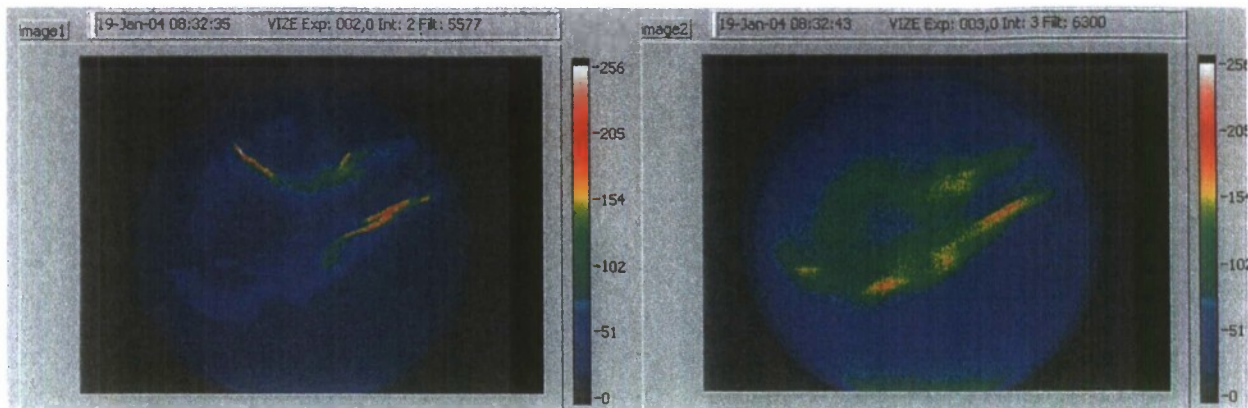
January 20, 2004

At the start of the event (0500 UT) there was an arc located south of the station (200 km). Several arcs emanate from this quasi-steady arc but they propagate until reaching a fixed location (overhead) where they decay. There is a data gap between 0600 and 0810 UT probably due to the sun's day glow. When observations resume (see image displayed below) the aurora consists of a north-south arc located near the western edge of the FOV. At 0840 UT there is a steady, wide arc placed poleward of the site and some rays aligned N-S.
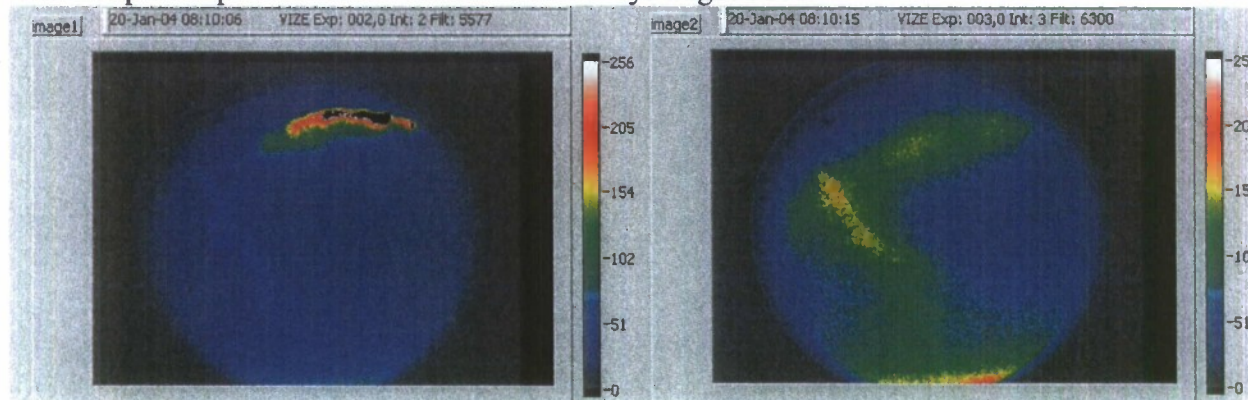
January 24, 2004

Data gap due to the presence of the dayside airglow between 0510 and 0900 UT. When data resumes there is an aurora placed almost overhead. It is steady and shows a single east-west aligned arc. However, this arc has some structure and is accompanied with additional shorter arcs. This display becomes very variable and moves poleward and then equatorward. The arcs are very bright but then decay by 0930 UT, when they become steady and faint. The aurora moves poleward and westward between 0930 and 1000 UT.
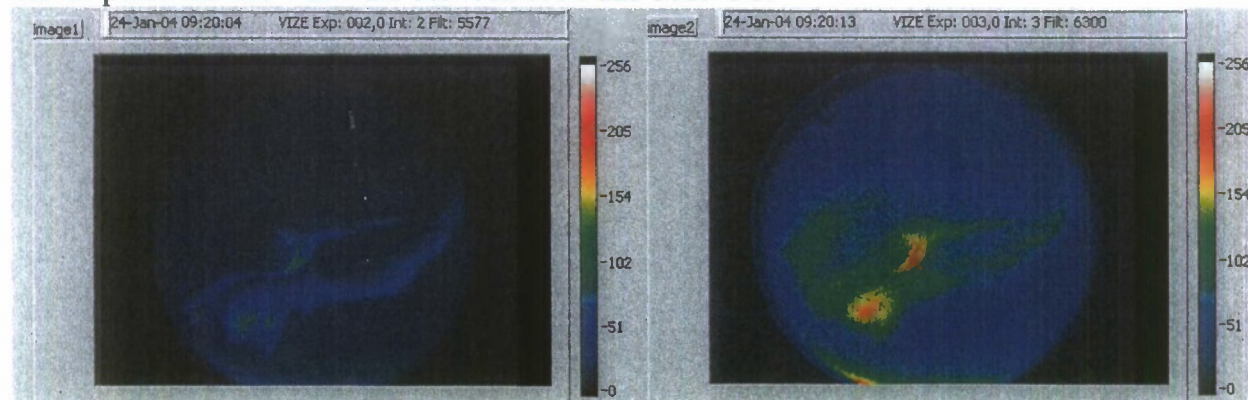
THE END

Vize Island Cusp Aurora Records, Winter: 2004-2005

November 20, 2004

On this day the aurora is spotty and small-segment aurora develops before 0800 UT. The aurora is mainly south of Vize Island. After 0720 UT the aurora moves overhead as seen in the plots stay at this location for an hour and then retracts south.
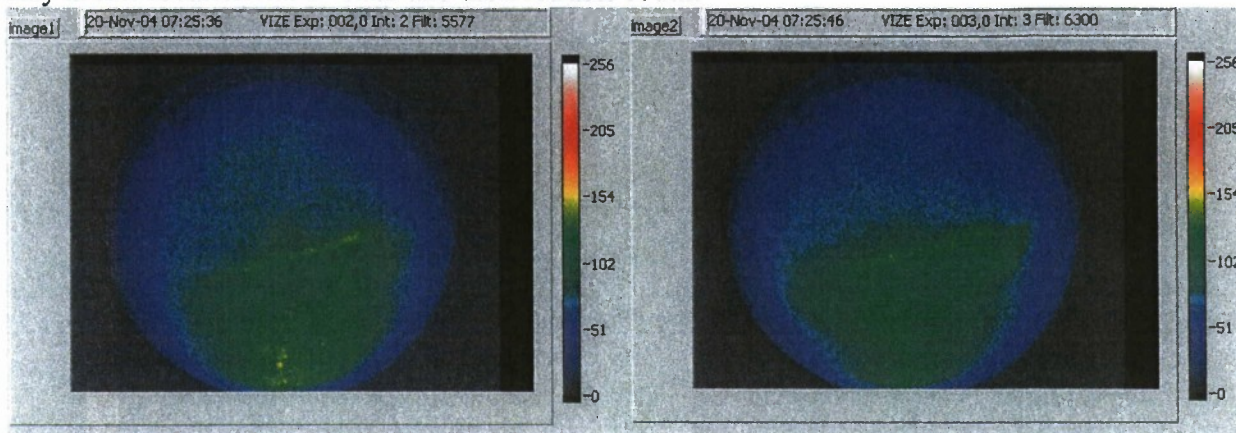

November 21, 2004

Near 0500UT the aurora is north of Vize, this may correspond to a Bz north IMF configuration/ There is a brightness at 0510-0513 UT. There is a dat gap between 0523 and 0750 UT. After the gap the cusp aurora is well north as figure shows.
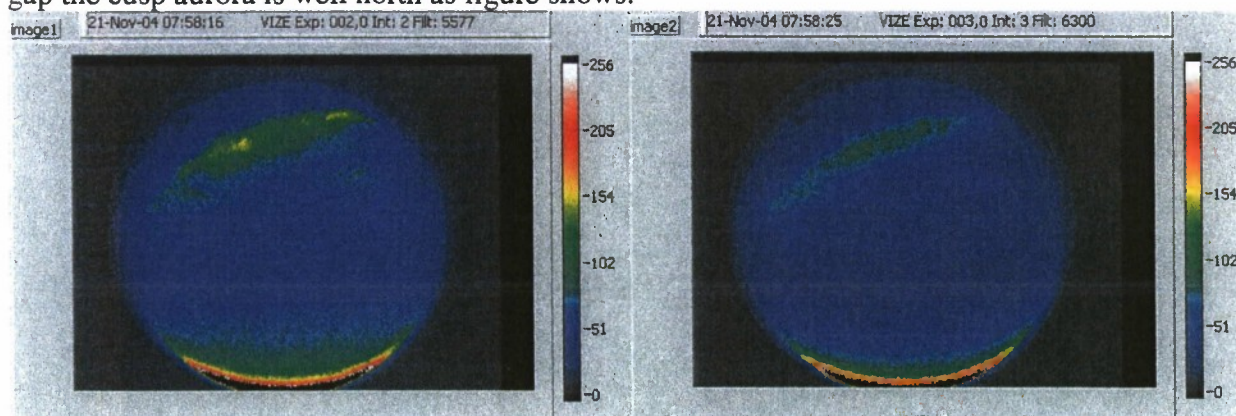
November 23, 2004

The imager only operated until 0605 UT. However, it observed a unique set of arcs that seem to drift westward. They were observed in both red and green lines. The Sun is seen to appear near 0600 UT.
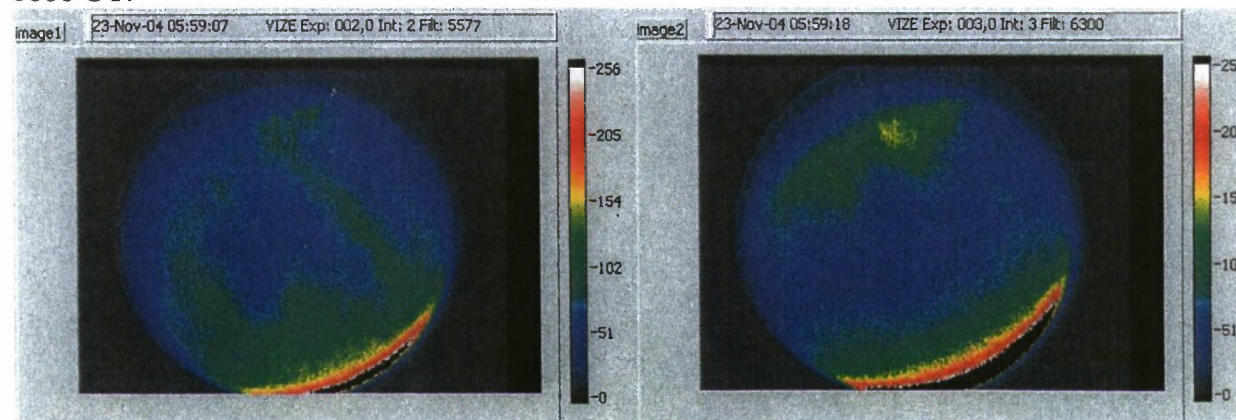
December 07, 2004

The images start at 0715 UT when the aurora is well north of Vize Island. They are very active and drift in and out and move north. After 0820 UT they seen to move south. The arc seen below seems to be rotating counter clockwise.
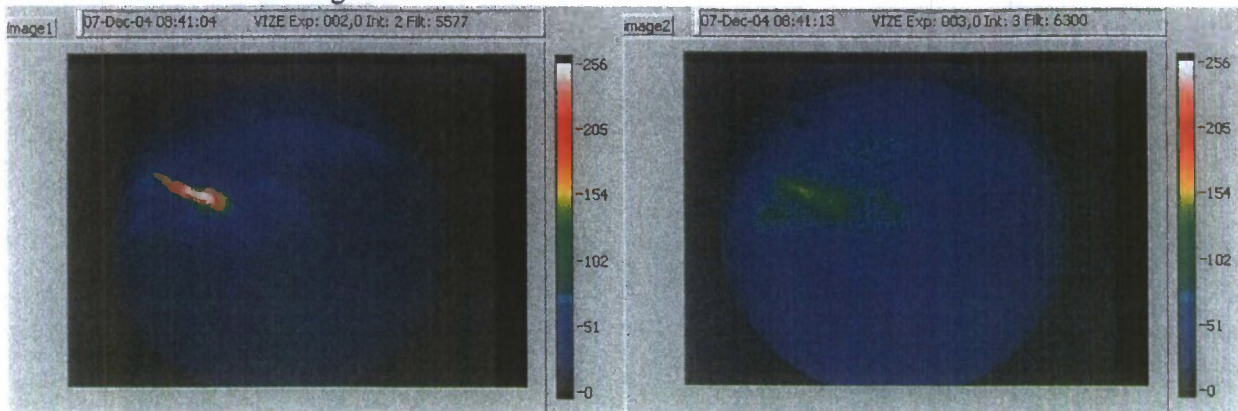

December 08, 2004

It is cloudy between 0520 and 0650 UT. However, some arcs are seen through the clouds. This is a unique event that seems to endorse previous observations of southward-directed arcs that were observed during the 2003-2004 winter. Cusp arc moves poleward then equatorward.
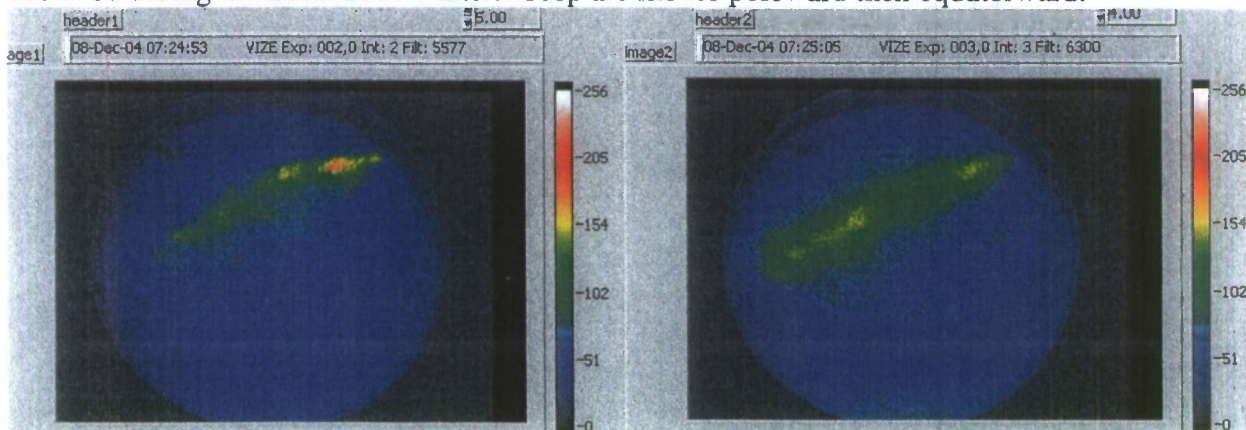

December 09, 2004

On this day there is one event of N-S aligned arc starting from the cusp aurora. This is seen in the 1st figure. The green line aurora is to the south and red line to the north. The second figure shows a series of parallel arcs. The parallel arcs last for tens of min.
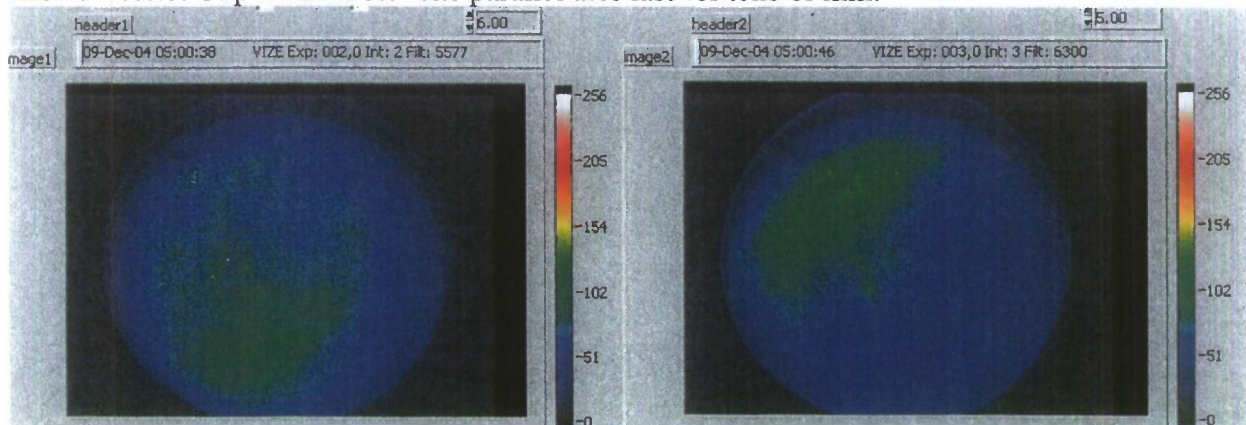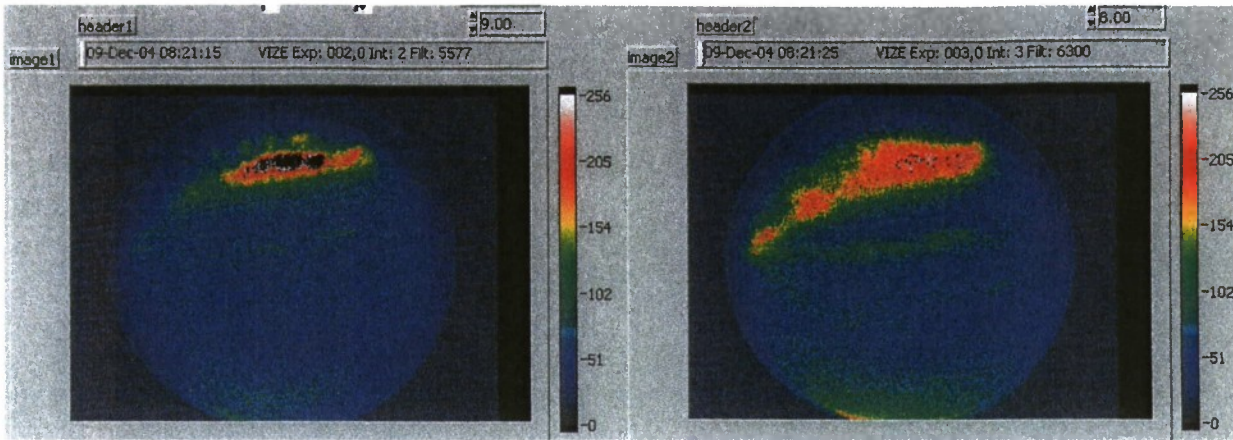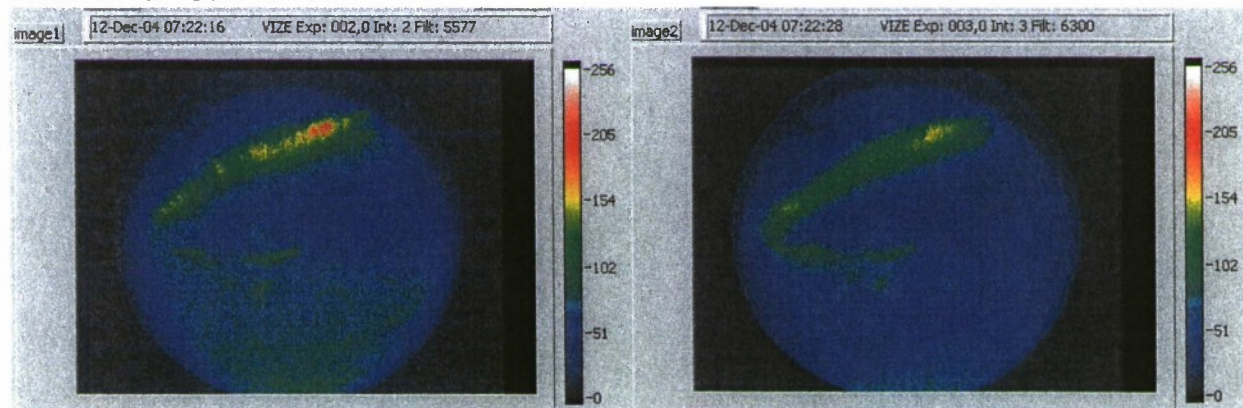
December 11, 2004

Two bands in the green & red lines are seen near local mid day. They persist in the FOV for many minutes. They persist for at least 1 hour. This is until 0830 UT. Multiple horizontal arcs are seen frequently.
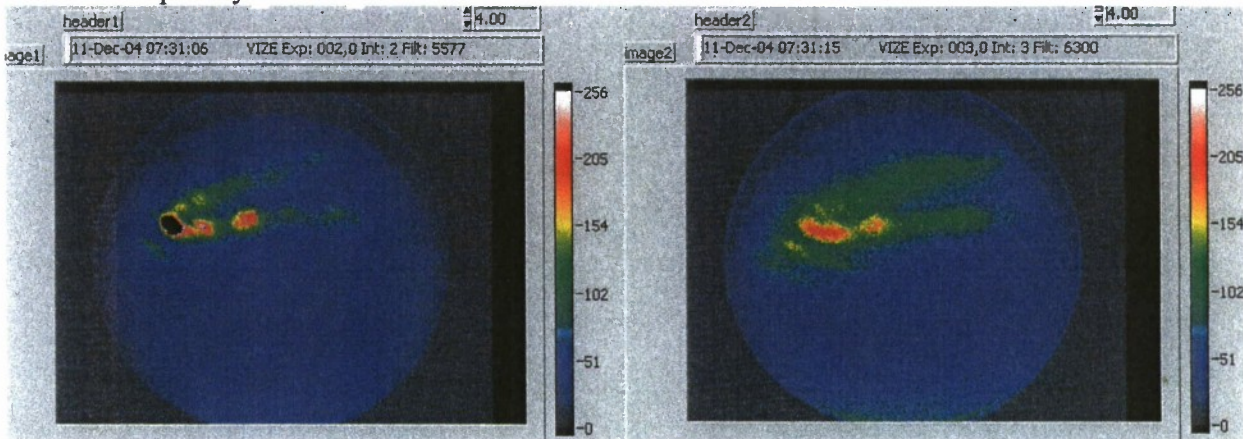
December 12, 2004

There are multiple arcs before 0700 UT. These arcs move from slightly south to overhead, where they persist most of the time. After this time, the pattern displayed in the figure is observed for about 30 min.
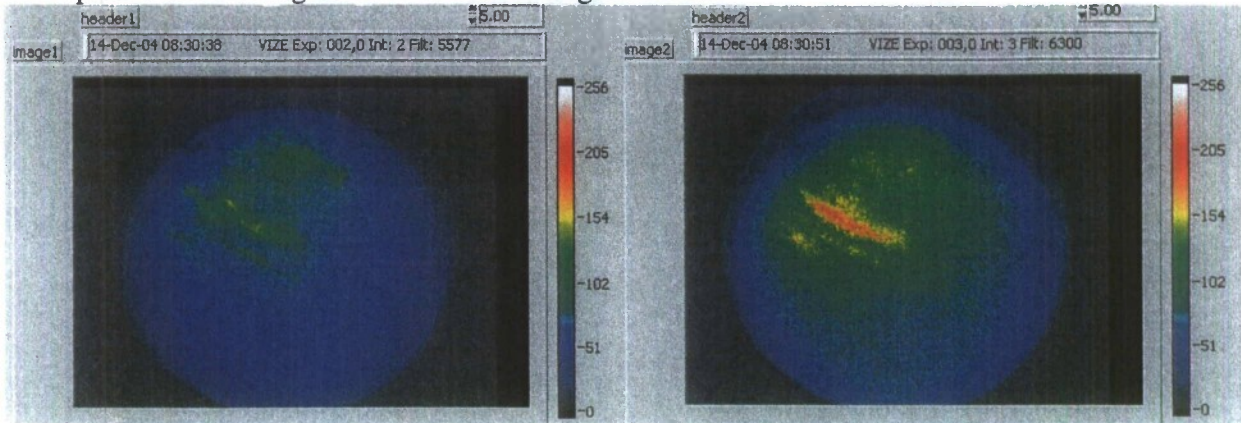
December 13, 2004

After 0500 UT, there exist arcs aligned in the N-S direction located to the north of the site. However, a haze is seen to the north and the arc images come blurry. Sky condition is overcast at 0600 UT and later. Near 0820 UT, the overcast sky condition continues but some arcs are seen

north of the site. It is quite difficult to distinguish the arc alignment. The weather did not improve throughout the night.
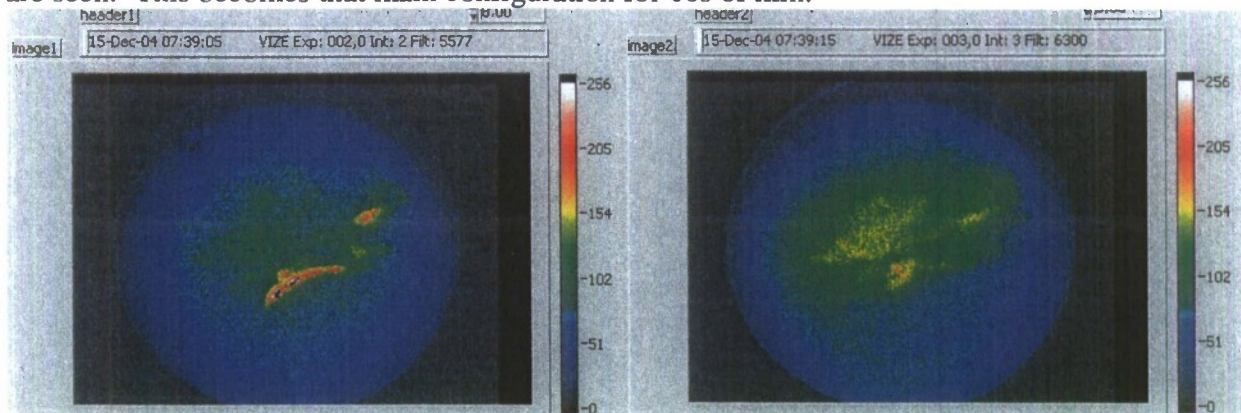
December 14, 2004

The images between 0500 and 0600 indicate some haze. At 0600 UT there is an indication of a northward-located cusp aurora. At 0656 UT, the aurora is well defined (no clouds) and placed almost overhead. One or two arcs are seen overhead, they are dynamic and quite bright. there is a short period of N-S aligned arcs as seen in Figure below.

December 15, 2004

A very persistent and steady single arc that is placed first north and then overhead the station. After 0640 UT, it develops a series of rays and curls. After 0720UT a series of discrete segments are seen. This becomes that main configuration for 10s of min.


December 18, 2004

Cloudy, some spotty aurora is seen. No proper characterization of the arcs is possible. Data are not usable.
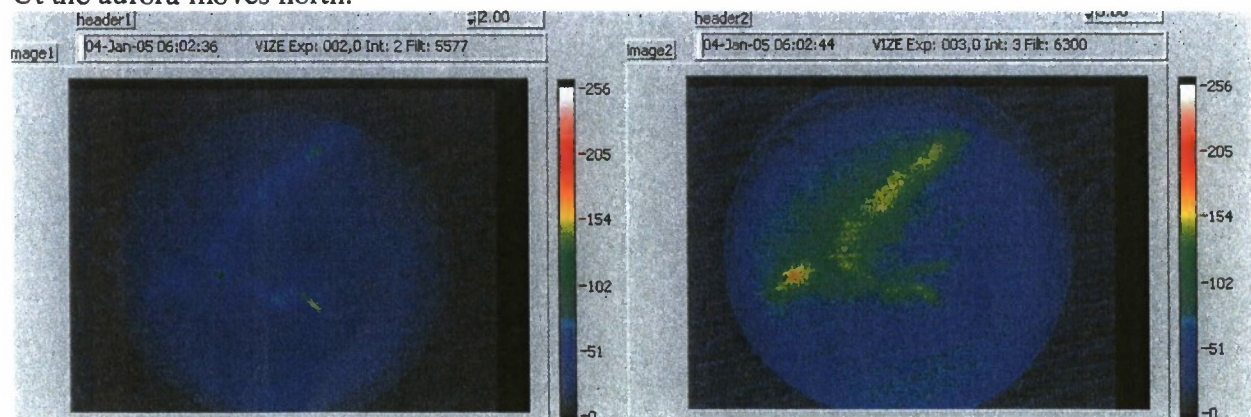

January 03, 2005

The aurora starts at 0600 UT with displays of corona-type aurora. The small arc segments are seen to move poleward and fading as they displace north. Two bands are visible at 0658 and the aurora persists more or less uniformly for 10 min. There is a sense of a westward displacement of the aurora. This motion stays even when the aurora pattern continuously change. Near 0800 UT the corona-type aurora returns with displays of a very dynamic nature. The sampling rate is below of what is desired. After 0830 UT the single arc return to the FOV and remains until the end of our observation period corresponding to 0900 UT.
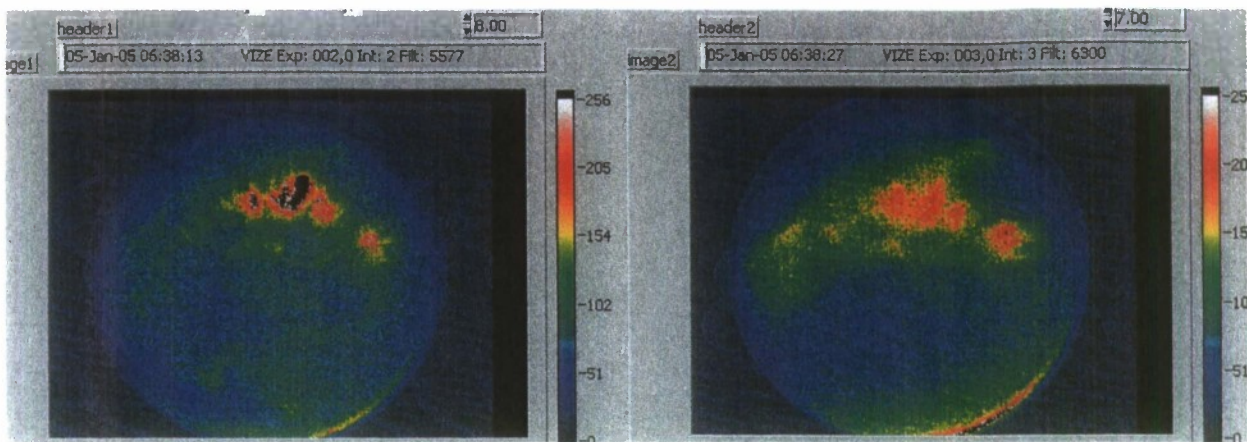
121
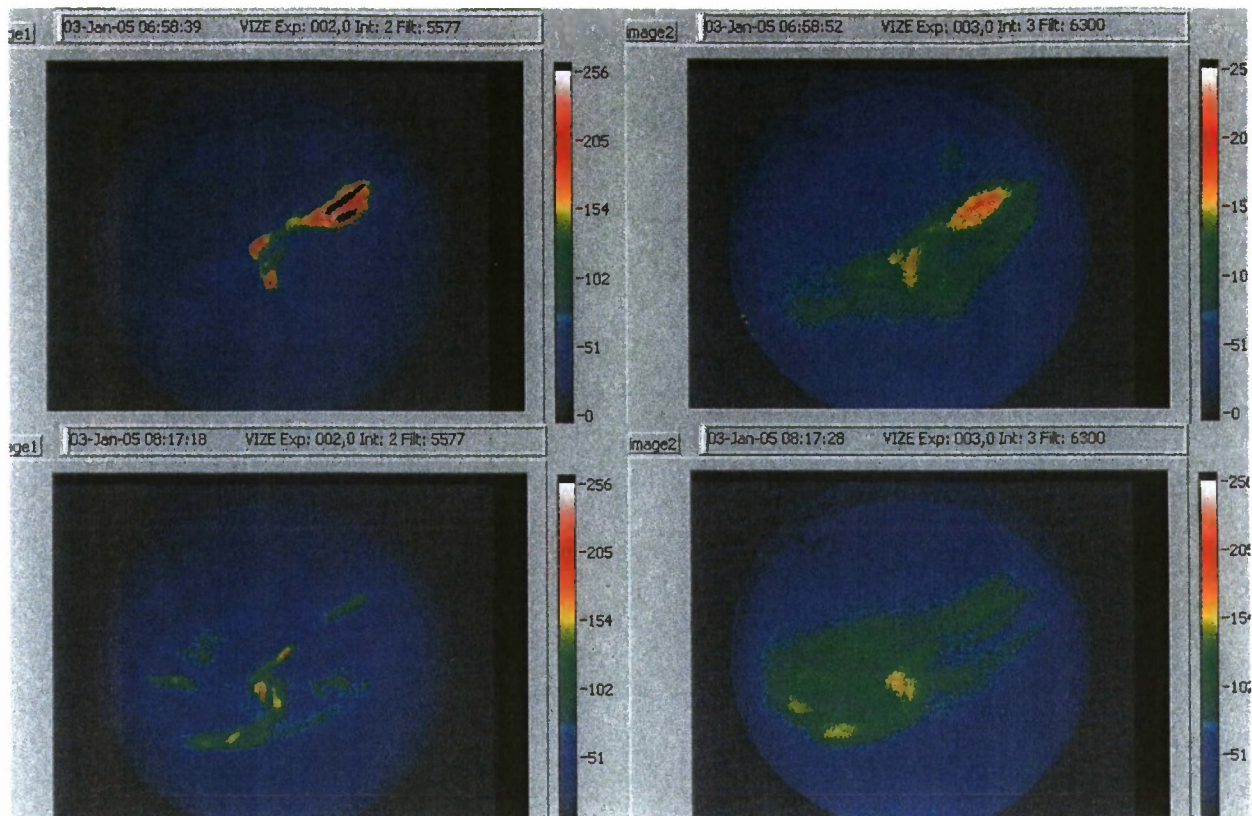
January 04, 2005

This is a dynamic aurora with characteristics changing quite often. There is a corona neat 0540 UT and then suddenly at 0602 UT it develops N-S aligned arcs. Several auroral arcs are seen later located south. Aurora seems to migrate south and then suddenly moves north and a single arc is seen way north. Looks like a typical Bz north aurora. The display continues with a series of "crewcut" arcs. Green line is seen between 0650 and 0710 UT accompanied with weak red line. After 0720 UT the aurora moves south and remains overhead for tens of min. Aftyer 0830 Ut the aurora moves north.

January 05, 2005

At the beginning the aurora is nearly overhead then slowly moves north and develops a second arc. New arcs are created south of the equatorward of the present arc, which vanishes as the new structure moves poleward. At 0620 UT a single arc moves north and remains there for tens of min. The arc seen below last for few minutes during a dynamic excursion of some N-S aligned arcs. After 0800 UT the aurora drifts south and becomes quite dynamic.

header1 05-Jan-05 06:38:13 VIZE Exp: 002,0 Int: 2 Filt: 5577
header2 05-Jan-05 06:38:27 VIZE Exp: 003,0 Int: 3 Filt: 6300

January 06, 2005

At the beginning, 0500 UT, there exists a steady aurora located well north of the site. Some clouds seem to be placed also north that make the green line almost useless. At 0602 UT there is a small spot near the center of the arc. This is brighter than the rest of the aurora; it drifts westward. The north aurora remains in place for the rest of the observations sometimes developing southward striations as seen in Figure below. Haze comes back at the end of the observations.

image1 06-Jan-05 08:10:08 VIZE Exp: 002,0 Int: 2 Filt: 5577
image2 06-Jan-05 08:10:17 VIZE Exp: 003,0 Int: 3 Filt: 6300